Biomimetic Copper-Guanidine Complexes for Multi-Phase Reactions

Biomimetische Kupfer-Guanidin-Komplexe für Mehrphasenreaktionen

Von der Fakultät für Mathematik, Informatik und Naturwissenschaften der RWTH Aachen University zur Erlangung des akademischen Grades einer Doktorin der Naturwissenschaften genehmigte Dissertation

vorgelegt von

Larissa Daniela Laurini, M. Sc.

aus

Aachen

Berichter:	Univ.-Prof. Dr. rer. nat. Sonja Herres-Pawlis Univ.-Prof. Dr. rer. nat. Marcellus Liauw
Tag der mündlichen Prüfung:	17.12.2024

"There is no better school for a scientist than nature;
the mountains are the textbook."

David Brower (environmentalist and mountaineer)

Eidesstattliche Versicherung

Larissa Daniela Laurini

erklärt hiermit, dass diese Dissertation und die darin dargelegten Inhalte die eigenen sind und selbstständig, als Ergebnis der eigenen originären Forschung, generiert wurden.

Hiermit erkläre ich an Eides statt

1. Diese Arbeit wurde vollständig oder größtenteils in der Phase als Doktorandin dieser Fakultät und Universität abgefertigt;

2. Sofern irgendein Bestandteil dieser Dissertation zuvor für einen akademischen Abschluss oder eine andere Qualifikation an dieser oder einer anderen Istitution verwendet wurde, wurde dies klar angezeigt;

3. Wenn immer andere eigene- oder Veröffentlichungen Dritter herangezogen wurden, wurde diese klar benannt;

4. Wenn aus anderen eigenen- oder Veröffentlichungen Dritter zitiert wurde, wurde stets die Quelle hierfür angegeben. Diese Dissertation ist vollständig meine eigene Arbeit, mit der Ausnahme solcher Zitate;

5. Alle wesentlichen Quellen von Unterstüzung wurden genannt;

6. Wenn immer ein Teil dieser Dissertation auf der Zusammenarbeit mit anderen basiert, wurde von mir klar gekennzeichnet, was von anderen und was von mir selbst erarbeitet wurde;

7. Teile dieser Arbeit wurden zuvor veröffentlich und zwar in: Eine Auflistung aller Veröffentlichungen befindet sich im Abschnitt **"List of Publications and Conferences"** auf Seite III.

Aachen, den

Larissa Daniela Laurini

Preface

Collaborative Work

Parts of this work were obtained in the context of cooperation projects:

Prof. Dr. Lars Lauterbach and coworkers, Institute of Applied Microbiology RWTH Aachen University
Performance and interpretation of antimicrobial studies (Section 3.1.5)

Regina Schmidt, WG Herres-Pawlis, Institute of Bioinorganic Chemistry
Perfomance, data analysis and interpretation of EPR spectroscopic measurements (Section 3.3)

Prof. Dr. Karine Loubière and coworkers, École Nationale Supérieure Des Ingénieurs En Arts Chimiques Et Technologiques (ENSIACET) Toulouse
Performance of calibration experiments as well as mass transfer experiments with a red band-pass filter, image post-processing via MATLAB© algorithm (Arthur Béteille)
Data analysis and interpretation of MATLAB© data (Karine Loubière)
(4.1)

Prof. Dr. Michael Schlüter and coworkers, Institute of Multiphase Flows, Hamburg University of Technology
Performance and interpretation of Taylor flow experiments (Section 4.2)

Prof. Dr. Ulrich Nieken and coworkers, Institute of Chemical Engineering, Stuttgart University
Performance and interpretation of bubble column experiments (Section 4.2)

Parts of this work were obtained in cooperation with students' research projects as part of their qualification:

"Katalytische Studien an Bisguanidin-haltigen Tyrosinase-Modellen" ("Catalytic Studies on Bisguanidine-Based Tyrosinase Models"), Stefanie Zimmer, Bachelor's thesis **2020**. (Section 3.1.3)

"Tyrosinase Model System: Oxygenation of Phenol Derivates Catalyzed by a Bisguanidine Copper Bis(-oxo) Complex", Heliana Maria Núñez Ponce, research internship **2020**. (Section 3.1.3)

"Katalytische Oxygenierung phenolischer Substrate mit einem Bisguanidin-basierten Tyrosinase-Modellsystem" ("Catalytic Oxygenation of Phenolic Substrates with a Bisguanidine based Tyrosinase Model System"), Salvatore Marco Conte, research internship **2021**. (Section 3.1.3)

"Hybridguanidin-Kupferkomplexe zur mechanistischen Untersuchung von Tyrosinase -Aktivität" ("Hybridguanidine copper complexes for mechanistic studies on tyrosinase activity"), Nils Jannis Becker, Bachelor's thesis, **2021**. (Section 3.3)

"A New Hybrid Guanidine Ligand for the Catalytic Oxygenation of Phenolic Substrates" Martin Alexander Schäfer, research internship **2022**. (Section 3.2)

List of Publications and Conferences

Parts of this thesis have been published as followed:

First-author Publications

L. Laurini, M. Paul, A. Hoffmann, S. Herres-Pawlis, *Control of the Formation and Reaction of Copper-Oxygen Adduct Complexes in Multiphase Streams. In: Reactive Bubbly Flows. Fluid Mechanics and Its Applications*, by M. Schlüter, D. Bothe, S. Herres-Pawlis, U. Nieken, Vol 128, Springer, Cham, Germany, **2021**. DOI: https://doi.org/10.1007/978-3-030-72361-3_3

"Reactive Mass Transfer around Isolated Bubbles Rising in a Thin-Gap Cell"
Laurini, L., Béteille, A., Fink, G., Herres-Pawlis, S. and Loubière, K, *Chem. Eng. Technol.*, **2023**, *46*, 1664-1672. DOI: https://doi.org/10.1002/ceat.202300031

"From Phenols to Antimicrobial Phenazines: Tyrosinase-like Catalytic Activity of a Bisguanidine Based Bis(μ-oxido) Complex"
L. Laurini, S. M. Conte, K. Hüser, P. R. F. Cordero, H. M. Núñez Ponce, S. Zimmer, L. Lauterbach, S. Herres-Pawlis, *Eur. J. Inorg. Chem.*, **2024**, e202300700. DOI: https://doi.org/10.1002/ejic.202300700

Co-author Publications

S. Gast, U. Tuttlies, L. Laurini, F. Kexel, D. Merker, L. Böhm, M. A. Taborda, M. Sommerfeld, M. Kraume, M. Schlüter, S. Herres-Pawlis, U. Nieken, *Investigation of Reactive Bubbly Flows in Technical Apparatuses. In: Reactive Bubbly Flows. Fluid Mechanics and Its Applications*, by M. Schlüter, D. Bothe, S. Herres-Pawlis, U. Nieken, Vol 128, Springer, Cham, Germany, **2021**. DOI: https://doi.org/10.1007/978-3-030-72361-3_24

Publication resulting from collaborative working during the time as doctoral candidate not discussed in this work:

"Kinetic Investigation of the Reaction of Dioxygen with the Copper(I) Complex $[Cu(Pim^{iPr_2})(CH_3CN)]CF_3SO_3$ $\{Pim^{iPr_2}$ *= Tris[2-(1,4-diisopropylimidazolyl)]phosphine}"*
M. Lerch, M. Weitzer, T.-D. J. Stumpf, L. Laurini, A. Hoffmann, J. Becker, A. Miska, R. Göttlich, S. Herres-Pawlis, S. Schindler, *Eur. J. Inorg. Chem.* **2020**, *33*, 3143-3150. DOI: https://doi.org/10.1002/ejic.202000462

Conference contributions

09/2019 Oral presentation at Annual Meeting DFG priority program SPP1740 *"Reactive Bubbly Flows"* (Title: *"N-Donor Stabilized Oxo and Peroxo Species and their Activity in Hydroxylation Reactions"*)

01/2020 Flash Talk presentation and Poster presentation at New Year’s Symposium of the Department of Organic Chemistry at RWTH Aachen University (Tilte: *"Copper Bisguanidine Complexes as Tyrosinase Model Systems for Catalytic Hydroxylation and Oxidation of Phenolic Substrates”*)

03/2020 Poster presentation at the KCT conference in Freiburg (Title: *“Modeling Tyrosinase with a Copper Bisguanidine Complex Catalyzing the Oxygenation of Various Phenolic Substrates”*)

06/2021 Oral presentation at Master’s Open Day of RWTH Aachen University (Title: *"News from Tyrosinase Model Systems”*)

03/2023 Oral presentation at New Year’s Symposium of the Department of Organic Chemistry at RWTH Aachen University (Title: *"Copper Guanidine Complexes for Reactive Mass Transfer in-between Gas and Liquid Phase of Single Rising Bubbles"*)

03/2024 Poster presentation at 10th BioSC Forum - Internal retreat (Title: *"LignoPharm from the Valorisation of Lignin to New Pharmaceuticals"*)

08/2024 Oral presentation at 17th EurBIC conference in Muenster (Title: *"Bisguanidine Copper Complexes: Biomimetic Catalysts for Mass Transfer Studies And Synthesis of Antimicrobial Phenazines"*)

Danksagung

Auf den folgenden Seiten möchte ich allen Menschen danken, die mich im Laufe meiner Promotion sowohl wissenschaftlich als auch privat unterstützt haben und mit ihrem Einsatz zu dieser Dissertation beigetragen haben.

Zunächst möchte ich mich bei Prof. Dr. Sonja Herres-Pawlis für die Möglichkeit zur Erstellung dieser Dissertation bedanken. Für wissenschaftliche Fragen stand ihre Tür immer offen und wir führten zahlreiche anregende Diskussionen. Im Rahmen von diversen Kooperationsprojekten wurde mir der Austausch mit Wissenschaftler*innen aus unterschiedlichen Fachrichtungen ermöglichst. Durch die Teilnahme an nationalen Konferenzen konnte ich außerdem meine Fähigkeiten zur Kommunikation von Wissenschaft ausbauen.

Bei Prof. Dr. Ulrich Nieken und seinen Mitarbeitern*innen, insbesondere Dr. Ute Tuttlies und Dr. Sebastian Gast, sowie dem Arbeitskreis von Prof. Dr. Michael Schlüter und seinen Mitarbeitern*innen, insbesondere Dr. Felix Kexel möchte ich mich für die erfolgreiche Zusammenarbeit im Rahmen des Kooperationsprojektes Sonderschwerpunktprogramm 1740 „Reaktive Blasenströmungen“ bedanken. Außerdem danke ich Prof. Dr. Lars Lauterbach und seinen Mitarbeitern*innen für unsere erfolgreiche Zusammenarbeit im Rahmen von bakteriellen Studien.

Prof. Dr. Karine Loubière danke ich für die Ermöglichung eines Forschungsaufenthaltes in ihrer Arbeitsgruppe am ENSIACET in Toulouse. Ich bedanke mich außerdem bei Emmanuel Cid und Alain Portier für ihre Unterstützung im Labor und bei technischen Fragen in dieser Zeit. Arthur Béteille danke ich für die Durchführung von Experimenten und Kalibrierungsmessungen sowie die Auswertung der Messdaten.

Dem Deutschen Akademischen Austauschdienst danke ich für die finanzielle Förderung meines Auslandsaufenthaltes am ENSIACET in Toulouse im Rahmen eines Kurzzeitstipendiums.

Ich bedanke mich bei Herrn Prof. Marcel Liauw für die Übernahme des Zweitgutachtens.

Mein Dank geht an Dr. Alexander Hoffmann für Korrekturen zahlreicher wissenschaftlicher Arbeiten, Hilfestellung bei labortechnischen Problemen und die Finalisierung von Kristallstrukturen.

Claudia Nelleßen und Gwenda Golm danke ich für die organisatorische Unterstützung im Arbeitskreis sowie ihre stetige Hilfsbereitschaft und Hilfestellung bei Finanz- und Verwaltungsfragen.

Ein großer Dank gilt dem gesamten Arbeitskreis Herres-Pawlis. Eine angenehme Arbeitsatmosphäre und die wissenschaftliche Unterstützung tragen entscheidend zur Motivation während der Promotion bei. Die gemeinsame Zeit sowohl im Labor, beim Mittagessen als auch bei privaten Veranstaltungen wie Running-Dinnern und Weihnachts-/Karnevalsfeiern habe ich stets sehr geschätzt. Bei meinen Laborpartnerinnen Dr. Melanie Paul, Christine Müller und Dr. Rosalie Dalhoff möchte ich mich für den anregenden fachlichen Austausch, unzählige Korrekturen von Vorträgen und wissenschaftlichen Arbeiten sowie die amüsanten Saalputze bedanken. Dr. Rosalie Dalhoff und Christine Müller, sowie Dr. Martin

Fuchs, Dr. Regina Schmidt, Dr. Henrika Hüppe und Tobias Seitz danke ich außerdem für das Korrekturlesen dieser Arbeit. Dr. Melanie Paul sowie Dr. Henrika Hüppe danke ich für die Durchführung von Einkristall-Röntgendiffraktometrie-Messungen und der Unterstützung bei der anschließenden Datenauswertung. Ganz besonders möchte ich Dr. Regina Schmidt danken, die mich nicht nur wissenschaftlich durch fachlichen Austausch im gemeinsam bearbeiteten Themenfeld unterstützt hat, sondern mich auch privat durch viele Höhen und Tiefen begleitete.

Stefanie Zimmer, Heliana Núñez Ponce, Nils Becker, Salvatore Conte und Martin Schäfer danke ich für ihre Unterstützung bei Laborarbeiten in Rahmen ihrer Abschluss-/Forschungsarbeiten.

Ich danke allen weiteren Mitarbeitern des Institutes für Anorganische Chemie für die gute Zusammenarbeit. Besonderer Dank gilt hierbei dem technischen Personal aus mechanischer und elektronischer Werkstatt, der Glasbläserei und der Materialausgabe, ohne die eine reibungslose Laborarbeit nicht möglich wäre. Brigitte Pütz danke ich für die Ausdauer bei der Durchführung zahlreicher Massenspektrometrie-Messungen. Dr. Gerhard Fink danke ich für die Unterstützung bei komplexen Nuclear-Magnetic-Resonance (NMR) Messungen und die Auswertung von DOSY-NMR Messungen. Des Weiteren gilt mein Dank Brigitte Pütz, Barbara Bailly-Kaminski, Irmgard Kalf und Manuela Lumbardu-Böhme für viele nette Gespräche sowie immerwährende Hilfsbereitschaft und Unterstützung bei der Betreuung studentischer Praktika. Guido Kirf danke ich für akute Hilfe bei technischen Notfällen und die tatkräftige Hilfe bei der Erneuerung meiner Glovebox.

Markus Reichelt vom DWI Aachen danke ich für die Durchführung von Tensiometer-Messungen zur Bestimmung der Oberflächenspannung.

Für ihre moralische Unterstützung, sowie schöne (sportliche) Zeiten abseits des Labors möchte ich meinen Freunden und insbesondere der „Bambi Gruppe“ danken. Ein großer Dank gilt außerdem Nils Jansen, der mich vor allem in stressigen Zeiten der Schreibphase motiviert und unterstützt hat.

Meinen Eltern danke ich für die finanzielle Unterstützung meines Studiums und das immer vorhandene offene Ohr bei Problemen jeglicher Art. Meiner gesamten Familie danke ich für ihre vielfältige Unterstützung und den stetigen Rückhalt während des Studiums und der Promotion.

Zuletzt geht ein großer Dank an meinen Partner Lucas Stüwe für das Korrekturlesen von großen Teilen dieser Arbeit, die Motivation in schwierigen Phasen der Promotion und dass er mir in allen bisherigen Höhen und Tiefen zur Seite stand.

Abstract

Many synthesis pathways of basic chemicals used in industrial processes are oxidation reactions utilizing simple, gaseous oxidants like molecular oxygen or air. Continuous flow reactors or semi-batch reactors are most commonly used in which the gaseous oxidant is bubbled through the liquid phase containing further reactants dissolved in the reaction mixture. To create an accessible oxidizing agent, cost-intensive and/or hazardous transition metal catalysts are needed for oxygen activation. In nature, oxygen activation is mediated by metalloenzymes like tyrosinase. The enzyme consists of a catalytically active Cu_2O_2 peroxido center stabilized by six histidine N-donor ligands. While most enzymes are working substrate-specific, tyrosinase converts phenols as well as *ortho*-dihydroxybenzenes to the related *ortho*-quinones. New inexpensive, environmentally-friendly oxidation catalysts for industrial applications are needed mimicking the natural catalytic activity of tyrosinase.

In this study, the catalytically active Cu_2O_2 peroxido center of tyrosinase is mimicked by synthetic peroxido as well as isoelectronic oxido complexes. Therein, the Cu_2O_2 center is stabilized by bisguanidine, hybrid guanidine or diamino ligands.

The intermediate species present during the catalytic hydroxylation and subsequent oxidation of phenols mediated by tyrosinase is still under debate. Therefore, a synthetic model of the intermediate is generated using a hybrid guanidine ligand and investigated via X-ray diffraction (XRD) and electron paramagnetic resonance (EPR) spectroscopy.

A bisguanidine ligand is used to synthesize an oxido complex able to convert a broad spectrum of non-natural substrates like naphthols, quinolinols and indolols. The resulting *ortho*-quinone products are unstable under ambient conditions and are transformed into stable phenazine products in a following condensation reaction with 1,2-phenylenediamine. As naturally occurring phenazine derivatives function as anti-microbial agents, the antibacterial behavior of synthesized phenazine products is tested evaluating their potential as antibiotics.

Industrial oxidation processes are focusing on maximizing yield and selectivity of the desired product with minimal use of reactants. A significant influencing factor is the mass transfer of the gaseous oxidizing agent into the liquid phase where the reaction takes place. Formation and decay of Cu_2O_2 species as well as catalytic conversion of phenolic substrates are involving the reaction of molecular oxygen with a liquid reaction mixture. These consecutive and competitive consecutive reactions are investigated herein to get deeper insights in the influencing factors of mass transfer. Therefore, several types of (confined) reaction set-ups are used: Small Taylor flows ($V = 0.03$ l) with bubble movements limited to one direction over Hele-Shaw cells allowing movements in two directions ($V = 0.08$ l) to unconfined bubble columns near to industrial conditions (V = 2 l). Thereby, the independence of mass transfer from the chemical system used is studied. Additionally, the influence of bubble / reactor parameters on the selectivity of a competitive consecutive reaction is investigated.

Kurzzusammenfassung

Viele industrielle Synthesen von Plattformchemikalien basieren auf Oxidationsreaktionen mit einfachen, gasförmigen Oxidationsmitteln wie molekularem Sauerstoff oder Luft. Meist werden kontinuierliche Rohrreaktoren oder halbkontinuierliche Rührkesselreaktoren verwendet, in denen die flüssige Phase, in der alle weiteren Reaktanten gelöst sind, vom gasförmigen Oxidationsmittel durchströmt wird. Zur Erzeugung eines reaktiven Oxidationsmittels werden teure, oft umweltschädliche Übergangsmetallkatalysatoren benötigt. In der Natur wird die Sauerstoffaktivierung durch Metalloenzyme wie Tyrosinase katalysiert, die aus einem katalytisch aktiven Cu_2O_2-Peroxidozentrum bestehen, das durch sechs Histidin-N-Donor-Liganden stabilisiert wird. Während Enzyme meist substratspezifisch arbeiten, ist die Tyrosinase in der Lage sowohl Phenole als auch *ortho*-Dihydroxybenzole in die entsprechenden *ortho*-Chinone umzuwandeln. Die Nachbildung des katalytisch aktiven Zentrums der Tyrosinase bietet einen neuen Zugang zu umweltfreundlichen Oxidations - katalysatoren für industrielle Anwendungen.

In dieser Studie wird das katalytisch aktive Cu_2O_2-Zentrum von Tyrosinase mittels synthetischer Peroxido- und Oxidokomplexe stabilisiert durch Bisguanidin-, Hybridguanidin- oder Diaminoliganden nachgeahmt. Welches Zwischenprodukt bei der katalytischen Umsetzung von Phenolen durch Tyrosinase die entscheidende Rolle spielt, ist noch nicht hinreichend geklärt. Daher wird ein synthetisches Modell des Zwischenprodukts unter Verwendung eines Hybridguanidin-Liganden synthetisiert und mittels Röntgenbeugung (XRD) und paramagnetischer Elektronenresonanzspektroskopie (EPR) untersucht.

Ein Bisguanidin-stabilisierter Oxido-Komplex wird zur Umsetzung eines breiten Spektrums synthetischer Substrate wie Naphthole, Chinolinole und Indolole zu *ortho*-Chinonen eingesetzt. Da diese unter Umgebungsbedingungen instabil sind, folgt eine Kondensation mit 1,2-Phenylendiamin zu stabilen Phenazin-Produkten. Natürlich vorkommende Phenazinderivate zeigen ein antimikrobielles Verhalten, daher wird das Potential der synthetisierten Phenazine abschießend in Bakterienstudien untersucht.

Industrielle Oxidationsprozesse streben die Maximierung von Ausbeute und Selektivität des gewünschten Produkts bei minimalem Reaktantenverbrauch an. Ein wichtiger Einflussfaktor ist dabei der Stoffübergang des gasförmigen Oxidationsmittels in die Reaktionsmischung. Bildung und Zerfall von Cu_2O_2-Spezies, sowie die katalytische Umwandlung von phenolischen Substraten erfolgt durch die Reaktion von molekularem Sauerstoff mit einem flüssigen Reaktionsgemisch. Die verschiedenen Arten von (konkurrierenden) Folgereaktionen werden genutzt, um tiefere Einblicke in die Einflussfaktoren des Stofftransfers zu erhalten. Dazu werden verschiedene Reaktionsaufbauten verwendet: Von kleinen Taylor-Strömungen ($V = 0{,}03$ l) mit eindimensionaler Blasenbewegung über zweidimensionale Hele-Shaw-Zellen ($V = 0{,}08$ l), bis hin zu industrienahen, uneingeschränkten Blasensäulen (V = 2 l). Dabei wird die Unabhängigkeit des Stoffübergangs vom eingesetzten chemischen System, sowie der Einfluss von Blasen-/ Reaktorparametern auf die Selektivität einer konkurrierenden Folgereaktion untersucht.

List of Compounds

Compounds resynthesized according to literature are marked with an asterisk symbol (*). Compounds provided by the working group are noted with a paragraph symbol (§) Compounds purchased are listed for completeness and are marked with a hash symbol (#). Newly synthesized compounds with unconfirmed molecular structure are listed with a dollar symbol ($). Complexes are numbered analogously to their related ligand species. Copper(I) precursor complexes are abbreviated with **Pr**, bis(μ-oxido) dicopper(III) complexes are named **O** and μ-η^2:η^2-peroxido dicopper(II) species are listed as $^{\mathbf{S}}$**P**. Complexes analysed via X-ray diffraction are noted with a tilde symbol (~).

Ligands:

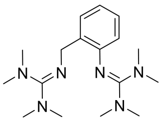

TMG$_2$tol *
L1

$C_{17}H_{30}N_6$
318.47 g mol^{-1}

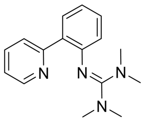

TMGphpy
L2

$C_{16}H_{20}N_4$
268.36 g mol^{-1}

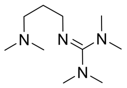

TMGdmap §
L3

$C_{10}H_{24}N_4$
200.33 g mol^{-1}

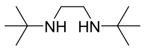

DBED #
L4

$C_{10}H_{24}N_2$
172.32 g mol^{-1}

Complexes:

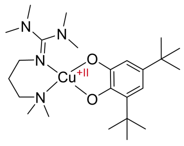

[Cu(3,5-DTBC)(TMGdmap)] *~
[3,5-DTB-CAT3]

$C_{24}H_{44}CuN_4O_2$
484.19 g mol^{-1}

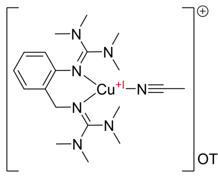

[Cu(TMG$_2$tol)(CH$_3$CN)](CF$_3$SO$_3$) *
[Pr1]OTf

$C_{20}H_{33}CuF_3N_7O_3S$
572.13 g mol^{-1}

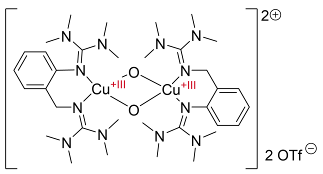

[Cu$_2$O$_2$(TMG$_2$tol)$_2$](CF$_3$SO$_3$)$_2$ *
[**O1**](OTf)$_2$

$C_{36}H_{60}Cu_2F_6N_{12}O_8S_2$
1094.16 g mol^{-1}

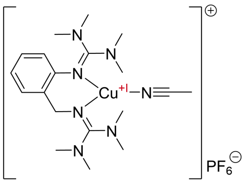

[Cu(TMG$_2$tol)(CH$_3$CN)]PF$_6$ *
[**Pr1**]PF$_6$

$C_{19}H_{33}CuF_6N_7P$
568.03 g mol^{-1}

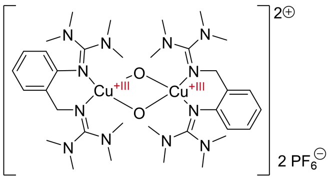

[Cu$_2$O$_2$(TMG$_2$tol)$_2$](PF$_6$)$_2$ *
[**O1**](PF$_6$)$_2$

$C_{34}H_{60}Cu_2F_{12}N_{12}O_2P_2$
1085.96 g mol^{-1}

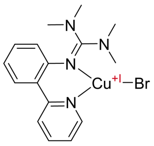

[Cu(TMGphpy)Br] $^{\$}$
[**Pr2**Br]

$C_{16}H_{20}BrCuN_4$
411.81 g mol^{-1}

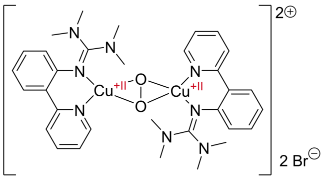

[Cu$_2$O$_2$(TMGphpy)$_2$Br$_2$] $^{\$}$
[$^{\mathbf{S}}$**P2**](Br)$_2$

$C_{32}H_{40}Br_2Cu_2N_8O_2$
855.63 g mol^{-1}

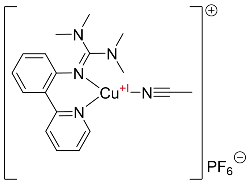

[Cu(TMGphpy)(CH$_3$CN)]PF$_6$ $^{\$}$
[**Pr2**]PF$_6$

$C_{18}H_{23}CuF_6N_5P$
517.93 g mol^{-1}

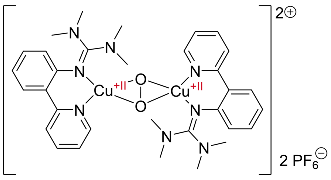

[Cu$_2$O$_2$(TMGphpy)$_2$](PF$_6$)$_2$ $^{\$}$
[$^{\mathbf{S}}$**P2**](PF$_6$)$_2$

$C_{32}H_{40}Cu_2F_{12}N_8O_2P_2$
985.75 g mol^{-1}

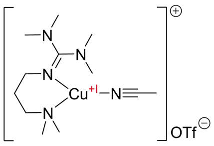

[Cu(TMGdmap)(CH$_3$CN)](CF$_3$SO$_3$) *
[**Pr3**]OTf

$C_{13}H_{27}CuF_3N_5O_3S$
453.99 g mol^{-1}

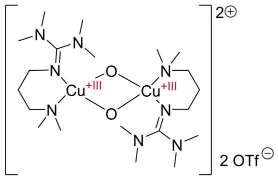

[Cu$_2$O$_2$(TMGdmap)$_2$](CF$_3$SO$_3$)$_2$ *
[**O3**](OTf)$_2$

$C_{22}H_{48}Cu_2F_6N_8O_8S_2$
857.88 g mol^{-1}

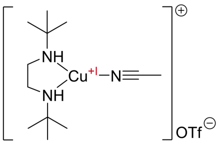

[Cu(DBED)(CH$_3$CN)](CF$_3$SO$_3$) *
[**Pr4**]OTf

$C_{13}H_{27}CuF_3N_3O_3S$
425.98 g mol^{-1}

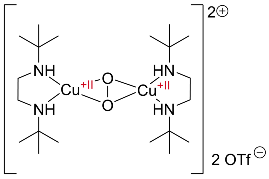

[Cu$_2$O$_2$(DBED)$_2$](CF$_3$SO$_3$)$_2$ *
[$^{\mathbf{S}}$**P4**](OTf)$_2$

$C_{22}H_{48}Cu_2F_6N_4O_8S_2$
801.85 g mol^{-1}

Abbreviations & Symbols

ν_P	stoichiometric coefficient of product
ν_S	stoichiometric coefficient of substrate
$^{\mathrm{S}}\mathrm{P}$	side-on µ-η^2:η^2-peroxido dicopper(II) complex
$^{\mathrm{T}}\mathrm{P}$	end-on *trans*-µ-1,2-peroxido dicopper(II) complex
Ar	Archimedes number
D	diffusion coefficient
d	in-plane equivalent bubble diameter (HSC)
d_bubble	bubble diameter (TF / bubble column)
d_cylinder	cylinder diameter (TF / bubble column)
E	enhancement factor
h	gap width (HSC)
k	reaction rate constant
k_L	mass transfer coefficient
n	reaction order
n_cat	amount of catalyst
n_P	amount of product
n_S	amount of substrate
Pe	Péclet number
Re	Reynolds number
Sc	Schmidt number
Sh	Sherwood number
V_b	mean bubble velocity
Y	yield
2-I-Anil	2-iodaniline
2-Py-ZnBr	bromo-2-pyridinylzinc
4-OMe-Ph	*para*-methoxyphenol
$[\mathrm{Cu(CH_3CN)_4}](\mathrm{CH_3SO_3})$	tetrakisacetonitrile copper(I) trifluoromethanesulfonate
$[\mathrm{Cu(CH_3CN)_4}]\mathrm{PF_6}$	tetrakis(acetonitrile)copper(I) hexafluorophosphate
L-DOPA	L-3,4-dihydroxyphenylalanine
A	copper(I) complex [**Pr4**]OTf (Reactive Mass Transfer Studies)
$\mathrm{Amin_{phpy}}$	2(2-aminophenyl)pyridine
B	molecular oxygen ($\mathrm{O_2}$) (Reactive Mass Transfer Studies)
C	peroxido complex [$^{\mathbf{S}}$**P4**]$(\mathrm{OTf})_2$ (Reactive Mass Transfer Studies)
CAT	catecholate

CH_3CN	acetonitrile
CP2	C-C coupled product 5,5'-dimethoxy-[1,1'-biphenyl]-2,2'-diol (Reactive Mass Transfer Studies)
CP3	C-O coupled product 2,6-bis(4-methoxyphenoxy)cyclohexa-2,5-diene-1,4-dione (Reactive Mass Transfer Studies)
CSI-MS	cold-spray ionization mass spectrometry
d	dublet (NMR)
DBED	di-*tert*-butylethylendiamine
DCM	dichlormethane
DFT	density functional theory
DMEG	dimethylethylenediamine
DOSY	diffusion-ordered-spectroscopy
DTB	di-*tert*-butyl
DTBC	3,5-di-*tert*-butylcatechol
DTBP	2,4-di-*tert*-butylphenol
DTBQ	3,5-di-*tert*-butyl-*ortho*-quinone
EDTA	ethylenediaminetetraacetic acid
EPR	electron-paramagnetic-resonance
ESI-MS	electrospray ionization mass spectrometry
EtOAc	ethylacetate
fps	frame per second
GV	gray-level
HCl	hydrochloric acid
Hex	*n*-hexane
HSC	Hele-Shaw cell
IR	infrared
LED	light-emitting-diode
LMCT	ligand-to-metal charge transfer
m	multiplet (NMR)
MeOH	methanol
MO	molecular orbital
N_{His}	histidine
NEt_3	triethylamine
NMR	nuclear magnetic resonance
O	side-on bis(µ-oxido) dicopper(III) complex
O_{Gly}	glycine
O_{Tyr}	tyrosine
OTf	triflate (CF_3SO_3)
P	phenazine product
PCA	phenazine-1-carboxylic acid
PCN	phenazine-1-carboxylamide

$Pd[P(Ph_3)]_4$	tetrakis(triphenylphosphin)palladium(0)
PDA	1,2-phenylenediamine
Pr	copper(I) precursor complex
PTFE	polytetrafluoroethylene
q	quintuplet (NMR)
QP1	quinone intermediate 4-methoxycyclohexa-3,5-diene-1,2-dione (Reactive Mass Transfer Studies)
ROI	region-of- interest
rR	resonance Raman
rt	room temperature
S	phenolic substrate
s	singlet (NMR)
S_{Cys}	cysteine
S_{Met}	methionine
S_{Ph}	substrate *para*-methoxyphenol (Reactive Mass Transfer Studies)
SC-XRD	single-crystal X-ray diffraction
SFM	SuperFocusMixer
SQ	seminquinone
t	triplet (NMR)
TF	Taylor-flow
THF	tetrahydrofuran
TMG	tetramethylguanidine
TMGbenza	2-2-((dimethylamino)methyl)phenyl-1,1,3,3-tetramethylguanidine
TMGbenzN*i*Pr_2	2-(2-((di-isopropylamino)methyl)phenyl)-1,1,3,3-tetramethylguanidine
TMGbenzNEt_2	2-(2-((diethylamino)methyl)phenyl)-1,1,3,3-tetramethylguanidine
TOF	turn-over-frequency
TON	turn-over-number
tyr	tyrosinase
UV/Vis	ultraviolet / visible

List of Figures

List of Schemes

List of Tables

Contents

1 State-of-the-Art

Chemical industrial products like polymers, pharmaceuticals or fertilizers are indispensable in our modern life. For many of those products oxidation processes involving large quantities of heavy metals are used to convert basic materials like petroleum or hydrogen to fine chemicals and needed intermediates of higher oxidation state (Figure 1.1).[1–5] Until the middle of last century discharge of industrial wastewater into rivers or the sea was a common method of waste disposal: "dilution as a solution". As a result, environmental problems like heavy metal poisoning of humans and animals emerged.[1] A prominent example is the Minamata disease caused by mercury poisoning of fish and sea food: Between 1950 and 1970 in Minamata Bay (Japan) the chemical factory Chisso discharged wastewater containing high concentrations of methylmercury directly into the sea causing food poisoning through the main food source (fish and seafood).[6,7] Another thoroughly investigated case is the Itai-Itai disease resulting from a cadmium contamination: During the 20th century the Jinzu river (Japan), the main water source for rice farming in the Toyama plain, was used to dispose wastewater from zinc mining containing high concentrations of its by-product cadmium.[8] A rather unknown example is the Gressenich disease: In the 1960s in Stolberg near Aachen (Germany), grazing animals like cattle, sheep and goats were poisoned with cadmium and lead which was leaking into their pasture from lead and zinc mines. People growing up in close proximity to those mines exhibited high lead contamination in their blood over decades.[9]

In the 1990s, an awareness of environmental pollution caused by the (chemical) industry emerged. To prevent further pollution and diminish the amount of waste produced twelve principles leading towards a “greener”, environmentally friendlier chemistry were defined. Three of those are: the design of atom economic synthesis routes, a change towards catalytic instead of stoichiometric reaction pathways and the replacement of hazardous chemicals.[10,11] Thereby, these rules should not be tackled individually; more likely they are considered as a cohesive design concept in which the implementation of several changes maximizes the impact on the environment.[12] As an example, switching from a stoichiometric to a catalyzed reaction mechanism decreases the energy input needed. Thus, the reaction’s efficiency increases while improving its selectivity. In addition, by reducing the amount of side-product the number of purification steps needed decreases. Lastly, the quantity of reagents may be minimized as well.[11,13]

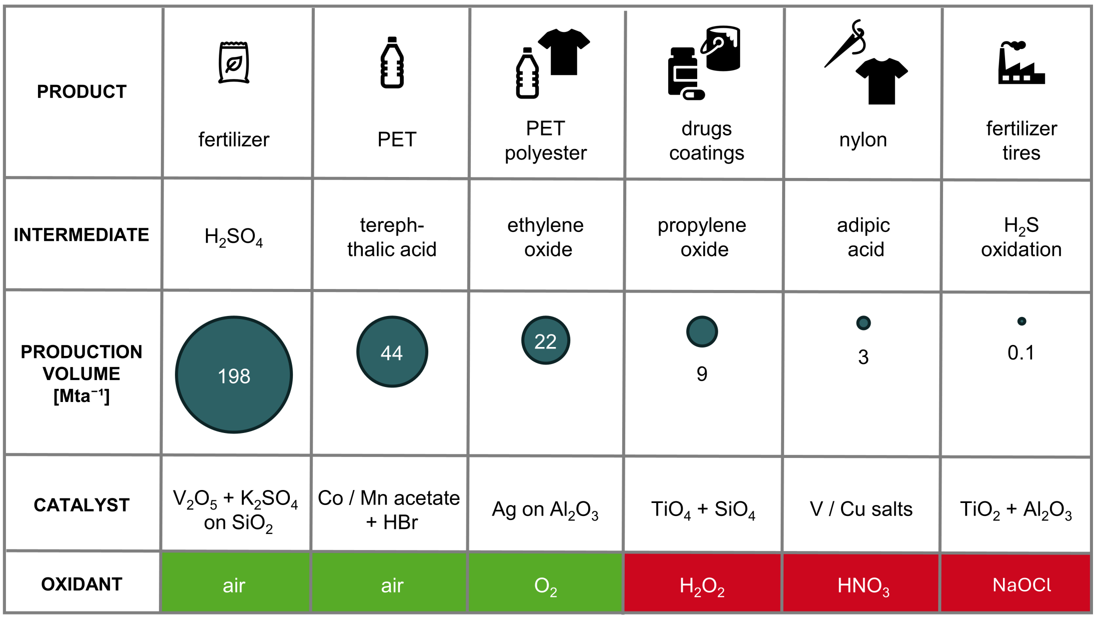

PRODUCT	fertilizer	PET	PET polyester	drugs coatings	nylon	fertilizer tires
INTERMEDIATE	H_2SO_4	tereph-thalic acid	ethylene oxide	propylene oxide	adipic acid	H_2S oxidation
PRODUCTION VOLUME $[Mta^{-1}]$	198	44	22	9	3	0.1
CATALYST	V_2O_5 + K_2SO_4 on SiO_2	Co / Mn acetate + HBr	Ag on Al_2O_3	TiO_4 + SiO_4	V / Cu salts	TiO_2 + Al_2O_3
OXIDANT	air	air	O_2	H_2O_2	HNO_3	NaOCl

Figure 1.1: Examples of industrial oxidation processes with the production volume of the intermediate generated in Mt a^{-1} and the resulting final product given as icon above. Below catalyst and oxidant used are given. Hazardous oxidants are marked in red while environmentally friendly ones are colored green.[1–5]

If we take a look at industrial oxidation reactions once again, some of them are using hazardous chemicals as oxidizing agent like acids, peroxides or perchlorates (Figure 1.1 marked in red). A good, environmentally friendly alternative many industrial processes are already using is molecular oxygen or air.[1–5] To activate molecular oxygen and generate an accessible oxidizing agent metal catalysts reducing the inert triplet ground state molecule in an highly reactive peroxide anion are needed. In industrial applications mostly toxic transition metal catalysts like vanadium, cobalt or manganese salts are used (Figure 1.1 marked in green).[1–5,14,15] Thus, parts of the "green" chemistry principles are already implemented avoiding hazardous, cost-intensive oxidants by replacing them with inexpensive molecular oxygen. Nevertheless, expensive and toxic metal catalysts are still necessary for activation. As a result, new environmentally friendly metal catalysts changing their oxidation state to reversibly binding and release molecule oxygen are lacking. An example are iron or copper based catalysts common in enzyme-catalyzed biological reactions.[16–21]

1.1 Oxygen Activation, Binding and Transport in Nature

In nature, biological processes like electron transfer or binding and release of molecular oxygen are controlled by a special type of enzymes called metalloproteins.[17,18,21–23] These highly reactive biocatalysts consist of one or more metal centers coordinated by amino acids and a surrounding protein structure. Their reactivity results from their high redox potential (+0.22 V to +0.68 V):[18,24] By switching the oxidation state of the metal center(s) inert molecules like CO_2, water or molecular oxygen can be activated through oxidation.[18,25] A popular example is the oxygen carrier hemoglobin in the red blood cells of higher organisms like human and other mammals or birds.[18,23] As a result of its ability to reversibly bind and release oxygen, the concentration of O_2 in human blood is thirty times higher ($9{\cdot}10^{-3}$ M) than in pure water ($3{\cdot}10^{-4}$ M).[18] Two rather unknown metalloproteins performing a similar reaction in the respiratory chain of invertebrates like spiders, crabs, worms and mussels are hemerythrin and hemocyanin. Some metalloproteins are not only able to transport molecular oxygen but also activate it to catalyze hydroxylation or oxidation reactions. Examples are the methane monooxygenase or tyrosinase. The methane monooxygenase oxidizes methane to methanol used as energy resource by a special type of bacteria called methanotrophs.[26–28] Tyrosinase transforms phenols as well as catechols to *ortho*-quinones during the synthesis of the cell pigment melanin.[17,29,30] As most metalloproteins the aforementioned species contain iron (hemoglobin, hemerythrin and methane monooxygenase) or copper (hemocyanin, tyrosinase) metal centers.[18,21]

Metalloproteins as catalysts for oxidation reactions would fulfill many requirements of "green" chemistry: An environmentally friendly catalyst functioning under mild reaction conditions with atom-efficient synthesis pathway in a non-toxic solvent (water).[31] However, most enzymes only promote the formation of a certain product.[18,32] Their active site is tightly surrounded by protein residues controlling the substrate accessibility.[33] An exception displays the copper enzyme tyrosinase capable to convert monophenols as well as diphenols to *ortho*-quinones.[17,29]

1.1.1 Copper Proteins

Copper enzymes can be divided in two main groups, classical and non-classical copper proteins, including several subtypes. Classical copper proteins are divided in the mononuclear types I and II and the binuclear type III to which tyrosinase belongs. The group of non-classical copper proteins contains binuclear $\mathrm{Cu_A}$ and $\mathrm{Cu_B}$ centers, coupled type II / type III trimers and tetranuclear $\mathrm{Cu_Z}$ centers. Within a subtype all copper proteins consist of the same active center and only differ in the surrounding secondary protein structure (Figure 1.2).[25,34–38]

Taking a deeper look into classical copper proteins, the mononuclear copper(II) center of type I is coordinated by three strongly bound donor units (2x histidine, 1x cysteine) located in plane with the copper atom and one or two weakly bound axial ligands resulting in an over all distorted tetrahedral or trigonal-bipyramidal coordination geometry (Figure 1.2). Due to a strong ligand-to-metal charge transfer (LMCT) from the cysteine ligand ($\mathrm{S_{Cys}}$) to the copper center an strong absorption band can be observed, resulting in an intense blue color giving them the trivial name "blue copper proteins". Catalyzing the electron transfer in the respiratory chain of bacteria, plants and algae, they are a crucial part of photosynthesis.[18,24,35] With their distorted tetrahedral coordinated active center type I copper proteins stabilize a geometry in between the preferential configuration of Cu(I) (tetrahedral) and Cu(II) (square-planar). Thus, the change of oxidation state is facilitated by a lower reorganization barrier speeding up the electron transfer.[34] Consequently, they show high redox potentials ranging from +0.22 V (azurin) over +0.39 V (plastocyanin) up to +0.68 V (rusticyanin).[24]

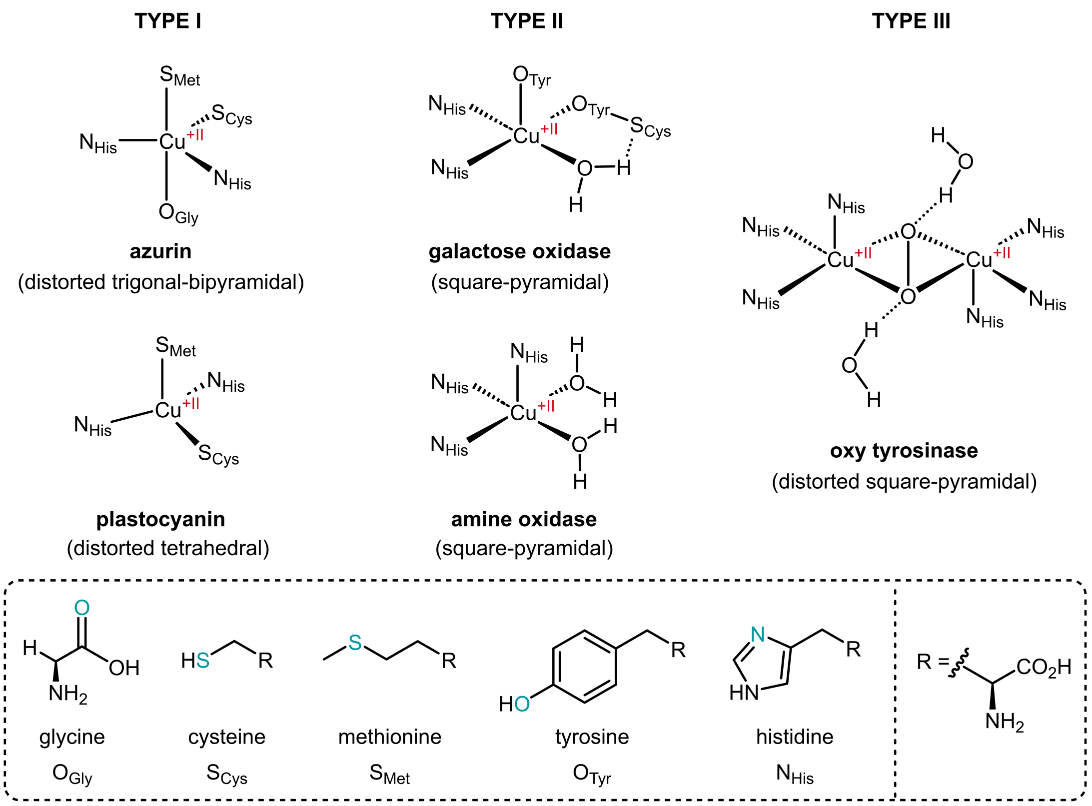

Figure 1.2: Natural examples of type I / II / III copper proteins with their coordinating ligands of amino acids / water and corresponding molecular geometry.[34,36–40]

In type II copper proteins the mononuclear Cu(II) is coordinated in a square-planar or square-pyramidal geometry by two histidine and two or three further N- or O-donors like water or other amino acids (Figure 1.2). Since the cysteine S-donor with its strong LMCT is missing, type II copper proteins do not show an intense blue color like type I and are therefore called "normal" copper proteins.[34,35,37] They catalyze the direct activation of O_2 and substrate binding reactions like oxidation of alcohols to aldehydes in mushrooms (galactose oxidase), capture of cytotoxic superoxides ($O_2^{\cdot -}$; Figure 1.3) in mammals and yeast (Cu-Zn superoxide dismutase) or cleavage of organic amines regulating histamine and dopamine in the metabolism of bacteria, yeast plants and animals (amine oxidase).[18,34,37,39,40]

The active site of type III, the only binuclear type of classic copper proteins, displays major differences in comparison with type I and II: two copper(II) atoms are coordinated square-pyramidally by two bridging peroxide units and three histidine ligands. Two histidines are located in plane with the peroxides while the last histidine ligand of each copper center is located orthogonally to the plane and in opposite direction towards each other (Figure 1.2).[38] All type III copper proteins contain the same active center. Thus, hemocyanin, catechol oxidase and tyrosinase are all able to reversibly bind and release molecular oxygen. However, their function varies due to the substrate accessibility controlled by their secondary protein structure:[18,25,33,38] In hemocyanin the active site is shielded by a bulky phenylalanine residue.[41,42] In catechol oxidase this bulky residue is more flexible enabling rearrangement of the active site in the presence of a substrate molecule. In tyrosinase this blocking phenylalanine residue is replaced by a smaller cysteine ligand.[43] Consequently, substrate coordination is inhibited in hemocyanin while catechol oxidase and tyrosinase both show diphenolase activity converting catechols to *ortho*-quinones.[18,42,44] In addition, tyrosinase is displaying monophenolase activity: catechols as well as simple phenols can be catalyzed to *ortho*-quinones. In contrast to catechol oxidase, tyrosinase has a flexible histidine ligand stabilizing a necessary ternary intermediate state in the conversion of monophenols.[38,45] This outstanding substrate flexibility in comparison with other enzymes which normally show substrate-specific functionality[32] is used by nature in the synthesis of the cell pigment melanin. Thereby, various types of monophenolic and diphenolic substrates are hydroxylated and / or oxidized to *ortho*-quinones.[30,46,47]

1.1.2 Catalytic Activity of Tyrosinase

Melanin is a cell pigment coloring the skin, fur and feathers of mammals and birds. Two types of the pigment are existing: phaeomelanin displaying a brownish, grayish or black color and eumelanin with a yellowish to reddish coloration.[46] The rate-limiting enzyme catalyzing the biosynthesis of phaeo- and eumelanin is tyrosinase. If the enzyme is missing or its function is inhibited we see the orphan disease called albinism: no cell pigments are produced and skin, fur or feather are completely colorless.[48] While eumelanin synthesis is only mediated by tyrosinase (Scheme 1.1), phaeomelanin formation needs further enzymes (DOPAchrome tautomerase), amino acids (L-cysteine) and the presence of metal cations (Cu^{2+}, Zn^{2+}).[46]

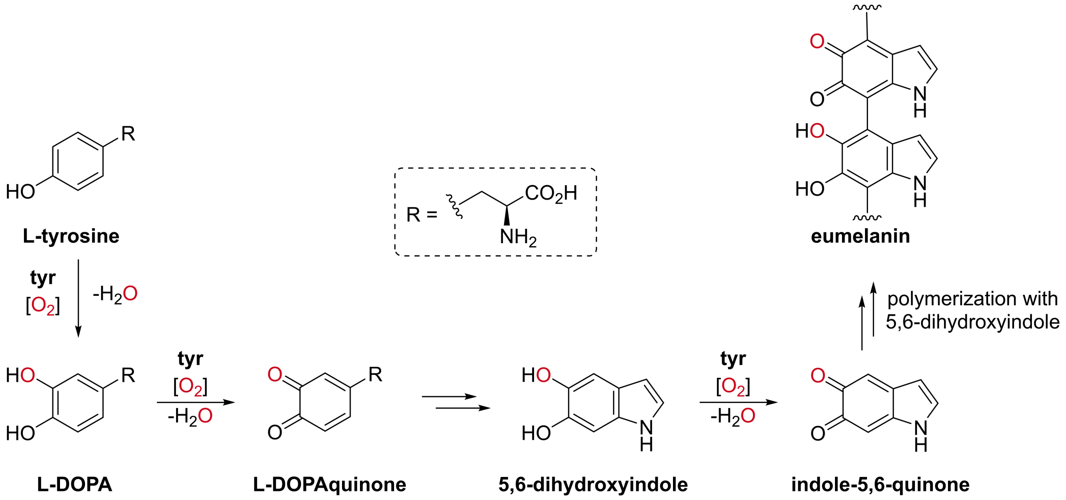

Scheme 1.1: Synthesis pathway of the natural biopolymer and cell pigment eumelanin catalyzed by the enzyme tyrosinase (tyr).[30]

Two of the main building block of eumelanin are 5,6-dihydroxyindole and indol-5,6-quinone. The synthesis pathway starts with the slow and thus rate-determining hydroxylation of the amino acid L-tyrosine ($1 \cdot 10^{-3}\,\mathrm{s}^{-1}$) to the catechol L-3,4-dihydroxyphenylalanin (L-DOPA) followed by a fast oxidation to L-DOPAquinone ($1 \cdot 10^{-7}\,\mathrm{s}^{-1}$). Both reaction steps are catalyzed by the enzyme tyrosinase. Subsequently, ring closure via intramolecular cyclization and elimination of CO_2 leads to the formation of 5,6-dihydroxyindole which is further oxidized by tyrosinase to indole-5,6-quinone. Lastly, several non-enzymatic polymerization steps result in the biopolymer eumelanin (Scheme 1.1).[30]

How exactly the oxygen activation and hydroxylation / oxidation during melanin synthesis is mediated by tyrosinase is still under debate. An important contribution was the determination of the deoxy-, oxy- and met-tyrosinase molecular structures from bacteria in 2006. The crystallographic studies revealed a reduced species (deoxy form) consisting of two copper(I) centers each coordinated by three histidine ligands. In the oxy-form two copper(II) atoms are connected by two O atoms with an peroxide bridge in between them. Additionally, both copper centers are coordinated by three histidine ligands. The met-form displays a similar structure, however, the connecting peroxide bridge is replaced by an hydroxido bridge (circled species in Scheme 1.2). Although, the molecular structure of the catalytically active species was revealed, new insights regarding the catalytic pathway and, in particular, the substrate coordination to the active center were still lacking. In subsequent catalytic activity studies, the met form displayed oxidation activity converting diphenols to *ortho*-quinones. In contrast, the oxy form catalyzed oxidation as well as hydroxylation reactions (diphenols and monophenols to *ortho*-quinones).[38] These findings were in accordance with early theoretical studies based on electro-chemical features.[29,49–51]

Crystallographic and theoretical studies based on the complete molecular structure of tyrosinase are complicated and time-consuming. The catalytically active center is coordinated by a large secondary protein structure consisting of hundreds of amino acids.[18,38] To simplify studies of the catalytic pathway and gain insights in the active center of the enzyme, synthetic model complexes mimicking the catalytically active center were established in parallel. These systems consist of two copper(II) centers connected by two O atoms and a peroxide bridge in between them, a Cu_2O_2 center, identical to the active center in oxy and met tyrosinase. The Cu_2O_2 center is coordinated by strong N-donor ligands like benzimdazole, pyridine or imine groups similar to the histidine ligands in tyrosinase. Due to the missing secondary protein structure the resulting synthetic model systems are smaller and thus easier to calculate in theoretical studies than the original enzyme.[52–59]

The diphenolase pathway (diphenols like catechol to *ortho*-quinones) was fully described in 2010 by Tuczek and coworkers using synthetic model complexes based on pyridinylimine ligands.[56] The diphenolase pathway is in accordance with the data generated from the crystallographic structure of tyrosinase. Nevertheless, the monophenolase cycle remains under discussion.[38,50,51,56,60]

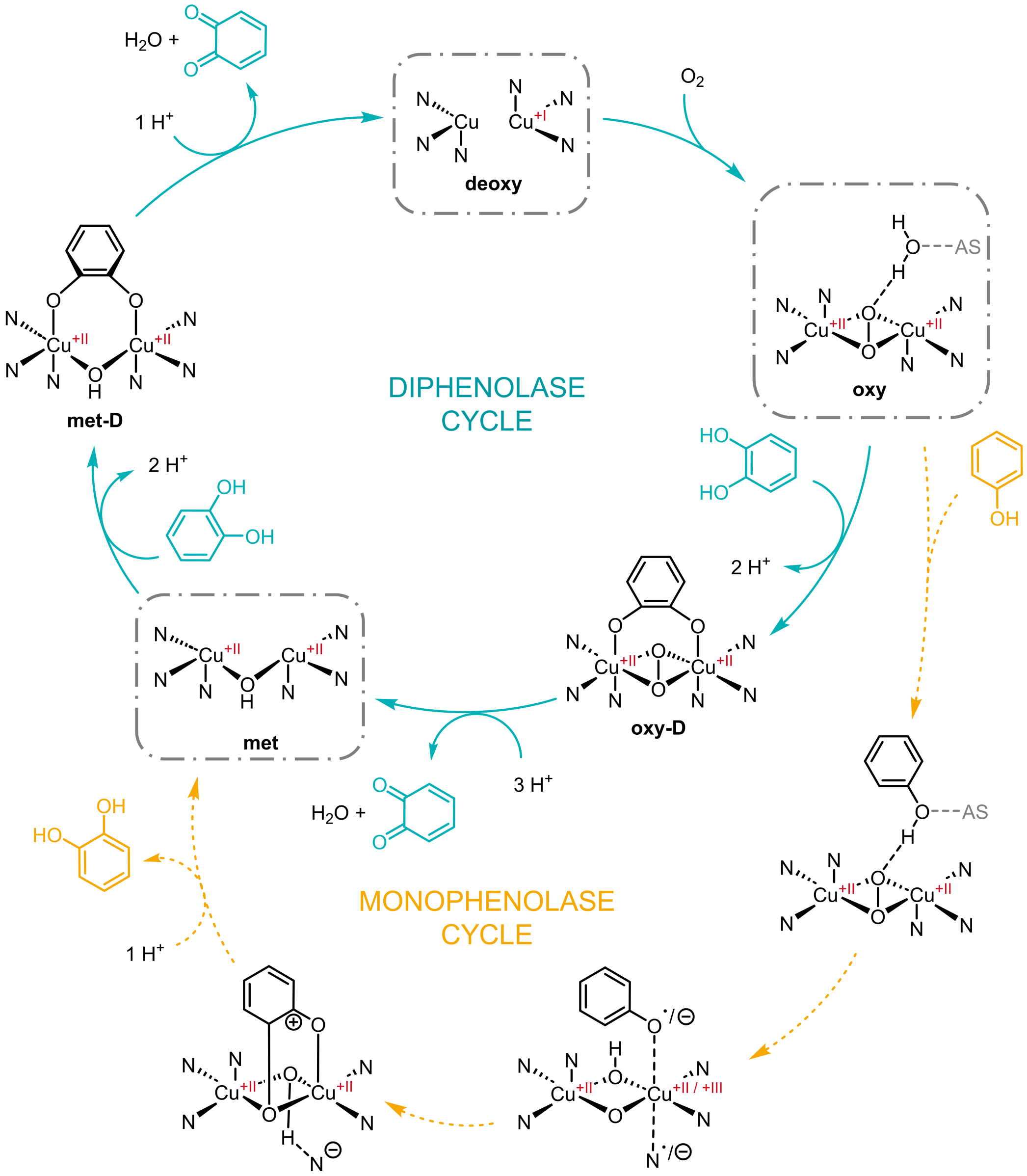

Scheme 1.2: Catalytic activity of tyrosinase displayed in two separate cycles: the monophenolase cycle after Solomon and coworkers showing the hydroxylation of phenol to catechol and subsequent oxidation to *ortho*-benzoquinone catalyzed by oxy tyrosinase (orange, dashed arrows)[45] and the diphenolase cycle after Tuczek and coworkers showing the oxidation of catechols to *ortho*-benzoquinones mediated by oxy as well as met tyrosinase (turquoise, solid arrows).[56] Molecular structures of tyrosinase forms known from crystallographic data are framed (black, dashed).N = N-donor.[38]

The diphenolase pathway depicted in Scheme 1.2 starts with the catalytically active oxy form of tyrosinase. The substrate, for instance catechol, is deprotonated and coordinated via its O atoms to the Cu_2O_2 center generating the oxy-D form. With the protons present from substrate deprotonation, an *ortho*-quinone product and water are released resulting in the met form of tyrosinase with two Cu(II) atoms bridged by a µ-hydroxido unit.

Analogous to the oxy form, met-tyrosinase is able to oxidize diphenolic substrates. By coordination of a further deprotonated catechol the met-D species is formed with an catecholate coordinated to the copper centers by its O atoms. In the presence of another proton, a second *ortho*-quinone product and water are eliminated giving the reduced deoxy form of tyrosinase. Finally, binding of molecular oxygen to the deoxy-form restores the catalytically active oxy-tyrosinase species to start the diphenolase cycle all over again.[56]

Within the monophenolase cycle, substrate binding to the copper centers of tyrosinase oxy form is still under debate. Especially the question, which species performs the initiating deprotonation step is intensively discussed. Tuczek and coworkers who described the diphenolase cycle mentioned above, assumed a simultaneous deprotonation of incoming substrates by the released *ortho*-diphenolates during formation of the reaction products (*ortho*-quinones and water).[61] However, experiments of other working groups starting from protonated monophenolic substrates showed only formation of radical coupling products. In contrast, converting previously deprotonated monophenols, desired *ortho*-quinones were obtained.[51,62] Therefore, different intermediate species being present (oxido / hydroxido / radical intermediate)[50,51] or the deprotonation being mediated by a histidine residue of the protein structure from tyrosinase were suspected.[50] Only recently Solomon and coworkers published a new pathway for the monophenolase activity of tyrosinase (Scheme 1.2) on the basis of theoretical and experimental studies with model complexes.[45]

Just as the diphenolase cycle, the monophenolase pathway begins with the oxy form of tyrosinase. In contrast, no beforehand deprotonation of the substrate molecules is taking place. Instead, the Cu_2O_2 core functions as proton acceptor.[45] Already in the oxy form of tyrosinase hydrogen bonding interactions between water molecules coordinated to the Cu_2O_2 center and the second sphere residues of the protein structure are weakening the O-O bond.[43] This finding is in agreement with the crystal structure of tyrosinase showing a water molecule coordinated to the Cu_2O_2 core.[38]

Due to the hydrogen bonding interactions between substrate and Cu_2O_2 core a cleavage of the weakened O-O bond and hydrogen transfer to one of the O atoms is taking place forming a µ-oxido-µ-hydroxido intermediate. During this transition state, the non-protonated µ-oxido is bound to the *ortho*-C atom of the phenolate while its O atom is coordinated to one of the copper centers. In presence of a proton, a catechol product is abstracted and the met form of tyrosinase already known from the diphenolase cycle is formed. As described earlier, met tyrosinase then catalyzes the formation of desired *ortho*-quinone products converting the previously formed catechol product.[45]

The newly published monophenolase pathway provides an explanation for the ongoing discussion about the extraordinary substrate flexibility of oxy tyrosinase in contrast to catechol oxidase (only diphenolase activity).[29,49–51] As the formation of catechols from monophenols proceeds via µ-oxido-µ-hydroxido intermediate the flexible histidine ligand and the coordinating water molecules within the secondary protein structure, only present in the catalytically active Cu_2O_2 center of oxy tyrosinase, are necessary to mediate the proton transfer from the substrate molecule to the Cu_2O_2 core.[38,43,45]

The formation of oxy tyrosinase is crucial to start the diphenolase as well as the monophenolase cycle. Oxy tyrosinase is formed by binding molecular oxygen to the deoxy form of tyrosinase. This highly complex process is mediated by the copper centers transferring molecular oxygen – a paramagnetic species in an inert triplet ground state – into an accessible singlet species via charge delocalization and subsequent intersystem crossing.

1.1.3 Oxygen Binding in Type III Copper Proteins - Formation of a Cu_2O_2 Center

Tyrosinase needs to bind molecular oxygen to change from the deoxy form into the catalytically active oxy form to perform catalytic hydroxylation and oxidation reactions.[29,45,56] O_2 is a paramagnetic triplet species with two unpaired electrons unable to undergo reactions with diamagnetic singlet species containing only paired electrons like most organic compounds. In the triplet ground state of molecular oxygen, the unpaired electrons are located in two anti-bonding π-orbitals with the same energy and display parallel spin resulting in a paramagnetic diradical with poor reactivity and a low redox potential (-0.33 V). In contrast, in the excited singlet state, both electrons are in one orbital displaying opposite spin while the second π-orbital is unoccupied resulting in a highly reactive, diamagnetic species with positive redox potential (+0.65 V) (Figure 1.3).

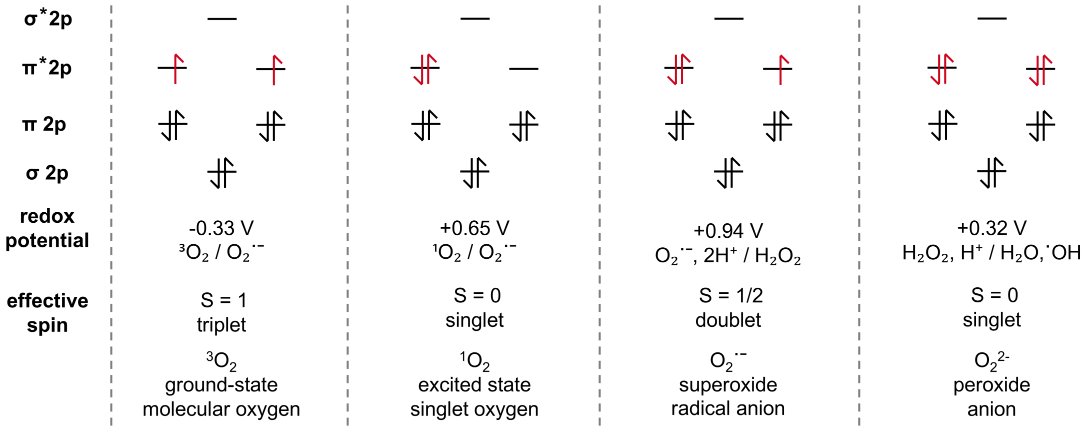

Figure 1.3: Molecular orbital (MO) diagrams as well as related effective spin and redox potentials of molecular oxygen (ground state), singlet oxygen (excited state) and two further reactive oxygen species accessible via reduction of molecular oxygen with e.g. transition metals.[63]

Within a redox reaction electrons are transferred from the reductant to the oxidant. To enable this electron transfer, both species need to be in the same electronic state (singlet or triplet). In contrast to paramagnetic molecular oxygen, most organic compounds display diamagnetic behavior. Thus, ground-state triplet oxygen only accepts a pair of electrons with parallel spin while most organic compounds contain paired electrons showing opposite spin. Consequently, the electron transfer between those species is spin-forbidden.[37,64] An exception are singlet species consisting of transition metals like deoxy tyrosinase. Those are able to mediate singlet-triplet intersystem crossing by changing their oxidation state.

The reaction pathway of binding molecular oxygen to type III copper proteins could be clarified via density functional theory (Scheme 1.3). Therefore, molecular structure data of hemocyanin containing the same catalytically active Cu_2O_2 center as tyrosinase were used.[65,66]

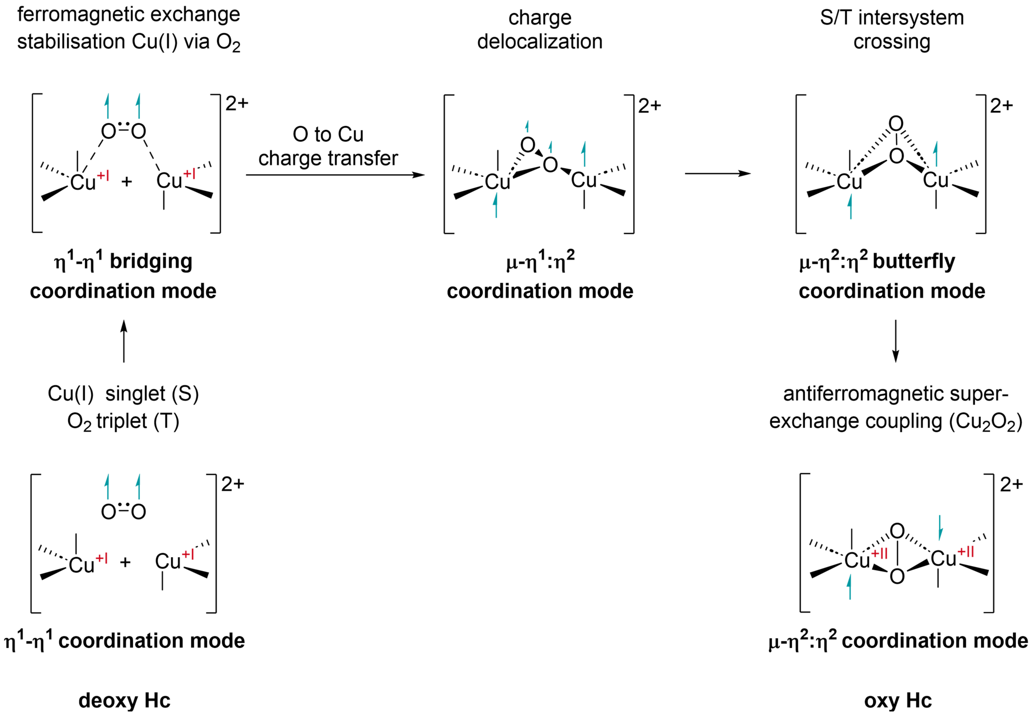

Scheme 1.3: Pathway of the molecular oxygen binding process to type III copper protein Cu_2O_2 centers determined via density functional theory calculations on the basis of oxy and deoxy hemocyanin molecular structures.[65]

The protein structure surrounding the catalytically active center in copper proteins plays an important role in the activation process of molecular oxygen: Hydrogen bonds formed between the protein residues and the copper(I) centers in the deoxy form hold both Cu(I) species in close proximity ($\sim$ 4.5 Å) towards each other favoring interactions with O_2 molecules.[66] In the initial step, the dioxygen molecules are coordinated by the Cu(I) atoms enabling ferromagnetic coupling between the copper centers via the half-occupied O_2 orbitals stabilizing the triplet ground state. Due to the coordination of the O atoms as peroxides, the distance between copper atoms and oxygen atoms is reduced ($\sim$ 3.5 Å). Consequently, a charge transfer between O atoms and Cu atoms is taking place resulting in a charge delocalization of the two unpaired electrons over the Cu_2O_2 center. Therefore, a butterfly coordination mode with an 145° Cu-O-Cu angle is formed with paired electrons in the coordinated peroxides and unpaired electrons on the Cu atoms. The orthogonal orientation of the peroxide π-orbitals enables interactions with the *d*-orbitals of the Cu atoms allowing a triplet-singlet intersystem crossing. The former unpaired electrons on both copper centers with parallel spin are transferred into unpaired electrons with antiparallel spin. Thus, a formal singlet state is formed stabilized by antiferromagnetic super exchange coupling of both Cu atoms over the bridged peroxides within the Cu_2O_2 center (Scheme 1.3).[65] To be exact, an over-all singlet state is generated by two unpaired electrons in a so called broken symmetry state. Therein, the singlet state formed by antiferromagnetic super exchange between both unpaired electrons is superposing their individual triplet states. Consequently, a diamagnetic species with no conventional measurable overall spin is formed.[67–69]

Type III copper proteins favor this simultaneous two electron reduction forming a Cu_2O_2 center. In contrast, with synthetic model systems also sequential two electron reduction to peroxides or one electron reductions to superoxides are observed.[17,65]

1.2 Synthetic Cu_2O_2 Model Systems

Today, numerous copper oxygen binding motifs are known with varying copper to dioxygen ratio: CuO_2 (1:1), Cu_2O_2 (2:1), Cu_3O_2 (3:1) and Cu_4O_2 (4:1).[17] Within the class of Cu_2O_2 species five different types were found of which the three most popular are: The end-on *trans*-μ-1,2-peroxido dicopper(II) species ($^{\mathbf{T}}\mathbf{P}$), the side-on μ-η^2:η^2-peroxido dicopper(II) species ($^{\mathbf{S}}\mathbf{P}$) and the side-on bis(μ-oxido) dicopper(III) species (**O**) (Figure 1.4).[38,53,70–77]

1.2.1 Structures of Cu_2O_2 Binding Motifs

The first Cu_2O_2 species to be fully characterized was a $^{\mathbf{T}}\mathbf{P}$ complex crystallized 1988 by Karlin and coworkers.[70] The Cu_2O_2 center in $^{\mathbf{T}}\mathbf{P}$ species consists of two Cu(II) atoms with a Cu-Cu distance of 4.36 Å end-on *trans* bound to a peroxide ion with an O-O bond length of 1.43 Å. Each Cu atom is coordinated trigonal-bipyramidally by four N-donor ligands and one of the peroxides O atoms. Thereby are two N-donors located equatorial in plane with the peroxide bridge and two are bound axially (Figure 1.4)[70,71] Single crystals as well as solutions display a blue to violet color.[70,71,78,79]

A year later, Kitajima and Moro-oka published the first fully characterized $^{\mathbf{S}}\mathbf{P}$ species. In contrast to the $^{\mathbf{T}}\mathbf{P}$ complexes, the two Cu(II) atoms are coordinated side-on to both peroxides with an O-O bridge in between. This results in a shorter Cu-Cu distance (3.40 - 3.60 Å) while the O-O distance stays nearly the same (1.41 Å). Both copper centers are coordinated by three further ligands of which two are located with the two peroxide atoms in plane (bond length: $\sim$ 2.0 Å). The third ligand is located axially elongated perpendicular to the Cu_2O_2 plane (bond length: $\sim$ 2.4 Å) whereby both axial ligands are orientated anti towards each other (Figure 1.4).[17,38,53,72,73] The coordination geometry is identical to the Cu_2O_2 species found in nature like the active sites of hemocyanin[73] and tyrosinase.[38] Most synthetic model systems consist of a tridentate ligand.[17,53,54,72] Although, some bidentate systems missing the axially coordinated ligand are also known.[75,80–82] Just like $^{\mathbf{T}}\mathbf{P}$ species, $^{\mathbf{S}}\mathbf{P}$ show blue to violet colored solutions and single crystals.[38,53,72]

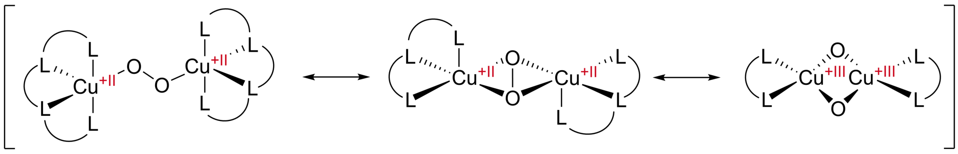

trans-μ-1,2-peroxido dicopper(II) ^{T}P

μ-η^2:η^2-peroxido dicopper(II) ^{S}P

bis(μ-oxido) dicopper(III) O

rR O_2^{16} / (O_2^{18}) [cm^{-1}]	830 (± 46)	740 (± 40)	600 (± 28)
UV/Vis [nm]	550, 600 (shoulder)	350, 550	300, 400
O-O [Å]	1.43	1.41	2.29 – 2.34
Cu-O [Å]	1.85	1.90 – 1.93	1.80 – 1.81
Cu-Cu [Å]	4.36	3.40 - 3.60	2.74 – 2.87

Figure 1.4: Coordination geometries of the isoelectronic Cu_2O_2 $^{\mathbf{T}}\mathbf{P}$, $^{\mathbf{S}}\mathbf{P}$ and **O** with related Cu-Cu, O-O and Cu-O bond length as well as characteristic UV/Vis and resonance Raman (rR) features.[17,38,53,54,70–80,83–89]

The **O** type was crystallized for the first time by Tolman and coworkers in 1996.[74] Analogous to $^{\mathbf{S}}\mathbf{P}$ the peroxides are coordinated side-on to both copper atoms in a square planar geometry with two further ligands. However, **O** complexes contain Cu(III) atoms with a higher oxidation state and are missing the O-O bridge leading to a shorter Cu···Cu distance (2.74 – 2.87 Å) while the O···O distance is elongated (2.29 – 2.34 Å) (Figure 1.4).[74–77] Most ligand systems stabilizing an **O** species are bidentate,[51,75,85–91] although, a few systems with three or four donors exist showing a weakly axial interaction with the copper centers (distance ∼ 2.6 Å).[54,74,76,77,84] Unlike $^{\mathbf{T}}\mathbf{P}$ and $^{\mathbf{S}}\mathbf{P}$, solutions and single crystals of **O** complexes are colored red, orange or brown.[74,75,87,92]

The three Cu_2O_2 species $^{\mathbf{T}}\mathbf{P}$, $^{\mathbf{S}}\mathbf{P}$ and **O** are isoelectronic isomers (Figure 1.4).[17] Due to their specific structures, distinct spectroscopic features can be observed for each species. Resonance Raman (rR) spectroscopic measurements show a distinct signal for each Cu_2O_2 complex ($^{\mathbf{T}}\mathbf{P}$: ∼ 830 cm^{-1},[17] $^{\mathbf{S}}\mathbf{P}$: ∼ 740 cm^{-1}[54,80,84] and **O**: ∼ 600 cm^{-1}[74,77,85,87]). UV/Vis spectra display characteristic LMCT shifts: $^{\mathbf{T}}\mathbf{P}$: 500 and 600 nm,[70,78,79,83] $^{\mathbf{S}}\mathbf{P}$: 350 and 550 nm,[52–54,80,84] **O**: 300 and 400 nm.[74,75,77,85–89] The equilibrium between $^{\mathbf{T}}\mathbf{P}$, $^{\mathbf{S}}\mathbf{P}$ and **O** can be shifted from one species to another by the choice of ligand structure,[54,80,91] counter ion[74,91,93] or solvent.[54,74] Hereby, electronic effects resulting from the choice of ligand have a larger impact than the change of counter ions or solvents.[54,74,91] However, mixtures of two species formed simultaneously are also known. Their equilibrium can be stabilized to one species by the choice of ligands.[79,93,94]

Although a large amount of $^{\mathbf{T}}\mathbf{P}$, $^{\mathbf{S}}\mathbf{P}$ and **O** species mimicking the molecular oxygen activation function of tyrosinase were published since the early 1980's,[17,38,53,54,70–80,83–89] species additionally able to mediate the hydroxylation and oxidation of external substrates are intensively studied only within the last fourteen years. Most of them are $^{\mathbf{S}}\mathbf{P}$[61,82,95–98] containing the same μ-η^2:η^2-peroxido dicopper(II) center as tyrosinase, although, a few **O** species transforming phenols, catechols or phenolates are also known.[51,87,88]

1.2.2 Catalytically Active Synthetic Cu_2O_2 Model Systems

Within the group of Cu_2O_2 species, only $^{\mathbf{S}}\mathbf{P}$ and **O** complexes displaying catalytic activity towards phenolic substrates are published until now. They are generated by the conversion of copper(I) precursor species with molecular oxygen.[17] Their catalytic activity can be described using the technical-chemistry key figures TON and TOF: The turn-over-number (TON) gives the ratio of substrate molecules converted per catalyst molecule while the turn-over-frequency (TOF) is a time-based number giving the amount of substrate conversion per catalyst over time.

The history of hydroxylation and oxidation catalysts based on $^{\mathbf{S}}\mathbf{P}$ complexes begins 1984 with Karlin and coworker's first attempt to synthesize a catalytically active complex. A Cu_2O_2 species however, could not be obtained as the ligand, two bis(pyridinylethylamines) connected by an xylyl spacer, is hydroxylated during the conversion of Cu(I) precursors with O_2.[99] The first catalytic N-donor systems able to mediate the formation of *ortho*-quinones from phenolic substrates were presented by Réglier et al. and Bulkowski. Their hexa- / tetradentate N-donor systems are working with triethylamine as auxilary base to deprotonate the substrate before catalytic conversion (Figure 1.5).[59,100] Without the usage of an auxilary base, formation of C-C coupling dimers instead of desired *ortho*-quinones was monitored by others.[51,62]

Aside from these two milestones, only little process was made in the following two decades: Circumventing the problem of substrate deprotonation and C-C coupling product formation, Casella and co workers as well as Stack and coworkers converted phenolates instead of phenols. While Casella's group worked with a bulky imidazole N-donor ligand with a benzyl bridge, similar to the histidine function in the natural catalyst tyrosinase, Stack's group used a small purchasable bidentate N-donor ligand with *tert*-butyl function: di-*tert*-butylethylenediamine (DBED) (Figure 1.5).[58,81]

Within the last fourteen years, more systems were reported converting simple phenols: In 2010, Tuczek and coworkers were the first able to prove their catalytically active center converting 2,4-di-*tert*-butylphenol (DTBP) to the corresponding *ortho*-quinone (TON: 18, TOF: $1\,h^{-1}$) to be a $^{\mathbf{S}}\mathbf{P}$ complex. The ligand system is similar to the one published by Reglier back in 1990. However, instead of a hexa- or tetradentate bulky system they simplified the ligand to a smaller bidentate species combining a pyridinyl with an imidinyl donor. Their reaction conditions are adapted from Reglier and Bulkowski (20 °C, DCM) along with the usage of triethylamine as auxiliary base for substrate deprotonation (Reglier-Bulkowski conditions).[61] Changing the flexible imidinyl-donor to a more bulky and rigid triazolyl unit resulted in a five times faster conversion of DTBP (TON: 24, TOF: $5\,h^{-1}$) while the substrate scope could be extended to further simple phenols. This ligand is the fastest, most active $^{\mathbf{S}}\mathbf{P}$ known so far (TON: 48, TOF: $48\,\mathrm{h}^{-1}$; substrate: *para*-methoxyphenol) (Figure 1.5).[96]

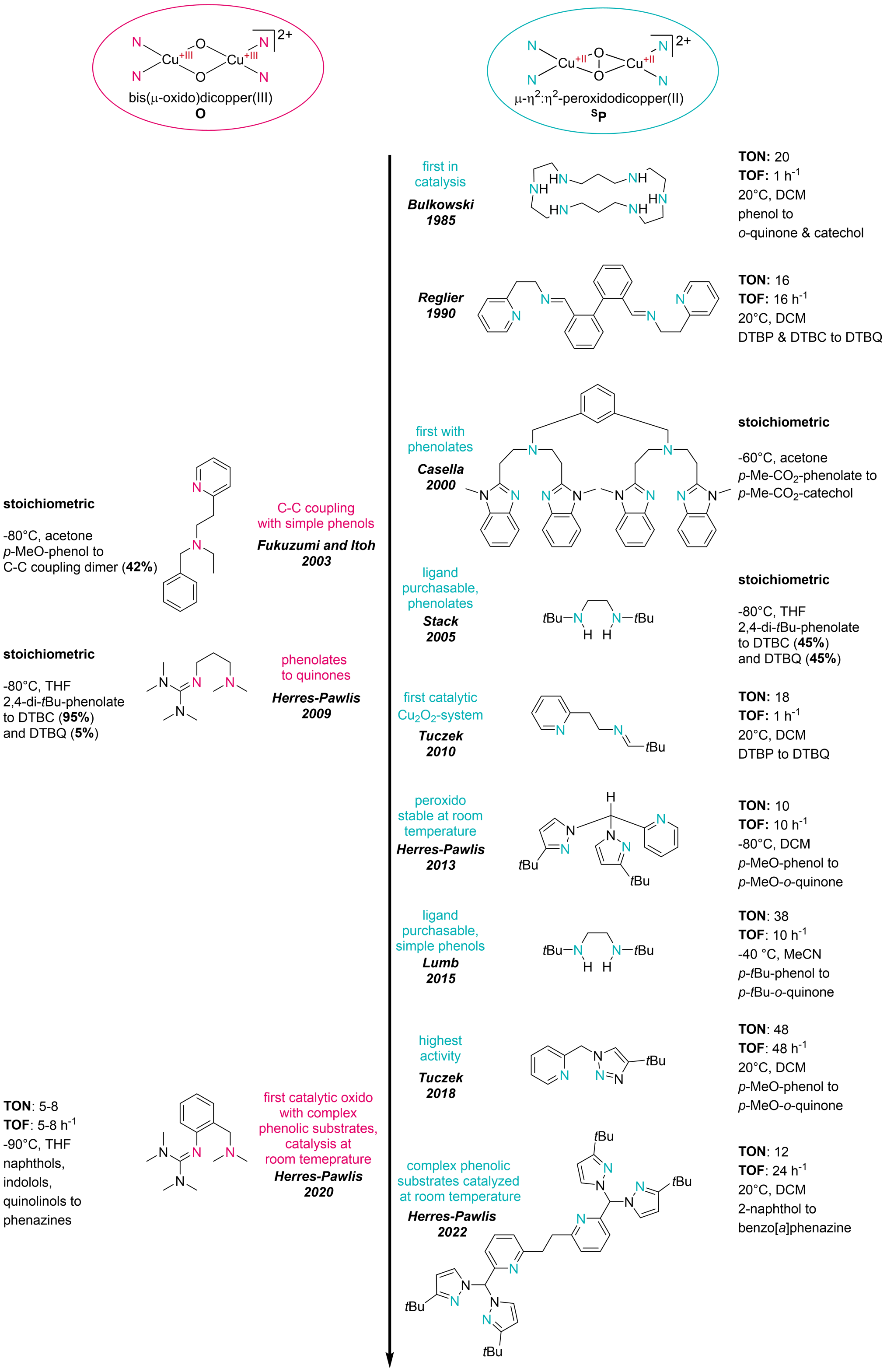

Figure 1.5: Chronological development of catalytically active bis(μ-oxido) species (**O**, left) and μ-η^2:η^2 peroxido ($^{\mathbf{S}}\mathbf{P}$, right) complexes displaying catalytic activity towards phenolic substrates.

Simultaneously, Lumb and coworkers as well as Herres-Pawlis and coworkers were focusing on catalytically active $^{\mathbf{S}}\mathbf{P}$ systems: Lumb's group revived the purchasable bidentate ligand DBED (Figure 1.5) already used by Stack and coworkers[81] for phenolate conversion. By applying Reglier-Bulkowski conditions, Lumb and coworkers successfully generated *ortho*-quinones from phenols. They were the first proving *ortho*-quinone formation via NMR spectroscopic measurements as their reaction product, *para*-*tert*-butyl-*ortho*-quinone, is one of the rare *ortho*-quinones stable under ambient conditions.[82] Additionally, the working group investigated several consecutive reactions like the coupling to biphenols and subsequent oxidation to benzoxepines. Therby, the formed *ortho*-quinones are converted into essential building blocks for the synthesis of organic compounds.[101]

In contrast to the simple and small DBED ligand, Herres-Pawlis and coworkers focused on more bulky tridentate ligands with pyridinyl and pyrazolyl N-donors similar to the histidine units in tyrosinase (Figure 1.5). The resulting $^{\mathbf{S}}\mathbf{P}$ species display an extraordinary stability at room temperature and are able to convert more complex phenolic substrates like 8-quinolinole or 2-naphthol.[95,97,98] However, the first pyridinylbispyrazolylmethane ligand published in 2013 only performs catalytic conversion at low temperatures ($-80\,°\mathrm{C}$). Addition of an ester function to the pyridinyl unit resulted in ligand capable to form *ortho*-quinone at room temperature ($20\,°\mathrm{C}$). The newest pyridinylbispyrazolyl ligand, just published last year, connects two tridentate units to an even bigger ligand by an ethylene bridge resulting in a long stability at room temperature (Figure 1.5). Within this study, unstable *ortho*-quinone products were isolated as stable phenazines through a subsequent condensation reaction with 1,2-phenylenediamine (PDA).[97]

Unlike to the large amount of catalytically active $^{\mathbf{S}}\mathbf{P}$ established until now, only three bis(µ-oxido) species able to convert phenolic substrates are known: First hydroxylation and oxidation activity of an **O** species was proven by Fukuzumi and Itoh in 2003 performing C-C coupling reactions with *para*-methoxyphenol.[51] In 2009 Herres-Pawlis and coworkers successfully converted phenolates to catechols and traces of *ortho*-quinone with an **O** complex.[88] The last **O** species, published in 2020 by the same working group, marked a huge milestone, being the first catalytically active bis(µ-oxido) complex converting a broad spectrum of phenolic substrates (Figure 1.5). For the first time in Cu_2O_2 catalysis, unstable *ortho*-quinone products were captured during a condensation reaction with PDA and isolated as stable phenazines.[87] Changing the counter ion of the oxido species from the weakly-coordinating PF_6^- to the coordinating I^-, an **O** complex is formed able to catalyze the conversion of naphthols, quinolinols and indolols to *ortho*-quinones at room temperature.[102]

Since the 1950's, the condensation reaction with PDA was used to prove the catalytic activity of tyrosinase via formation of fluorescent phenazines.[103] This method was transferred to several *ortho*-quinone forming reactions converting the highly-reactive *ortho*-quinone products[104,105] into phenazines stable at ambient conditions and verifiable via fluorescence, NMR or UV/Vis spectroscopic measurements.[87,106,107] Phenazines are a promising substrate class for pharmaceutical uses as phenazine derivatives naturally synthesized by soil bacteria function as antibiotics preventing fungal disease on crop plants.[108,109] Experiments using this natural derivatives against various groups of bacteria displayed a high antimicrobial effect.[110]

Taking a general look on the structure of Cu_2O_2 model systems with regard to the natural enzyme tyrosinase, all structures have one thing in common: besides the Cu_2O_2 center all ligand system are based on N-donors. While tyrosinase is stabilized by six histidine ligands, the Cu_2O_2 model systems show a broad spectrum of N-donors ranging from small secondary amine and imine functions over more bulky pyridinyl, pyrazolyl and triazolyl units to large benzimidazolyl groups (Figure 1.5). A ligand class known to stabilize Cu_2O_2 species by combining strong N-donors with a tunable ligand scaffold are guanidines: The N-donors vary from small methyl to bulky imidazolyl groups, they can be connected over a bridging unit or contain further hetero atoms like oxygen and sulfur. The selection is enlarged even more by bridging two or more guanidine units to form bis- or trisguanidines.[111]

1.3 Guanidines as Ligands for Cu_2O_2 Model Systems

Guanidines are neutral organic bases consisting of an imine function linked with two N-donor atoms.[112,113] Due to their high basicity they are moisture- and air-sensitive.[114–116] The unusually high basicity compared to other organic bases like triethylamine (pK_s = 10.8)[117] with pK_s values of 15.6 (pentamethylguanidine) results from the delocalization of the π-electrons within the imine function and the connected N-donor atoms. By including more bulky organic groups with a higher sterical demand like isopropyl the delocalization within the guanidine unit can be lowered decreasing its basicity as well as the σ-donor character of the N atoms (pentaisopropylguanidine: $pK_s = 13.8$).[112,113,118] The organic groups linked to the N-donor atoms as well as the imine function can be controlled by the choice of the amine derivatives used for the guanidine synthesis.[111,114,115]

1.3.1 Synthesis of Guanidine Ligands

The first synthesis of guanidines was described in 1964 by Eilingsfeld and coworkers.[119] The group used phosgene to chlorinate urea derivatives generating chloroformamidinium chlorides. Afterwards, the so-called Vilsmeier salts were converted with primary aromatic amines to penta-substituted guanidines.[119] In 1984, Kantlehner et al. extended the method using aliphatic primary amines.[114] At the beginning of the last century, the strong σ-donor properties of guanidines were identified as suitable ligand building blocks. Simultaneously, Pohl et al.[116] and Wittmann et al.[115] presented the first bi- and tridentate guanidine ligands. The group of Sundermeyer modified the synthesis routes described before[114,119] by adding triethylamine as an auxiliary base and optimizing the purification process.[115] In contrast, Pohl et al. developed an alternative, less hazardous access to bisguanidine ligands converting tetramethylguanidine with dibromopropane.[116] In the following decade, various ligands containing one,[120] two,[111,121] three[122] or even four[123] guanidine moieties were synthesized.

All guanidine synthesis routes known so far required either purchasable urea derivatives or guanidine units as starting material.[114–116,119] To create more tunable guanidine ligands a new synthesis route based on the ones with phosgene[114,115,119] was established by Herres-Pawlis et al.[111] in 2005 (Scheme 1.4). Thereby, secondary amines are converted with phosgene and triethylamine as auxiliary base to create the desired urea derivative. That way, the structure and properties of the final guanidine unit can be designed. In a second conversion with phosgene the urea derivative is transferred into the related Vilsmeier salt. Subsequent reaction with a primary diamine using triethylamine as auxiliary base forms the desired guanidinium chloride. By the choice of the diamine derivative used, structure and properties of the guanidine backbone unit are defined. Basic work-up with stoichiometric amounts of sodium hydroxide followed by washing with an excess of potassium hydroxide solution gives the free guanidine base. Using this method, a broad variety of bidentate guanidine ligands with the ability to modify the guanidine N-donor units as well as the connecting backbone unit can be synthesized.[111]

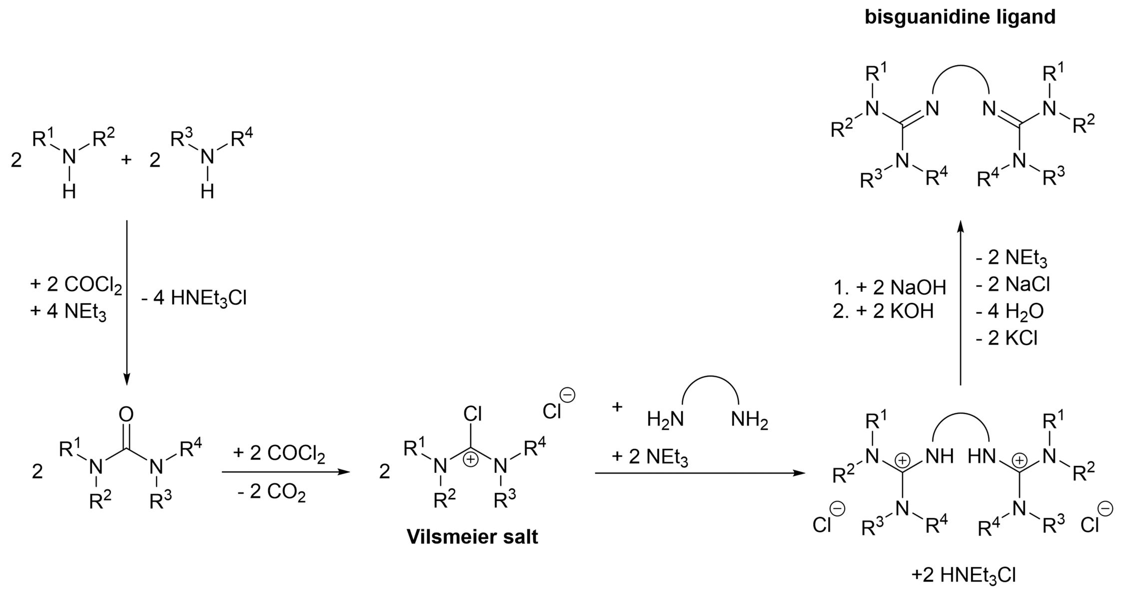

Scheme 1.4: Versatile synthesis route for bisguanidine ligands established by Herres-Pawlis et al. in 2005.[111] Starting from secondary amines, individually designing the guanidine units, over the related Vilsmeier salt which is converted with a primary diamine, defining the backbone unit, to give the final desired bisguanidine ligand.

Modify the N-donor function as well as the connecting spacer unit is a crucial feature in the design of catalytically active Cu_2O_2 species. Several bidentate guanidine ligands stabilizing bis(µ-oxido) centers are published within the last 15 years, however, only a few of them display catalytic activity converting phenolic substrates.[85–88,90,102] Consequently, systematic variation and optimization of functional groups is a key element on the way to new catalytically active Cu_2O_2 systems.

1.3.2 Types of Bidentate Guanidine Ligands

Bisguanidine ligands are sorted in different classes depending on their overall structure and are named after the building units they consist of. For the two classes of bidentate guanidines, a distinction is made whether both N-donor functions are guanidine units (bisguanidine) or a guanidine N-donor and another donor function are combined (hybrid guanidine) (Figure 1.6 top row). The variety of guanidine units ranges from simple methyl groups to longer C-H chains like propyl or bulky isopropyl groups.[90,111] Further variance is created bridging both N-donors with simple methyl or propyl chains to cyclic guanidine units[111,124] (Figure 1.6 bottom row). In hybrid guanidines, many different donor units exist besides the guanidine N-donor: Further N-donors like tertiary amines[87,90] and N atom containing spacer units (quinoline)[120] or other hereto atoms like S-donors (methylsulfane)[125] and O-donors (methylesters)[126] (Figure 1.6 middle row, right). The spacer units, connecting both donor function and defining the ligands bite angle, range from simple alkyl groups (ethyl,[115] propyl[88,111,125]) over aromatic groups (benzyl,[87,90,102,126] quinolinyl[120]) to complex and bulky benzodioxole[127] or chiral groups (R,R-cyclohexane)[128] (Figure 1.6 middle row).

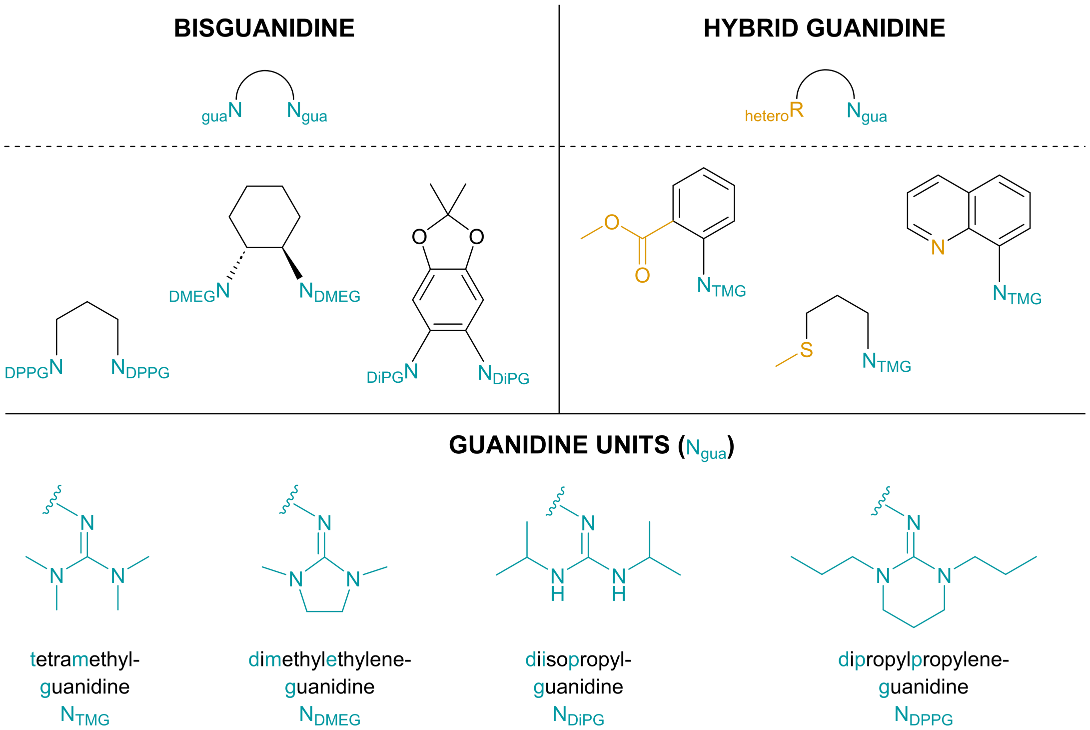

Figure 1.6: Example of bidentate guanidine ligands sorted by their ligand class: bisguanidines with two guanidine N-donors and hybrid guanidines combining a guanidine N-donor with another N-, S- or O-donor group.[111,120,125–128]

The trivial names of guanidine ligands are formed combining the name of the guanidine unit(s) included with the bridging spacer group: The bisguanidines TMG_2p and TMG_2tol

both contain two **T**etra**M**ethyl**G**uanidine units. The first one is bridged by a **p**ropane group while the latter has a **tol**uene spacer. In the hybrid guanidines DMEGbenza and DMEGanil a **D**i**M**ethyl**E**thylene**G**uanidine is connected to an N-donor containing spacer: **benz**yl**a**mine or **anil**ine, respectively (Figure 1.7).

1.3.3 Cu_2O_2 Species Stabilized by Guanidine Ligands

Guanidine ligands stabilizing Cu_2O_2 species to function as tyrosinase model systems are known since the early 2000‘s (Figure 1.7). Predominantly, **O** species are formed using coordinating solvents like acetonitrile or tetrahydrofuran.[85–88,90,102,129] However, mixtures between **O** and $^{\mathbf{S}}\mathbf{P}$ species were monitored with non-coordinating solvents like dichloromethane.[130] Only four years ago, a hybrid guanidine ligand stabilized **O** species stabilized by TMGbenza reached a huge milestone being the first **O** species converting a broad spectrum of phenolic substrates.[87] A year later, variations of the amine donor function led to further catalytically active O species based on the same guanidine unit (tetramethylguanidine, TMG) and spacer (benzylamine, benza) (Figure 1.7 dashed box).

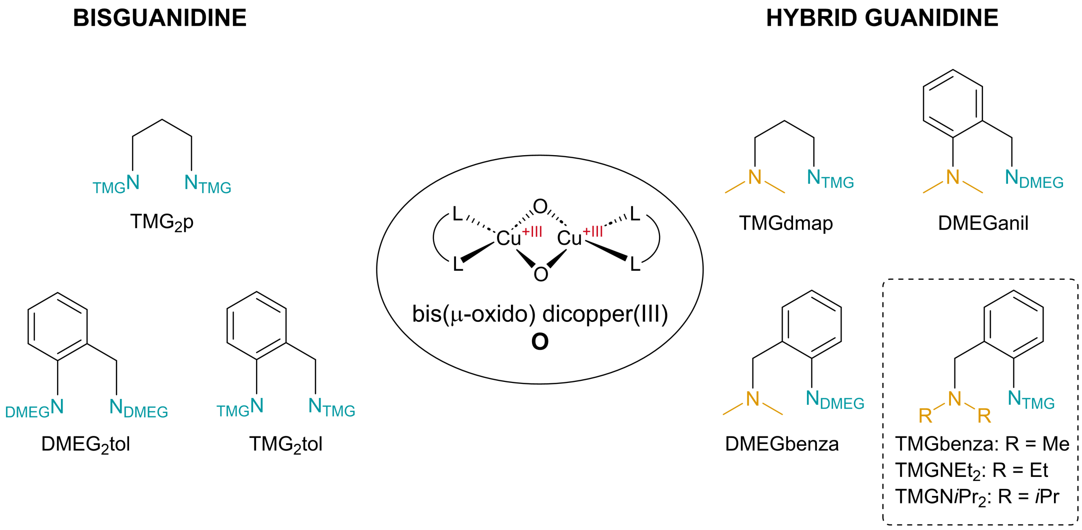

Figure 1.7: Summary of bidentate guanidine ligands stabilizing bis(μ-oxido) species mimicking the natural enzyme tyrosinase. Cu_2O_2 model systems displaying catalytic activity towards phenolic substrates are rectangular-dashed framed.[85–88,90,102,129,130]

Cu_2O_2 species like bis(μ-oxido) complexes show characteristic absorption bands in the visible region (300 – 600 nm) accompanied by an intensively colored reaction solution. In contrast, Cu(I) precursor solutions used to generate the Cu_2O_2 species, are often colorless or light yellowish.[52,54,71,74,78,87,92,131] These strong color changes during the complex formation are ideal for optical analytical methods like UV/Vis spectroscopy or colorimetric measurements. The formation of Cu_2O_2 species involves the interaction of reactants in different physical states. Molecular oxygen has to undergo a phase transfer into the liquid reaction mixture containing the diluted Cu(I) precursor species to form an **O**, $^{\mathbf{S}}\mathbf{P}$ or $^{\mathbf{T}}\mathbf{P}$ species. Thus, the availability of molecular oxygen in the liquid phase influences the reaction progress. On laboratory scale, this influencing factor is negligible as usually a oxygen-saturated reaction mixture is used. In contrast, industrial oxidation processes use either flow reactors with a continuous gas and liquid flow or semi-batch reactors with a gaseous reactant bubbling through a liquid phase at rest. Thereby, locally varying concentrations of the gaseous reactant occur influencing the reaction process massively. Thus, gas bubble volume, flow velocity as well as mixing of gas and liquid phase are important factors to control the formation of desired products besides the reaction kinetics.[5,132] Cu_2O_2 species based on guanidine ligands could be a useful tool to get a deeper insight in the interplay of reaction kinetics, mass transfer and hydrodynamics as well as locate optimization possibilities to increase yield and selectivity of the desired reaction product.

1.4 Applications of Cu_2O_2 Model Systems in Multi-Phase Flow Studies

Chemical process industries focus on improving yield and selectivity of the desired reaction product while minimizing the amount of resources used to lower process costs and waste formation. In most cases, formed reaction products are quantified analyzing the product stream leaving the reactor or tank.[133] In the case of oxidation reactions molecular oxygen or air (oxidant) is bubbled through the liquid reactants in a reactor. In this case, the oxidant has to cross the boundary layer between liquid and gas phase to initiate a chemical reaction.[134] The mass transfer of gaseous reactant from the gas into the liquid phase is influenced by physical quantities like the contact time between gas and liquid or the flow velocity of the ascending gas bubble (rising velocity). Consequently, reaction kinetics, mass transfer between the gas-liquid interphase and fluid dynamics within the flow reactor are competing with each other. As a result, oxidant availability and, therefore, desired product formation can vary massively on the local scale.[133,135,136] For a reliable prediction of yield and selectivity the intrinsic kinetics of the chemical reaction (unhindered by mixing and mass transfer) as well as local mass transfer and concentration fields have to be determined.[135,137]

The large amount of bubbles created by a continuous gas flow inside a solution is called bubble swarm. The mass transfer from the bubble swarm into the reaction solution involves many interfacial effects complicating a precise description of the process. To simplify the studies, the interlinked processes of intrinsic reaction kinetics, mass transfer and fluid dynamics can be investigated separately by reducing the complex system of a bubble swarm in a large, three-dimensional reactor to a smaller number of bubbles or a confined space.[133–135]

1.4.1 SuperFocusMixer (SFM): Determination of Intrinsic Reaction Kinetics

The intrinsic reaction kinetics can be determined using a micro mixing device (cross section 0.5 mm x 0.5 mm). In the SuperFocusMixer (SFM) liquid or diluted reactants are merged within a very short mixing time of ∼ 10 ms minimizing the limitations resulting from the mixing process. An alternating arrangement of micro-channels in the focusing zone creates a high surface area decreasing the influence of diffusion between the two phases. In the course of the focusing zone, the channels gradually reduce in diameter until they all open up into the mixing channel and merge the previously separated solutions together (Figure 1.8). The flow rates of both solutions are controlled with a syringe pump. Variation of the flow rate results in a longer or shorter contact time between the reactants affecting reaction kinetics and product formation. At a certain point of the mixing channel, the product formation is monitored in-situ via UV/Vis spectroscopy. With the amount of product formed in relation to the reactants flow rate used the intrinsic reaction kinetics can be calculated.[137,138]

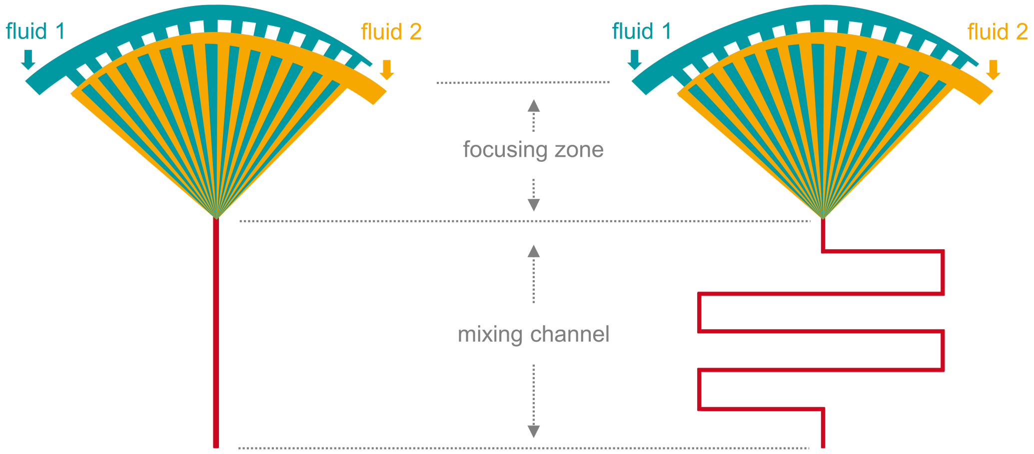

Figure 1.8: Schematic layout of different SuperFocusMixers (SFM) containing a focusing zone with micro-channel structure able to merge liquid reactants within ∼ 10 ms in the small mixing channel (0.5 x 0.5mm). Left: short mixing channel (60 mm), right: long mixing channel (200 mm).[137]

1.4.2 Taylor Flow (TF) and Hele-Shaw Cell (HSC): Local Mass Transfer Studies on a Small Scale

To get deeper insights in the local mass transfer from a gaseous reactant to a liquid reaction mixture, defined and reproducible hydrodynamic conditions are necessary. By restricting the mobility of freely rising gas bubbles in one or two directions in space well-defined flow fields are created. Size, shape and flow velocity of each bubble result in a different region of fluid flow behind it called bubble wake. With a small bubble diameter resulting in a slow flow velocity, laminar flows are created leading to a steady bubble wake without any vortex. With increasing bubble diameter and flow velocity, the fluid flow becomes more turbulent and vortices are forming within the bubble wake. Due to the turbulent fluid flow, the liquid boundary layers at the bubble surface are mixed with the bulk liquid behind the bubble. This phenomenon is called back-mixing and is visible by the formation of vortices. Using a confined geometry, the influence of different flow fields (laminar vs. turbulent) on the mass transfer within the gas-liquid interphase can be studied systematically.[133,135,136,139]

In the Taylor flow setup, single gas bubbles are forced in vertically aligned, confined tubes. The bubble fills the cross-section of the tube completely, only separated from the walls by a thin liquid film. Consequently, the bubble's diameter is defined by the wide of the tube's cross-section. The bubble's movements are limited to one direction in space, upward. The confined channel geometry, forces the bubble in an elongated bullet shape rising in a continuous fluid flow (laminar or turbulent) with a constant flow velocity independent from their volume. Thus, the buoyancy force of the rising bubble only depends on the tube's diameter (Figure 1.9, left). A minimum tube diameter, depending on the liquid and gas phase used, must be exceeded to ensure a buoyancy driven bubble movement unlimited by the surface tension of the liquid phase. With increasing diameter, the flow velocity rises leading to a more and more turbulent flow as well as the appearance of vortices in the bubble wake. Monitoring the occurring flow patterns at different tube diameters, the influence of these hydrodynamic phenomena on the mass transfer between gas and liquid phase can be investigated. To extend the investigation time for high resolution measurements like Raman spectroscopy, a counterflow aligned with the flow velocity can be used. The rising bubble is held at a fixed position without influencing the buoyancy force driven bubble movements.[133,136,139]

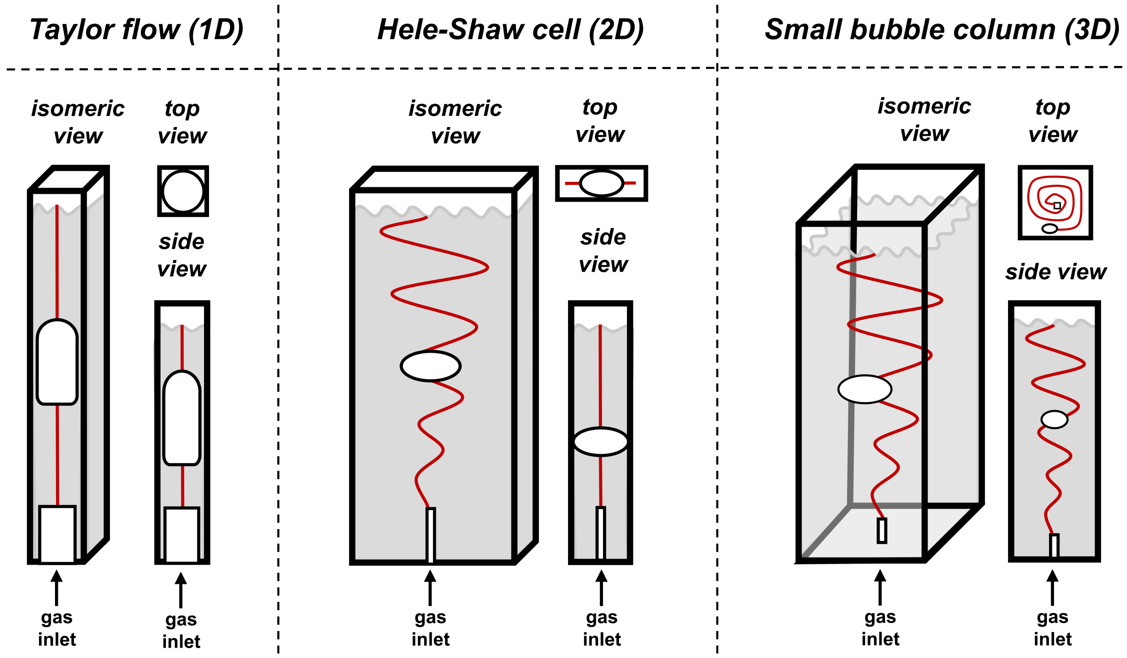

Figure 1.9: Schematic drawings with top, side and isomeric views of single rising bubble setups used to study the influence of mass transfer and hydrodynamics in gas-liquid interphases on chemical reactions. Left: Taylor flow setup confined in two dimensions. The bubble fills the entire cross-section only able to move upwards. Middle: Hele-Shaw cell limited in one direction. Bubbles are rising upwards with alternating lateral movements. Right: Small bubble column with an unconfined geometry in which only one bubble rises at a time displaying helical movements.

Confined in two dimensions, Taylor flows are a suitable tool for systematic mass transfer studies. Nevertheless, the conditions are far away from modeling the interactions and artificial effects taking place in a 3D bubble column like an industrial flow reactor. An alternative confined geometry only restricted in one plane is a Hele-Shaw cell (HSC). In this planar thin-gap cell single bubbles are rising vertically in a fluid medium at rest. HSC display an intermediate between a one-dimensional Taylor flow and a three-dimensional bubble column. Due to the small gap width of 1 mm ($<$ bubble diameter), bubble movements are restricted to two directions in space: sideways and upward. Only a thin lubrication film separates the bubble's surface from the cell walls (Figure 1.9, middle). In contrast to the Taylor flow, bubble diameters vary leading to a broad spectrum of bubble volumes. As the buoyancy force depends on the bubble volume and significantly influences the bubble's flow velocity a wide range of bubble motion regimes can be monitored. To calculate diameter and flow velocity, the in-plane projected area and the perimeter of each bubble are tracked. Monitoring the position of each bubble in both directions over time, flow velocity and bubble motion can be determined. The mass transfer from the gaseous reactant into the reaction solution is measured indirectly monitoring the product formation in the vicinity and wake of the bubble. After calibration, time- and gap-averaged concentration fields of the gaseous reactant can be calculated.[92,131]

Using a reaction solution counterflow, Taylor flows can study mass transfer on rising single bubbles for a long distance. However, they lack a realistic bubble movement and related motion regimes as the confined geometry only allows movements in one direction. The geometry of a HSC, confined in one direction in space, enables a wide range of bubble motion regimes. Nevertheless, a HSC focuses on a small region of interest lacking information of the bubble's behavior (diameter change, deformation) over a long-distant ascent. To study rising bubbles in an unconfined environment over a long distance, compromises between an accurate determination of bubble parameters and experimental setups near to industrial conditions have to be made.[92,131,140]

To precisely monitor bubble parameter changes over a long-distant ascent, three-dimensional bubble columns with two moving cameras in horizontal and vertical plane are used. As the bubble is freely rising, an accurate determination of bubble parameters requires motion data with a high frame rate of 100 – 250 frames per second (fps) from two dimensions in space. As every single bubble generates a larger data set, analysis are only possible for single rising bubbles.[141] A setup close to industrial conditions are three-dimensional bubble columns with a gas sparger creating bubble swarms in a liquid reaction medium. Due to the large number of bubbles (5,000 – 35,000), single tracking of motion regimes for each bubble is impossible. Instead, a single camera at fixed positions is used. A low frame rate, slower than the bubble flow velocity, prevents double tracking of the same bubble during its ascent. Parameters like bubble volume and flow velocity are calculated assuming a rotational symmetry for each bubble resulting in time- and gap-averaged results instead of a precise bubble geometry generated with two cameras monitoring single bubbles.[140]

Using the aforementioned tools and setups, the intrinsic reaction kinetics, the mass transfer in the gas-liquid interphase and the influence of hydrodynamics can be studied. An individual investigation of the superimposing factors enables deeper insights to precisely describe each reaction step and reliably predict yield and selectivity of the desired product. For systematic studies tunable chemical systems are needed providing a broad spectrum of reaction kinetics and reaction types as well as reaction products quantifiable in-situ. A chemical system meeting those needs are Cu_2O_2 model systems formed by the conversion of molecular oxygen with a copper complex. Reaction rate as well as reactant and product characteristics like color or fluorescence can be controlled by the choice of ligand and anion of the copper complex.

1.4.3 Cu_2O_2 Species for Reactive Mass Transfer Studies

Most Cu_2O_2 species are unstable at ambient conditions and decay to stable compounds like a bis(µ-hydroxido) complex over time. Thus, formation and decay of $^{\mathbf{T}}\mathbf{P}$, $^{\mathbf{S}}\mathbf{P}$ and **O** species belong to a reaction type called consecutive reaction: an intermediate (Cu_2O_2 species (C)) is formed by two or more reactants (Cu(I) precursor complex (A) + molecular oxygen (B)) which further reacts to a final product (bis(µ-hydroxido) complex (D)). If the Cu_2O_2 species displays catalytic activity and converts phenolic substrates into desired reaction products (E), we have a so-called competitive-consecutive reaction: A consecutive reaction (formation and subsequent substrate conversion) in which both reaction steps need the same reactant (molecular oxygen) and thus impede each other (Figure 1.10).

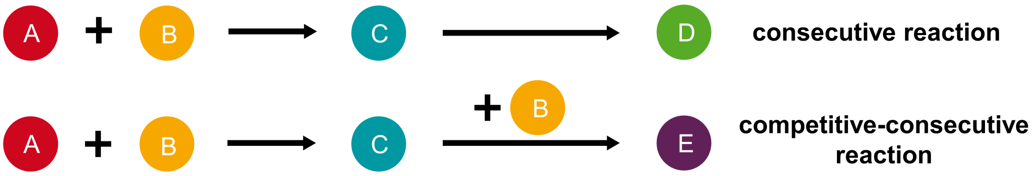

Figure 1.10: Examples of reaction types mediated by Cu_2O_2 model systems. Top row: A consecutive reaction e.g. formation and subsequent decay of a Cu_2O_2 species. Bottom row: A competitive-consecutive reaction e.g. formation of a Cu_2O_2 species and subsequent conversion of phenolic substrates competing about oxygen as reactant.

Ideally consuming the gaseous reactant accelerates the mass transfer rate and product formation can be improved with suitable mixing conditions (consecutive reaction). Depending of the reaction type used, formation of one product over another could be controlled as well (competitive-consecutive reaction).[134,139]

To undergo a chemical reaction, a mass transfer of the gaseous reactant into the liquid phase is necessary. This phase transition is influenced by many factors given by the chemical system used: The reaction kinetics (reaction rate constant and reaction order) directly affect the reaction speed. Gas solubility varies depending on the gas and solvent. Reactants may function as surface active agent changing the surface tension of the solvent and hinder the free mobility of the interface. Consumption of the gaseous reactant results in shrinkage of the bubble increasing the pressure inside of it and speeding up physical driven mass transfer. All these factors either improve or hinder the reaction mass transfer compared to a purely diffusion driven mass transfer between gas and liquid phase without a chemical reaction in the liquid phase. As an example: If the reaction rate constant is small compared to the diffusion coefficient, the reaction speed is slow and thus limited by the reaction kinetics. In contrast, with a rate constant way higher than the diffusion coefficient, all reactants in the liquid are immediately converted and the reaction is limited by the mass transfer between gas and liquid phase. These phenomena are described mathematically by the enhancement factor E, a dimensionless number characterizing whether the mass transfer is increasing or decreasing the reaction rate. The enhancement factor is influenced by the diffusion coefficient between gas and liquid phase D, the liquid phase mass transfer coefficient k_L, the reaction rate constant k and the reaction order n (Equation 1.1).[134,135,139]

$$E = \frac{1}{k_L} \cdot \sqrt{\frac{2}{n+1} \cdot k \cdot D \cdot c^{\,n-1}} \tag{1.1}$$

By the formation of a Cu_2O_2 center, a copper(I) precursor complex diluted in a liquid phase is converted with a gaseous reactant (molecular oxygen). This consecutive reaction can be extend to a competitive-consecutive reaction by adding a phenolic substrate and usage of a catalytically active **O** or $^{\mathbf{S}}$**P** species. Thus, Cu_2O_2 species are a useful tool to reach the goal of a precise reaction description as well as prediction of the product's yield and selectivity: With their tunable reaction kinetics and spectroscopic features (color, fluorescence) they mediate consecutive as well as competitive consecutive reaction in organic solvents close to industrial conditions.

2 Objective and Outline

2.1 Objective

To convert basic chemicals into fine chemicals of higher oxidation state, many industrial processes are using oxidation reactions including hazardous transition metal catalysts.[1–5] In these processes, transition metals are playing a key role by transferring inactive gaseous oxidants like molecular oxygen into active oxidizing species.[1–5,14,15] In nature, metallo enzymes incorporating transition metals like copper or iron are catalyzing oxygen activation processes. Thereby, tyrosinase stands out with an unusual substrate flexibility: The enzyme converts the phenol derivative L-tyrosine as well as the dihydroxybenzene L-DOPA into the *ortho*-quinone L-DOPAquinone during melanin synthesis.[30,46,47] Thereby, the intermediate species present in the monophenolase cycle of tyrosinase converting L-tyrosine to L-DOPA is still under debate. The catalytically-active center of tyrosinase consists of two copper(II) atoms connected by two O atoms with a peroxide bridge in between them, a so-called Cu_2O_2 species.[38] As industrial oxidation processes are lacking new environmentally friendly oxidation catalysts, mimicking the catalytic function of tyrosinase by modeling the catalytically-active Cu_2O_2 center is a main goal.

The objective of this work is to investigate the catalytic activity of Cu_2O_2 species stabilized by guanidine N-donor ligands towards various phenolic substrates using a method successfully implemented by Herres-Pawlis and coworkers in an earlier study. Thereby, resulting unstable *ortho*-quinone products are converted in a condensation reaction with 1,2-phenylenediamine into stable phenazine products.[87] Naturally occurring phenazine derivates like phenazine-1-carboxylic acid display antimicrobial behavior protecting crop plants against fungal diseases.[108–110] Thus, isolated phenazine products will undergo antibacterial tests performed by biologists within a cooperation project investigating their function as potential antibiotic.

To capture the intermediate species present in the monophenolase cycle, a Cu_2O_2 species based on a hybrid guanidine ligand is synthesized and converted with several phenolate derivates. Additionally, side products formed in the presence of protons are synthesized and isolated to exclude their formation instead of the desired intermediate species. Subsequently, the formed reaction mixtures and side-products will be investigated via electron-paramagnetic-resonance (EPR) spectroscopy and single-crystal X-ray diffraction (SC-XRD).

Industrial processes are focused on operating profitably, thus, synthesis pathways are optimized to maximize yield and selectivity of desired reaction product while decreasing the amounts of side products and chemical waste formed.[133] Oxidation reactions using gaseous oxidants combined with a liquid reaction mixture are influenced by three main factors: the reaction kinetics, the fluid dynamics and the mass transfer between gas and liquid phase.[133,135,136] These factors can be studied separately using reaction setups with a confined geometry like the Taylor flow or the Hele-Shaw cell. Thereby, data of the individual factors are generated which are ideally transferable to larger reaction setups by the use of key figures independent from the setup used like dimensionless numbers or scaling laws. However, understanding this complex interplay is a key factor to control the desired product's formation.[133–135] Thus, reactive mass transfer studies using setups near to industrial conditions are needed.

Cu_2O_2 species are formed by the conversion of molecular oxygen with a copper(I) precursor complex dissolved in aprotic solvents. During the consecutive reaction of their formation and decay, a strong color change is visible accompanied by characteristic UV/Vis transition signals. Additionally, some Cu_2O_2 species are mediating a competitive consecutive reaction by formation of a catalytically-active Cu_2O_2 center and subsequent conversion of phenolic substrates to the related *ortho*-quinone products. Therefore, Cu_2O_2 species are ideal candidates for reactive mass transfer studies.

In this work the reactive mass transfer during formation and decay of Cu_2O_2 species stabilized by bisguanidine and diamino ligands will be studied in a Hele-Shaw cell setup monitoring the on going reaction with a high-speed grey-level camera. Scaling laws proposed in earlier studies with water and dye will be revised to reveal the main influencing factor(s) on the reactive gas-liquid mass transfer.

To get more information about controlling selectivity within competitive consecutive reactions, the conversion of a simple phenol by a Cu_2O_2 species based on a diamino ligand will be studied in different mass transfer reaction setups in cooperation projects with chemical engineers. To begin with, the reaction rates of the competing reactions and the molecular oxygen concentration fields have to be determined. Therefore, the Taylor flow setup combined with a UV/Vis detector monitoring the rising single bubble of molecular oxygen is used. Subsequently, the determined data are transferred into a large unconfined bubble column near to industrial conditions. Influencing hydrodynamic factors like gas inlet size, bubble size and rising velocity are studied using a large bubble swarm monitored via inline infrared (IR) spectroscopy.

2.2 Outline

Results obtained and experiments performed within this work are structured as followed:

All results obtained are divided in two main parts depending on their research focus. Chapter 3 discusses chemical questions and investigations like ligand synthesis, catalytic activity studies, studies of the monophenolase cycle and bacterial tests. The focus of Chapter 4 is on engineering questions tackled in cooperation projects with chemical engineers. Thereby, mass transfer between gas phases and liquid phases is studied using Cu_2O_2 species and molecular oxygen in various (confined) reaction setups.

Chapter 3 is further divided into three sections: In Section 3.1, the resynthesis of a known bisguanidine ligand is described. Cu_2O_2 species based on this ligand are formed and their conversion of naphthols, quinolinols, indolols and carbazolol to *ortho*-quinones followed by a condensation with 1,2-phenylenediamine is studied. Mass spectrometry spectra of the conversion of selected substrates are recorded to investigate on going side reactions and byproducts formed. Resulting desired phenazine products are isolated and tested for their antimicrobial behavior towards four types of gram-positive as well as four types of gram-negative bacteria by biologists. In section 3.2 the development and synthesis of a new hybrid guanidine ligand is described. The formation of Cu_2O_2 species during the conversion of Cu(I) precursor complexes of the new ligand with molecular oxygen is investigated via inline UV/Vis spectroscopy. Subsequently, catalytic activity tests with naphthols, quinolinols and indolols followed by a condensation with 1,2-phenylendiamine are performed. The studies of intermediate species present in the monophenolase cycle of tyrosinase are discussed in section 3.3. A possible side product of the conversion of a phenol substrate is resynthesized and analyzed via SC-XRD. Subsequently, EPR spectra of the reaction solution converting the related phenolate species are recorded and compared to the EPR spectrum of the side product.

Going on to Chapter 4, reactive mass transfer investigation performed with a consecutive reaction using a Hele-Shaw cell are outlined in section 4.1. Several Cu_2O_2 species are pre-tested regarding their reaction kinetics matching the needs of the Hele-Shaw cell setup. Afterwards, reactive mass transfer investigations are performed on the related formation and decay reaction of the Cu_2O_2 species. With the data obtained, proposed scaling laws from earlier studies are reviewed and optimized. Reactive mass transfer investigation performed on the consecutive reaction of a Cu_2O_2 species with a simple phenol are summarized in section 4.2. First, concentration fields of molecular oxygen are determined in the Taylor flow. Subsequently, results are transferred onto a large bubble column with bubble swarms and reactive mass transfer studies are repeated.

All results discussed are summarized in chapter 5 giving an overview of new insights found during this work. Additionally, new objectives to be tackled in future studies are outlined.

Detailed synthesis routes and descriptions of performed experiments as well as instrumental details are given in chapter 6.

Recorded mass spectrometry spectra and full data sets of SC-XRD measurements are available in chapter 8.

3 Cu_2O_2 Model Systems Based on Bidentate Guanidine Ligands

Parts of this chapter are already published in:

L. Laurini, Master thesis, RWTH Aachen University, Aachen, **2019**.[142]
L. Laurini, S. M. Conte, K. Hüser, P. R. F. Cordero, H. M. Núñez Ponce, S. Zimmer, L. Lauterbach, S. Herres-Pawlis, *Eur. J. Inorg. Chem.* **2024**, *27*, e202300700.[143]

Bidentate guanidine ligands are able to stabilize Cu_2O_2 species mimicking the catalytically active center of the naturally occurring enzyme tyrosinase. Using bidentate guanidine ligands, predominantly bis(µ-oxido) dicopper(III) complexes (**O** species) are formed which are an isoelectronic isomer to the µ-η^2:η^2-peroxido dicopper(II) complex ($^{\mathbf{S}}\mathbf{P}$ species) in the active center of tyrosinase.[17,85–88,90,102,129] Most enzymes are working substrate-specifically,[32] in contrast, tyrosinase displays an extraordinary substrate flexibility: The enzyme converts numerous phenols as well as catechols to quinones in the biosynthesis of the cell pigment melanin.[30] Mimicking the catalytic function of tyrosinase, environmentally-friendly oxidation catalysts able to transform a broad variety of phenolic substrates could be developed.[61,82,87,90,95–98]

The first catalytically active model systems were established by Bulkowski in 1985[100] and Réglier in 1990.[59] Their hexa- / tetradentate N-donor systems converted simple phenolic substrates like phenol and 2,4-di-*tert*-butylphenol to *ortho*-quinones using triethylamine as an auxiliary base with a ratio of 1:50:100 ([catalyst]:[substrate]:[triethylamine]; $T = 20\,°\mathrm{C}$, dichloromethane). With a few exceptions like 3,5-*tert*-butyl-*ortho*-quinone,[82] most *ortho*-quinones are highly-reactive and unstable under ambient conditions.[104–107] Thus, their short lifetime was studied via in-situ UV/Vis spectroscopy. *Ortho*-quinones show characteristic absorption bands around 400 nm.[61,82,144] The established *Bulkowski-Réglier* method[59,100] was later adapted by Tuczek and coworkers.[61,145] Changing the bulky tetradentate N-donor ligand to a bidentate species with a pyridinyl and a triazolyl unit resulted in the Cu_2O_2 model system with the highest activity until now.[96] Especially within the last fourteen years, numerous model systems able to convert phenolic substrates were found.[61,82,87,90,95–98] Most of them are containing a $^{\mathbf{S}}\mathbf{P}$ center analogous to the enzyme tyrosinase.[61,82,95–98]

In parallel, the hydroxylation and oxidation activity of several guanidine stabilized **O** species towards phenolic substrates was investigated by Herres-Pawlis and coworkers using *Bulkowski-Réglier* conditions.[85,86,88] However, only two systems converted phenolic substrates successfully to desired *ortho*-quinone products. The bisguanidine ligand 2,2'-(((dimethylamino)methylene)amino)benzyl)-1,1,3,3-dimethylethyleneguanidine, so called DMEG$_2$tol, based on an tolyl spacer with two dimethylethylenguanidine (DMEG) N-donor units, was able to convert 8-quinolinol catalytically to the corresponding *ortho*-quinone.[86] The hybrid guanidine ligand 2-(3-(dimethylamino)propyl)-1,1,3,3-tetramethylguanidine (TMGdmap), based on a propylene spacer connecting a tetramethylguanidine (TMG) and a dimethylamine N-donor unit, transformed 2,4-di-*tert*-butylphenolate stoichiometrically to the desired *ortho*-quinone and catechol products (Figure 3.1).[88]

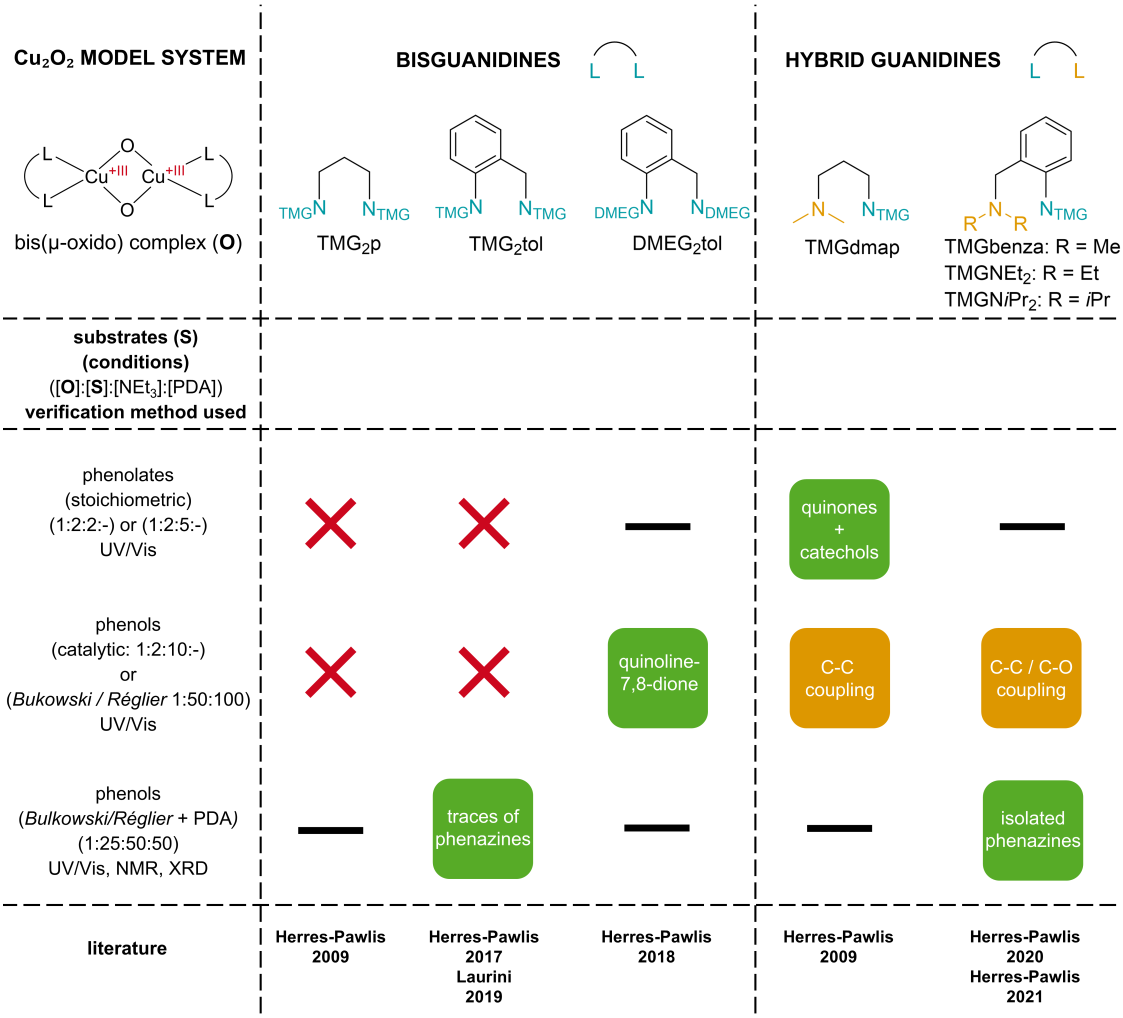

Cu$_2$O$_2$ MODEL SYSTEM	**BISGUANIDINES**			**HYBRID GUANIDINES**	
bis(μ-oxido) complex (**O**)	TMG$_2$p	TMG$_2$tol	DMEG$_2$tol	TMGdmap	TMGbenza: R = Me TMGNEt$_2$: R = Et TMGN*i*Pr$_2$: R = *i*Pr
substrates (S) **(conditions)** ([**O**]:[**S**]:[NEt$_3$]:[PDA]) **verification method used**					
phenolates (stoichiometric) (1:2:2:-) or (1:2:5:-) UV/Vis	✗	✗	—	quinones + catechols	—
phenols (catalytic: 1:2:10:-) or (*Bukowski / Réglier* 1:50:100) UV/Vis	✗	✗	quinoline-7,8-dione	C-C coupling	C-C / C-O coupling
phenols (*Bulkowski/Réglier* + PDA) (1:25:50:50) UV/Vis, NMR, XRD	—	traces of phenazines	—	—	isolated phenazines
literature	**Herres-Pawlis 2009**	**Herres-Pawlis 2017** **Laurini 2019**	**Herres-Pawlis 2018**	**Herres-Pawlis 2009**	**Herres-Pawlis 2020** **Herres-Pawlis 2021**

Figure 3.1: Literature-known bidentate guanidine ligands stabilizing bis(μ-oxido) dicopper(III) complexes (**O** species) tested in the stoichiometric and / or catalytic hydroxylation and subsequent oxidation to desired *ortho*-quinone products.[85–88,90,142] A green box indicates the desired reaction product was received while an orange one gives the reaction product formed instead. Reactions showing no activity are marked with a red cross. If no data are available, the entry is marked with a black horizontal line.

After extension of the established *Bulkowski-Réglier* method with a subsequent condensation reaction using 1,2-phenylenediamine (PDA) inspired by Tuczek and coworkers,[106] phenazine products, stable under ambient conditions and verifiable via NMR spectroscopy, could be formed instead of the former highly-reactive *ortho*-quinones. Using this adapted method with a reaction temperature of −90 °C and a reaction time of 1 h, the first catalytically active **O** species could be presented by Herres-Pawlis and coworkers in 2020. The **O** species is stabilized by the hybrid guanidine ligand 2-2-((dimethylamino)methyl)phenyl-1,1,3,3-tetramethylguanidine (TMGbenza) consisting of a benzylamine spacer connected to a TMG N-donor and a dimethylamine N-donor. Interestingly, structurally-challenging substrate classes, never tested with Cu_2O_2 model systems before, like naphthols, quinolinols and indolols were successfully converted to *ortho*-quinones and isolated as stable phenazine products (Figure 3.1). In contrast, using established structurally simple substrates like *para*-*tert*-butylphenol and *para*-methoxyphenol, only C-O coupled products of one substrate molecule and the desired quinone product could be detected.[87] One year later, two further catalytically active **O** species based on the structure of TMGbenza were published. Both ligands contain the same benzylamine spacer connecting a TMG unit to an dialkylamine N-donor (Figure 3.1). Thereby, the ligands vary in their alkyl unit within the amine N-donor, resulting in a longer reaction time for the catalytic conversion with increasing alkyl group size (Me: 1 h, Et: $2-3$ h, *i*Pr: $2-3$ h).[90]

Some **O** species stabilized by bidentate guanidine ligands like 2-(2((bis(dimethylamino)-methylene)amino)benzyl)-1,1,3,3-tetramethylguanidine (TMG_2tol) or TMGdmap were published as catalytically inactive due to a lack of *ortho*-quinone or C-C coupled biphenol formation with phenolic substrates under *Bulkowski-Réglier* conditions monitored via UV/Vis spectroscopy.[85,88] This could result from the conversion to C-O coupling products instead of *ortho*-quinones as it was monitored with TMGenza and other benzylamine based hybrid guanidines.[87,90] Preliminary work focussing on the **O** species stabilized by TMG_2tol using the new extended method combing *Bulkowski-Réglier* conditions with a subsequent PDA condensation indicated a catalytic activity towards naphthols, quinolinols and indolols (Figure 3.1).[142]

3.1 Cu_2O_2 Studies with TMG_2tol (L1)

The bisguanidine ligand 2-(2((bis(dimethylamino)methylene)amino)benzyl)-1,1,3,3-tetramethylguanidine (TMG_2tol, **L1**) was first published by Herres-Pawlis and coworkers in 2017. Conversion of bisguanidine ligand **L1** with copper(I) salt tetrakis(acetonitrile)copper(I) hexafluorophosphate ($[Cu(CH_3CN)_4]PF_6$) resulted in the formation of the copper(I) complex $[Cu(TMG_2tol)]_2[PF_6]_2{\cdot}CH_3CN$. By injection of $[Cu(TMG_2tol)]_2[PF_6]_2{\cdot}CH_3CN$ diluted in acetonitrile into oxygen-saturated tetrahydrofuran (THF) at −78 °C the bis(µ-oxido) complex $[Cu_2O_2(TMG_2tol)_2](PF_6)_2$ ([**O1**]$(PF_6)_2$) was formed in situ. The presence of an oxido species was proven by its characteristic UV/Vis absorption bands at 290 nm and 395 nm. [**O1**]$(PF_6)_2$ is stable at −78 °C for several hours.[85]

The oxido complex [**O1**]$(PF_6)_2$ was stated as inactive towards phenolic substrates as no desired *ortho*-quinone product or C-C radical-coupled product (biphenol) was observed under *Bulkowski-Réglier* conditions via UV/Vis spectroscopy.[85] In contrast, preliminary work extending the reaction conditions by a condensation with PDA indicated a hydroxylation and oxidation activity ([[**O1**]$(PF_6)_2$]:[S]:[NEt_3]:[PDA] = 1:50:100:100, c([**O1**]$(PF_6)_2$) = 2 mol %, T = −78 °C). A broad spectrum of phenolic substrates ranging from structurally simple ones like phenol or *para*-methoxyphenol as well as structurally challenging alcohols like naphthols, quinolinols, indolols and 7-hydroxycumarin were investigated. Thereby, no catalytic activity was monitored using phenols or 7-hydroxycumarin (Figure 3.2 marked in red). However, converting naphthols, quinolinols and indolols, *ortho*-quinone no signals around 400 nm could be monitored in the UV/Vis spectra.[142]

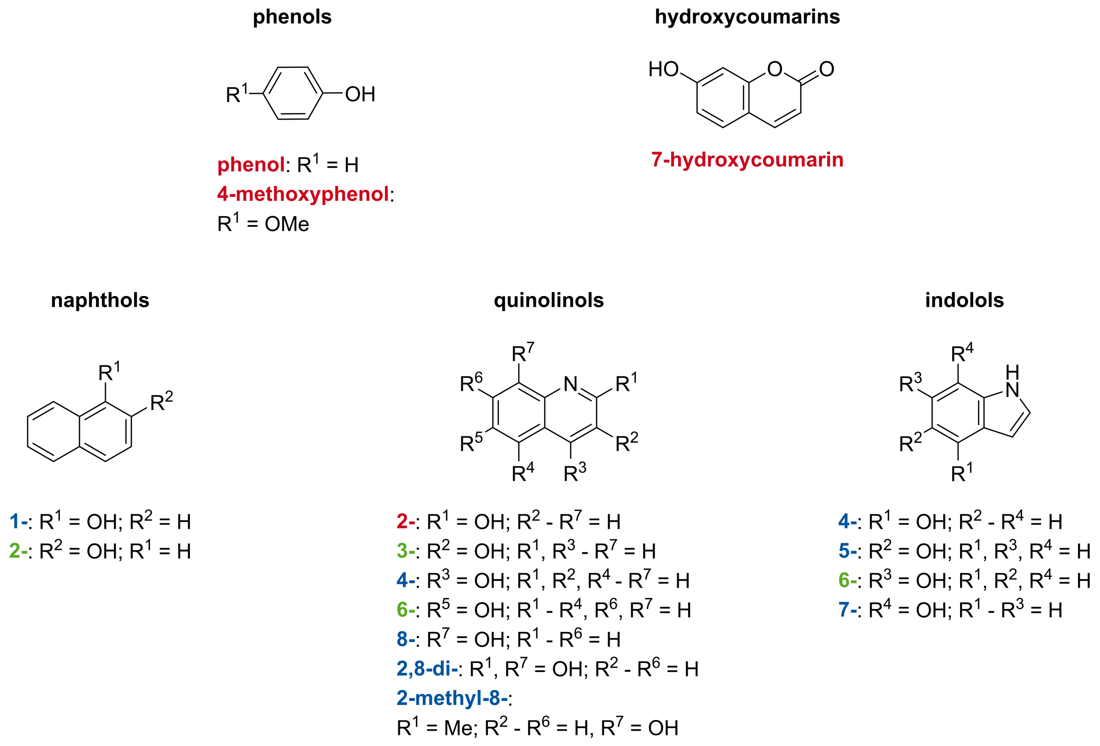

Figure 3.2: Results of preliminary work studying the catalytic activity of bis(µ-oxido) complex [**O1**]$(PF_6)_2$ ($[Cu_2O_2(TMG_2tol)_2](PF_6)_2$) in 2019 under *Bulkowski-Réglier* conditions extended with a subsequent condensation with PDA ([[**O1**]$(PF_6)_2$]:[S]:[NEt_3]:[PDA] = 1:50:100:100; c([**O1**]$(PF_6)_2$) = 2 mol %, T = −78 °C). The reaction was monitored via in-situ UV/Vis spectroscopy and the resulting reaction mixture was analyzed with NMR spectroscopy afterwards. Substrates which displayed phenazine signals in the NMR spectrum indication catalytic activity are marked in green. If ortho-quinone signals were visible in the UV/Vis spectrum and no phenazine product appeared in the NMR spectrum substrates are colored blue. If no catalytic activity was monitored the substrate is listened in red.[142]

Due to the low concentrations necessary for UV/Vis analysis, only 2-naphthol, 3-, 6-quinolinol and 6-indolol displayed traces of desired phenazine product signals in their NMR spectra (Figure 3.2 marked in green).[142] A verification of *ortho*-quinone products resulting from quinolinols, naphthols and indolols via UV/Vis signals is not possible as those are not covered in literature. As no phenazine products could be isolated, a catalytic hydroxylation and oxidation activity of the TMG_2tol based **O** species has not be proven yet.

3.1.1 Resynthesis of TMG_2tol (L1)

TMG_2tol (**L1**) was resynthesized based on the published synthesis route.[85] 2-Aminobenzylamine was converted with chloro-N,N,N',N'-tetramethylformamidinium chloride (TMG Vilsmeier salt) and triethylamine as auxiliary base (Scheme 3.1). The process was optimized extending the reflux time from three to five hours and purifying the ligand by fractional distillation of the crude product under vacuum. TMG_2tol was obtained as a slightly yellowish oil nearly doubling the yield compared to the literature procedure (75%, Lit.: 42%). A more detail synthesis protocol can be found in the experimental part (Section 6.3.1).

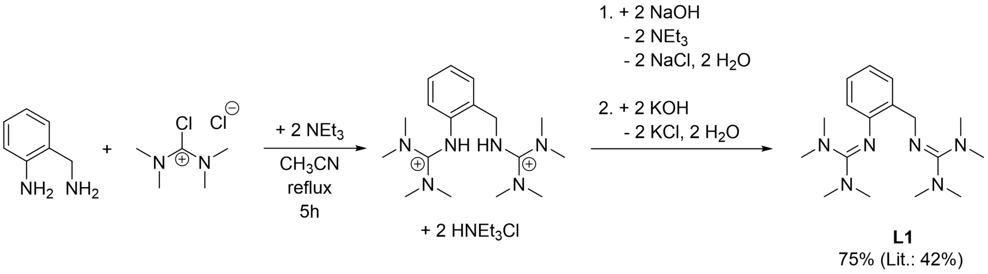

Scheme 3.1: Optimized synthesis route of the bisguanidine ligand TMG_2tol (**L1**) firstly published in 2017 by Herres-Pawlis and coworkers.[85] The bidentate ligand consists of two TMG guanidine units and a connecting tolyl spacer.

3.1.2 Synthesis of Oxido Complex $[Cu_2O_2(TMG_2tol)_2](PF_6)_2$ ($[O1](PF_6)_2$)

The bis(μ-oxido) complex [**O1**]$(PF_6)_2$ was formed in-situ (Scheme 3.2). First, a solution of the copper(I) precursor complex $[Cu(TMG_2tol)(CH_3CN)]PF_6$ ([**Pr1**]PF_6) was synthesized. Therefore, TMG_2tol (0.2 mmol) diluted in acetonitrile was added to a solution of copper(I) hexafluorophosphate ($[Cu(CH_3CN)_4]PF_6$; 0.2 mmol) in acetonitrile. Subsequently, the formed colorless solution of [**Pr1**]PF_6 ($c = 0.04\,mol\,l^{-1}$) was injected into oxygen-saturated THF at $-78\,°C$.

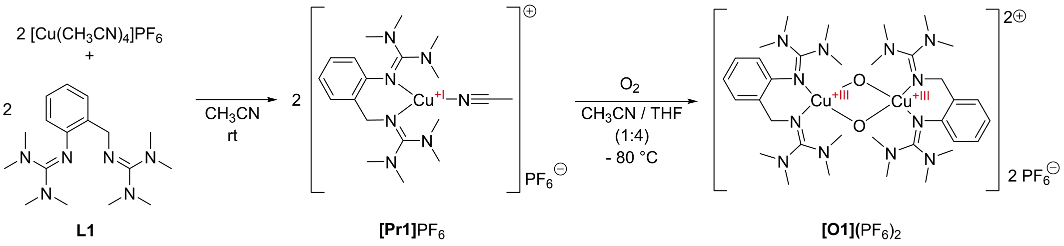

Scheme 3.2: Synthesis of the bis(μ-oxido) complex $[Cu_2O_2(TMG_2tol)_2](PF_6)_2$ ([**O1**]$(PF_6)_2$).

The solution turned reddish-brown and was stirring at −80 °C for 10 minutes to ensure complete formation of [**O1**]$(PF_6)_2$ ($n = 0.1\,\text{mmol}$, $c = 0.004\,\text{mol}\,\text{l}^{-1}$).

3.1.3 Catalytic Activity Studies with Oxido Complex [O1]$(PF_6)_2$

Three-fold determination of yield and TON was done with the assistance of following students: Stefanie Zimmer (bachelor thesis), Heliana M. Núñez Ponce (research internship) and Salvatore M. Conte (research intership).

The hydroxylation and oxidation activity of bis(μ-oxido) complex [**O1**]$(PF_6)_2$ indicated in recent studies[142] was reviewed using the new extended method of Herres-Pawlis and coworkers. Therein, a tenfold amount of reactants in comparison to UV/Vis studies to ensure a sufficient amount of desired phenazine product large enough to be purified and isolated for NMR analysis was used ([[**O1**]$(PF_6)_2$]:[S]:[NEt_3]:[PDA]) 1:25:50:50; c([**O1**]$(PF_6)_2$ = 4 mol%).[87] Analogous to earlier studies with [**O1**]$(PF_6)_2$,[142] the hydroxylation and oxidation reaction temperature was increased to −78 °C as the catalyst species remained stable at this temperature for several hours.[85]

The substrate scope was modified as described in the following: The substrate class of phenols was excluded as only formation of undesired C-O coupled side-products was monitored by Herres-Pawlis and coworkers. Additionally, no hydroxylation and oxidation activity towards phenols was monitored in earlier studies with [**O1**]$(PF_6)_2$ (section 3.1 and Figure 3.2). 2-, 8-, 2-methyl-8-quinolinol as well as 2,8-quinolin-diol were excluded from the substrate class of quinolinols. The keto-enol tautomerization equilibrium between 2-quinolinol and quinolin-2-one is primary on the ketone side with a ratio of 1:95.[146,147] In contrast to the enol form (2-quinolinol), the ketone tautomer (quinolin-2-one) is not convertible in an hydroxylation reaction by Cu_2O_2 species, the first step of the catalytic conversion to *ortho*-quinones. The *ortho*-quinone products of 8-quinolinol and 2,8-quinolin-diol, 7,8-quinolin-dione and 2-methyl-7,8-quinolin-dione, are not able to form corresponding phenazine products in a condensation reaction with PDA. This was assigned to a lower electrophilicity (smaller Fukui f_+ function) of the corresponding C atoms by Herres-Pawlis and coworkers.[87] The Fukui functions f_+ / f_- describe the electron density in a frontier orbital of a molecule or atom for the addition (f_+) or removal (f_-) of an electron, the initial part of an nucleophilic (f_+) or electrophilic (f_-) reaction.[148,149] A low Fukui f_+ function indicates an atom not favored for the nucleophilic attack,[149,150] in this case the N atom of the PDA.

To complete the substrate class of quinolinols, 5-quinolinol was added to the substrate spectrum. Although, 7-quinolinol, 2-indolol and 3-indolol were considered for completeness, all of them were rejected due to the following reasons: The quinone product resulting from the conversion of 7-quinolinol, 7,8-quinolin-dione, does not under go a condensation reaction with PDA as discussed earlier. Analogous to 2-quinolinol, 2- and 3-indolol display keto-enol tautomerization. The equilibrium strongly depends on the solvent and was not tested for tetrahydrofuran which was used in this study.

Finally the substrate class of carbazolols was introduced adding 2- and 4-carbazolol to the substrate spectrum. In the hydroxylation and subsequent oxidation of 2-carbazolol, two possible products depending on the position of the initial hydroxylation reaction can be formed: 12H-indolo[2,3-a]phenazine (C1-position) or 5H-indolo[2,3-b]phenazine (C3-position). The preferred hydroxylation position was not calculated via the Fukui f_- function as done by Herres-Pawlis and coworkers for naphthols, quinolinols and indolols.[87] Consequently, both possible reaction products will be stated. A summary of the substrate scope investigated in the hydroxylation and subsequent oxidation with [**O1**]$(PF_6)_2$ is displayed in Scheme 3.3.

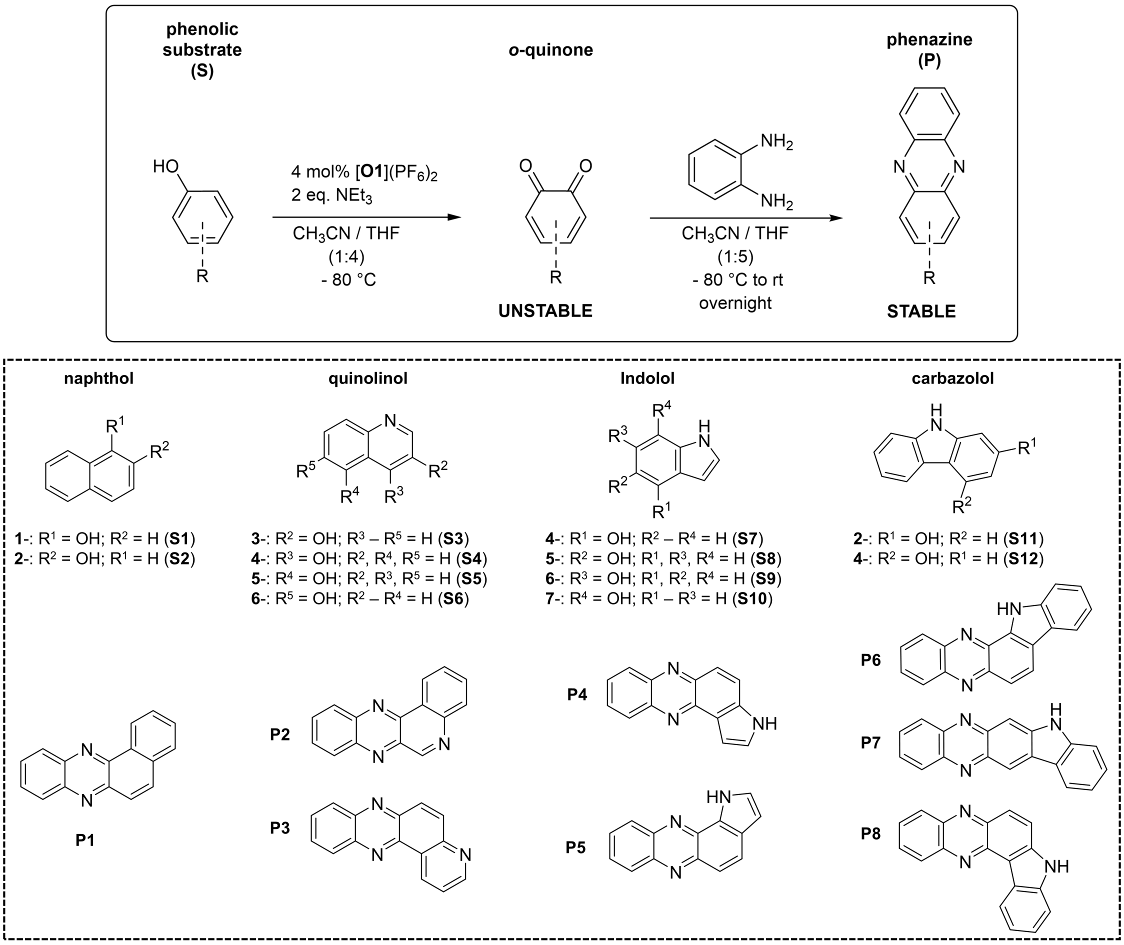

Scheme 3.3: Catalytic hydroxylation and subsequent oxidation reaction of phenolic substrates performed with bis(μ-oxido) complex $[Cu_2O_2(TMG_2tol)_2](PF_6)_2$ ([$\mathbf{O_1}$]$(PF_6)_2$) to *ortho*-quinones under *Bulkowski-Réglier* conditions[59,100] extended with a following condensation with PDA in accordance to Herres-Pawlis and coworkers[87] ([[**O1**]$(PF_6)_2$]:[S]:[NEt_3]:[PDA] = 1:25:50:50; c([**O1**]$(PF_6)_2$) = 4 mol %, T(hydroxylation/oxidation) = −80 °C, T(PDA condensation) = room temperature (rt)). Phenolic substrates (S) are converted to highly reactive *ortho*-quinones by [**O1**]$(PF_6)_2$. Subsequent conversion with PDA results in phenazine products (P) stable under ambient conditions and verifiable via NMR spectroscopy.

Catalytic hydroxylation experiments were started with the formation of bis(µ-oxido) complex [**O1**]$(PF_6)_2$ as described earlier in Section 3.1.2. Subsequently, the substrate solution consisting of the phenolic substrates (S) and the auxiliary base triethylamine (NEt_3) was added to the reaction mixture starting the hydroxylation. The solution was stirred at −80 °C during the formation of the *ortho*-quinone intermediates. The hydroxylation and subsequent oxidation was terminated removing the cooling bath and adding PDA diluted in THF. The reaction mixture was stirred at room temperature (rt) overnight. Formed phenazine products (P) as well as unconverted substrate were isolated via column chromatography and characterized with NMR spectroscopy. Yields and turn-over-numbers were calculated using the mass of the isolated fractions after purification via column chromatography and the amount of catalyst used (4 mol %). The turn-over-frequency was determined in relation to the duration of the hydroxylation and subsequent oxidation.

The yield (Y) of a reaction is defined as the amount of desired product P actually formed (n_P) in relation to the maximum amount of P possible. Thereby, the maximum of P is in accordance with the amount of substrate added at the beginning (n_S) (Equation 3.1).[5]

$$Y = \frac{n_{\mathrm{P},0} - n_\mathrm{P}}{n_\mathrm{S}} \cdot \frac{\nu_\mathrm{R}}{\nu_\mathrm{P}}$$

For a reaction $\nu_\mathrm{S}\ \mathrm{S} \longrightarrow \nu_\mathrm{P}\ \mathrm{P}$ with stoichiometric coefficients ν_S and ν_P

in the case $\nu_\mathrm{S} = \nu_\mathrm{P} = 1$ and $n_{\mathrm{P},0} = 0$

$$Y = \frac{n_\mathrm{P}}{n_\mathrm{R}} \tag{3.1}$$

To characterize the performance of the catalyst, the turn-over-number (TON) can be calculated. The ratio between amount of product formed (n_P) and amount of catalyst used ((n_cat)) is an indicator for the capacity of the catalyst: the number of catalytic cycles performed before the deactivation of the catalyst (Equation 3.2). A reaction with a high TON is thus more efficient than one with a low TON as the catalyst converts more amount of reactant to the desired product before it is deactivated.[5]

$$\mathrm{TON} = \frac{n_\mathrm{P}}{n_\mathrm{cat}} = \frac{Y}{c_\mathrm{cat}} \tag{3.2}$$

To compare the catalyst performance with regard to the reaction time the turn-over-frequency (TOF) can be determined. The TOF is given as the TON per time (Equation 3.3). Comparing two reactions with the same TON which differ in their reaction time, the one with a short reaction time results in a higher TOF and has therefore a higher performance producing a larger amount of desired product per time.[5]

$$TOF = \frac{TON}{reaction\ time} \tag{3.3}$$

3.1.3.1 Finding the Ideal Reaction Time for the Catalytic Hydroxylation and Subsequent Oxidation with [O1](PF_6)$_2$

A first experiment using 6-indolol (**S9**) as substrate in the catalytic hydroxylation and subsequent oxidation mediated by [**O1**](PF_6)$_2$ was performed with a reaction time of one hour, analogous to Herres-Pawlis and coworkers. Only a low yield (4%) of desired product 1-H-pyrrolo[2,3-a]phenazine (**P5**) was reached while 50% of the substrate, **S9**, remained unconverted (Entry 1 in Table 3.1). A decrease of unconverted substrate **S9** to 26% could be observed with increasing reaction time (3 h), although the yield of desired product **P5** did not increase (Entry 2 in Table 3.1). Even a prolongation of the reaction time to five or eight hours did not lead to higher product yields. However, the amount of unconverted substrate was minimized to 1%.

With a yield of 3–4% and a catalyst concentration of 4 mol% **S9** was only converted with a TON of 1 to the desired phenazine product by [**O1**](PF_6)$_2$ (Entry 3 and 4 in Table 3.1). Thus, no significant catalytic activity towards 6-indolol could be determined. Yield loss due to side reactions forming C-C and/or C-O coupled products, which could not be isolated but were identified via mass spectrometry (MS). The results of the MS measurements are discussed in Section 3.1.3.4.

First hydroxylation and subsequent oxidation experiments with [$\mathbf{O_1}$](PF_6)$_2$ converting 2-naphthol (**S2**) and 6-quinolinol (**S6**) were conducted with a reaction time of five and eight hours. Both substrates were successfully transformed to the desired phenazine products. In the case of **S2**, the yield of desired product benzo[a]phenazine (**P1**) considerably increased with extending reaction time (14 % after 5 h, 31 % after 8 h; Entry 5 and 6 in Table 3.1). However, a large amount of substrate **S2** remained unconverted (37 % after 8 h). In contrast, the conversion of **S6** revealed only a slight increase of the desired product's yield (pyrido[3,2-a]phenazine (**P3**)) with longer reaction times (11 % **P3** after 5 h, 16 % **P3** after 8 h), while no unconverted substrate **S6** was isolated after eight hours reaction time (Entry 7 and 8 in Table 3.1).The high amounts of desired phenazine products **P1** and **P3** reached during the conversion of **S2** and **S6** with [**O1**](PF_6)$_2$ are in contrast to the low activity of this oxido species towards **S9**. Although, no unconverted substrate **S9** was monitored indicating full conversion, only 4% of desired phenazine product **P5** were gained. Consequently, a limitation of the catalytic activity of [$\mathbf{O_1}$](PF_6)$_2$ towards specific substrates groups is found.

Table 3.1: Summary of catalytic hydroxylation and subsequent oxidation experiments mediated by bis(µ-oxido) complex [**O1**]$(PF_6)_2$ ($[Cu_2O_2(TMG_2tol)_2](PF_6)_2$) performed with varied reaction time and following condensation with PDA overnight. Substrates (**S**) used are given with related isolated yields of unconverted substrate and desired phenazine product (**P**).

entry	reaction time [h]	substrate	Y[a] [%] (unconverted substrate)	Y[a] [%] (phenazine product)	TON[b] (phenazine product)	phenazine product
1	1	**S9**	50	4	1	**P5**
2	3	**S9**	26	3	1	**P5**
3	5	**S9**	1	3	1	**P5**
4	8	**S9**	1	4	1	**P5**
5	5	**S2**	86	14	4	**P1**
6	8	**S2**	37	31	8	**P1**
7	5	**S6**	0	11	3	**P3**
8	8	**S6**	0	16	4	**P3**

[a] Isolated yield after purification via column chromatography; Reaction conditions: catalytic oxygenation at -80°C; PDA condensation at room temperature, overnight. [b] TON calculated using the isolated product yield and the concentration of [**O1**]$(PF_6)_2$ (4 mol%).

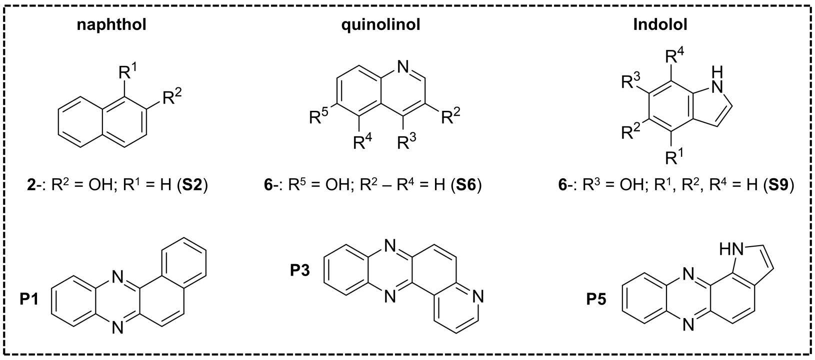

3.1.3.2 Conversion of Various Substrate Classes with [O1]$(PF_6)_2$

To verify the presumed inactivity of [**O1**]$(PF_6)_2$ towards specific substrate groups, the study was enlarged to the full substrate scope selected at the beginning of this chapter based on earlier findings of catalytic studies with **O** species (Section 3.1.2 and Scheme 3.3). As no or only 1% unconverted substrate was isolated after 8 h reaction time converting **S2** and **S6** (Entry 6 and 8 in Table 3.1) indicating full conversion of the substrate used, the duration of further hydroxylation and subsequent oxidation experiments was set to this length of time.

In the catalytic hydroxylation and subsequent oxidation of 4-quinolinol (**S4**), 5-quinolinol (**S5**), 4-indolol (**S7**) and 7-indolol (**S10**) mediated by [**O1**]$(PF_6)_2$ followed by a condensation with PDA no phenazine products were observed (Entry 4,5,7 and 10 in Table 3.2). Experiments converting the newly introduced substrate class of carbazolols did not result in isolated phenazine products as well: With 2-carbazolol (**S11**) traces of a phenazine product signals were spotted in the NMR spectrum. However, the amount was too low for further characterization while 4-carbazolol (**S12**) did not show any phenazine signals

(Entry 11 and 12 in Table 3.2). Nevertheless, [**O1**]$(PF_6)_2$ showed a slight activity towards 1-naphthol (**S1**), 3-quinolinol (**S3**), 5-indolol (**S8**) and 6-indolol (**S9**) with isolated phenazine yields between 3 and 5 % (Entry 1,3,8 and 9 in Table 3.2).

Table 3.2: Phenolic substrates **S** investigated in the catalytic hydroxylation and subsequent oxidation with bis(μ-oxido) complex [**O1**]$(PF_6)_2$ ($[Cu_2O_2(TMG_2tol)_2](PF_6)_2$)followed by a condensation with PDA as well as averaged, isolated yields and TON of desired phenazine products **P**. Conversion reactions displaying catalytic activity (TON >1) are highlighted in green.

entry	substrate (S)	Y[a] [%]	TON[b]	phenazine product (P)
1	**S1**	1	<1	**P1**
2	**S2**	**31**	**8**	
3	**S3**	5	1	**P2**
4	**S4**	0	0	
5	**S5**	0	0	**P3**
6	**S6**	**16**	**4**	
7	**S7**	0	0	**P4**
8	**S8**	4	1	
9	**S9**	4	1	**P5**
10	**S10**	0	0	
11	**S11**	<1	<1	**P6** or **P7**
12	**S12**	0	0	**P8**

[a] Isolated yield after purification via column chromatography; Reaction conditions: catalytic oxygenation at -80°C, 8 h; PDA condensation at room temperature (20 °C), overnight.
[b] TON calculated using the isolated product yield and the concentration of [**O1**]$(PF_6)_2$ (4 mol%).

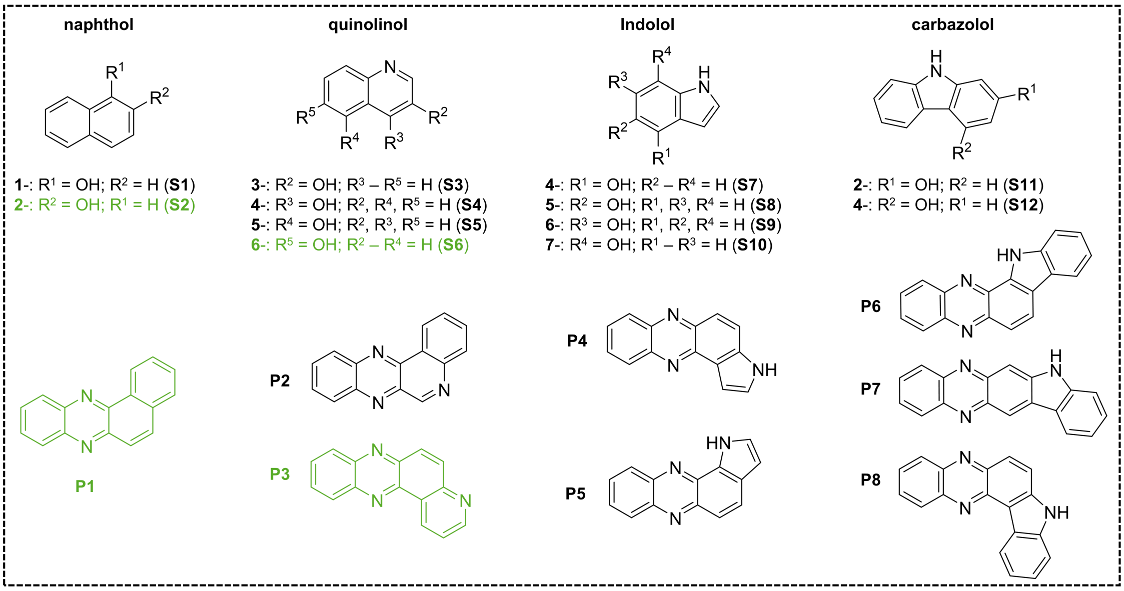

1-: R^{1} = OH; R^{2} = H (**S1**)
2-: R^{2} = OH; R^{1} = H (**S2**)

3-: R^{2} = OH; R^{3} – R^{5} = H (**S3**)
4-: R^{3} = OH; R^{2}, R^{4}, R^{5} = H (**S4**)
5-: R^{4} = OH; R^{2}, R^{3}, R^{5} = H (**S5**)
6-: R^{5} = OH; R^{2} – R^{4} = H (**S6**)

4-: R^{1} = OH; R^{2} – R^{4} = H (**S7**)
5-: R^{2} = OH; R^{1}, R^{3}, R^{4} = H (**S8**)
6-: R^{3} = OH; R^{1}, R^{2}, R^{4} = H (**S9**)
7-: R^{4} = OH; R^{1} – R^{3} = H (**S10**)

2-: R^{1} = OH; R^{2} = H (**S11**)
4-: R^{2} = OH; R^{1} = H (**S12**)

The catalytic hydroxylation and oxidation activity of [**O1**]$(PF_6)_2$ was investigated towards a broad spectrum of twelve substrates out of four substrate classes. A catalytic activity could only be proven for 2-naphthol (TON 8) and 6-quinolinol (TON 4). Towards all other substrates only a non catalytic activity (TON ≤ 1) or no activity at all (TON 0) could be monitored for the **O** species stabilized by the bisguanidine ligand TMG_2tol.

3.1.3.3 Blank Experiments with Copper Salt $[Cu(CH_3CN)_4]PF_6$ as Catalyst

The limited catalytic activity of bis(µ-oxido) complex [**O1**]$(PF_6)_2$ only converting specific phenolic substrates indicates the inhibition of desired catalytic hydroxylation and subsequent oxidation to *ortho*-quinones by side reactions or decay of the unstable *ortho*-quinone intermediates. The used copper salt, $[Cu(CH_3CN)_4]PF_6$, is known to catalyze the conversion of di-*tert*-butylphenol to the corresponding *ortho*-quinone without the need for a supporting ligand system.[151] As a consequence, blank experiments using the pure copper salt in the catalytic conversion were performed to exclude $[Cu(CH_3CN)_4]PF_6$ as a possible catalyst. Therefore, the most reactive substrate out of each substrate class (**S2**, **S6** and **S8**) was selected for catalytic investigations using the pure copper salt under the given reaction conditions (Scheme 3.4).

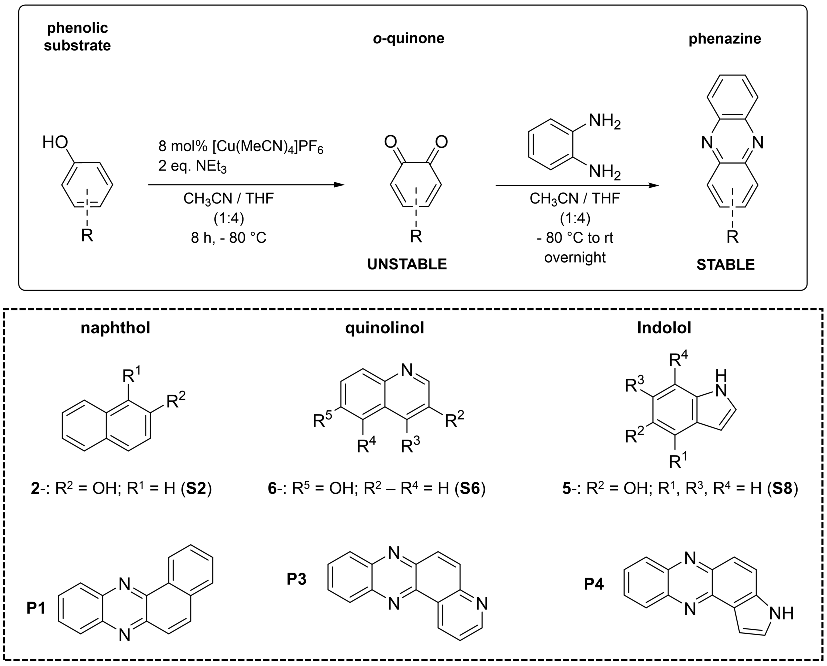

Scheme 3.4: Performed blank experiments using copper salt ($[Cu(CH_3CN)_4]PF_6$) instead of oxido complex [**O1**]$(PF_6)_2$ for the catalytic hydroxylation and subsequent oxidation of phenolic substrates. All other reaction conditions remained unchanged ($T = -80\,°C$, $t = 8\,h$; $[[Cu(CH_3CN)_4]PF_6]:[S]:[NEt_3]:[PDA] = 2:25:50:50$).

All three tested substrates were successfully converted into the desired phenazines with small yields of 4 - 5 % (Table 3.3). The obtained yields with pure copper salt are within the same range as the ones of the catalytic conversion of **S1**, **S3**, **S8** and **S9** with **O1**$(PF_6)_2$. Consequently, a clear distinction between the catalytic activity of bis(µ-oxido) complex **O1**$(PF_6)_2$ and the catalytic activity of the pure copper salt towards those substrates is impossible. As a result, an actual catalytic activity of **O1**$(PF_6)_2$ in the hydroxylation and subsequent oxidation of phenolic substrates could only be proven for **S2** (31 %, TON 8) and **S6** (16 %, TON 4) (Entry 2 and 6 in Table 3.2).

Table 3.3: Summary of blank experiments performed with copper salt $[Cu(CH_3CN)_4]PF_6$ instead of catalyst [**O1**]$(PF_6)_2$ in the catalytic hydroxylation and subsequent oxidation of phenolic substrates **S** followed by PDA condensation as well as averaged, isolated yields and TON of desired phenazine products **P**.

entry	substrate	Y[a] [%]	TON[b]	phenazine product
1	S2	5	1	P1
2	S6	5	1	P3
3	S8	4	1	P4

[a] Isolated yield after purification via column chromatography; Reaction conditions: catalytic oxygenation at -80°C, 8 h; PDA condensation at room temperature, overnight. [b] TON calculated using the isolated product yield and the concentration of $[Cu(CH_3CN)_4]PF_6$ (8 mol%).

3.1.3.4 Mass Spectrometry of Catalytic Conversions of Phenolic Substrates Mediated by [O1]$(PF_6)_2$

In the catalytic conversion of phenolic substrates several side reactions are known to occur. Converting di-*tert*-butylphenol, Tuczek and coworkers[151] as well as Lumb and coworkers[101] observed a C-C coupling reaction generating a tetra-*tert*-butyl-biphenol (Scheme 3.5 above).

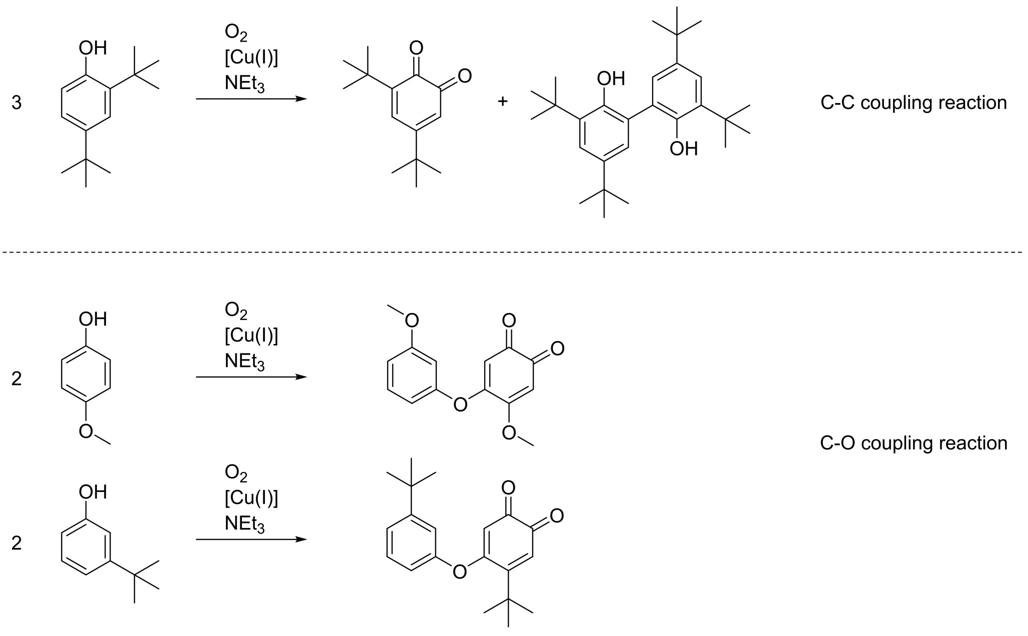

Scheme 3.5: C-C and C-O coupling reactions observed by Tuczek and coworkers as well as Lumb and coworkers as side-reactions during the catalytic hydroxylation and subsequent oxidation of phenolic substrates.[96,101,151]

Using 3-*tert*-butylphenol or 4-methoxyphenol a C-O coupling reaction between two substrate molecules with subsequent *ortho*-quinone formation took place (Scheme 3.5 below).[96]

This was also observed by Herres-Pawlis and coworkers converting *para*-*tert*-butylphenol with an oxido complex stabilized by hybrid guanidine TMGbenza, which is structurally related to TMG_2tol stabilizing [**O1**]$(PF_6)_2$ used in this work.

To investigate whether these side reactions are inhibiting the conversion of phenolic substrates mediated by bis(µ-oxido) complex [**O1**]$(PF_6)_2$ to *ortho*-quinones and the subsequent conversion with PDA to phenazines, electrospray ionization mass spectrometry (ESI-MS) and cold-spray ionization mass spectrometry (CSI-MS) was performed. Therefore, one substrate out of each substrate class showing no or only slight phenazine formation was selected. Mass spectrometry was performed at two points of the reaction using substrates 1-naphthol (**S1**), 4-quinolinol (**S4**) and 4-indolol (**S7**): The first one directly after addition of the substrate solution at low temperature (−80 °C; CSI-MS). The second one after eight hours reaction time followed by condensation with PDA and work-up at room temperature (rt; ESI-MS).

Table 3.4: Side-products and fragments found in the CSI-MS spectrum of the catalytic conversion of 1-naphthol (S1) with [**O1**]$(PF_6)_2$ measured after addition of the substrate solution at −80 °C.

	m/z detected	m/z calculated	molecular formula	molecular structure
A	102.1281	102.1277	$C_6H_{16}N^+$	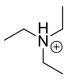
B	176.1184	176.1188	$C_{10}H_{14}N_3^{\cdot}$	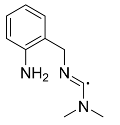
C	319.2605	319.2605	$C_{17}H_{31}N_6^+$	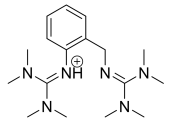
D	349.2202	349.0707	$C_{20}H_{13}O_6^+$	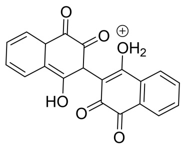
E	381.1823	381.1823	$C_{17}H_{30}CuN_6^+$	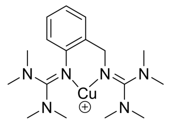
F	461.3026	461.1384	$C_{30}H_{21}O_5^+$	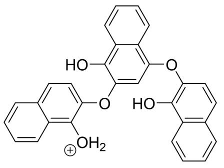
G	603.3442	603.1802	$C_{40}H_{27}O_6^+$	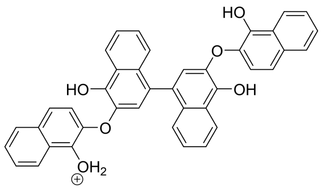

Starting with 1-naphthol, the CSI-MS spectrum recorded after addition of the substrate solution at low temperature indicated the formation of C-O as well as C-C coupling products of **S1** and desired *ortho*-quinones. C-C coupling of two substrate molecules and subsequent hydroxylation followed by oxidation resulted in two *ortho*-quinones with hydroxy groups in *para*-position and coupling with each other in *meta*-position (Entry D in Table 3.4).

C-O coupling taking place after hydroxylation, instead of oxidation to the desired *ortho*-quinones, led to larger coupling products consisting of three or four substrate molecules (Entry F and G). In addition, auxiliary base triethylamine (Entry A) as well as fragments of the copper containing catalyst species (Entry E) and the ligand TMG_2tol (Entry B and C) were visible in the MS spectrum (Table 3.4).

MS measurements performed after the conversion reaction with PDA showed the condensation of two PDA molecules and two substrates in alternate sequence (Entry D) as well as the C-O coupling products and triethylamine (Entry A, C and E). Moreover, small amounts of 2,3-dinitroso-phenazine (Entry B), a substance resulting from condensation and subsequent oxidation of two PDA molecules, were identified (Table 3.5). Neither unconverted substrate **S1** nor the desired phenazine product benzo[a]phenazine (**P1**) could be detected via CSI-MS or ESI-MS.

Table 3.5: Side-products and fragments found in the ESI-MS spectrum of the catalytic conversion of 1-naphthol (**S1**) with [**O1**]$(PF_6)_2$ and subsequent condensation with PDA measured after extraction of the crude reaction mixture at room temperature.

	m/z detected	m/z calculated	molecular formula	molecular structure
A	102.1279	102.1277	$C_6H_{16}N^+$	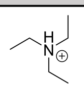
B	239.2253	239.2253	$C_{12}H_7N_4O_2^+$	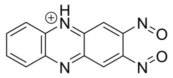
C	461.3037	461.1384	$C_{30}H_{21}O_5^+$	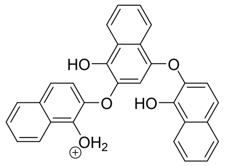
D	479.1875	479.1866	$C_{32}H_{23}N_4O^+$	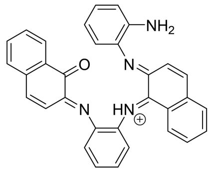
E	603.3453	603.1802	$C_{40}H_{27}O_6^+$	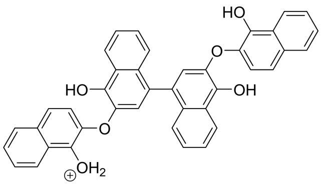

In literature, PDA is known to form condensation products with itself under the presence of an oxidizing agent like molecular oxygen or a catalyst like copper(II).[152,153] In the presence of an oxido-peroxido molybdenum catalyst, aromatic amines are converted into nitroso products (Scheme 3.6).[154] Consequently, with the oxido catalyst [**O1**](PF_6)$_2$ and dissolved oxygen present in the reaction mixture, two PDA molecules could undergo condensation with each other forming 2,3-diaminophenazine which is oxidized to 2,3-dinitrosophenazine afterwards (Entry B in Table 3.5).

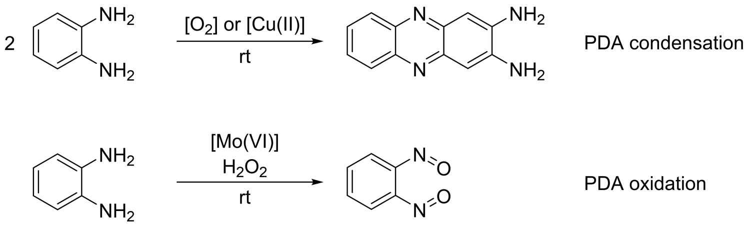

Scheme 3.6: Condensation and oxidation reactions of *ortho*-phenylenediamine (PDA) mediated by oxizing catalysts like molecular oxygen, hydrogen peroxide, copper(II) or molybdenum(VI).[152–154]

In the catalytic conversion of 4-quinolinol, CSI and ESI mass spectra did not show any C-C or C-O coupling products. In the CSI spectrum only the auxiliary base triethylamine and fragments of the ligand species could be identified (Table 3.6).

Table 3.6: Side-products and fragments found in the CSI-MS spectrum of the catalytic conversion of 4-quinolinol (**S4**) with [**O1**](PF_6)$_2$ measured after addition of the substrate solution at −80 °C.

	m/z detected	m/z calculated	molecular formula	molecular structure
A	102.1281	102.1277	$C_6H_{16}N^+$	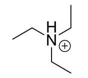
B	176.1182	176.1188	$C_{10}H_{14}N_3^{\cdot}$	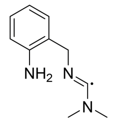
C	204.1494	204.1495	$C_{12}H_{18}N_3^+$	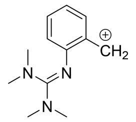
D	319.2603	319.2605	$C_{17}H_{31}N_6^+$	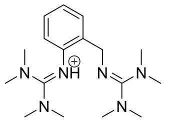

The ESI spectrum of the conversion with 4-quinolinol, recorded after the condensation reaction with PDA, showed unconverted substrate **S4** (Entry C) as well as traces of the desired phenazine product quinolino[3,4-b]quinoxaline (**P2**) (Entry G). Analogous to the conversion with **S1**, 2,3-dinitrosophenazine was detected (Entry H) resulting from the condensation of two PDA molecules and subsequent oxidation. Additionally, 1,2-dinitrosobenzene could be identified (Entry B) presumably formed via oxidation of PDA[154] (Scheme 3.6). As in the CSI spectrum, triethylamine (Entry A) and ligand fragments (Entry D,E and F) were identified as well (Table 3.7).

Table 3.7: Side-products and fragments found in the ESI-MS spectrum of the catalytic conversion of 4-quinolinol (**S4**) with [**O1**]$(PF_6)_2$ and subsequent condensation with PDA measured after extraction of the crude reaction mixture at room temperature.

	m/z detected	m/z calculated	molecular formula	molecular structure
A	102.1279	102.1277	$C_6H_{16}N^+$	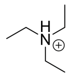
B	137.6050	137.0346	$C_6H_5N_2O_2^+$	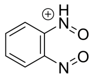
C	146.0601	146.0600	$C_9H_8NO^+$	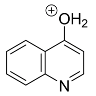
D	160.1340	160.0995	$C_{10}H_{12}N_2^{\cdot+}$	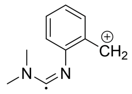
E	176.1183	176.1188	$C_{10}H_{14}N_3^{\cdot}$	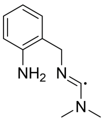
F	204.1497	204.1495	$C_{12}H_{18}N_3^+$	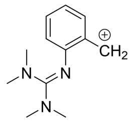
G	232.1446	232.0869	$C_{15}H_{10}N_3^+$	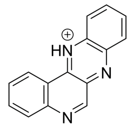
H	239.2252	239.0564	$C_{12}H_7N_4O_2^+$	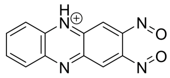
I	319.2608	319.2605	$C_{17}H_{31}N_6^+$	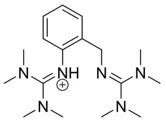

In the catalytic conversion of 4-indolol (**S7**), ESI-MS spectra recorded after the condensation reaction with PDA did not show any C-C or C-O coupling products. Unconverted substrate **S7** or desired phenazine product 1H-pyrrolo[2,3-a]phenazine (**P5**) were not monitored as well. Instead, the ESI-MS spectrum displayed nitroso products presumably resulting from PDA oxidation (1,2-dinitrosobenzene, Entry B) or condensation of two PDA molecules followed by oxidation (2,3-dinitrosophenazine, Entry F). Besides, only reactants like triethylamine (Entry A) and ligand fragments (Entry C,D,E and G) could be assigned (Table 3.8).

Table 3.8: Side-products and fragments found in the ESI-MS spectrum of the catalytic conversion of 4-indolol (**S7**) with [**O1**](PF_6)$_2$ and subsequent condensation with PDA measured after extraction of the crude reaction mixture at room temperature.

	m/z detected	m/z calculated	molecular formula	molecular structure
A	102.1277	102.1277	$C_6H_{16}N^+$	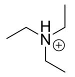
B	137.6049	137.0346	$C_6H_5N_2O_2^+$	
C	160.1338	160.0995	$C_{10}H_{12}N_2^{\cdot+}$	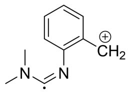
D	176.1181	176.1188	$C_{10}H_{14}N_3^{\cdot}$	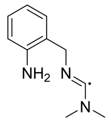
E	204.1495	204.1495	$C_{12}H_{18}N_3^+$	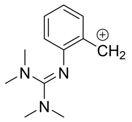
F	239.2249	239.0564	$C_{12}H_7N_4O_2^+$	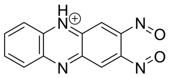
G	319.2605	319.2605	$C_{17}H_{31}N_6^+$	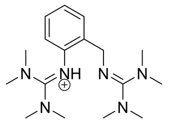

3.1.4 Summary

In 2017, the bis(μ-oxido) complex [**O1**](PF_6)$_2$ stabilized by the bisguanidine ligand TMG_2tol was stated as catalytically inactive since no *ortho*-quinone products could be identified using *Bulkowski-Réglier* conditions.[85] However, a study in 2019 extending the reaction pathway by a condensation with PDA indicated a hydroxylation and oxidation activity towards naphthols, quinolinols and indolols as signals around 400 nm of desired *ortho*-quinone products could be monitored in the UV/Vis spectra. Furthermore, for some substrates traces of desired phenazine product signals were visible in the NMR spectra.[142] Nevertheless, a catalytic hydroxylation and oxidation activity could not be proven as no phenazine products could not be isolated and UV/Vis signals of *ortho*-quinones resulting from quinolinols, naphthols and indolols are not covered in literature.

In this chapter, the indicated catalytic activity of [**O1**](PF_6)$_2$ was further analyzed using a method established by Herres-Pawlis and coworkers in 2020. The amount of reactants was upscaled by a factor of ten compared to earlier UV/VIS studies and desired phenazine reaction products were isolated via column chromatography. First, the reaction conditions were optimized for [**O1**]$(PF_6)_2$ resulting in the conversion of phenolic substrates over a course of eight hours at −80 °C with a ratio of 1:25:50:50 ([[**O1**]$(PF_6)_2$]:[S]:[NEt_3]:[PDA]). Thereby, catalytic activity was validated towards 2-naphthol (Y = 31%, TON 8) and 6-quinolinol (Y = 16%, TON 4). Some further substrates, 1-naphthol, 3-quinolinol, 4-indololol, 5-indolol and 2-carbazolol, displayed a slight activity (Y = 1 – 5%). However, yield and TON of related phenazine products were in the same range as experiments performed with pure copper(I) salt ([$Cu(CH_3CN)_4$]PF_6; Y = 4 – 5%). Thus, a clear distinction between the catalytic activity of [**O1**]$(PF_6)_2$ and the copper(I) salt was impossible (Figure 3.3).

Since functional tyrosinase model complexes are known to undergo C-C or C-O coupling reactions,[96,101,151] the reaction mixture of the catalytic conversion was investigated via mass spectrometry. Therein, the formation of C-C- as well as C-O coupled molecules instead of the desired *ortho*-quinones could be monitored. Furthermore, nitroso species and coupled PDA molecules were found. As no *ortho*-quinones products suitable for a condensation with PDA were formed, PDA underwent condensation with itself to N-C coupled products and / or was oxidized to 2,3-dinitrosobenzene as well as 2,3-dinitrosophenazine.

The results obtained highlight the importance of PDA condensation and phenazine product isolation to validate catalytic hydroxylation and oxidation activity. Most *ortho*-quinone products are unstable and those impossible to isolate. Additionally, literature UV/Vis data are only known for a few of those. As a consequence, the formation of reaction products can only be indicated qualitatively by the appearance of a signal near the literature known data range (∼ 400 nm). However, since pure copper(I) salt is also able to convert phenolic substrate, a clear distinction between catalyst activity and copper salt catalysis is impossible. Thus, the appearance of a *ortho*-quinone signal in the UV/Vis spectrum does not necessarily validate catalytic activity of the tested catalyst as the copper(I) salt used is also partially active. As a consequence, product isolation as stable phenazines is an option to reliably identify catalytically active Cu_2O_2 species.

Comparing the gained results with the study of Herres-Pawlis in 2020 (t = 1 h, T = −90 °C), only two substrates, 2-naphthol and 6-quinolinol, were converted successfully by [**O1**]$(PF_6)_2$ (t = 8 h, T = −80 °C) to desired phenazine products in contrast to nine, 1-, 2-naphthol, 3-, 4-, 6-quinolinol and 4-, 5-, 6-, 7-indolol, with the **O** species stabilized by TMGbenza (Figure 3.3). Additionally, [**O1**]$(PF_6)_2$ displayed a lower performance than the TMGbenza **O** species: Converting 2-naphthol both catalysts generated the same amount of desired benzo[a]phenazine (**P1**) (Y = 31%, TON 8). However, the TMGbenza species displays a higher TOF ($8\,h^{-1}$) as [**O1**]$(PF_6)_2$ ($1\,h^{-1}$) due to the shorter reaction time.

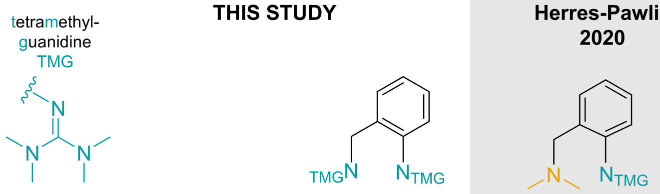

S	P	THIS STUDY		Herres-Pawlis 2020
		-----------------	**TMG_2tol**	**TMGbenza**
		$[Cu(CH_3CN_4)]PF_6$	**$[O1](PF_6)_2$**	**$[Cu_2O_2(TMGbenza)_2](PF_6)_2$**
		THF, -80°C, 8 h	**THF, -80°C, 8 h**	**THF, -90°C, 1 h**
S1	**P1**	-----------------	1% (TON <1)	22% (TON 6)
S2		5% (TON 1)	**31% (TON 8)**	31% (TON 8)
S3	**P2**	-----------------	5% (TON 1)	32% (TON 8)
S4		-----------------	0%	21% (TON 5)
S5	**P3**	-----------------	0%	-----------------
S6		5% (TON 1)	**16% (TON 4)**	30% (TON 8)
S7	**P4**	-----------------	0%	19% (TON 5)
S8		4% (TON 1)	4% (TON 1)	26% (TON 7)
S9	**P5**	-----------------	4% (TON 1)	27% (TON 7)
S10		-----------------	0%	31% (TON 8)
S11	**P6 / P7**	-----------------	1% (TON 1)	-----------------
S12	**P8**	-----------------	0%	-----------------

Conditions: [catalyst]:[S]:[NEt_3]:[PDA] = 1:25:50:50; c(catalyst) = 4 mol%; c([$Cu(CH_3CN_4)]PF_6$) = 8 mol%

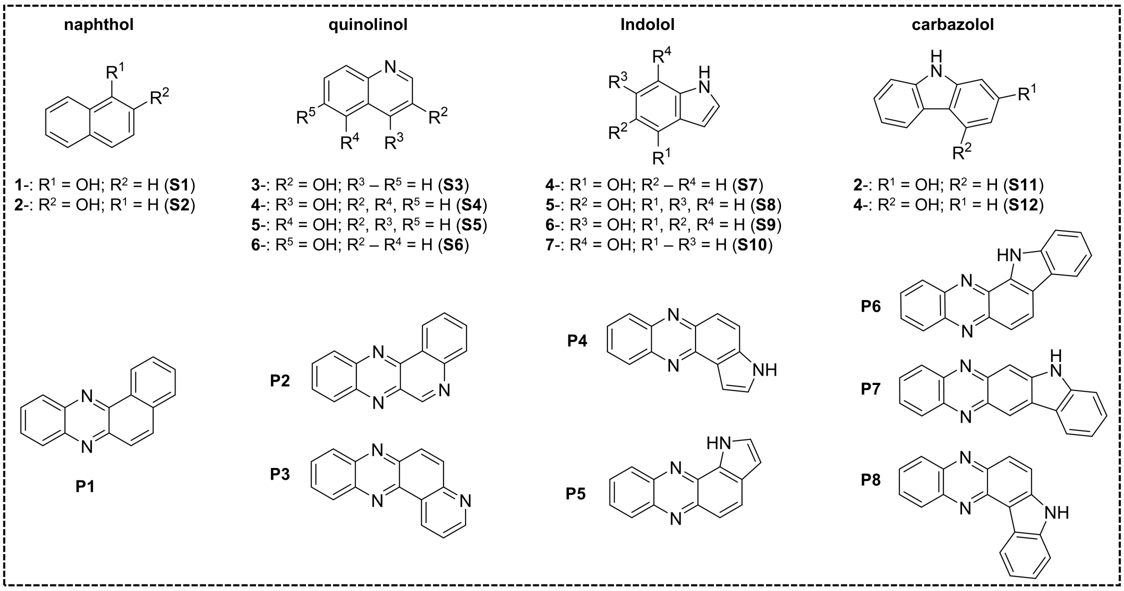

1-: R^1 = OH; R^2 = H (**S1**)
2-: R^2 = OH; R^1 = H (**S2**)

3-: R^2 = OH; $R^3 – R^5$ = H (**S3**)
4-: R^3 = OH; R^2, R^4, R^5 = H (**S4**)
5-: R^4 = OH; R^2, R^3, R^5 = H (**S5**)
6-: R^5 = OH; $R^2 – R^4$ = H (**S6**)

4-: R^1 = OH; $R^2 – R^4$ = H (**S7**)
5-: R^2 = OH; R^1, R^3, R^4 = H (**S8**)
6-: R^3 = OH; R^1, R^2, R^4 = H (**S9**)
7-: R^4 = OH; $R^1 – R^3$ = H (**S10**)

2-: R^1 = OH; R^2 = H (**S11**)
4-: R^2 = OH; R^1 = H (**S12**)

Figure 3.3: Comparison of yield and TON of the catalytic hydroxylation and subsequent oxidation of phenolic substrate **S** to *ortho*-quinone intermediates followed by a condensation with PDA to phenazine products **P** mediated by (i) copper salt $[Cu(CH_3CN)_4]PF_6$, (ii) bisguanidine TMG_2tol based bis(μ-oxido) complex [**O1**]$(PF_6)_2$ and the **O** species stabilized by hybrid guanidine TMGbenza.

This study underlines the higher activity of hybrid guanidine stabilized **O** complexes in contrast to bisguanidine based ones. These results might be related to the lower electron density of the ligand due to the combination of an amine donor with a guanidine unit. The **O** species coordinated by TMGbenza is only stable at −90 °C[87] while the O complex formed with TMG_2tol tolerates higher temperatures up to −40 °C.[85] Consequently, with TMGbenza a less stable **O** species displaying a higher activity is formed. Moreover, an amine unit as second donor is less bulky compared to a second guanidine unit. Thus, a substrate coordination to the formed **O** species may be facilitated due to the larger coordination gap not being shielded by bulky donor units. For verification, DFT calculations are needed which are part of future projects.

Despite the lower performance of the TMG_2tol stabilized **O** species in contrast to TMGbenza based **O** complexes, the TMG_2tol system has several benefits: The ligand can be synthesized in a one step synthesis compared to TMGbenza needing at least three reaction steps. Further, 2-aminobenzylamine used for the synthesis of TMG_2tol with TMG-Vilsmeier salt is commercially available and inexpensive. In contrast, 2-dimethylaminobenzylamine necessary for TMGbenza has to be synthesized using hazardous chemicals like hydrazine.

In summary, [**O1**]$(PF_6)_2$ stabilized by TMG_2tol displays one of the rare catalytically active **O** species able to convert phenolic substrates to *ortho*-quinones intermediates subsequently condensated to desired phenazine products with a simple, time- and cost-efficient ligand synthesis pathway suitable for production in large-scale. The resulting phenazines are a promising substrate class for pharmaceutical uses as phenazine derivatives naturally synthesized by soil bacteria function as antibiotics[108,109] displayed a high antimicrobial effect against various groups of bacteria.[110]

3.1.5 Antimicrobial Studies with Phenazine Products Resulting from the Catalytic Conversion of Phenolic Substrates with [O1]$(PF_6)_2$

*Antimicrobial studies were performed by the working group of Prof. Lars Lauterbach at the institute of applied microbiology on the phenazines **P1** - **P5** synthesized and provided by me.*

In this study phenazine derivatives are synthesized by the condensation of *ortho*-phenylenediamine (PDA) with *ortho*-quinones. In nature, phenazine derivatives can be found in the plant-root-interphase of crop plants called rhizosphere.[108,155] Two of those are phenazine-1-carboxylamide (PCN) and phenazine-1-carboxylic acid (PCA) (Figure 3.4), formed by soil bacteria starting from chorismic acid.[108,156] In the rhizosphere of wheat, PCA and PCN are functioning as antibiotics preventing the spread of fungal disease like take-all which results in root death.[109] Experiments using PCA as antibacterial agent against various types of bacteria showed a high toxicity against gram-positive as well as gram-negative bacteria at low pH values. At pH values near the neutral range (>5) gram-negative bacteria were found to be resistant against the antimicrobial function of PCA while gram-positive bacteria could still be destroyed.[110]

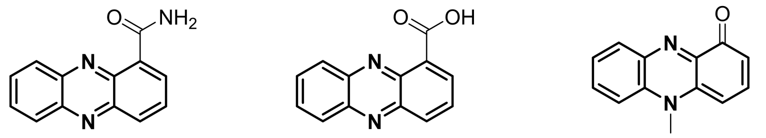

phenazine-1-carboxylamide
(**PCN**)

phenazine-1-carboxylic acid
(**PCA**)

5-methylphenazin-1-one

Figure 3.4: Naturally occurring phenazine derivatives. The phenazine moiety of each molecule is highlighted in bold.

The phenazine derivatives benzo[a]phenazine (**P1**), quinolino[3,4-b]quinoxaline (**P2**), pyrido[3,2-a]phenazine (**P3**), 3H-pyrrolo[3,2-a]phenazine (**P4**) and 1H-pyrrolo[2,3-a]phenazine (**P5**) synthesized in the catalytic hydroxylation and subsequent oxidation with bis(µ-oxido) complex $[\mathbf{O1}](\mathrm{PF_6})_2$ followed by a condensation with PDA are structural modifications of PCA (Figure 3.5). Thus, these phenazines may function as antimicrobial agents representing a potential source material for antibiotics. Their antimicrobial activity was evaluated against various gram-negative and gram-positive bacterial strains using the disk-diffusion assay as well as the plate count method. The experiments were performed by Lauterbach and coworkers on the isolated and purified phenazine products provided by me.

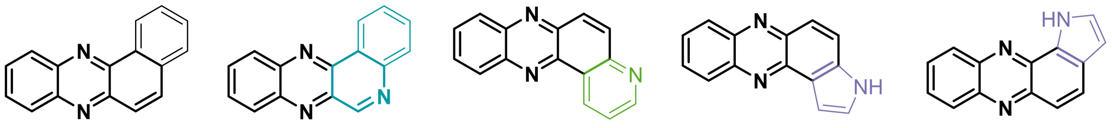

benzo[a]phenazine
P1

quinolino[3,4-b]quinoxaline
P2

pyrido[3,2-a]phenazine
P3

3H-pyrrolo[3,2-a]phenazine
P4

1H-pyrrolo[2,3-a]phenazine
P5

Figure 3.5: Phenazines synthesized in the catalytic conversion of phenolic substrates with bis(µ-oxido) complex $[\mathbf{O_1}](\mathrm{PF_6})_2$ and subsequent condensation with PDA. The phenazine moiety of each molecule is highlighted in bold. Further structural features are highlighted in different colors: quinolinyl moiety (turquoise), pyridinyl moiety (green) and pyrrolyl moiety (violet).

Within the antimicrobial tests, the bioactivity of phenazines **P1**, **P2**, **P3**, **P4** and **P5** against gram-positive bacterium *Bacillus subtilis* was clearly demonstrated. However, the inhibitory effect was limited to this particular bacterium as all further tested gram-positive species (*Staphylococcus aureus*, *Streptococcus dysgalactiae* and *Streptomyces griseus*) did not display any reduction in bacterial growth. Taking a look at gram-negative bacteria tested, *Pseudomonas putida* PG5 was susceptible to phenazines **P3** and **P5**. Additionally, *Escherichia coli* investigated with the plate count method at high amounts of phenazine showed inhibitory effects for phenazines **P1** and **P4**. However, no effect was monitored with this bacterial strain in the disk diffusion assay using lower amounts pf phenazines. Further gram-negative bacteria tested did not show any inhibitory effect. These results suggest the possibility of distinct inhibition mechanisms associated with specific structural features of the tested phenazines.

Limitations of the inhibitory effects to specific groups of bacteria were already observed in studies with naturally-occuring phenazine derivatives like PDA and 5-methylphenazin-1-one (Figure 3.4). At pH values near neutral range (>5), the growth of gram-positive bacteria is sucessfully inhibited while gram-negative bacteria demonstrate a high resistance. This was attributed to their negatively-charged outer cell membrane functioning as additional barrier against the deprotonated PCA in neutral solution. In contrast, at low pH values (<5) PCA is protonated and uncharged leading to a lack of repulsion against the cell walls of gram-negative as well as gram-positive bacteria. Consequently, a permissive accumulation of PCA in the cells is taking place resulting in an inhibition of bacterial growth.[110,157] However, the inhibitory effect of investigated phenazines in this study was limited to only one gram-positive bacterium as other tested gram-positive species showed no reduction in bacterial growth. For gram-positive species, resistance mechanisms against specific types of phenazine derivatives are presumed like the use of efflux pumps for detoxification.[158]

As aforementioned, some naturally occurring bacteria are able to produce phenazine derivatives like PCA and PCN. With the bacterium *Pseudomonas aeruginosa*, which is able to synthesize PCA and PCN, an antagonizing effect could be monitored in an efficacy study on antibiotics.[159] The interaction of two chemicals (e.g. antibiotic and PCA / PCN) leads to a change of their function or an impede of their reaction mode minimizing their desired effects (e.g. inhibition of bacterial growth). This mechanism is called antagonistic effect. The antagonism not only promotes the bacterium's antibiotic resistance, it also contributes to its virulence. Thus, the intricate interplay between bacterial phenazine derivatives and antibiotics leads to potential consequences in microbial communities and infections. While phenazines are commonly recognized to induce the production of reactive oxygen species, rendering them effectively against a broad range of bacteria,[160] the phenazines investigated in this study possess unique structures that likely modify their antimicrobial mechanisms.

Taking a look at the phenazines used in this study, **P2** contains a quinolinyl moiety (Figure 3.5 marked in turquoise), which is known to inhibit gyrases and topoisomerases.[161] Additionally, **P2** also consists of a quinoxalinyl moiety (Figure 3.5), which inhibits nucleotide synthesis and are reported to be highly active against gram-positive bacteria.[162] These structural characteristics may explain the increased susceptibility of *B. subtilis* towards **P2** compared to other tested phenazines.

The phenazine **P3** contains a pyridine ring (Figure 3.5 marked in green), while **P4** and **P5** feature pyrrolyl moieties (Figure 3.5 marked in violet). Antimicrobials containing these N-heterocyclic rings have diverse modes of action, including the inhibition of DNA gyrase during replication, as exemplified by the pyridine-containing nalidixic acid or the antibiotics Clorobiocin and Coumermycin A_1 combining aminocoumarins with a 5-methylpyrrole-2-carboxyl moiety.[163,164] Thus, the pyridinyl and pyrrolyl structural features of phenazines **P3** and **P5** may account for the extended antimicrobial spectrum observed against gram-negative *Pseudomonas putida* in the disk diffusion assay. Nevertheless, the resistance towards **P4**, also containing a pyrrolyl moiety, remains unclear.

To summarize, targeted studies are required precisely elucidating how the tested phenazines work as antibacterial agents. Additionally, a more detailed assessment comparing their activities with known, structurally-related antimicrobials or clinically established antibiotics is needed to fully gauge their efficacy. Lastly, expanding the range of tested microorganisms will give a comprehensive overview of the antimicrobial behavior of the phenazines investigated here.

3.2 Cu_2O_2 studies with TMGphpy

Experiments to optimize the reaction conditions of the TMGphpy ligand synthesis, the formation of Cu_2O_2 species with TMGphpy and the determination of catalytic results were performed by Martin Schäfer during his research internship.

The previous chapter investigated the catalytic hydroxylation and oxidation activity of the bis(µ-oxido) complex [**O1**]$(PF_6)_2$ stabilized by bisguanidine ligand 2-(2((bis(dimethylamino)methylene)amino)benzyl)-1,1,3,3-tetramethylguanidine (TMG_2tol). In comparison to 2-2-((dimethylamino)methyl)phenyl-1,1,3,3-tetramethylguanidine (TMGbenza), a hybrid guanidine ligand containing the same benzylaminyl backbone as TMG_2tol, the catalytic activity was significantly reduced. The TMG_2tol based **O** species only converted two substrates, 2-naphthol and 6-quinolinol, successfully to the desired phenazines (TON 4 – 8, TOF $0.5 \ - \ 1\,h^{-1}$) while the **O** species coordinated by TMGbenza transformed nine different substrates in a shorter reaction time (TON 5 – 8, TOF $5 \ - \ 8\,h^{-1}$).[87] Bisguanidine TMG_2tol consists of two bulky, electron-rich guanidine units attached to the benzylamine backbone. In contrast, in TMGbenza one of the guanidine units is replaced by a smaller dimethylamine N-donor group. Consequently, the two guanidine units in TMG_2tol seem to hinder substrate coordination and subsequent hydroxylation at the Cu_2O_2 center. Variation of the amine donor unit at the TMGbenza hybrid guanidine, investigated by Herres-Pawlis and coworkers, led to similar results: The catalyst performance decreases with increasing sterical demand of the alkyl substituent. Resulting **O** species based on the hybrid guanidine ligands 2-(2-((diethylamino)methyl)phenyl)-1,1,3,3-tetramethylguanidine (TMGbenzNEt_2) and 2-(2-((di-isopropylamino)methyl)phenyl)-1,1,3,3-tetramethylguanidine (TMGbenzN$i$$Pr_2$) were still able to reach comparable yields and TON, however, longer reaction times were needed resulting in a decreasing TOF.[87,90] Due to the rotatable alkyl groups on the amine donor as well as on the TMG guanidine unit of TMGbenzNEt_2 and TMGbenzN$i$$Pr_2$, the Cu_2O_2 center is more shielded with increasing alkyl group size on the amine donor compared to TMGbenza incorporating methyl groups (Figure 3.6).

To create a more rigid N-donor group with less sterical demand than a guanidine or NEt_2 group, a new hybrid guanidine ligand with a pyridinyl N-donor instead of an amine group was synthesized. Therein, the pyridinyl group creates a more rigid and less bulky N-donor in contrast to the NEt_2 or N$i$$Pr_2$ group. Rotation around the N atom taking place in N-dialkyl groups is excluded while the electron-rich aromatic ring has an electron-withdrawing effect towards the N-donor. The new hybrid guanidine ligand 1,1,3,3-tetramethyl-2-(2-(pyridin-2-yl)phenyl)guanidine (TMGphpy, **L2**) consists of a 2-phenylpyridine spacer with a pyridine donor group incorporated and a TMG guanidine donor at the phenyl ring. The 2-phenylpyridine spacer results in a ligand structure analogous to TMG_2tol, TMGbenza, TMGbenzNEt_2 and TMGbenzNiPr_2: a TMG guanidine donor in the 2-position on a phenyl ring combined with a further N-donor in the 1-position in one C atom distance bridged by 3 C atoms (analogous structure features marked in bold in Figure 3.6).

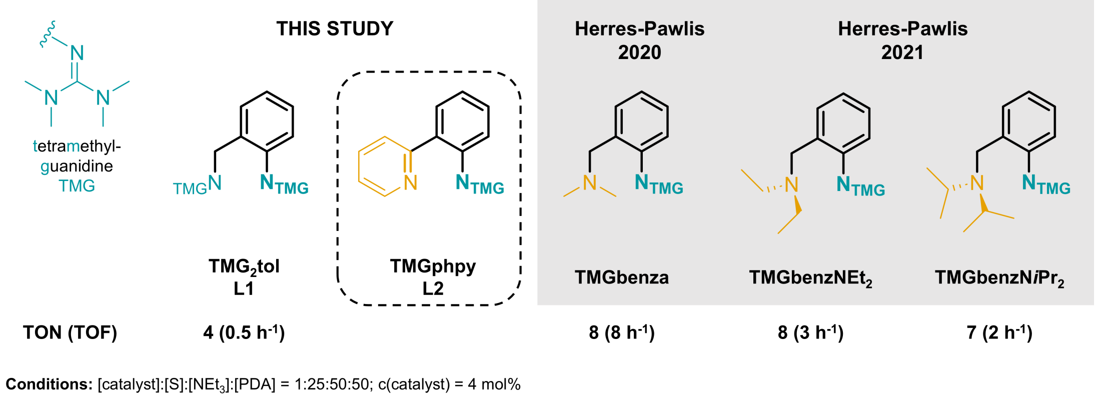

Figure 3.6: Structures of bisguanidine (TMG_2tol) and hybrid guanidine ligands (TMGbenza,[87] $TMGbenzNEt_2$, TMGbenzN*i*Pr_2[90]) stabilizing **O** species investigated in the catalytic hydroxylation and subsequent oxidation with 6-quinolinol followed by a condensation with PDA. Related TON and TOF of desired phenazine product pyrido[3,2-a]phenazine (**P3**) are given in comparison to the newly synthesized hybrid guanidine ligand TMGphpy (dashed box). Analogous structure features are highlighted in bold.

3.2.1 Synthesis of the New Hybrid Guanidine Ligand TMGphpy (L2)

3.2.1.1 Synthesis of Primary Amine 2-(2-Aminophenyl)pyridine

The primary amine 2-(2-aminophenyl)pyridine was synthesized based on a literature procedure.[165,166] The synthesis route consists of a Pd(0) catalyzed Negishi cross-coupling reaction connecting organometallics of low nucleophilicity to aryl halides under mild reaction conditions.[167] The organozinc pyridin-2-ylzinc(II) bromide is converted with the aryl halide 2-iodoaniline using tetrakis triphenylphosphine palladium(0) over a course of 24 hours at room temperature (20 °C) (Scheme 3.7). In contrast to the original protocol, pyridin-2-ylzinc(II) bromide was commercially purchased instead of freshly synthesized from activated zinc.[165,166]

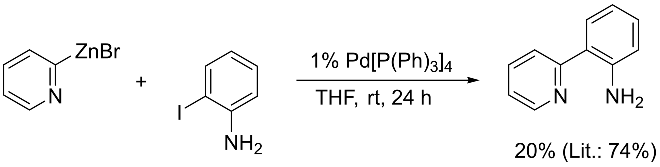

Scheme 3.7: Synthesis route of the primary amine 2-(2-aminophenyl)pyridine after Rieke and Kim using a Pd(0) catalyzed Negishi cross-coupling reaction to combine the organozinc compound pyridin-2-ylzinc(II) bromide with 2-iodoaniline under mild reaction conditions.[165,166]

2-(2-aminophenyl)pyridine was obtained as a yellow oil ($Y = 20\%$ Lit.: 74%; based on 2-iodoaniline) which turned red after one week at ambient conditions (air contact, room temperature). Recorded ^1H NMR data were in accordance to literature data.[165] The amount of obtained amine product was significantly lower than expected from the literature protocol. Moreover, a large amount of 2-iodoaniline (67%) remained unconverted (entry 1 in Table 3.9). The poor reaction performance compared to literature is probably related to the purchased organozinc compound. Organo zinc compounds are known to be highly air-sensitive,[168] thus the species is maybe partially deactivated in contrast to freshly synthesized pyridin-2-ylzinc(II) bromide. To maximize the reaction yield, the reaction conditions were optimized: Both, a higher reaction temperature (reflux; 66 °C) as well as a doubling of reaction time (48 h) led to the same slight increase in desired product formation (25%; entry 2 and 3 in Table 3.9). Combining both factors, the hightest amount of product was reached (35%) while only 12% of 2-iodoaniline were regained (entry 4 in Table 3.9 marked in red). With a further extension of reaction time to 69 h no increase in product formation or substrate conversion could be monitored (entry 5 in Table 3.9). A detailed synthesis protocol can be found in Section 6.3.2.1 in the experimental part.

Table 3.9: Variations of temperature (T) and reaction time (t) tested for the Pd(0) catalyzed Negishi cross-coupling reaction of pyridin-2-ylzinc(II) bromide and 2-iodoaniline to form desired primary amine product 2-(2-aminophenyl)pyridine. Reaction conditions reaching the highest amount of desired product are highlighted in red.

entry	T [°C]	t [h]	scale factor[a]	X [b] [%]	Y (educt)[c] [%]	Y (product)[c] [%]
1	20	24	0.5	33	67	20
2	reflux	24	0.5	n.d.	n.d.	25
3	20	48	1	35	65	25
4	reflux	48	1	88	12	35
5	reflux	69	1.5	90	10	31

[a] based on n(2-iodoaniline) = 8 mmol in literature; [b] calculated from isolated amount of 2-iodoaniline after column chromatography; [c] isolated yield after column chromatography; n.d. = not determined

The optimized reaction conditions (reflux, 48 h reaction time) resulted in an increased yield of 2-(2-aminophenyl)pyridine to 35%. However, the amount obtained is still half as much as stated in literature (74%).[165,166] As an alternative to freshly synthesized organozinc compound, commercially available pyridin-2-ylzinc(II) bromide was used in this study. Thus, literature amounts could be reached by freshly synthesizing pyridin-2-ylzinc(II) bromide. Organozinc compounds are formed converting activated zinc with the aryl halide needed.[165] Zinc activation is performed by refluxing alkali metals like potassium or sodium with zinc in toluene or benzene.[169] Consequently, pyridin-2-ylzinc(II) bromide synthesis requires a combination of dangerous reaction steps in which various hazardous chemicals are necessary. As a result, the idea of organozinc compound synthesis was discarded.

3.2.1.2 Guanidine Synthesis with 2-(2-Aminophenyl)pyridine

The new hybrid guanidine ligand 1,1,3,3-tetramethyl-2-(2-(pyridin-2-yl)phenyl)guanidine (TMGphpy, **L2**) was synthesized based on the literature-known general protocol for bisguanidine ligands outgoing from the primary amine 2-(2-aminophenyl)pyridine.[111]

The primary amine 2-(2-aminophenyl)pyridine was converted in a condensation reaction with chloro-N,N,N',N'-tetramethylformamidinium chloride (TMG Vilsmeier salt) using triethylamine as an auxiliary base. The byproduct, triethylaminiumchloride, was removed through addition of stoichiometric amounts of sodium hydroxide. Subsequent second deprotonation step with potassium hydroxide solution resulted in the desired free guanidine base TMGphpy (Scheme 3.8).

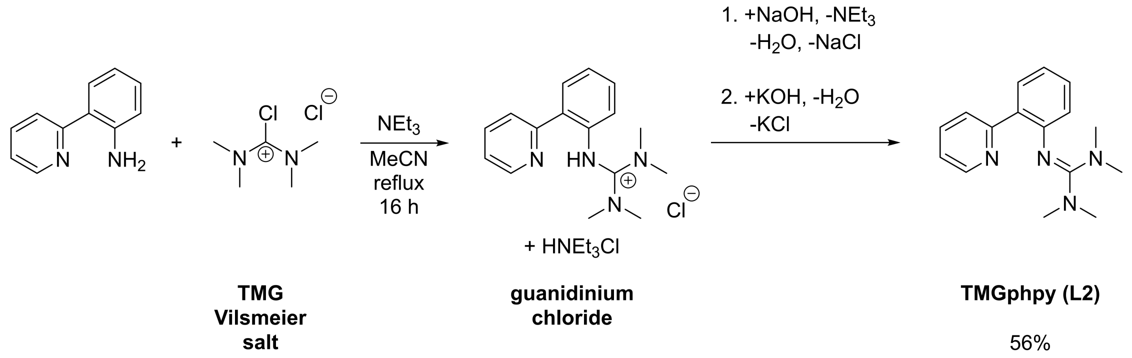

Scheme 3.8: Synthesis route of the new hybrid guanidine ligand TMGphpy (**L2**) based on a literature-known general protocol for bisguanidines.[111] The primary amine was converted with TMG Vilsmeier salt to a guanidinium chloride. After two deprotonation steps, the desired hybrid guanidine **L2** was obtained.

A first experiment performed over a course of eight hours under reflux and subsequent stirring with sodium hydroxide over 2 days resulted in 60% of crude product. After purification, 30% of the desired guanidine ligand TMGphpy were obtained. An increase of the reaction time to sixteen hours under reflux and a shorter stirring time with sodium hydroxide (overnight) led to a high increase of crude product amount (85%) as well as purified hybrid guanidine ligand **L2** (56%). However, the crude product still contained large amounts of tetramethylurea which was removed during purification via fractional distillation under nitrogen atmosphere. Guanidine ligands are prone to protonation, thus, TMGphpy was stored in a glovebox under nitrogen atmosphere to ensure moisture-free conditions.

The new hybrid guanidine ligand TMGphpy was analyzed via ^{1}H and ^{13}C NMR spectroscopy, IR spectroscopy, mass spectrometry and UV/Vis spectroscopy. In accordance to literature, methyl groups of the TMG moiety in **L2** displayed a broad signal at 2.46 ppm in the ^{1}H NMR spectrum characteristic for guanidine ligands containing an aromatic spacer. In the ^{13}C NMR spectrum a typical broad signal at 39.4 ppm could be assigned to the TMG moiety's methyl groups analogous to earlier findings (Figure 8.5 and 8.6 in the appendix).[87,90,111] All signals were unambiguously assigned to related atoms by 2D-NMR spectroscopy (COSY, HMBC; HSQC). A complete list of NMR signals assigned to the molecule structure can be found in Section 6.3.2.1 in the experimental part. In the UV/Vis spectrum, TMGphpy displayed two signals at 276 nm and 322 nm (Figure 8.3 in the appendix). In consistency with other guanidine ligands,[85–87,90,111] vibration bands of the C=N bond in the guanidine moiety were monitored between 1552 cm^{-1} and 1586 cm^{-1} in the IR spectrum (Figure 8.4 in the appendix). The exact molecular mass of TMGphpy ($[C_{16}H_{20}N_4 + H]^+$) calculated as 269.17607 $g\,mol^{-1}$ was verified via high resolution mass spectrometry (HR-MS) and found to be 269.17573 $g\,mol^{-1}$.

3.2.2 Formation of Cu_2O_2 Species with TMGphpy

Cu_2O_2 species mimicking the catalytically active center of the enzyme tyrosinase are formed by the conversion of copper(I) complexes stabilized by N-donor ligands with molecular oxygen.[55,85–88,90,97] As described in Section 1.2.1, three isoelectronic Cu_2O_2 isomers a trans-μ-1,2-peroxido dicopper(II) species ($^{\mathbf{T}}\mathbf{P}$), a μ-η^2:η^2-peroxido dicopper(II) species ($^{\mathbf{S}}\mathbf{P}$) or a bis(μ-oxido) dicopper(III) species (**O**) can be formed. Those can be distinguished by their characteristic *ligand-to-metal charge transfer* (LMCT) transitions in the UV/Vis spectrum. Typically, $^{\mathbf{T}}\mathbf{P}$ show blue to violet colored solutions with two signals around 550 nm and 600 nm.[70,72,78,79,83] Solutions of $^{\mathbf{S}}\mathbf{P}$ species have a similar color displaying signals at 350 nm and 550 nm.[53,54,72,80,84] In contrast, most solvated **O** species are colored red, orange or brown due to the red-shift in their UV/Vis signals around 300 nm and 400 nm.[74,75,85–87,92]

To investigate whether the new ligand TMGphpy is able to stabilize a Cu_2O_2 species, copper(I) precursor complexes are formed converting the ligand species with various copper(I) salts. Subsequently, the solutions is injected into oxygen-saturated solvent with an UV/Vis immersion probe inside it to study the ongoing reaction (Scheme 3.9).

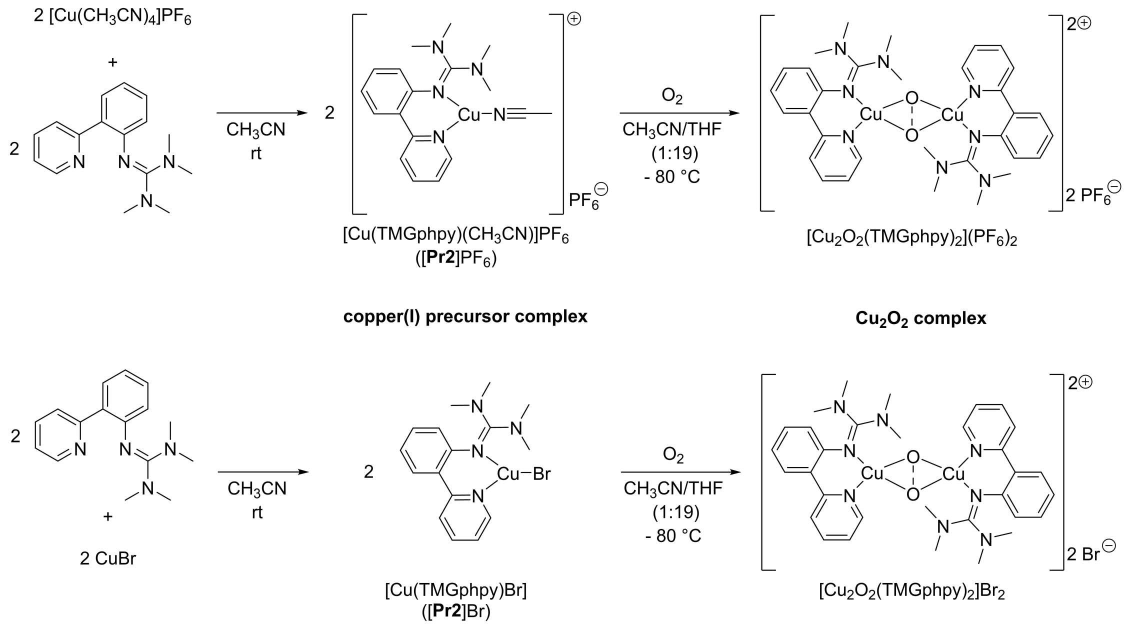

Scheme 3.9: Conversion of copper(I) salts $[Cu(CH_3CN)_4]PF_6$ and CuBr with the new ligand TMGphpy to form copper(I) precursor complexes **Pr2**]PF_6 and [**Pr2**Br]. Subsequent addition of precursor solutions to oxygen-saturated THF at −78 °C leads to the formation of a Cu_2O_2 species.

First, **L2** is diluted in acetonitrile (CH_3CN) and added to a solution of copper(I) salt in CH_3CN. Therefore, two different copper(I) salts are used: one with a coordinating anion, copper(I)bromide (CuBr), and another one with a weakly-coordinating anion, tetrakis(acetonitrile)copper(I) hexafluorophosphate ($[Cu(CH_3CN)_4]PF_6$) (Scheme 3.9).

The resulting copper(I) precursor complex solutions of $[Cu(TMGphpy)(CH_3CN)]PF_6$ ([**Pr2**]PF_6) and [Cu(TMGphpy)Br] ([**Pr2**Br]) displayed a yellow color. Subsequently, each copper(I) precursor solution was injected in oxygen-satured tetrahydrofuran (THF) at -80 °C to form the corresponding Cu_2O_2 species (Scheme 3.9). After injection of the copper(I) precursor solutions, the reaction mixtures turned dark yellow. A detailed description of performed solution preparation can be found in section 6.4 and Section 6.5.1 in the experimental part.

In the case of the weakly-coordinating anion PF_6^-, a maximum at 328 nm was formed over a course of 30 minutes (Figure 3.7, above left). No steady absorbance verifying a complete formation of the new Cu_2O_2 species could be monitored. Instead, after 35 minutes the maximum started to decrease indicating an incomplete formation of the Cu_2O_2 species $[Cu_2O_2(TMGphpy)_2](PF_6)_2$ (Figure 3.7, above right).

Using the coordinating anion Br^- a shoulder was formed at 328 nm within 5 min which was steady for 15 min afterwards indicating a complete formation of $[Cu_2O_2(TMGphpy)_2]Br_2$ (Figure 3.7, below, left). In contrast to $[Cu_2O_2(TMGphpy)_2](PF_6)_2$ formed with weakly-coordinating anion PF_6^-, a steady absorbance is reached with coordinating anion Br^- forming $[Cu_2O_2(TMGphpy)_2]Br_2$. However, the maximum absorbance is below the one with weakly-coordinating anions (Figure 3.7 below, right).

The maxima at 328 nm monitored during the conversion of ([**Pr2**]PF_6) and ([**Pr2**Br]) with oxygen-saturated THF indicate the formation of a µ-η^2:η^2-peroxido dicopper(II) complex (**^{S}P**). In contrast to literature (350 and 550 nm),[53,54,72,80,84] the signal at 328 nm is slightly blue-shifted and the signal at 550 nm is missing completely. The presumed **^{S}P** species is depicted in Scheme 3.9.

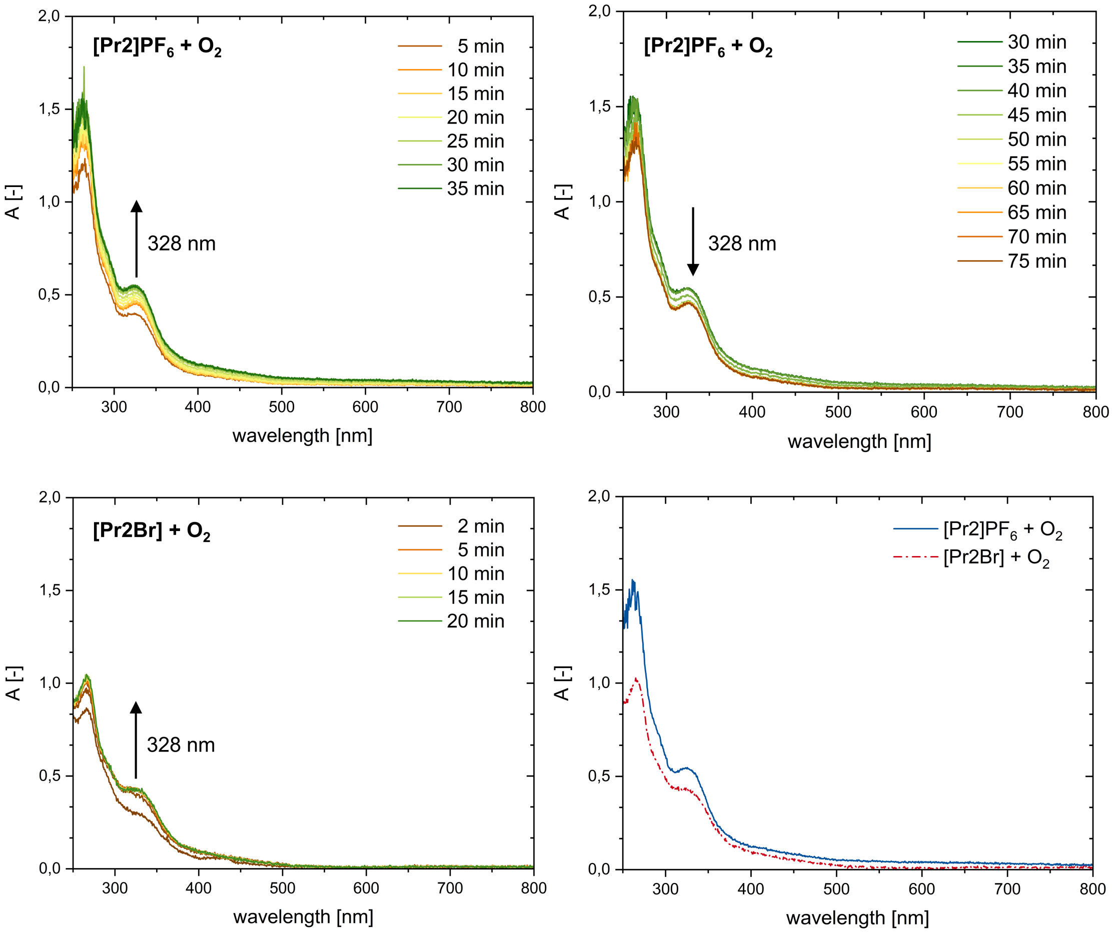

Figure 3.7: UV/Vis spectra monitoring the conversion of copper(I) precursor complexes [**Pr2**]PF_6 and [**Pr2**Br] with molecular oxygen at −80 °C in-situ (c([**Pr2**]PF_6) = c([**Pr2**Br]) = 0.5 mM, CH_3CN:THF = 1:19). Left above (**Pr2**]PF_6 + O_2): Formation of a maximum at 328 nm. Right above ([**Pr2**]PF_6 + O_2): Decay of the maximum at 328 nm. Left below ([**Pr2**Br] + O_2): Formation of a maximum at 328 nm. Right below: Comparison of maxima formed during the conversion of [**Pr2**]PF_6 and [**Pr2**Br] with O_2.

As no steady absorbance could be monitored during the conversion of [**Pr2**]PF_6 with molecular oxygen, the experiment was repeated at a lower temperature of −100 °C. Thereby, the signal formation at 328 nm took 50 minutes until a stable absorbance was reached which stayed constant for 90 min (Figure 3.8, left). Compared to the formation at −80 °C, the time until maximum absorbance was reached is extended (1.5 times). Presumably, full formation was reached indicated by a stable absorbance over a long time period. The signal at $-100\,°\mathrm{C}$ displayed a higher maximum (A(328 nm) = 0.717) in contrast to the increasing temperature of $-80\,°\mathrm{C}$ (A(328 nm) = 0.551). However, a transition at 550 nm typical for a $^{\mathrm{S}}\mathbf{P}$ species is still missing. Furthermore, precursor solution [**Pr2**]PF$_6$ (330 nm) as well as diluted ligand TMGphpy (322 nm) displayed similar UV/Vis signals (Figure 3.8, right). Thus, the presumed formation of an $^{\mathrm{S}}\mathbf{P}$ species could not be verified via UV/Vis spectroscopy.

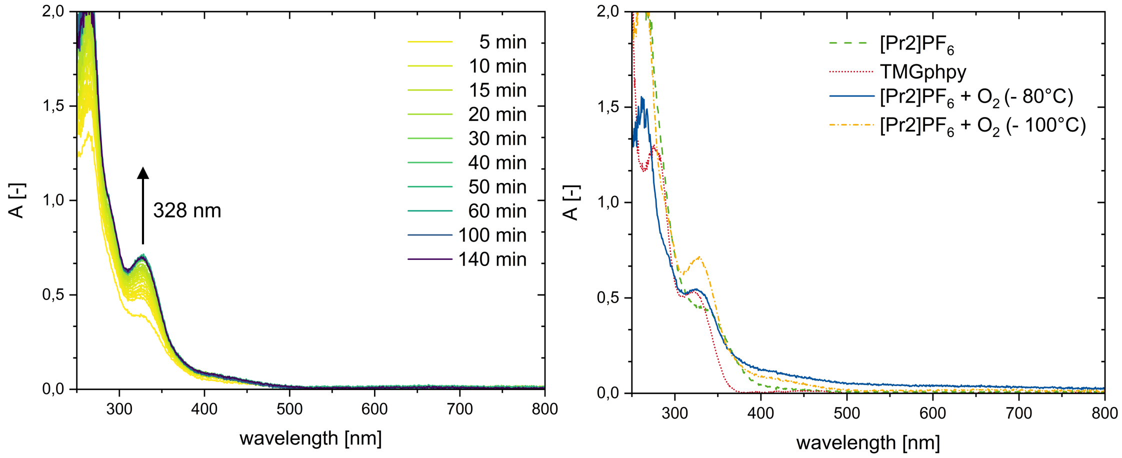

Figure 3.8: UV/Vis spectrum monitoring the conversion of copper(I) precursor complex [**Pr2**]PF$_6$ with molecular oxygen at $-100\,°\mathrm{C}$ in-situ (left; (c([**Pr2**]PF$_6$) = 0.5 mM, CH$_3$CN:THF = 1:5). UV/Vis spectra of the maximum absorbance reached during the reaction of [**Pr2**]PF$_6$ with O$_2$ at $-80\,°\mathrm{C}$ and $-100\,°\mathrm{C}$ as well as ligand TMGphpy diluted in THF and precursor solution [**Pr2**]PF$_6$ at $-80\,°\mathrm{C}$ (c([**Pr2**]PF$_6$) = 0.5 mM, CH$_3$CN:THF = 1:19).

3.2.3 Catalytic Activity Studies with [Cu$_2$O$_2$(TMGphpy)$_2$](PF$_6$)$_2$ ([$^{\mathrm{S}}$P2](PF$_6$)$_2$)

Like the natural enzyme tyrosinase, several Cu$_2$O$_2$ species are able to convert phenolic substrates to the related *ortho*-quinone products.[59,82,87,88,95,96,100] As most *ortho*-quinones are unstable under ambient conditions,[104–107] verifying their formation is challenging. In 2020 Herres-Pawlis and coworkers used a condensation reaction of highly-reactive *ortho*-quinones with *ortho*-phenylenediamine (PDA) to prove the catalytic activity of a bis(µ-oxido) species. The resulting phenazine products are stable at ambient conditions and verifiable via NMR spectroscopy.[87]

The catalytic activity of the presumed $^{\mathrm{S}}\mathbf{P}$ species based on the newly synthesized hybrid guanidine ligand TMGphpy ([Cu$_2$O$_2$(TMGphpy)$_2$](PF$_6$)$_2$; [$^{\mathrm{S}}\mathbf{P2}$](PF$_6$)$_2$) was investigated using the reaction conditions of Herres-Pawlis and coworkers[87] just as in the experiments with the TMG$_2$tol stabilized **O** species in the previous chapter (Section 3.1.3) with a reaction time of 3 h at $-80\,°\mathrm{C}$ ([[$^{\mathrm{S}}\mathbf{P2}$](PF$_6$)$_2$]:[S]:[NEt$_3$]:[PDA] = 1:25:50:50; c([$^{\mathrm{S}}\mathbf{P2}$](PF$_6$)$_2$) = 4 mol %). The substrate scope was minimized to one substrate out of each substrate group (naphthols, quinolinols, indolols) successfully converted in previous studies with TMG$_2$tol and TMGbenza (Scheme 3.10).

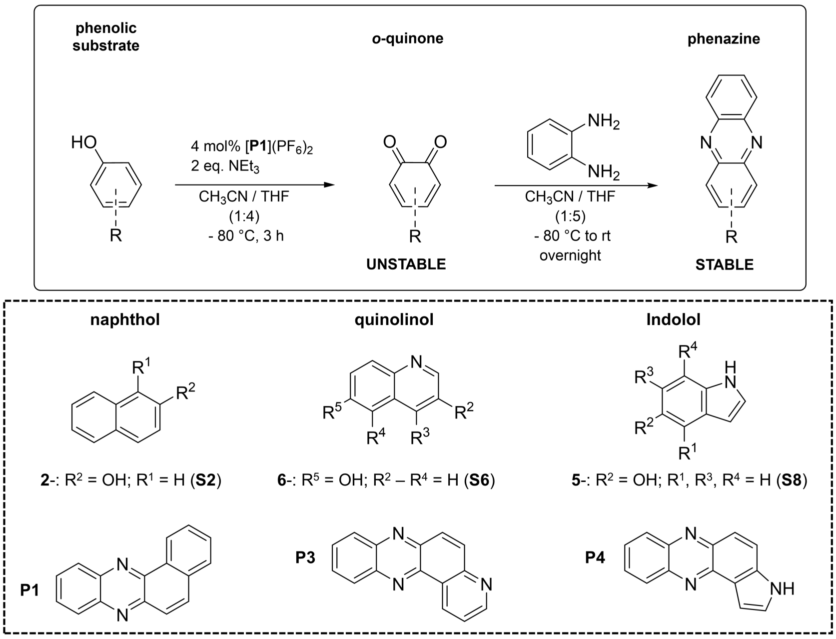

Scheme 3.10: Catalytic hydroxylation and subsequent oxidation of phenolic substrates mediated by presumed peroxido species $[^{\mathbf{S}}\mathbf{P2}](PF_6)_2$ followed by a condensation with PDA ($c([^{\mathbf{S}}\mathbf{P2}](PF_6)_2)$ = 4 mol%). Phenolic substrates (S) are converted to highly reactive *ortho*-quinones by $[^{\mathbf{S}}\mathbf{P2}](PF_6)_2$ over a course of three hours at −80 °C. A following condensation with *ortho*-phenylendiamine (PDA) at room temperature (20 °C) overnight transformed the unstable intermediates into stable phenazine products **P** verifiable via NMR spectroscopy ($[[^{\mathbf{S}}\mathbf{P2}](PF_6)_2]$:[S]:$[NEt_3]$:[PDA] = 1:25:50:50).

All three tested substrates were converted successfully to the related phenazine derivative. However, only conversions with 2-naphthol (**S2**) reached higher yields (10 %, TON 3) than blank experiments performed with pure copper salt (4 – 5 %, TON 1; Section 3.1.3.3). Experiments using 6-quinolinol (**S6**) and 5-indolol (**S8**) resulted in phenazine amounts in the same range as blank experiments (S6: 4 %, TON 1; S8: 5 %, TON 1). Consequently, a catalytic activity of presumed $^{\mathbf{S}}\mathbf{P}$ species $[Cu_2O_2(TMGphpy)_2](PF_6)_2$ was only verified for substrate **S2** (Table 3.10).

Table 3.10: Phenolic substrates **S** investigated in the catalytic hydroxylation and subsequent oxidation with presumed peroxido species $[^{\mathbf{S}}\mathbf{P2}](PF_6)_2$ ($[Cu_2O_2(TMGphpy)_2](PF_6)_2$) followed by a condensation with PDA as well as averaged, isolated yields and TON of desired phenazine products **P**. Conversion reactions displaying catalytic activity (TON >1) are highlighted in green.

entry	substrate	Y[a] [%]	TON[b]	phenazine product
1	S2	10	3	P1
2	S6	4	1	P3
3	S8	5	1	P4

[a] Isolated yield after purification via column chromatography; Reaction conditions: catalytic oxygenation at -80°C, 3 h; PDA condensation at room temperature, overnight. [b] TON calculated using the isolated product yield and the concentration of $[^{\mathbf{S}}\mathbf{P2}](PF_6)_2$ (4 mol%).

3.2.4 Summary

The primary amine 2-(2-aminophenyl)pyridine was resynthesized successfully. To avoid the handling of hazardous chemicals, a purchased organozinc compound was used decreasing the yield of desired amine product (20 %; Lit.: 74 %). Optimizing the reaction conditions by increasing the reaction temperature to reflux and prolonging the reaction time to 48 h, half of the yield reported in literature could be reached (35 %; Lit.: 74 %).[165,166]

Subsequently, 2-(2-aminophenyl)pyridine was converted with TMG-Vilsmeier salt based on a literature-known general-procedure for bisguanidines[111] forming the new hybrid guanidine ligand TMGphpy. By increasing the reaction time from 8 to 16 h the amount of TMGphpy could be doubled from 30 to 56 %. However, the amount of tetramethylurea impurities was nearly the same in both experiments as similar losses occurred during purification (30%). Urea is formed during guanidine degradation with water. Therefore, long stirring of guanidinium chloride with sodium hydroxide solution may have led to partial degradation and urea formation. As a consequence, removal of the byproduct triethylaminiumchloride through addition of sodium hydroxide should be limited to a few hours stirring instead of one day. Furthermore, tripling the reaction time to 24 hours under reflux may further improve the formation of TMGphpy.

Evaluating the ability of TMGphpy to form Cu_2O_2 species, the newly synthesized hybrid guanidine ligand was converted with diluted copper(I) salts to form copper(I) complex solutions. Those were subsequently injected in oxygen-saturated THF at low temperatures (−80 °C) and the reaction was monitored via UV/Vis spectroscopy in-situ. A signal at 328 nm indicated the formation of a side-on peroxido complex. Still, the formation of a $^{\mathbf{S}}\mathbf{P}$ species could not be verified as one of the literature-known signals (350 and 550 nm[53,54,72,80,84]) is missing. To prove the presence of a Cu_2O_2 species, cold-spray ionization mass spectrometry measurements at low temperature should be performed. Further, guanidine ligands based on the same backbone structure as the new TMGphpy ligand are known to stabilize bis(μ-oxido) dicopper(III) species if the related copper(I) precursor species is converted with molecular oxygen.[85–87,90] Thus, TMGphpy presumably stabilizing a $^{\mathbf{S}}\mathbf{P}$ species would display an exception to the overall trend. To distinguish between **O** and $^{\mathbf{S}}\mathbf{P}$ species, further analytical methods like resonance Raman spectroscopy would be necessary.

Lastly, the catalytic activity of the presumed TMGphpy based $^{\mathbf{S}}\mathbf{P}$ species towards phenolic substrates was tested. 2-Naphthol, 6-quinolinol and 5-indolol were converted to unstable *ortho*-quinone intermediates and subsequently transferred into stable phenazine products by a condensation reaction with 1,2-phenylenediamine. A catalytic activity could solely be proven for 2-naphthol (10 %, TON 3). With further tested substrates only a slight conversion in the same range as test experiments with pure copper salt were monitored. As the formation of a Cu_2O_2 species could not be verified, a statement about influencing factors on the catalytic activity by the ligand structure is impossible.

3.3 Cu_2O_2 Studies with TMGdmap

Experiments to investigate the stability and catalytic activity of the bis(μ-oxido) complex ***[O3]****(OTf)$_2$ were performed by Nils Becker during his bachelor thesis. Mechanistic studies with TMGbenza were performed in cooperation with Regina Schmidt. EPR solutions were prepared by Nils Becker. Subsequent EPR spectroscopic measurements including data analysis and interpreating was done by Regina Schmidt during her PhD thesis.*[170]

The hybrid guanidine ligand 2-(3-(dimethylamino)propyl)-1,1,3,3-tetramethylguanidine (TMGdmap) was firstly published by Herres-Pawlis and coworkers in 2009. TMGdmap is able to stabilize a Cu_2O_2 center in form of a bis(µ-oxido) species. The oxido complex [**O3**]$(OTf)_2$ ($[Cu_2O_2(TMGdmap)_2](CF_3SO_3)_2$) displays stoichiometric hydroxylation and oxidation activity generating the related catechol product and traces of *ortho*-quinone from 2,4-di-*tert*-butylphenolate. Converting 2,4-di-*tert*-butylphenol the C-C coupling product 1,1'-bi(3,5-ditertbutyl-2-phenol) instead of the desired *ortho*-quinone product was formed.[88]

TMGdmap is structurally related with the hybridguanidine ligand 2-2-((dimethylamino)-methyl)phenyl-1,1,3,3-tetramethylguanidine (TMGbenza) presented in 2020 by Herres-Pawlis and coworkers. The oxido species stabilized by TMGbenza displays a broad hydroxylation and oxidation activity converting naphthols, quinolinols and indolols to the corresponding *ortho*-quinones. The unstable *ortho*-quinone intermediates were transferred into stable phenazine products in a subsequent condensation reaction (TON 5 - 8, TOF $5 - 8\,h^{-1}$).[87] TMGbenza as well as TMGdmap are hybrid guanidine ligands combining a tetramethylguanidine unit with a dimethylamine donor. TMGbenza consists of an aromatic tolyl spacer connecting both N donor groups. In contrast, TMGdmap contains an aliphatic propyl spacer. To investigate the influence of the spacer unit on the hydroxylation and oxidation activity, the ability of [**O3**]$(OTf)_2$ to convert naphthols, quinolinols and indolols was tested.

3.3.1 Stability of Oxido Complex $[Cu_2O_2(TMGdmap)_2](CF_3SO_3)_2$ ([O3]$(OTf)_2$)

To ensure the stability of the catalyst species over the whole reaction time, the stability of bis(µ-oxido) species [**O3**]$(OTf)_2$ coordinated by the hybrid guanidine ligand TMGdmap was investigated. Therefore, copper(I) salt ($[Cu(CH_3CN)_4](CF_3SO_3)$) and TMGdmap were separately diluted in acetonitrile. Subsequently, the copper (I) precursor complex [**Pr3**]OTf ($[Cu(TMGdmap)(CH_3CN)]CF_3SO_3$) was formed adding the diluted ligand to the copper(I) salt solution. Finally, [**O3**]$(OTf)_2$ was gained injecting the copper(I) precursor solution into oxygen-satured THF at −80 °C (Scheme 3.11). The formation of the oxido complex was monitored via in-situ UV/Vis spectroscopy using an immersion probe inside the reaction mixture (Figure 3.9).

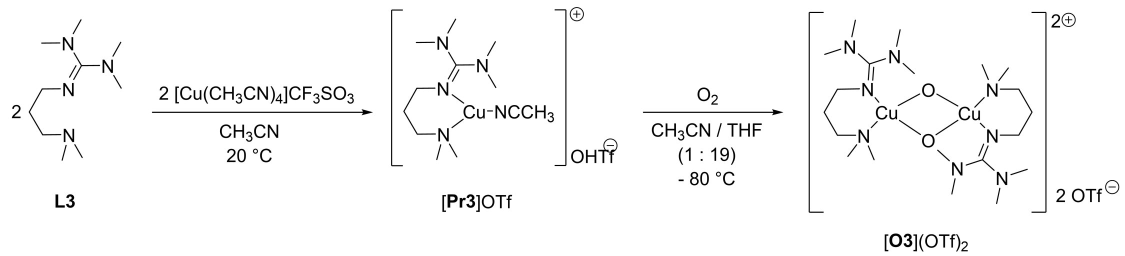

Scheme 3.11: Formation of copper(I) precursor complex [**Pr3**]OTf ($[Cu(TMGdmap)(CH_3CN)]CF_3SO_3$) combining diluted solutions of TMGdmap (**L3**) and copper(I) salt $[Cu(CH_3CN)_4](CF_3SO_3)$. Subsequent injection of [**Pr3**]OTf into oxygen-saturated THF at −78 °C results in the formation of bis(µ-oxido) complex [**O3**]$(OTf)_2$ ($[Cu_2O_2(TMGdmap)_2](CF_3SO_3)_2$).

The bis(µ-oxido) complex [**O3**]$(OTf)_2$ was formed within 25 min displaying two strong LMCT shifts at 294 nm and 391 nm in the UV/Vis spectrum in accordance to literature (Figure 3.9 a)).[88] [**O3**]$(OTf)_2$ was stable for 8.5 h at −80 °C (absorbance change <5 %) before the complex began to decay (Figure 3.9 b) and c)).

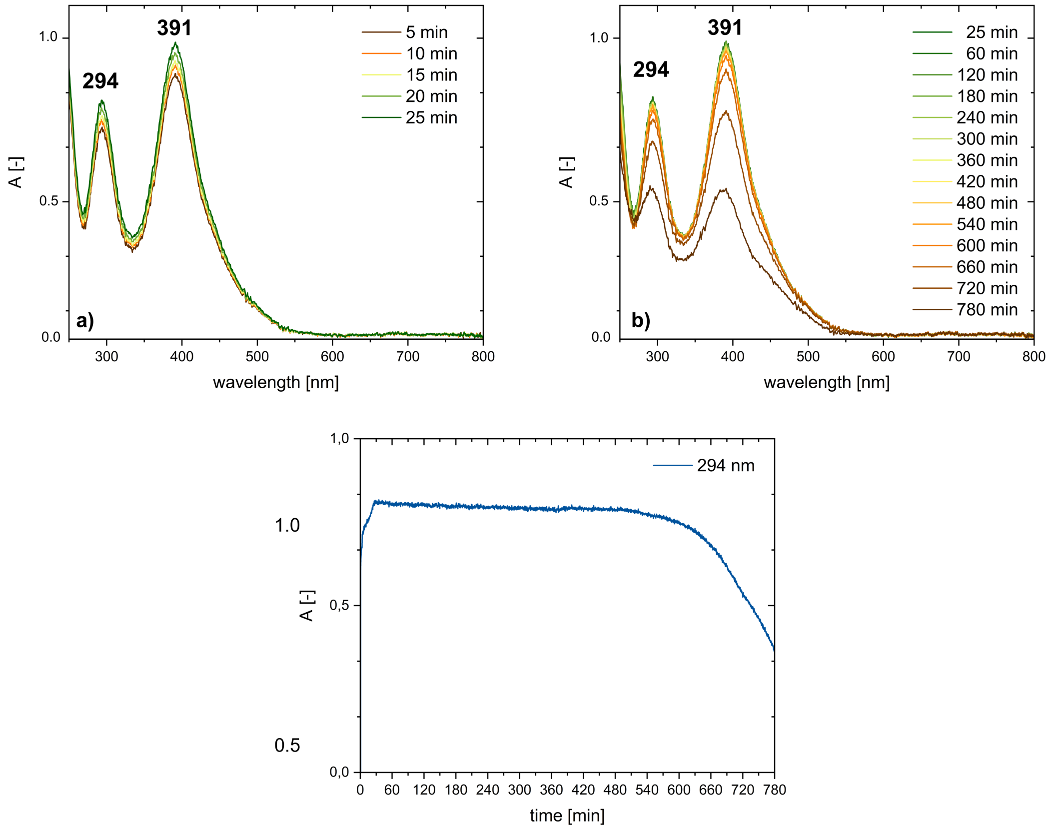

Figure 3.9: UV/Vis spectra of the formation (a) and the decay (b) of bis (µ-oxido) complex [**O3**]$(OTf)_2$ ($[Cu_2O_2(TMGdmap)_2](CF_3SO_3)_2$). The stability of [**O3**]$(OTf)_2$ over time is visualised in (c) displaying the absorbance variation of the ligand-to-metal charge transfer shift at 294 nm over time (c([**O3**]$(OTf)_2$) = 0.5 mM, T = −80 °C, CH_3CN:THF = 1:19).

3.3.2 Catalytic Activity Studies with [O3](OTf)$_2$

Catalytic studies with $[\mathbf{O3}](\mathrm{OTf})_2$ were performed using the reaction conditions of Herres-Pawlis and coworkers (molar ratio: $[\mathbf{O3}](\mathrm{OTf})_2]$:[S]:$[\mathrm{NEt_3}]$:[PDA] = 1:25:50:50; c(catalyst): 4 mol %). The reaction time was set to the maximum time needed for similiar hybrid guanidine stabilized oxido species to reach full conversion in earlier catalytic studies (3 h).[90] The reaction temperature was increased to −78 °C as $[\mathbf{O3}](\mathrm{OTf})_2$ was stable for 8.5 h at this temperature in the stability investigation performed in the previous chapter (Section 3.3.1). The broad spectrum of substrates was reduced to 2-naphthol (**S2**), 3-quinolinol (**S3**), 6-quinolinol (**S6**) and 5-indolol (**S8**) (Scheme 3.12) displaying the highest yields within their substrate group in earlier studies investigating the hybrid guanidine TMGbenza[87] and the bisguanidine ligand 2-(2((bis(dimethylamino)methylene)amino)benzyl)-1,1,3,3-tetramethylguanidine ($\mathrm{TMG_2tol}$) (Section 3.1.3). The catalyst species $[\mathbf{O3}](\mathrm{OTf})_2$ was formed in-situ injecting the copper(I) precursor solution of [**Pr3**]OTf in oxygen-saturated THF at −80 °C. Full formation of $[\mathbf{O3}](\mathrm{OTf})_2$ was ensured by stirred for 30 min at −80 °C (Scheme 3.11). Afterwards, the substrate solution containing a mixture of phenolic derivative and auxiliary base triethylamine was added to start the hydroxylation reaction (Scheme 3.12).

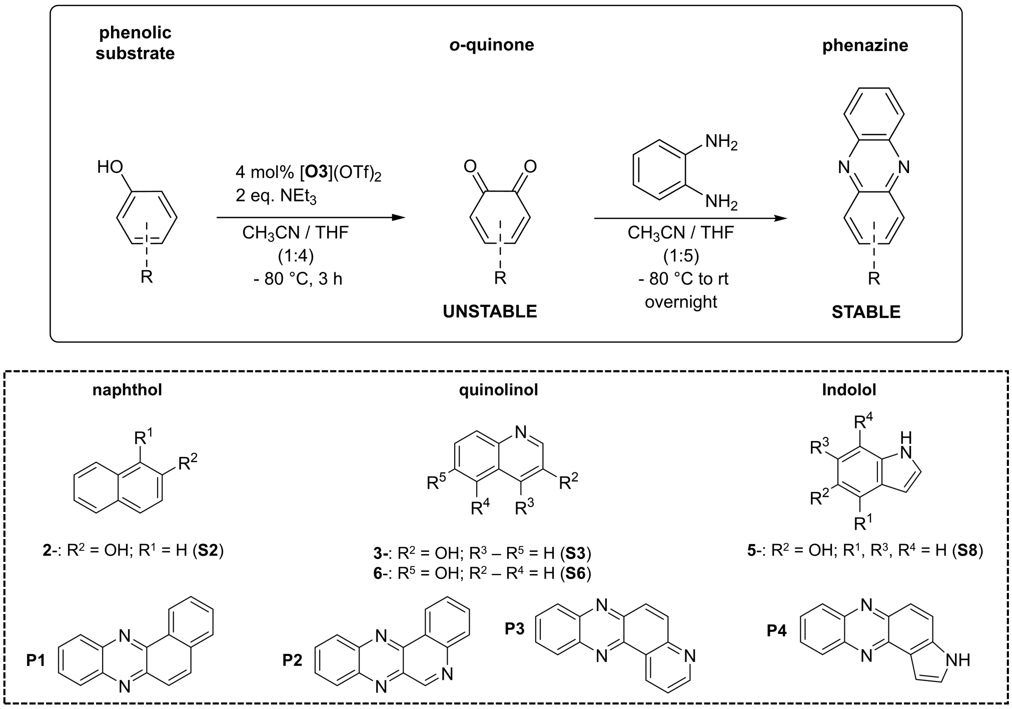

Scheme 3.12: Catalytic hydroxylation and subsequent oxidation of phenolic substrates mediated by bis(μ-oxido) complex $[\mathbf{O3}](\mathrm{OTf})_2$ ($[\mathrm{Cu_2O_2(TMGdmap)_2}](\mathrm{CF_3SO_3})_2$) (c($[\mathbf{O3}](\mathrm{OTf})_2$) = 4 mol%). Phenolic substrates (**S**) are converted to highly reactive *ortho*-quinones by $[\mathbf{O3}](\mathrm{OTf})_2$ over a course of three hours at −80 °C. A following condensation with 1,2-phenylenediamine (PDA) at room temperature (20 °C) overnight transformed the unstable intermediates in stable phenazine products **P** verifiable via NMR spectroscopy ($[\mathbf{O3}](\mathrm{OTf})_2]$:[S]:$[\mathrm{NEt_3}]$:[PDA] = 1:25:50:50).

Converting **S2**, **S3**, **S6** and **S8** small amounts of desired phenazine product were obtained for all four substrates (Table 3.11). However, the amounts reached with **S3**, **S6** and **S8** are below the ones reached within blank experiments performed with pure copper salt in a previous chapter (Section 3.1.3.3) A distinction between catalytic activity of pure copper(I) salt and the oxido species [**O3**]$(OTf)_2$ is impossible. Consequently, hydroxylation and oxidation activity of [**O3**]$(OTf)_2$ could only be verified for 2-naphthol (8 %, TON 2).

Table 3.11: Phenolic substrates **S** investigated in the catalytic hydroxylation and subsequent oxidation with bis(μ-oxido) complex [**O3**]$(OTf)_2$ ($[Cu_2O_2(TMGdmap)_2](CF_3SO_3)_2$) followed by a condensation with 1,2-phenylenediamine (PDA) as well as averaged, isolated yields and TON of desired phenazine products **P**. Conversion reactions displaying catalytic activity (TON >1) are highlighted in green.

entry	substrate	Y[a] [%]	TON[b]	phenazine product
1	S2	8	3	P1
2	S3	2	<1	P2
3	S6	5	1	P3
4	S8	1	<1	P4

[a] Isolated yield after purification via column chromatography; Reaction conditions: catalytic oxygenation at -80°C, 3 h; PDA condensation at room temperature, overnight. [b] TON calculated using the isolated product yield and the concentration of [**O3**]$(OTf)_2$ (4 mol%).

Catalytic activity studies performed with [**O3**]$(OTf)_2$ based on TMGdmap lead to new insights in guanidine ligand design for catalytically active oxido species. All four guanidine species, TMGdmap, TMGbenza, TMG_2tol and 2',2'-(propane-1,3-diyl)bis(1,1,3,3-tetramethylguanidine) (TMG_2p) are based on two N donor units connected within 3 C atom distance by a bridging spacer unit (Table 3.12, marked in red) and stabilize a bis(μ-oxido) species. The **O** species based on TMG_2p, a bisguanidine ligand with a flexible propyl spacer, is inactive towards phenolic substrates.[88] In the hybrid guanidine ligand TMGdmap, containing the same propyl spacer, one of the guanidine donor units is replaced by a dimethylamine unit. As a result, a slight catalytic activity could be monitored for the corresponding oxido complex (**S2**: 8 %, TON 2). Changing the flexible propyl spacer to a more rigid, electron-rich tolyl spacer, like in the hybrid guanidine TMGbenza and bisguanidine TMG_2tol higher amounts of desired phenazine products are reached (**S2**: 31 %, TON 8). However, the oxido species stabilized by hybrid guanidine TMGbenza was the most effective displaying the highest TOF (**S2**: TMG_2tol TOF 1 h^{-1}, TMGbenza TOF 8 h^{-1}) (Table 3.12).[87] As a consequence, the hybrid guanidine species TMGbenza consisting of a bulky guanidine N donor and a small dimethylamine N donor connected by an aromatic tolyl spacer was confirmed as the most effective guanidine ligand for the catalytic hydroxylation and subsequent oxidation of complex phenolic substrates like naphthol, quinolinols and indolols.

Table 3.12: Summary of hybrid guanidine and bisguanidine ligands stabilizing bis(μ-oxido) complexes and their hydroxylation and oxidation activity towards phenolic substrates 2-naphthol (**S2**) and 6-quinolinol (**S6**). Isolated yield and TON of related phenazine products **P1** and **P3** are given. Substrates converted catalytically (TON > 1) are highlighted in green.

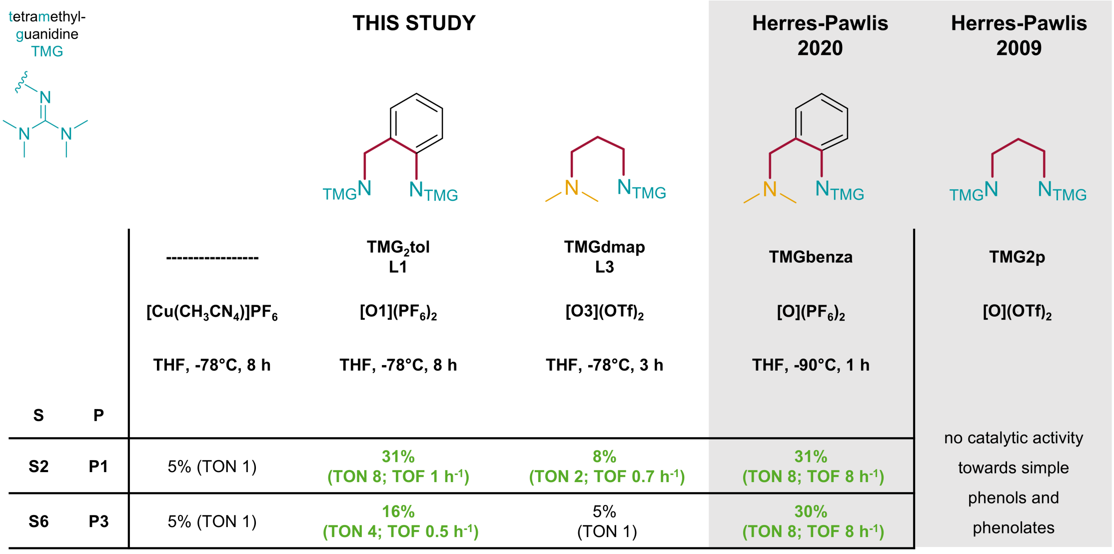

			THIS STUDY		Herres-Pawlis 2020	Herres-Pawlis 2009
		-----------------	**TMG$_2$tol** **L1**	**TMGdmap** **L3**	**TMGbenza**	**TMG2p**
		[Cu(CH_3CN_4)]PF_6	**[O1]$(PF_6)_2$**	**[O3]$(OTf)_2$**	**[O]$(PF_6)_2$**	**[O]$(OTf)_2$**
		THF, -78°C, 8 h	**THF, -78°C, 8 h**	**THF, -78°C, 3 h**	**THF, -90°C, 1 h**	
S	**P**					
S2	**P1**	5% (TON 1)	**31%** **(TON 8; TOF 1 h^{-1})**	**8%** **(TON 2; TOF 0.7 h^{-1})**	**31%** **(TON 8; TOF 8 h^{-1})**	no catalytic activity towards simple phenols and phenolates
S6	**P3**	5% (TON 1)	**16%** **(TON 4; TOF 0.5 h^{-1})**	5% (TON 1)	**30%** **(TON 8; TOF 8 h^{-1})**	

3.3.3 Mechanistic Studies with [O3]$(OTf)_2$

The enzyme tyrosinase is capable to convert mono-phenols as well as diphenols into *ortho*-quinone products by catalytic hydroxylation and subsequent oxidation.[17,29] The current scientific community is in agreement on the diphenolase pathway of tyrosinase, oxidizing catechols to *ortho*-quinones, fully published by Tuczek and coworkers in 2010.[56] However, substrate binding in the monophenolase cycle of phenols, first hydroxylated to catechol and subsequently oxidized to the final *ortho*-quinone product, is not fully uncovered yet.

Reaction mechanisms published 30 to 15 years ago, postulated a symmetric μ-η^1:η^1-catecholate-μ-hydroxidodicopper(II)-intermediate [**CAT1**] to be formed after substrate addition to the catalytically active species ([**O3**]).[29,38,56,171] The substrate molecule, coordinated to the copper center as a catecholate ligand, is a redoxactive, "non-innocent" ligand. Thus, a one-electron-transfer (ET) can take place forming the semiquinone species [**SQ1**], an isoelectronic isomer. This valence tautomerism can be influenced by the choice of the N-donor ligands at the catalytically active center or by the substituents of the substrate species used. The orthogonality of copper and oxygen molecule orbitals in the square-planar geometry of [**CAT1**] can be distorted, resulting in an orbital overlap necessary for the ET.[172–175] Protons, released by the addition of the substrate molecule to the active species, lead to the release of the *ortho*-quinone product and the byproduct water. The intermediate species decays into two copper(I) complexes ([**Pr3**]). In the presence of molecular oxygen, the catalytically active species ([**O3**]) can be regained closing the catalytic cycle (Scheme 3.13).[56]

In contrast, earlier findings postulated the presence of an asymmetric μ-η^2:η^1-catecholate-μ-hydroxidodicopper(II)-complex **[CAT2]** instead of the symmetric **[CAT1]** species.[176–179] This is in accordance with the recently published new pathway for the monophenolase activity of tyrosinase by Solomon and coworkers.[43] Analogue to the valence tautomerism between **[CAT1]** and **[SQ1]**, the asymmetric **[CAT2]** species can undergo an ET to an isoelectronic isomer, the asymmetric semiquinone complex **[SQ2]**.[172–175] As in the case of symmetrical species, the presence of protons results in dissociation of the intermediate complex and product release. The formed copper(I) complexes **[Pr3]** can be reactivated by molecular oxygen starting the catalytic pathway all over again (Scheme 3.13).[43]

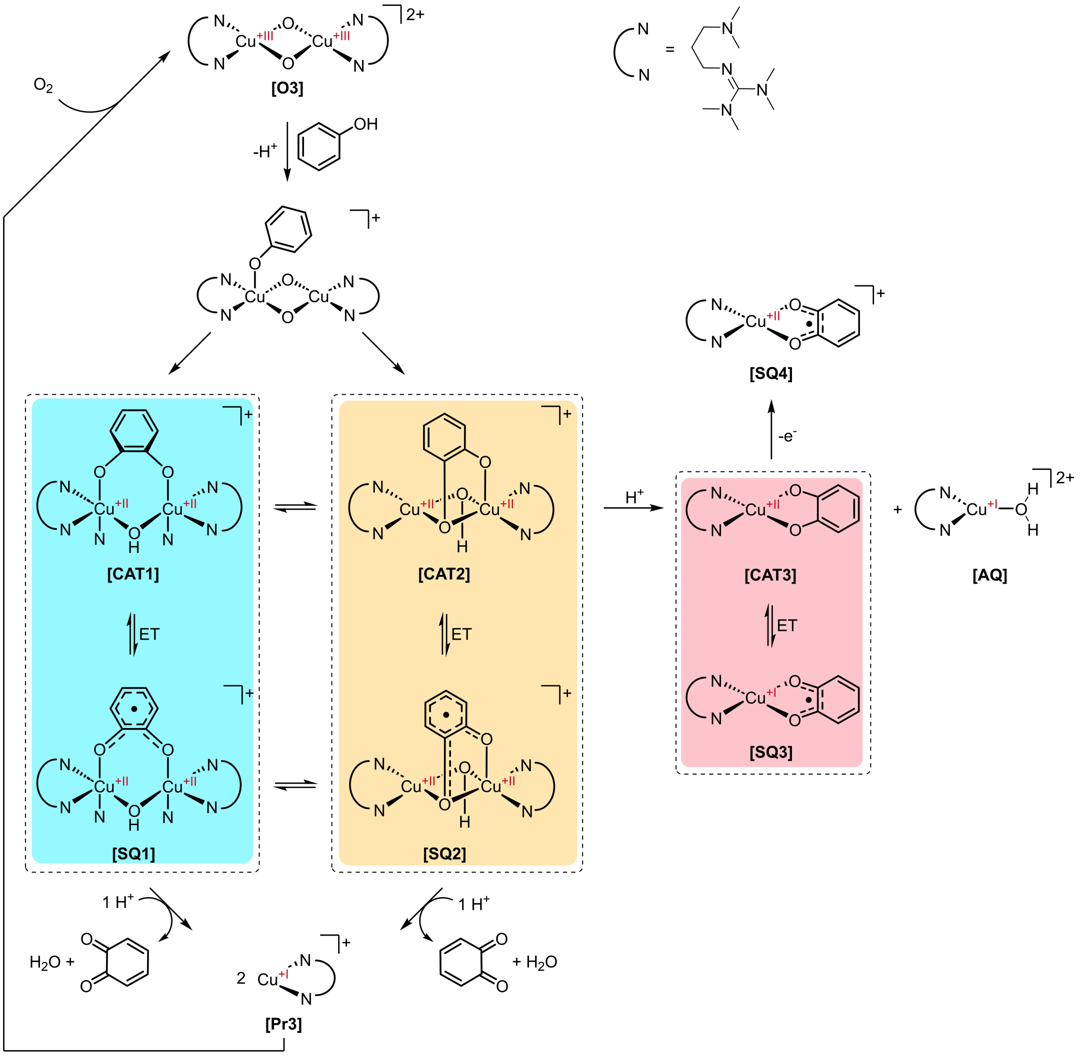

Scheme 3.13: Variations of the monophenolase pathway: Via the symmetric catecholate complex **[CAT1]** and its isoelectronic semiquinone isomer **[SQ1]** after Tuczek et al.[56] (blue box) or via the asymmetric catecholate complex **[CAT2]** and the isoelectronic isomer **[SQ2]** after Solomon et al.[43] (yellow box). Protonation of the intermediate instead of product elimination results in the catecholate complex **[CAT3]** and its isoelectronic isomer **[SQ3]** (red box).[177]

Within the catalytic cycle side-reactions can take place leading to deactivated species. One of them is protonation of the intermediate complexes. Protons, abstracted during substrate addition, are bonding with the hydroxido-bridge instead of releasing an *ortho*-quinone product molecule. The Cu_2O_2 center breaks up and two new complexes, a copper(II)-catecholate complex [**CAT3**] and an aqua-complex [**AQ**] are formed. Analogous to [**CAT1**] and [**CAT2**], an ET from the catecholate to the copper center takes place resulting in the isoelectronic copper(I) semiquinone species [**SQ3**]. Additionally, oxidation of [**CAT3**] can lead to the copper(II) semiquinone species [**SQ4**] (Scheme 3.13).[177]

To investigate the intermediate species present during the monophenolase cycle, the hydroxylation of phenolates mediated by the bis(µ-oxido) species [**O3**]$(OTf)_2$ will be monitored via electron paramagnetic resonance (EPR) spectroscopy. The intermediate species [**CAT1**] and [**CAT2**] are isoelectronic copper(II) isomers which differ in their molecular structure. Copper(II) species are paramagnetic as they contain an unpaired electron. All other species present during the catalytic cycle are diamagnetic with only paired electrons ([**Pr3**]: Cu(I) and [**O3**]: Cu(III); Scheme 3.13). Consequently, [**CAT1**] and [**CAT2**] can be distinguished by their EPR spectra. For the symmetric [**CAT1**] species and rhombic EPR spectrum is expected while an axial spectrum indicates the formation of the asymmetric [**CAT2**] complex (Figure 3.10).[18,180] To stop the catalytic cycle at the formation of the intermediate species, phenolates instead of phenols are used as substrates. Due to absence of protons, product elimination and decay of the intermediate species is prevented. The isoelectronic semiquinone species [**SQ1**] and [**SQ2**], formed by an ET from the aromatic catecholate center of [**CAT1**] and [**CAT2**] to the Cu_2O_2 center, are also present within the reaction mixture. However, Cu(II)-semiquinone complexes display no EPR signal and are those not detectable. Although semiquinones are a radical species containing an unpaired electron, Cu(II)-semiquinone complexes are EPR silent in conventional spectroscopy. Due to the overall even number of unpaired electrons they display diamagnetic features resulting from a large zero field splitting in the triplet ground state only detectable with high-frequency EPR spectroscopic measurements (Figure 3.10).[67]

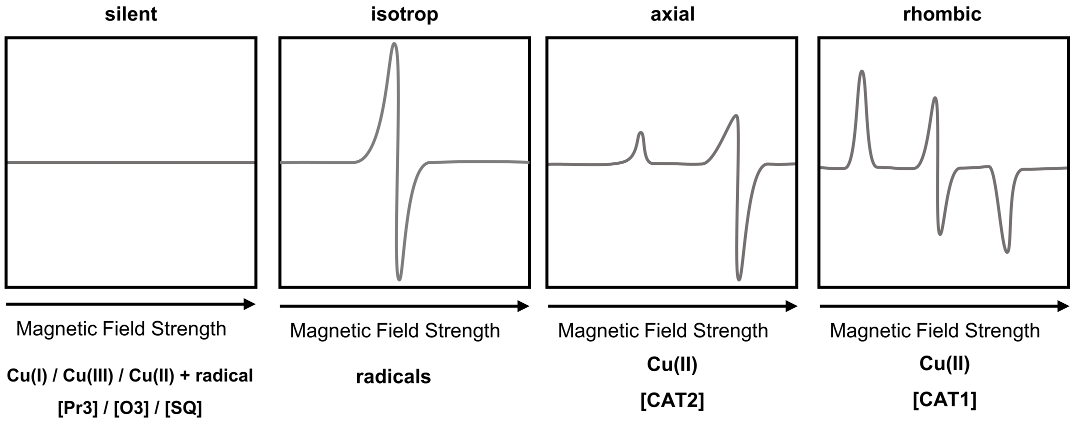

Figure 3.10: EPR spectra expected for the different types of species within the monophenolase cycle.[180]

To study the intermediate species present during the monophenolase pathway, the conversion of three different sodium phenolates by the bis(μ-oxido) species [**O3**]$(OTf)_2$ based on the hybrid guanidine TMGdmap (**L3**) is analyzed via EPR spectroscopy (Figure 3.11).

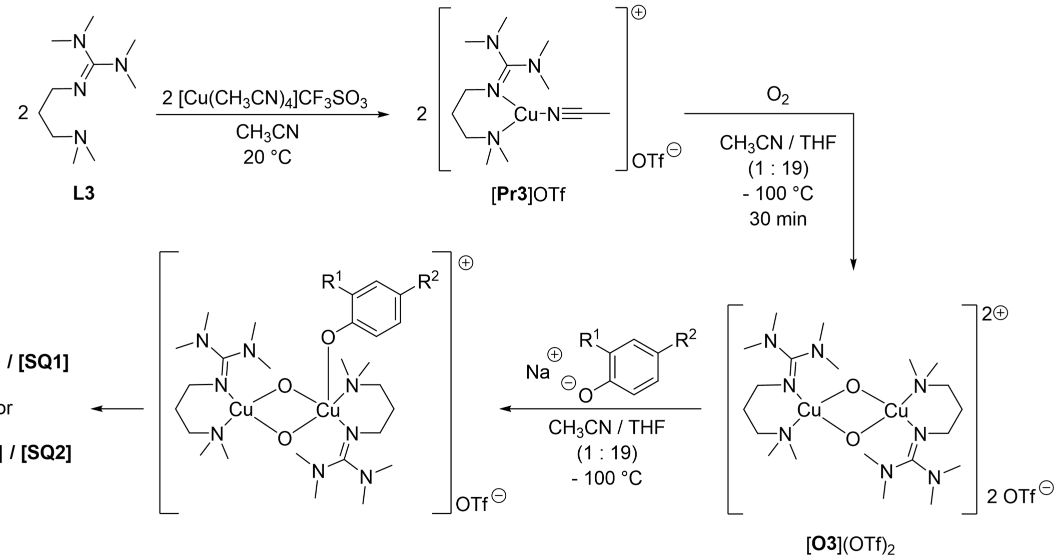

Scheme 3.14: Formation of the bis(μ-oxido) species [**O3**]$(OTf)_2$ ($[Cu_2O_2(TMGdmap)_2](CF_3SO_3)_2$) based on the hybrid guanidine ligand TMGdmap and subsequent conversion of sodium phenolates to form the intermediate species present in the catalytic cycle of the monophenolase pathway. Sodium phenolate: $R^1 = R^2 = H$, sodium 4-methylphenolate: $R^1 = H$, $R^2 = Me$, sodium 2,4-di-*tert*-butylphenolate: $R^1 = R^2 = t$Bu.

First, the oxido species [**O3**]$(OTf)_2$ is formed as described in Section 3.3.1 earlier. To ensure full formation of the catalyst species, the reaction mixture is stirred at −100 °C for 30 min. Subsequently, 2 equivalents of phenolate diluted in THF were added starting the formation of desired intermediate species (Scheme 3.14). Immediately, a sample was taken, transferred into an EPR tube and frozen in liquid nitrogen for EPR analysis.

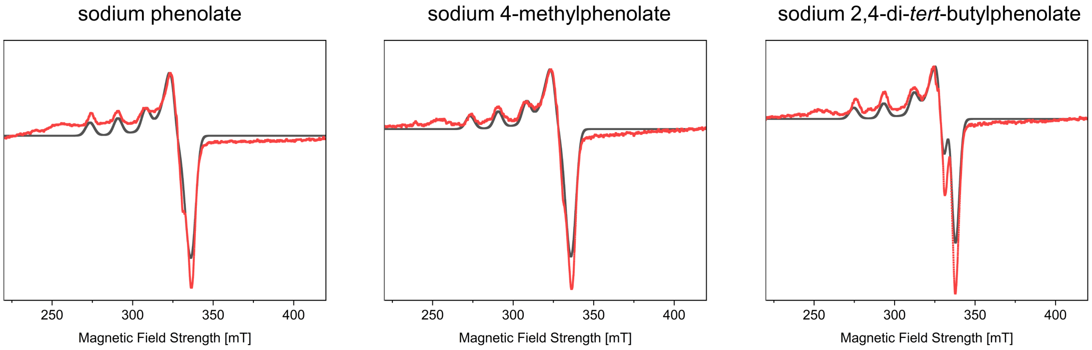

Figure 3.11: EPR spectra (black line) and simulation (red line) of sodium phenolate, sodium 4-methylphenolate and 2,4-di-*tert*-butylphenolate (2 eq.) converted by bis(μ-oxido) species [**O3**]$(OTf)_2$ ($[Cu_2O_2(TMGdmap)_2](CF_3SO_3)_2$; c = 5 mM) measured as frozen solution (77 K). Simulated spectra were obtained using the Matlab toolbox Easyspin.[181]

Analysis and interpretation of EPR spectra was performed by Regina Schmidt in her PhD thesis. Thereby, conversion of sodium phenolates with oxido complex **[O3]**$(OTF)_2$ displayed axial EPR spectra verifying the presence of the asymmetric intermediate **[CAT2]** (Figure 3.11).[170]

To prove the absence of protons and exclude the formation of the copper(II) catecholate side product **[CAT3]**, this complex was investigated as well. Therefore, the copper(II) catecholate complex Cu(II)-3,5-di-*tert*-butylcatecholate-TMGdmap (**[3,5-DTB-CAT3]**) was synthesized specifically and analyzed via EPR spectroscopy. **[3,5-DTB-CAT3]** was formed according to a literature-known two-step protocol: A suspension of activated copper(0) and 3,5-di-*tert*-butyl-*ortho*-benzoquinone was stirred overnight. After addition of TMGdmap and stirring a second time overnight the reaction mixure was filtered. Finally, the solution was covered with a pentane layer resulting in small black crystals after two days (Scheme 3.15).[182] Crystals of **[3,5-DTB-CAT3]** (Figure 3.12) were analyzed via single-crystal X-ray diffraction (SC-XRD) and EPR spectroscopy.

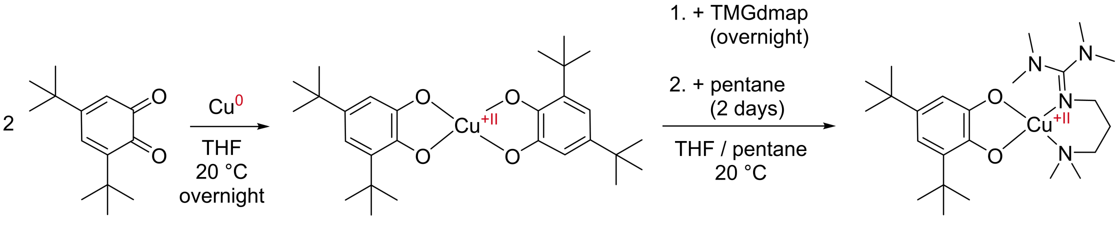

[3,5-DTB-CAT3]

Scheme 3.15: Formation of the catecholate species Cu(II)-3,5-di-*tert*-butylcatecholate-TMGdmap (**[3,5-DTB-CAT3]**) after Haase[182] starting from activated copper(0) and 3,5-di-*tert*-butyl-*ortho*-benzoquinone. Addition of TMGdmap and a pentane layer results in black crystals of **[3,5-DTB-CAT3]** suitable for single-crystal X-ray diffraction (SC-XRD).

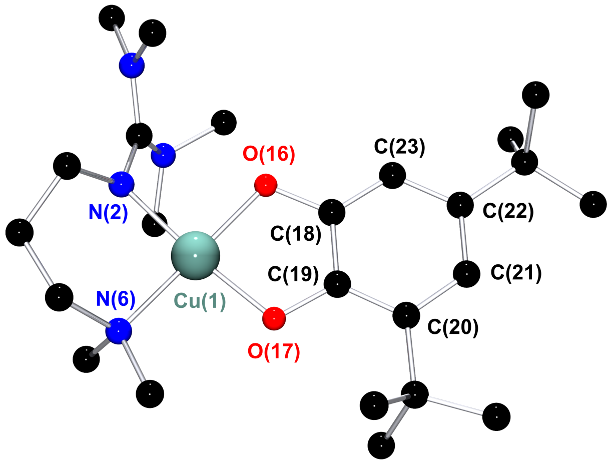

Figure 3.12: Molecular structure of TMGdmap stabilized copper(II) catecholate complex **[3,5-DTB-CAT3]** ([Cu(3,5-di-*tert*-butylcatecholate)(TMGdmap)]) in the solid state. H atoms are omitted for clarity.

[3,5-DTB-CAT3] crystallizes monoclinic in the space group $P2_1/n$. The copper center is fourfold-coordinated by two oxygen atoms from 3,5-di-*tert*-butyl-catecholate and two nitrogen atoms from TMGdmap (Figure 3.12).

To determine the coordination geometry of the metal center, the four-coordinate geometry index τ_4 was calculated. τ_4 is given as the substraction of the two larges bond angles at the metal center, α and β, from 360° divided by 141° (Equation 3.4). The geometry index ranges from 0 for an ideal square-planar coordination until 1 for ideal tetrahedral geometries. Intermediate structures or distorted geometry are resulting τ_4 values in between 0 and 1.[183]

$$\tau_4 = \frac{360^\circ - (\alpha + \beta)}{141^\circ} \tag{3.4}$$

With the two large bond angles of **[3,5-DTB-CAT3]** beeing $\alpha = 174.85^\circ$ and $\beta = 175.47^\circ$ (Table 3.13), τ_4 was calculated as 0.069 (Equation 3.5). Consequently, **[3,5-DTB-CAT3]** displays a nearly ideal square-planar geometry in agreement with the literature-known complex of Cu(II)-3,5-di-*tert*-butylcatecholate-TMGdmap (**K10**; $\tau_4 = 0.257$).

$$\tau_4 = \frac{360^\circ - (174.85^\circ + 175.47^\circ)}{141^\circ} \approx 0.069 \tag{3.5}$$

τ_4 in **[3,5-DTB-CAT3]** is slightly decreased compared to the literature value **K10** due to the larger bond angles at the metal center (O(17)-Cu(1)-N(2) and O(16)-Cu(1)-N(6); Lit.: 156.47° and 167.29°). Further bond angles at the copper center vary by two or three degree except for the O-Cu-O angle (86.66°, Lit.: 86.09°). All bond lengths are in accordance to the literature complex **K10** only varying in the second decimal place (Table 3.13).[182] Thus, Cu-O (1.8990 - 1.916 Å), Cu-N (1.979 - 2.060 Å) and C-O (1.340 - 1.347) bond lengths of **[3,5-DTB-CAT3]** and **K10** are within the range of literature values of other catecholate complexes (Cu-O: 1.870 - 1.964 Å, Cu-N: 1.966 - 2.283 Å and C-O: 1.388 - 1.364 Å; Table 3.13).[184–188]

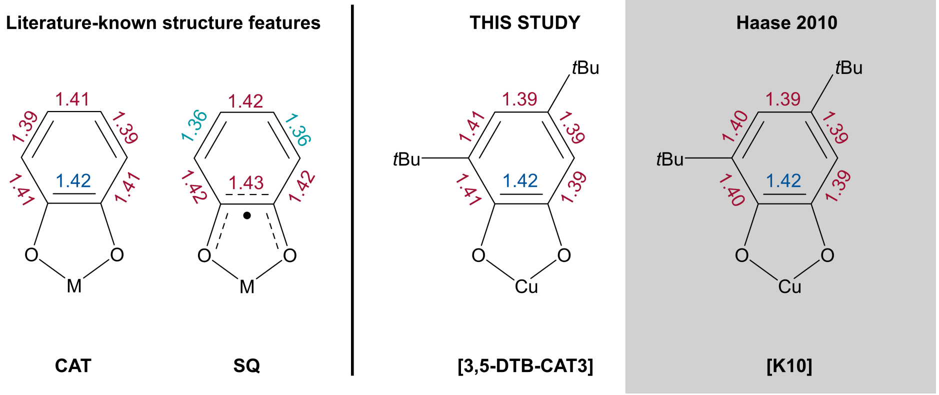

Figure 3.13: Bond lengths within the catecholate ring of **[3,5-DTB-CAT3]** and complex **[K10]** synthesized by Haase[182] compared to literature-known structure features of catecholate (**CAT**) and semiquinone (**SQ**) complexes.[174]

All C atoms within the catecholate C-ring of [**3,5-DTB-CAT3**] and **K10** have similar bond lengths (1.39 Å - 1.40 Å) with exception of the ones connected to the O atoms (C(18)-C(19): 1.42 Å; Table 3.13). This finding further underlines the presence of the catecholate species [**CAT3**] instead of the isoelectronic semiquinone isomer [**SQ3**]. Catecholate species incorporate three double bounds delocalized over the whole C-ring displaying nearly similar C-C bond lengths (1.39 Å - 1.41 Å) with one being slightly elongated (1.42 Å). In contrast, a semiquinone species containing a delocalized radical and two fixed double bonds would consist of two short C-C bonds (double bonds: 1.36 Å) and four longer C-C bonds (single bonds: 1.42 Å - 1.43 Å) (Figure 3.13).[174]

Table 3.13: Selected crystallographic data of Cu(II)-3,5-di-*tert*-butylcatecholate-TMGdamp complex [**3,5-DTB-CAT3**] and conformer [**K10**] synthesized by Haase[182] compared to literature-known data from other catecholate complexes.[184–188]

	THIS STUDY	**Haase 2010**	
	[Cu(3,5-DTBC)(TMGdmap)] **[3,5-DTB-CAT3]**	[Cu(3,5-DTBC)(TMGdmap)] **[K10]**	literature-known catecholate complexes
bond lengths [Å]			
Cu(1) – O(17)	1.8990(17)	1.915(1)	1.870 – 1.964
Cu(1) – O(16)	1.9013(17)	1.916(1)	
Cu(1) – N(2)	1.985(2)	1.979(1)	1.966 – 2.283
Cu(1) – N(6)	2.050(2)	2.060(1)	
O(16) – C(18)	1.340(3)	1.341(2)	1.388 – 1.364
O(17) – C(19)	1.347(3)	1.344(2)	
C(18) – C(19)	1.419(3)	1.424(2)	
C(19) – C(20)	1.407(3)	1.400(2)	
C(20) – C(21)	1.412(3)	1.395(2)	
C(21) – C(22)	1.394(3)	1.398(2)	
C(22) – C(23)	1.391(3)	1.393(2)	
C(23) – C(18)	1.386(3)	1.391(2)	
bond angles [°]			
N(2) – Cu(1) – N(6)	92.35(8)	94.61(6)	
O(17) – Cu(1) – O(16)	86.66(7)	86.09(5)	84.8 – 88.7
O(17) – Cu(1) – N(2)	174.85(8)	156.47(5)	
O(16) – Cu(1) – N(2)	88.19(8)	93.48(5)	
O(17) – Cu(1) – N(6)	92.80(8)	90.37(5)	
O(16) – Cu(1) – N(6)	175.47(8)	167.29(5)	
strucutural parameter			
τ_4	0.069	0.257	
space group	$P2_1/n$	$P2_1/n$	
Z	4	4	

The presence of **[CAT2]** during the hydroxylation and subsequent oxidation of sodium phenolates by oxido complex **[O3]**$(OTf)_2$ was proven by EPR spectroscopy displaying axial spectra (Figure 3.11). Protons should be absent within the reaction mixture preventing no formation of further catecholate complexes like **[3,5-DTB-CAT3]**. To verify the absence of **[3,5-DTB-CAT3]**, EPR spectra of the crystallized species as well as the complex diluted in THF were recorded. EPR measurement and analysis of the resulting spectra was done by Regina Schmidt during her PhD thesis.[170]

EPR analysis of solid and diluted **[3,5-DTB-CAT3]** reveal an axial spectra with comparable curve shape verifying an similar coordination geometry. Consequently, the catecholate species **[3,5-DTB-CAT3]** isolated in the solid state is also present in solution. Comparison of the EPR spectra from **[3,5-DTB-CAT3]** with the hydroxylation and subsequent oxidation reaction of sodium phenolates with **[O3]**$(OTf)_2$ demonstrates different curve shapes with no correlation (Figure 3.14). As a result, the absence of **[3,5-DTB-CAT3]** during the monophenolase cycle was proven.

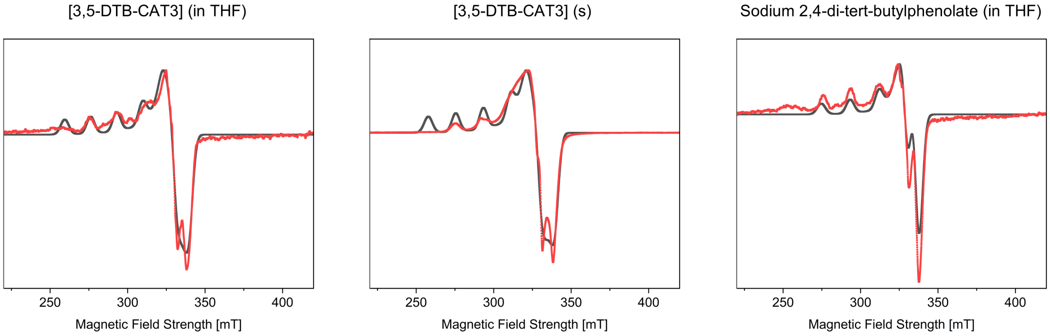

Figure 3.14: EPR spectra (black) and simulation (red) of **[3,5-DTB-CAT3]** diluted in THF (left) and in the solid state (middle) compared to the EPR spectrum of 2,4-di*tert*-butylphenolate (2 eq.) converted by bis(μ-oxido) species **[O3]**$(OTf)_2$ (c = 5 mM) measured as frozen solution (77 K). Simulated spectra were obtained using the Matlab toolbox Easyspin.[181]

3.3.4 Summary

Until today, the pathway of the monophenolase cycle of tyrosinase is intensively discussed. Especially, which of the two possible intermediate species **[CAT1]** and **[CAT2]** is formed during the catalytic conversion of the phenolic substrate is still unclear. To gain new information about the catalytic pathway, the hydroxylation and subsequent oxidation of sodium phenolates by the bis(μ-oxido) species **[O3]**$(OTf)_2$ was studied via EPR spectroscopy. Additionally, a possible side product, **[3,5-DTB-CAT3]**, resulting from protonation of the catalytic intermediate, was isolated and analyzed via SC-XRD and EPR spectroscopy. EPR spectra revealed the presence of an asymmetric **[CAT2]** species in agreement with earlier findings of several working groups[176–179] and the monophenolase cycle recently published by Solomon and coworkers.[43] The absence of possible side product **[3,5-DTB-CAT3]** was proven by comparison of EPR spectra.

4 Cu_2O_2 Species for Mass Transfer Investigations

Industrial processes are designed to cost-efficiently maximize yield and selectivity of the desired product. Reaction steps and synthesis pathways are optimized to minimize the amount of reactants used and side products as well as chemical waste formed.[133] In the case of oxidation processes, inexpensive gaseous oxidants like molecular oxygen or air combined with metal catalysts, creating an accessible oxidizing agent, are already implemented.[1–5] Gaseous oxidants are mostly used in combination with a liquid mass flow in which the reaction takes place. Further reactants can be implemented by dissolving them in the reaction mixture. Ideally, the reaction is only limited by the reaction kinetics and not by low concentration of oxidants due to inhibited mass transfer in the liquid phase. Consequently, the mass transfer of the oxidant from the gas into the liquid phase, where the reaction takes place, is a significantly influencing factor on the chemical reaction's efficiency. The mass transfer can be controlled by changing the gas bubble volume, the flow velocity of the gaseous and the liquid mass flow or enhanced mixing of gas and liquid phase.[5,132] Consequently, understanding the complex interplay between mass transfer, kinetics and hydrodynamics of a chemical reaction is crucial to accomplish full formation of a desired reaction product.

In industrial plants, continuously operated flow reactors or semi-batch reactors with the gaseous reactant bubbled through the liquid phase are most common.[5,132] If large amounts of bubbles incorporating the gaseous oxidant, a so-called bubble swarm, are reacting with further reactants dissolved in the liquid phase, several factors are competing with each other: the mass transfer of the gaseous reactant into the liquid phase, the kinetics of the chemical reaction taking place and the hydrodynamics of the mixing phases.[133,135,136] This complex interplay of factors can be simplified by studying single rising bubbles instead of a whole bubble swarm.Additionally, a reaction setup confined in one or two dimensions can be used.[133–135] Therefore, a tunable and flexible chemical reaction system is needed covering a broad spectrum of analytical methods. Ideally, reaction kinetics, reactants conditions (solvent, temperature, concentrations) as well as characteristic spectroscopic features can be tailored to the reaction setup used.

Depending on the reaction setup, the amount of solvent and reactants needed to perform mass transfer experiments varies massively. Setups like the Taylor-flow (TF) with small dimensions in the millimeter-scale contain a volume of $2 - 23\,\mathrm{ml}$,[133,135] while large bubble columns near to industrial conditions can require $1.5 - 44\,\mathrm{l}$.[141,189–191] To work cost-efficient and minimize synthesis efforts, inexpensive purchasable reactants and one-step synthesis pathways are preferred.

Cu_2O_2 species like bis(µ-oxido) complexes (**O**) and side-on µ-η^2:η^2-peroxido dicopper(II) ($^{\mathbf{S}}\mathbf{P}$) are formed by the conversion of molecular oxygen with a diluted copper(I) precursor complex. They show an intensive color change during their formation coming along with characteristic UV/Vis absorption bands.[55,85–88,90,102] Additionally, some Cu_2O_2 species are able to convert phenolic substrates to *ortho*-quinones by hydroxylation and subsequent oxidation.[55,87,90,102] Consequently, they display an ideal tool for gas liquid mass transfer investigations mediating consecutive reactions (formation + decay) as well as competitive consecutive reactions (formation + substrate conversion) between a gaseous reactant (molecular oxygen) and a liquid reaction mixture.

A Cu_2O_2 species already used in different mass transfer investigations is the oxido complex $[Cu_2O_2(TMG_2p)_2]I_2$ stabilized by the bisguanidine ligand 1,3-Bis(N, N, N', N'-tetramethylguanidino)propane (TMG_2p). The consecutive reaction of the oxido complex formation converting the copper(I) precursor species [Cu(bmtgp)I] and subsequent decay in the related hydroxido and alkoxido species was investigated in small scale setups like the SuperFocusMixer (SFM; $V = \sim 100\,\mathrm{ml}$) and the Hele-Shaw cell (HSC; $V = 80\,\mathrm{ml}$).[137] During the consecutive reaction of oxido complex formation and subsequent decay, the reaction mixture undergoes a strong color change from colorless over orange to green. Additionally, the oxido species displays two strong UV/Vis absorption signals at 300 and 395 nm (Table 4.1).[137,192]

Two other Cu_2O_2 species meeting the conditions of inexpensive reactants and a one-step synthesis pathway are the oxido complex $[Cu_2O_2(TMG_2tol)_2](CF_3SO_3)_2$ ($[\mathbf{O1}](OTf)_2$) based on the bisguanidine ligand 2-(2((bis(dimethylamino)methylene)amino)benzyl)-1,1,3,3-tetramethylguanidine (TMG_2tol, **L1**) and the peroxido complex $[Cu_2O_2(DBED)_2](CF_3SO_3)_2$ ($[^{\mathbf{S}}\mathbf{P4}](OTf)_2$) stabilized by the diamino ligand N,N'-di-*tert*- butylethylenediamine (DBED, **L4**).

The bisguanidine ligand TMG_2tol is formed in a simple one-step synthesis converting 2-aminobenzylamine, chloro-N,N,N',N'-tetramethylformamidinium chloride and the auxiliary base triethylamine. The related oxido complex $[\mathbf{O1}](OTf)_2$ is stable at temperatures below −50 °C. At higher temperatures, the **O** species decays into a stable hydroxido-complex. During formation and decay of $[\mathbf{O1}](OTf)_2$ the reaction mixture undergoes a color change from colorless over orange to green analogous to the **O** species based on TMG_2p. Thereby, $[\mathbf{O1}](OTf)_2$ displays two UV/Vis absorption bands at 290 and 395 nm. Due to the large aromatic backbone in TMG_2tol, the copper(I) precursor complex [**Pr1**](OTf) ($[Cu(TMG_2tol)(CH_3CN)](CF_3SO_3)$) is fluorescent. The broad absorption band formed at 475 nm ($\lambda_{\mathrm{excitation}} = 370\,\mathrm{nm}$) in the fluorescence spectrum is quenched during the formation of $[\mathbf{O1}](OTf)_2$ by injecting [**Pr1**](OTf) into an oxygen-saturated, aprotic solvent (tetrahydrofuran or acetonitrile).[85,192] In addition, $[\mathbf{O1}](OTf)_2$ catalyzes the conversion of phenolic substrates like naphthols, quinolinols and indolols to *ortho*-quinones as discussed earlier in Section 3.1.3 (Table 4.1).

The diamino ligand DBED is inexpensive and commercially available. The related peroxido complex [$^{\mathrm{S}}$**P4**](OTf)$_2$ is formed by injecting the diluted, colorless copper(I) precursor complex [**Pr4**]OTf ([Cu(DMEG)(CH$_3$CN)](CF$_2$SO$_3$)) into oxygen-saturated aprotic solvent (tetrahydrofuran, dichloromethane or acetone). [$^{\mathrm{S}}$**P4**](OTf)$_2$ displays a violet colored solution and is stable at temperatures below −10 °C. At above −10 °C, the peroxido species decays into a hydroxido complex displaying a blue colored reaction mixture. In the UV/Vis spectrum of [$^{\mathrm{S}}$**P4**](OTf)$_2$ a strong absorption band at 350 nm can be monitored. Apart from this, [$^{\mathrm{S}}$**P4**](OTf)$_2$ mediates the hydroxylation and subsequent oxidation of phenols like *para*-methoxyphenol to the related *ortho*-quinone (Table 4.1).[55]

Table 4.1: Properties and spectroscopic features of Cu$_2$O$_2$ species suitable for mass transfer investigations.[55,85,137,192]

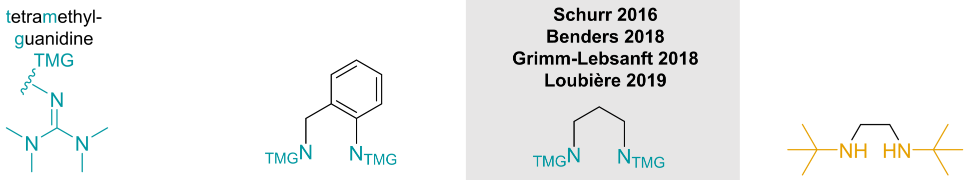

Schurr 2016
Benders 2018
Grimm-Lebsanft 2018
Loubière 2019

ligand	TMG$_2$tol	TMG$_2$p	DBED
Cu$_2$O$_2$ species	[Cu$_2$O$_2$(TMG$_2$tol)$_2$](OTf)$_2$ oxido complex (**O**)	[Cu$_2$O$_2$(TMG$_2$p)$_2$]I$_2$ oxido complex (**O**)	[Cu$_2$O$_2$(DBED)$_2$](OTf)$_2$ peroxido complex ($^{\mathrm{S}}$**P**)
$\lambda_{UV/Vis}$ [nm]	290, 395	300, 395	350
$\lambda_{fluorescence}$ ($\lambda_{excitation}$) [nm]	475 (370)	-----	-----
visible color change	colorless → orange → green	colorless → orange → green	colorless → violet → blue
$k_{formation}$ (temperature) [s^{-1}]	1.30 ± 0.02 (- 50 °C)	30 ± 4 (20 °C)	45 ± 1 (- 40 °C)
k_{decay} (temperature) [s^{-1}]	1.8 ± 0.3 (20 °C)	1.27 ± 0.03 (20 °C)	0.609 ± 0.06 (20 °C)
catalytic activity (phenols → *ortho*-quinones)	✓	✗	✓

Taking a look at the reaction kinetics, rate constants of formation and decay of the Cu$_2$O$_2$ species are influenced by the stabilizing ligand species. The oxido complex stabilized by the bisguanidine ligand TMG$_2$p ([Cu$_2$O$_2$(TMG$_2$p)]I$_2$), already used in various reactive mass transfer studies, incorporates an alkyl backbone between the coordinating guanidine N-donors. The **O** species is formed with a rate constant of $k_{\text{formation}} = 30\,\mathrm{s}^{-1}$ at room temperature (20 °C) and subsequently decays with $k_{\text{decay}} = 30\,\mathrm{s}^{-1}$ into two stable complex species (hydroxido and alkoxido).[137,192] Changing the stabilizing ligand system to a bisguanidine species with aromatic backbone, the related oxido complex [**O1**](OTf)$_2$ is unstable at room temperature. [**O1**](OTf)$_2$ is only stable at temperatures below −50 °C with a formation rate of $k_{\text{formation}} = 1.30\,\mathrm{s}^{-1}$; 23 times slower than the one of [Cu$_2$O$_2$(TMG$_2$p)]I$_2$. The rate constant of the decay of the oxido species at 20 °C, in contrast, is within the same order of magnitude ($k_{\text{decay}} = 1.8\,\mathrm{s}^{-1}$)[85,192] as the one of $[Cu_2O_2(TMG_2p)]I_2$. On the contrary, formation and decay constant of the peroxido complex $[^{\mathbf{S}}\mathbf{P4}](OTf)_2$ stabilized by diamino ligand DBED are both within the same magnitude compare to the one of $[Cu_2O_2(TMG_2p)]I_2$. Analogous to $[\mathbf{O1}](OTf)_2$, $[^{\mathbf{S}}\mathbf{P4}](OTf)_2$ is unstable at room temperature as well. The peroxido complex can be formed at temperatures below $-10\,°C$. Thereby, the rate constant of complex formation is 1.5 times faster ($k_{\text{formation}} = 45\,s^{-1}$) than the one of $[Cu_2O_2(TMG_2p)]I_2$, while the decay reaction is slowed down compared to the oxido systems ($k_{\text{decay}} = 0.609\,s^{-1}$).[55]

The ability of Cu_2O_2 species to mediate consecutive reactions as well as competitive consecutive reactions accompanied by a strong color change is a major advantage compared to colorimetric or fluorescent dyes regarding mass transfer investigations. Mediating a chemical reaction, further influencing factors on the mass transfer like reaction kinetics or an enhancement caused by the conversion of the gaseous reactant can be studied. Colorimetric or fluorescent dyes in contrast, only visualize the on-going mass transfer. They are unsuitable for investigating reactive mass transfer as no chemical reaction is taking place.

Reaction kinetics as well as spectroscopic features of reactions catalyzed by Cu_2O_2 species can be customized by the choice of ligand, counter ion or reaction conditions (temperature, substrate used, concentration). Due to the broad variety of reaction setups used for mass transfer investigations, the demands on reaction time and reaction speed vary massively. In setups with small dimensions like the Taylor-flow or the Hele-Shaw cell, the gas bubble has only a short length of 8 to 40 cm to rise.[131,133,135] Consequently, fast reactions taking place within the region of interest of the reaction setup are desired. In contrast, large bubble columns with a length of several meters are in need of slower reaction kinetics to monitor the on-going processes over the whole residence time of the bubble.[141,189]

4.1 Hele-Shaw cell (HSC) - Single Rising Bubbles in a Confined Small-Sized Setup

In earlier studies, formation and decay of the Cu_2O_2 species $[Cu_2O_2(TMG_2p)_2]I_2$ were used to investigate the mass transfer around a single molecular oxygen bubble rising in a thin-gap cell. Reactions were performed in a so-called Hele-Shaw cell (HSC). The strong color change during formation and decay was utilized to monitor the on-going reaction with a high-speed gray-level camera equipped with a red band-pass filter. After ad-hoc calibration, gap- and time-average molecular oxygen concentration fields were received. Based on these data, correlations found in HSC mass transfer studies using dye and water were proven.[193] The scaling law describes the correlation of the Reynolds number (Re) with the bubble's diameter (d), the gap width of the HSC (h) and the Archimedes number (Ar) (Equation 4.1). Thereby, Re describes the type of fluid flow present (laminar or turbulent) depending on the bubble's rising velocity. Ar gives the relation between the bubble's buoyancy force and the frictional force resulting from the liquid phase's viscosity.

In fluid mechanics, dimensionless numbers are used to describe the physical situation independently of the experimental scale. To transfer observations on a small scale such as the HSC to an application-relevant or industrial scale, the fluid mechanical situation has to be described by several dimensionless numbers such as Re or Ar. The mechanical description is often expressed in so-called scaling laws, in which all dimensionless numbers appear in terms of powers, whereby the exponent is often an empirical value.

A second scaling law proposed in HSC studies with water and dye (Equation 4.2) connecting the Sherwood number (Sh) with the Péclet number (Pe) could not be confirmed within the study using the Cu_2O_2 species $[Cu_2O_2(TMG_2p)_2]I_2$. Therein, Sh correlates the total mass transfer to the mass transfer caused by diffusion only, while Pe gives the ratio of advective transport rate (rising velocity dominated) to diffusion transport rate. Pe can also be described as the product of Re and the Schmidt number (Sc)(Equation 4.3), whereby Sc is the ratio between the kinematic viscosity (ν) and the diffusion coefficient of the gaseous reactant (D_{O_2}), in this case molecular oxygen (Equation 4.4).[131]

$$Re = 0.75 \cdot \left(\frac{h}{d}\right)^{\frac{1}{6}} \cdot Ar \tag{4.1}$$

$$Sh = 1.126 \cdot Pe^{0.5} \tag{4.2}$$

$$Pe = Sc \cdot Re \tag{4.3}$$

$$Sc = \frac{\nu}{D_{O_2}} \tag{4.4}$$

$$E = \frac{1}{k_L} \cdot \sqrt{\frac{2}{n+1} \cdot k \cdot D \cdot c^{\,n-1}} \tag{4.5}$$

Kinematic viscosity as well as diffusion coefficient are depending on the solvent used. The kinematic viscosity of the copper complex solutions based on acetonitrile is significantly smaller ($0.43 \cdot 10^{-6}\ \mathrm{m^2\,s^{-1}}$) as those of water ($1 \cdot 10^{-6}\ \mathrm{m^2\,s^{-1}}$).[131] Thus, the proposed scaling law connecting Sh to Pe (Equation 4.2) is dependent on the physico-chemical properties of the liquid phase. Consequently, scaling laws containing Pe are limited to a specific solvent and chemical system.

Further influencing factors, besides the physico-chemical properties of the chemical system, are the reaction kinetics (reaction rate constant k and reaction order n) as well as the properties and functions of the reactants. In the absence of a chemical reaction, mass transfer is only limited by the diffusion coefficient D of the gaseous molecules into the liquid phase. If a chemical reaction is taking place, mass transfer can also be limited by the transfer coefficient within the liquid phase k_L or the reaction rate constant k in the case

k is significantly smaller than D ($k \ll D$). If a reactant shows surface activating abilities, the solvents surface tension changes directly influencing k_L. A mathematical description of these influencing factors is the enhancement factor E (**??**).[134,135,139]

A distinction between all influencing factors or a concrete designation of a major influence is impossible due to lack of further data. Ideally, the proposed scaling laws should provide a correlation between controllable factors like bubble size, rising velocity or gap width. Additionally, mass transfer between the gaseous phase and the liquid phase should be independent from the reaction system or experimental setup used. The findings could then be transferred to any other reaction setup of various size and still gain the same mass transfer results. In the case of the HSC, most results are based on experiments performed with water and dye.[193,194] Reactive mass transfer studies, investigating the influencing factors to an on-going chemical reaction, were only performed once using a chemical reaction system based on the Cu_2O_2 species $[Cu_2O_2(TMG_2p)_2]I_2$. Thereby, only one of the scaling laws established in earlier experiments could be proven. To broaden the spectrum of reactive mass transfer investigations and optimize the proposed scaling laws, further experiments with similar chemical reaction systems based on Cu_2O_2 species are necessary.

4.1.1 HSC Studies with Oxido Complex $[Cu_2O_2(TMG_2tol)_2](CF_3SO_3)_2$ ([O1](OTf)$_2$) and Peroxido Complex $[Cu_2O_2(DBED)_2](CF_3SO_3)_2$ ([^{S}P4](OTf)$_2$)

Parts of this chapter are already published in:

L. Laurini, A. Béteille, G. Fink, S. Herres-Pawlis, K. Loubière, *Chem. Eng. Technol.* **2023**, *46 (8)*, 1664-1672.[92]

Reactive mass transfer investigations in the Hele-Shaw cell performed with the Cu_2O_2 species $[Cu_2O_2(TMG_2p)_2]I_2$ based on the bisguanidine ligand TMG_2p highlighted the strong influence of physico-chemical properties. To improve the proposed scaling laws, the spectrum of tested Cu_2O_2 species will be broadened in this study. Therefore, the oxido complex [**O1**](OTf)$_2$ ($[Cu_2O_2(TMG_2tol)_2](CF_3SO_3)_2$) based on the bisguanidine ligand TMG_2tol and the peroxido complex [^{S}**P4**](OTf)$_2$ ($[Cu_2O_2(DBED)_2](CF_3SO_3)_2$) stabilized by the diamino ligand DBED will be used. Both systems display ideal reaction conditions for reactive mass transfer investigations: A strong color change during formation and decay, cost-efficient availability on a large scale and a previously determined reaction rate constant for the final reaction step (decay of the Cu_2O_2 species). Additionally, their rate constants of formation and decay differ from those of $[Cu_2O_2(TMG_2p)_2]I_2$ investigated in the previous study (Table 4.1). A variation of reaction kinetics is crucial to find new correlations between parameters like bubble size, shape or rising velocity and the mass transfer from the gaseous into the liquid phase independent from the chemical system used.

In this study, HSC experiments were performed in the same setup used for studies with $[Cu_2O_2(TMG_2p)_2]I_2$ in 2019.[131] Single bubbles of molecular oxygen (d > 1 mm) are injected through a quartz glass capillary into a vertically-oriented thin-gap cell filled with copper(I) precursor complex diluted in acetonitrile at rest. The dimensions of the thin-gap cell are 400 x 200 mm with a gap width of 1 mm (Figure 4.1, front view). Due to the structure of the thin-gap cell, the gas bubble's diameter is larger than the gap width of the thin- gap cell. Consequently, bubble movements are confined in one dimension. As a result, the bubble can only rise inside the cell with oscillating movements from left to right. To avoid the falsification of data by air contact, the experiments are performed under nitrogen atmosphere. The thin- gap cell is illuminated by a collimated white light-emitting-diode (LED) back light panel from behind (Figure 4.1, side view). The rising gas bubble is monitored by a high-speed gray-level (GV) camera within a region-of-interest (ROI) window. The ROI window is horizontally-centered on the cell front ensuring a stationary bubble motion unaffected by transition effects resulting from the bubble injection into the liquid phase at the bottom of the cell or crossover from the liquid phase into the gas phase at the top of the cell (Figure 4.1, front view).

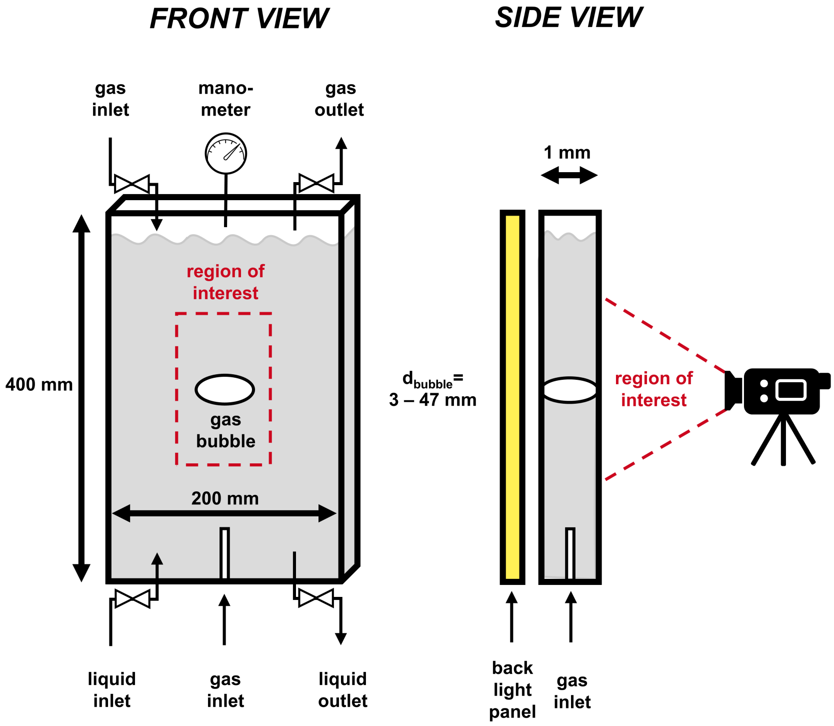

Figure 4.1: Technical drawing of the Hele-Shaw cell (HSC) used for mass transfer experiments.

The mass transfer of molecular oxygen from the gas bubble into the liquid phase initiates the consecutive reaction of formation and decay of the Cu_2O_2 species. Consequently, molecular oxygen is consumed during the formation of the final reaction product, the hydroxido complex (Figure 4.3). If the reaction kinetics are much faster than the diffusion of molecular oxygen into the liquid phase, the concentration of the green hydroxido complex is an indirect measure for the amount of molecular oxygen transferred into the liquid phase. As a result, molecular oxygen concentration fields can be calculated from the concentration of hydroxido complex in the liquid phase. To assign the recorded GV images of the rising molecular oxygen bubble to the related hydroxido complex concentrations, ad-hoc calibration had to be performed. Therefore, a concentration series varying from 0 $\mathrm{mol\,l^{-1}}$ to the maximal possible concentration of the final reaction product (hydroxido complex) was prepared. Subsequently, GV images of the reaction mixtures with known concentration of reactants are recorded before and after saturation with molecular oxygen. The related molecular oxygen concentration can be calculated using the stoichiometric factors of the reaction and the concentration of reactants used. Thereof, each GV can be assigned to the related concentration of molecular oxygen. Finally, the recorded GV images of mass transfer experiments can be compared to the ones recorded during calibration and the related concentration of molecular oxygen can be assigned. As a huge amount of images is recorded during each mass transfer experiment, a MATLAB© algorithm developed by Loubière and coworkers in the previous study,[131] was implemented to simplify and accelerate image processing. In addition to the oxygen concentration profiles, bubble parameters like the in-plane equivalent diameter d and rising velocity are determined using the MATLAB© algorithm.

The accuracy of the calibration has a massive impact on the O_2 concentration levels calculated from the GV images. To clearly distinct small as well as large concentration differences during calibration, a strong color change with high contrast between reactant and final product is essential.

4.1.1.1 Color Intensity Tests with [O1](OTf)$_2$ and [^{S}P4](OTf)$_2$

To check the color intensity of oxido complex [**O1**](OTf)$_2$ and peroxido complex [$^{\mathbf{S}}$**P3**](OTf)$_2$ the final decay product of both Cu_2O_2 species was formed in acetonitrile at room temperature converting the related copper(I) precursor complexes $[Cu(TMG_2tol)(CH_3CN)](CF_3SO_3)$ ([**Pr1**]OTf)) and $[Cu(DBED)(CH_3CN)](CF_3SO_3)$ ([**Pr4**]OTf)) with molecular oxygen (Figure 4.2). The maximum availability of molecular oxygen in the liquid reaction mixture is limited by the solubility of the gaseous reactant in the liquid phase (solvent). The solubility of molecular oxygen in acetonitrile at 20 °C is 8.1 $\mathrm{mmol\,l^{-1}}$.[195] During the reaction of one oxygen molecule with two copper(I) precursor complex molecules one Cu_2O_2 complex species is formed (Figure 4.3). Thus, the maximum concentration of copper(I) precursor complex converted by the molecular oxygen available at 20 °C in acetonitrile is about 16 $\mathrm{mmol\,l^{-1}}$. Consequently, HSC mass transfer studies as well as color intensity tests using Cu_2O_2 complexes were performed with a copper(I) precursor complex concentration of 16 $\mathrm{mmol\,l^{-1}}$ in the liquid phase.

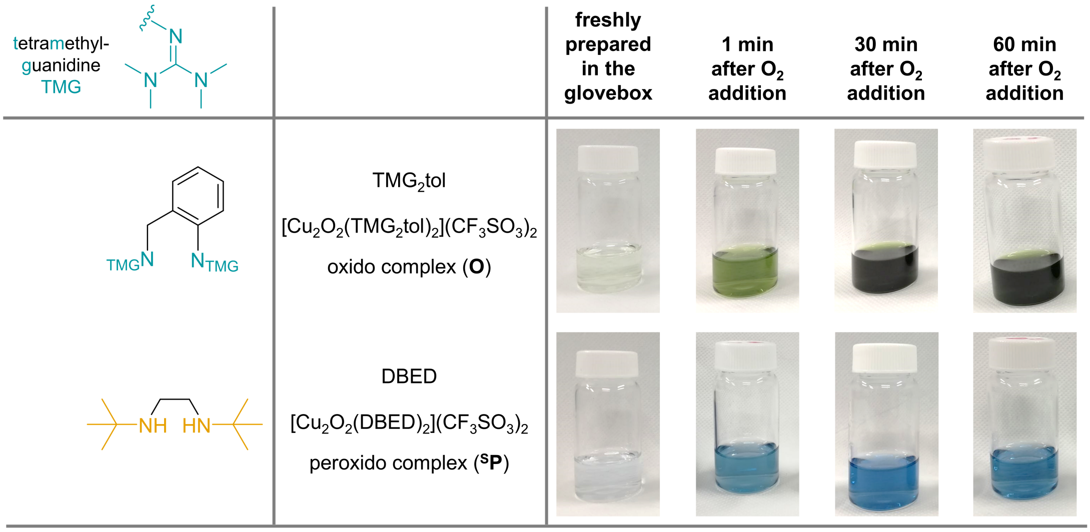

Figure 4.2: Images of copper(I) precursor solution of [**O1**](OTf)$_2$ ([Cu$_2$O$_2$(TMG$_2$tol)$_2$](CF$_3$SO$_3$)$_2$) and [$^{\mathbf{S}}$**P4**](OTf)$_2$ ([Cu$_2$O$_2$(DBED)$_2$](CF$_3$SO$_3$)$_2$) before and after molecular oxygen was bubbled through the reaction mixture (c([**Pr**]OTf) = ^{6} mmol l^{-1}).

[**Pr1**]OTf as well as [**Pr4**]OTf displayed a color change within seconds after the addition of molecular oxygen. For both reaction systems, the color of the related intermediate, the oxido complex ([**O1**](OTf)$_2$; orange) / peroxido complex ([$^{\mathbf{S}}$**P4**](OTf)$_2$; violet), could not be monitored. Instead, the solutions directly turned green ([**Pr1**]OTf) or blue ([**Pr4**]OTf) indicating a decay into the related stable hydroxido complex (Figure 4.3). The direct decay of formed Cu$_2$O$_2$ species was to be expected, as [**O1**](OTf)$_2$ and [$^{\mathbf{S}}$**P4**](OTf)$_2$ are only stable at low temperatures ($< -40\,°C$; Table 4.1). The hydroxido complex stabilized by the bisguanidine ligand TMG$_2$tol showed a dark green color of high intensity. During a first test run performed in the HSC setup, [**Pr1**]OTf was successfully converted to the related hydroxido complex. The on-going reaction of hydroxido complex formation could be monitored as an intensively green colored region around the molecular oxygen bubble rising within the [**Pr1**]OTf complex solution.

In contrast, the solution of the hydroxido complex containing the diamino ligand DBED was colored pale blue with a lower color intensity. A first test run performed within the HSC setup did not show a colored solution around or behind the oxygen bubble rinsing inside the [**Pr4**]OTf solution. However, the surface area at the top end of the liquid reaction mixture above the region of interest monitored by the high-speed camera turned bluish after a few minutes indicating hydroxido complex formation.

The decay rate of peroxido complex [$^{\mathbf{S}}$**P4**](OTf)$_2$ (k_{decay} = 0.609 s^{-1}) is three-times slower than the one of oxido complex [**O1**](OTf)$_2$ (k_{decay} = 1.8 s^{-1}). Consequently, the decay of [$^{\mathbf{S}}$**P4**](OTf)$_2$ is in need of a longer rising distance for the desired reaction step than the decay of [**O1**](OTf)$_2$. As the blue-colored hydroxido species related to [$^{\mathbf{S}}$**P4**](OTf)$_2$ is only present at the top of the HSC outside the ROI, this reaction system is not suitable to study mass transfer within the HSC setup used. Consequently, further mass transfer experiments to improve the data set of consecutive reaction based on Cu_2O_2 species were performed with the oxido complex [**O1**]$(OTf)_2$ stabilized by the bisguanidine ligand TMG_2tol.

4.1.1.2 Reactive Mass Transfer Studies with [O1]$(OTf)_2$

Reactive mass transfer studies were performed at the ENSIACET Toulouse during a co-operation project with the working group of Prof. K. Loubière. Mass transfer experiments performed with the red band pass filter as well as calibration measurements were performed by A. Béteille. Post-processing of images via MATLAB© calculating oxygen-concentration profiles and bubble parameters was done by A. Béteille. Data analysis and intepretation of MATLAB© data was done by K. Loubière.

Reactive mass transfer investigations to optimize the scaling laws proposed by Roudet and coworkers[193] were performed using the consecutive reaction of formation and decay of the oxido complex [**O1**]$(OTf)_2$ (Figure 4.3). To increase compatibility with previous studies, experiments were conducted in the Hele-Shaw cell setup used by Loubière and coworkers for reactive mass transfer investigations with the oxido complex $[Cu_2O_2(TMG_2p)_2]I_2$ in 2019. Further reaction conditions like solvent and temperature used as well as stoichiometry of the chemical reaction were identical to the study performed with $[Cu_2O_2(TMG_2p)_2]I_2$. Consequently, this study differs only in the molecular structure of the chemical system and its related reaction kinetic constants (Table 4.1).

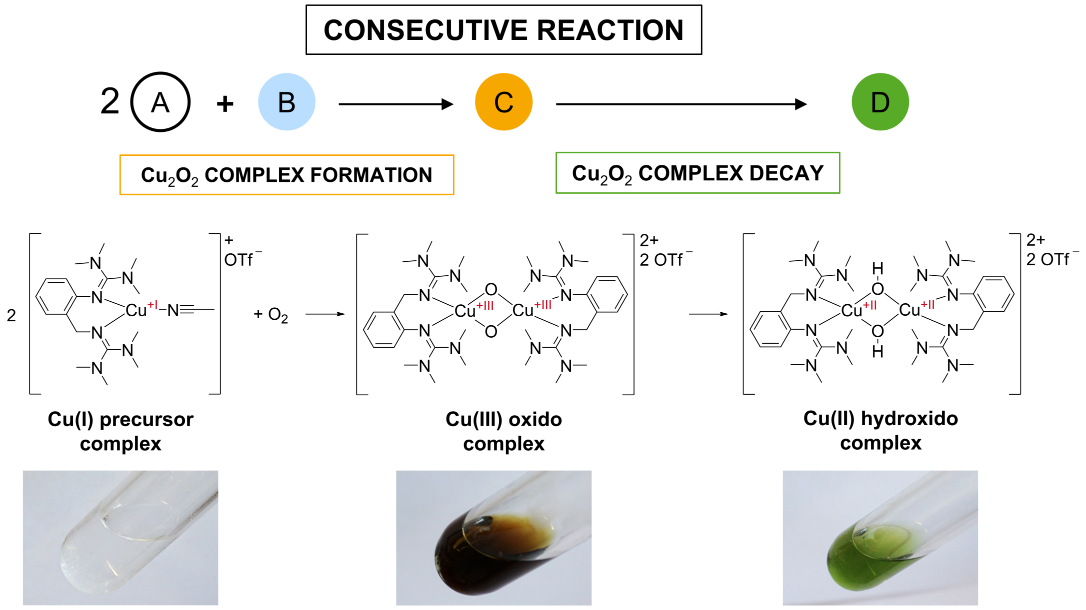

Figure 4.3: Consecutive reaction of formation and decay of oxido complex [**O1**]$(OTf)_2$ stabilized by bisguanidine ligand TMG_2tol with related colors of the formed copper complexes.

Experiments were performed by filling the HSC with copper(I) precursor complex solution (c([**Pr1**]OTf) $= 16\,\mathrm{mmol\,l^{-1}}$), being directly prepared in a glove box under nitrogen atmosphere beforehand. Subsequently, a GV background image of the reaction mixture was taken. Afterwards, a single bubble of molecular oxygen was released into the cell through the capillary at the bottom. For this purpose, the gas valve connected to an O_2 gas tank was open and closed quickly by hand. GV images (100 Hz; exposure time 0.6 ms; current 0.47 mA) of the rising gas bubble were taken within the ROI window (Figure 4.1). After the gas bubble had reached the phase boundary of the reaction mixture with the gas volume at the top of the cell, nitrogen bubbles were released into the cell through the capillary at the bottom. By bubbling nitrogen through the reaction mixture over the course of one minute, a uniformly mixed liquid phase was restored. A new experiment was started by recording another GV background image. A new molecular oxygen bubble was released into the cell afterwards. Due to the repeatedly performed formation of the green hydroxido complex, the hydroxido complex becomes more and more concentrated in the reaction mixture. Thus, the solution increases in color with the number of experiments performed. As a result, the process could only be repeated up to ten times before the color intensity between background image and formed hydroxido complex was to low to be distinguished by the GV camera.

This way, 88 isolated molecular oxygen bubbles were generated in the HSC and monitored with the high-speed GV camera. In the first step of the consecutive reaction, the colorless copper(I) precursor complex solution reacts with molecular oxygen to form the orange-colored Cu(III) oxido complex [**O1**]$(OTf)_2$. The oxido complex is unstable at ambient temperature and decays into a stable green copper(II) complex in the second reaction step (Figure 4.3). As formation and decay of the oxido complex are taking place in parallel, a direct formation of the final, green-colored reaction product, the related hydroxido complex, was expected. Nevertheless, the orange color of [**O1**]$(OTf)_2$ was visible for a short time in the vicinity of rising bubbles as well as in the near-field bubble wake (Figure 4.4).

The stability and formation rate constants of Cu_2O_2 species are determined using a so-called stopped-flow setup. Therein, the copper(I) precursor solution is injected into a temperature-controlled, oxygen-saturated solution. Subsequently, the formation of the Cu_2O_2 species is monitored via UV/Vis spectroscopy until a steady absorption is reached to calculate the reaction rate constant $k_{\text{formation}}$ afterwards.[85] The Cu_2O_2 species investigated in this study was stated unstable at ambient temperatures, as no steady formation of the oxido complex [**O1**]$(OTf)_2$ could be monitored in the stopped-flow setup. The colorless, oxygen-saturated solution directly turned green after injection of the colorless copper(I) precursor complex solution. Thus, the formed orange oxido complex immediately decayed into the green colored hydroxido complex. As formation and decay of the oxido complex are taking place in parallel, full formation of the oxido complex necessary to quantify the rate constant is impossible. Consequently, a rate constant could only be determined for the decay of the hydroxido complex.

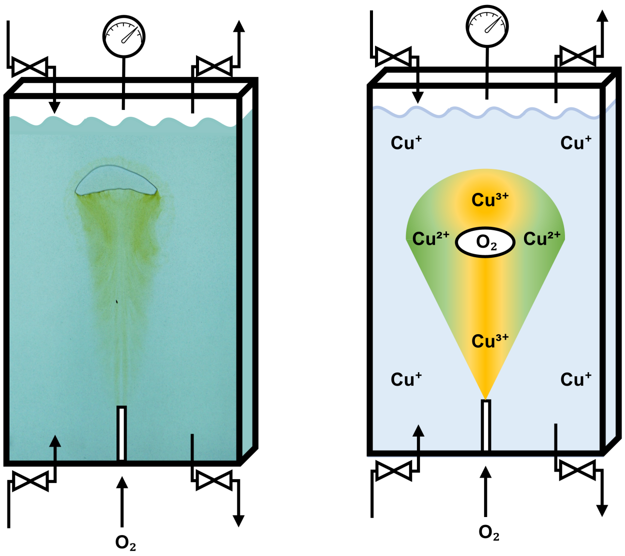

Figure 4.4: Original colored raw image of a single molecular oxygen bubble in a solution of [**Pr1**]OTf ([Cu(TMG$_2$tol)(CH$_3$CN)](CF$_3$SO$_3$)) (left). Schematic drawing of consecutive reaction taking place in the vicinity and wake of the rising molecular oxygen bubble (right).

In the HSC, the situation is different as the single bubbles of molecular oxygen are rising in an oxygen-free copper(I) complex solution. Due to the confined geometry of the HSC, vortices are formed in the region behind the bubble, which is called bubble wake. The vortices are creating turbulent flow regimes in which backmixing of oxygen-free solution with solution of high molecular oxygen concentration is taking place (Figure 4.4). Consequently, strong oxygen concentration gradients are existing in the vicinity of the bubble. These gradients locally slow down the oxygenation reaction enabling a short-time stability of the orange oxido complex. As a result, the orange color of the oxido complex and the green color of the hydroxido complex were both visible in the vicinity of the rising molecular oxygen bubble. This was not expected initially as stopped-flow measurements only monitored the green color hydroxido complex sucessfully at ambient temperatures.

The flattened bubbles are followed by contrasted regimes of oscillatory motions. In the case of small bubble diameters, the path is unsteady and oscillates horizontally. Molecular oxygen is collected by the released vortices in the bubble wake (Figure 4.5, left). With increasing bubble diameter, shape oscillation start to appear visibly by the distortion of the round bubble shape. Path oscillation is becoming more and more superposed by shape oscillation stabilizing the unsteady wake (Figure 4.5, middle). When reaching large bubble diameters, the previously oscillating wake stabilizes completely. A wide strip is formed instead and a halo can be observed in front of the bubble (Figure 4.5, right). A colored video recording of a rising single bubble can be found via a link given in Section 6.10.5 in the experimental part.

The in-plane equivalent diameter d of monitored rising single bubbles as well as their mean bubble velocity V_b were determined by A. Béteille from the GV images via the

MATLAB© algorithm.[131] Thereby, d ranges from 3 to 47 mm and V_b varies between 0.12 and 0.21 $\mathrm{m\,s^{-1}}$.

Figure 4.5: Gray-level images of single molecular oxygen bubbles (d = 3 to 47 mm) rising in a copper(I) precursor solution of [**Pr1**]OTf ([Cu(TMG$_2$tol)(CH$_3$CN)](CF$_3$SO$_3$)) recorded with a high-speed camera without red band-pass filter.

The orange oxido complex [**O1**](OTf)$_2$, briefly visible in the vicinity and near-field bubble wake, has a fast decay rate of 1.8 $\mathrm{s^{-1}}$ (determined via stopped-flow at 20 °C).[85] To assign the recorded GV images to the related concentration fields of molecular oxygen, a calibration with the formed reaction products is necessary. Therefore, an intense color change clearly distinguishable from the reaction mixture along a line in the bubble wake is essential. As the orange signal can only be captured in the vicinity of the bubble and the near-field bubble wake, this color signal is not suitable for calibration measurements. Instead, the stable decay product, the green-colored hydroxido complex, has to be used. Due to the fast decay rate, the orange oxido complex [**O1**](OTf)$_2$ is assumed to be completely decayed into the hydroxido complex in the far-field bubble wake.

The bubble's shape necessary to calculate the in-plane equivalent diameter and the mean bubble velocity, was clearly visible in the GV images. However, the contrast ratio between the copper(I) precursor solution and the green hydroxido complex was too low to determine concentration fields of molecular oxygen.

To increase the contrast ratio, the high-speed gray-level camera was equipped with a red band-pass filter (center wavelength 660 nm). Only red light with a wavelength of 660 nm is able to pass the filter. Consequently, the green-colored hydroxido complex only emitting light with a wavelength between 520 and 560 nm appears dark on the GV images recorded by the camera. In contrast, the background light consisting of wavelength of the whole visible spectrum (400 to 750 nm) incorporates red light.

Reactive mass transfer experiments investigation formation and decay of [**O1**](OTf)$_2$ were repeated by A. Béteille using the high-speed GV camera combined with the red band-pass filter. Lastly, calibration experiments with [**Pr1**]OTf concentration ranging from 0.5 to 16 $\mathrm{mmol\,l^{-1}}$ were performed by A. Béteille.

Recorded GV images of 36 rising molecular oxygen bubbles were post processed using the MATLAB© algorithm established by K. Loubière and coworkers.[131] Resulting gap- and time-averaged concentration profiles of molecular oxygen in the far-field bubble wake were used to calculate mean values of several dimensionless numbers (Reynolds number Re, Sherwood number Sh, Archimedes number Ar, Péclet number Pe and Schmidt number Sc). Image post processing as well as data analysis was performed by A. Béteille. The interpretation of the resulting data base was done by K. Loubière.

Reynolds numbers determined from the GV images were identical to the ones predicted with the scaling law proposed by Roig and coworkers (Equation 4.1).[193] These findings are proving the independency of hydrodynamic regimes present from the gap width of the thin-gap cell and the liquid phase used.

$$Re = 0.75 \cdot \left(\frac{h}{d}\right)^{\frac{1}{6}} \cdot Ar \tag{4.1}$$

$$Sh = 1.126 \cdot Pe^{0.5} \tag{4.2}$$

Consequently, the scaling law (Equation 4.1) predicts Re for single gas bubbles with known bubble diameter (d) rising in a thin-gap cell with gap width (h) filled with any type of solvent or chemically reactive solution. Considering chemically reactive solutions, the reactants are assumed to display no surface-activating properties.

Calculated Péclet and Sherwood numbers are increasing in parallel. For a given Péclet number, Sherwood numbers determined with [**O1**]$(OTf)_2$ are identical to the ones calculated with $[Cu_2O_2(TMG_2tol)_2]I_2$ in the previous study.[131] Consequently, Pe and Sh are proportional towards each other and independent from the chemical system used. A correlation for Pe and Sh was already proposed by Roig and coworkers in form of a scaling law based on experiments performed with dye in water (Equation 4.2).[193] However, the scaling law appeared to be unsuitable for the data generated via reactive mass transfer studies in acetonitrile. Consequently, the mass transfer of molecular oxygen from the gas bubble into the liquid phase is only affected by physico-chemical properties of the solvent like kinematic viscosity and the diffusion coefficients of the reactants inside the liquid phase.

The enhancement factor E could not be calculated in this study as no data are available for the reaction rate of the formation of [**O1**]$(OTf)_2$ ($k_{\mathrm{formation}}$) at 20 °C. Consequently, the influence of the reaction kinetics on the gas-liquid mass transfer cannot be quantified.

4.1.2 Summary

The reactive mass transfer between the gas and liquid interphase during formation and decay of the oxido complex [**O1**]$(OTf)_2$ ($[Cu_2O_2(TMG_2tol)_2](CF_3SO_3)_2$) was investigated. Earlier studies of the oxido complex performed in an oxygen-saturated reaction mixture with the stopped-flow setup at room temperature, revealed formation and decay of [**O1**]$(OTf)_2$ taking place in parallel. Consequently, only the green color of the decay product, a hydroxido complex, could be monitored. In contrast, in this study experiments performed in the Hele-Shaw cell revealed a local slow-down of the reaction due to oxygen concentration gradients resulting from backmixing in the vicinity of the bubble. As a result, the orange oxido species could be formed and monitored successfully against earlier expectations.

A total number of 88 single molecular oxygen bubbles rising in the copper(I) precursor solution of [**Pr1**]OTf ($[Cu(TMG_2tol)(CH_3CN)](CF_3SO_3)$) was recorded with a high-speed GV camera. Resulting GV images revealed a low contrast ratio between the colorless solution of [**Pr1**]OTf and the final green reaction product, the hydroxido complex $[Cu_2(OH)_2(TMG_2tol)_2](CF_3SO_3)_2$. Nevertheless, a superposing of path oscillation, monitored for small bubble diameters, by shape oscillation, dominant for large bubble diameters, could be verified with increasing bubble diameter.

A red band-pass filter was successfully implemented improving the contrast ratio between the initial reaction solution containing [**Pr1**]OTf and the final green-colored hydroxido complex solution. GV images of 36 rising single oxygen bubbles were recorded and subsequently analyzed using a MATLAB© algorithm.[193] Resulting gap- and time-averaged O_2 concentration profiles were used to determine mean values of several dimensionless numbers. Those are necessary to transfer observations made to other reaction setups in the form of scaling laws independently from the experimental scale.

Thereof, the independence of hydrodynamic regimes present from the gap width h of the thin-gap cell and the solvent used as liquid phase was proven. The proportionality of Péclet number and Schmidt number, already proposed in earlier studies, has been confirmed. Thereby, gas-liquid interfacial mass transfer only depends on the physico-chemical properties of the liquid phase and is independent from the chemical system used.

To propose a scaling law describing the correlation between the Péclet and the Schmidt number, further reactive mass transfer experiments conducted in different solvents are necessary. As the correlation is independent from the chemical system used, either the oxido complexes [**O1**]$(OTf)_2$ and $[Cu_2O_2(TMG_2p)_2]I_2$ already investigated in acetonitrile or other reaction system displaying an intense color contrast ratio during the reaction could be used.

Due to the instability of [**O1**]$(OTf)_2$ at room temperature, a reaction rate constant for the formation of the oxido complex cannot be calculated. Consequently, calculation of the enhancement factor quantifying the influence of the reaction kinetics on the mass transfer is impossible.

To circumvent the limitation of calculating key factors of the reactive mass transfer, further investigations should focus on reaction systems with known stoichiometry and reaction kinetics (reaction rate constant k, reaction order n).

Finally, the influence of reaction kinetics and physico-chemical properties of the liquid phase should be compared to designate the major influencing factor. In this way, scaling laws predicting the mass transfer between gas and liquid phase independent from the chemical system and liquid phase used can be designed. Ideally, the mass transfer can then be controlled by the variation of bubble size (diameter), bubble rising velocity and reaction setup design (gap width) in the future.

4.2 Bubble Columns Near to Industrial Conditions

The last chapter discusses mass transfer studies on a small scale in a confined geometry using the formation and subsequent decay reaction of an oxido complex. Thereof, an independence of the gas-liquid mass transfer from the chemical system used could be proven. Thus, the only influencing factors are the physico-chemical properties of the liquid phase and the dimensions and parameters of the reaction setup used. These findings are of high importance for the studies tackling reactive mass transfer studies. Therein, the influence of gas-liquid mass transfer on yield and selectivity of a chemical reaction is studied. The independence from the chemical system used is crucial, ensuring the influencing factors studied are not superimposed by an enhancement of the mass transfer resulting from the chemical system like a reactant functioning as surfactant.

Using reaction setups near to industrial conditions like an unconfined bubble column, the residence time of the gas bubble inside the reactor is drastically increased compare to small confined setup like the Hele-Shaw cell. Consequently, slower reaction kinetics, taking place over the whole length of the column are favored. If a new chemical system is introduced, the independence of the mass transfer from the chemical system has to be evaluated. Therefore, first investigations focusing on the hydrodynamic influencing factors on the chemical reaction are performed in a small, confined reaction setup like the Hele-Shaw cell or Taylor-flow. Subsequently, the influence of controllable factors like the bubble size or the rising velocity on yield and selectivity of the competitive consecutive reaction are studied in a small scale. Finally, information collected about the chemical system and adjustable factors are transferred to reactive mass transfer studies performed in a large scale bubble column.

4.2.1 Reactive Mass Transfer Studies with Peroxido Complex $[^{S}P4](OTf)_2$ and *Para*-methoxyphenol in a Large Scale Bubble Column

Parts of this chapter are already published in:

S. Gast, U. Tuttlies, L. Laurini, F. Kexel, D. Merker, L. Böhm, M. A. Taborda, M. Sommerfeld, M. Kraume, M. Schlüter, S. Herres-Pawlis, U. Nieken in *Fluid Mechanics And Its Applications* (Eds.: M. Schlüter, D. Bothe, S. Herres-Pawlis), Springer International Publishing, Cham (Germany), **2021**, pp. 621-642.[140]

Correlations like scaling laws for reaction systems of industrial interest are missing.[196] The majority of publications focuses on aqueous systems, not being able to realize high temperatures or pressures. In contrast, industrial applications are focusing on organic liquid phases as well as elevated temperature and pressure.[197] Studies performed in aqueous systems based on water are not transferable to organic liquid phases as the bubble's size and behavior vary with a change in the liquid viscosity, gas density and surface tension.[198] Additionally, those properties are strongly dependent on temperature.[197] The limited number of studies dealing with organic liquids at elevated temperature and pressure, focuses on the fluid dynamics of the bubbly flow. Reactive mass transfer investigations involving a chemical reaction are not performed due to safety reasons.[198–200]

In this chapter reactive mass transfer studies are performed in a large scale bubble column near to industrial conditions with tetrahydrofuran as solvent (Figure 4.6, right). Therefore, the catalytic conversion of *para*-methoxyphenol mediated by the peroxido complex [$^{\mathbf{S}}$**P4**](OTf)$_2$ ([Cu$_2$O$_2$(DBED)$_2$](CF$_3$SO$_3$)$_2$) is used. As all steps of the reaction pathway are in need of the reactant molecular oxygen, this reaction system is an ideal example of an competitive consecutive reaction (Figure 4.7).

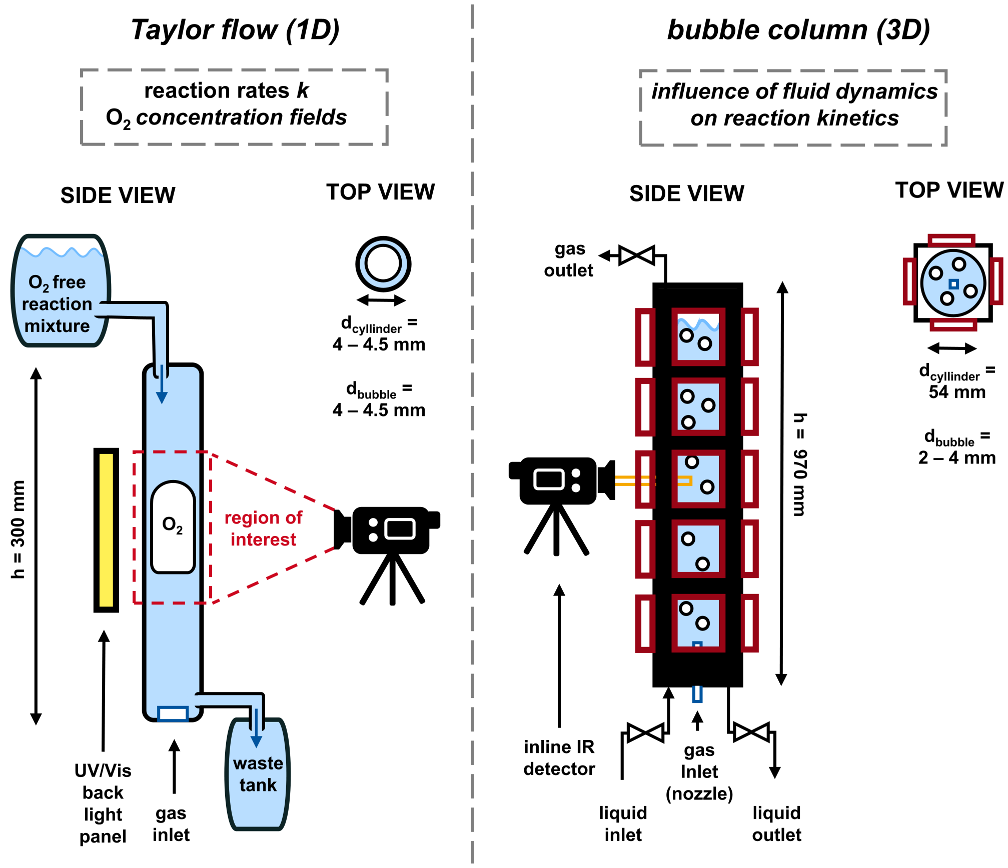

Figure 4.6: Schematic drawing of the Taylor-flow (left) and the large scale bubble column (right) used to study reaction mass transfer with the catalytic conversion of *para*-methoxyphenol mediated by the Cu$_2$O$_2$ complex [$^{\mathbf{S}}$**P4**](OTf)$_2$ ([Cu$_2$O$_2$(DBED)$_2$](CF$_3$SO$_3$)$_2$).

First, experiments in a confined Taylor-flow setup with single rising gas bubbles are performed to ensure the suitability of this chemical reaction as a model system for reactive mass transfer investigations. Additionally, more insights into the reaction kinetics are gained. Subsequently, the reaction system is transferred into a large scale industrial bubble column with a bubble swarm incorporating up to 15,000 bubbles with various bubble sizes rising at the same time. The bubble column has a height of 96.9 cm able to contain a volume of up to 2.2 l. Bubble sizes can be varied by the choice of the gas nozzle opening diameter at the bottom of the column from which the gas is inserted. Thereby, bubble diameters can range from 0.1 to 0.4 mm (Figure 4.6).

Bubbly flows are reaction systems with a massive volume in liter-scale. To minimize the expenses in terms of costs and time, chemicals used should either be purchasable or synthesizable in large amounts. For the chemical system used in this study, all chemicals (*N*,*N*'-di-*tert*-butylethylenediamine (DBED), tetrahydrofuran, molecular oxygen, triethylamine, *para*-methoxyphenol) are inexpensive and purchasable by various manufactures with the exception of the copper(I) salt (Figure 4.7). $[Cu(CH_3CN)_4](CF_3SO_3)$ is quite expensive, however, it can be synthesized cost-efficiently in gram level according to literature.[201]

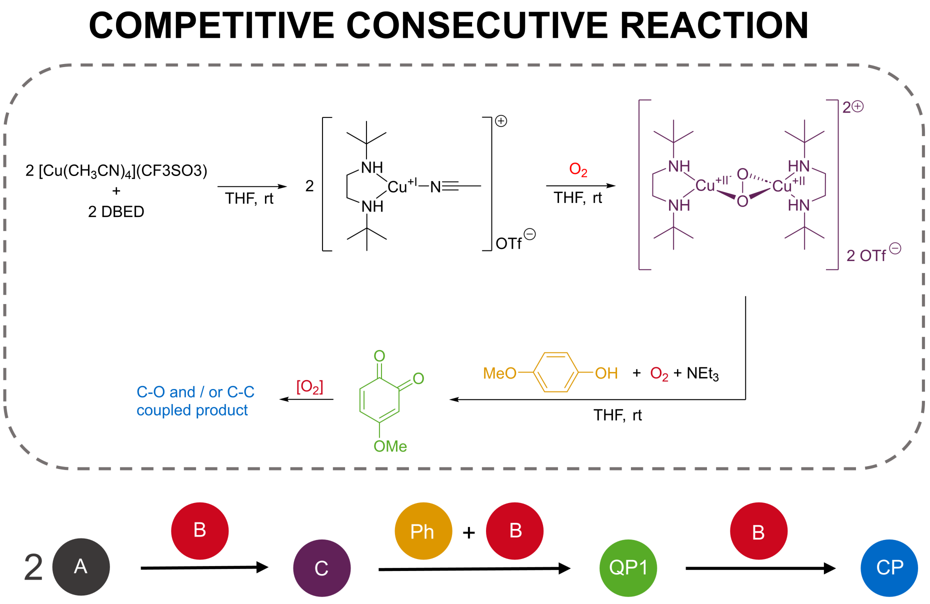

Figure 4.7: Presumed reaction pathway of the catalytic conversion of *para*-methoxyphenol mediated by $[^{S}\mathbf{P4}](OTf)_2$ ($[Cu_2O_2(DBED)_2](CF_3SO_3)_2$).

The core of the chemical reaction system used is the catalytically active Cu_2O_2 complex (**C**). The so-called ν-η^2:η^2-peroxido complex $[^{S}\mathbf{P4}](OTf)_2$ is synthesized in situ. At first, the copper(I) complex $[\mathbf{Pr4}]OTf$ ($[Cu(DBED)(CH_3CN)](CF_3SO_3)$; **A**) is formed by equimolar amounts of ligand DBED and copper(I) salt in the reaction solution. The following competitive consecutive reaction consists of three reaction steps activated by the addition of dioxygen to the reaction mixture. In the first step two copper(I) species (**A**) react with the molecular oxygen to give the Cu_2O_2 complex (**C**). Secondly, the complex oxidizes the substrate *para*-methoxyphenol (**Ph**) supported by the auxiliary base trimethylamine in a competitive consecutive step to the *ortho*-quinone intermediate 4-methoxycyclohexa-3,5-diene-1,2-dione (**QP1**). As most *ortho*-quinones are highly reactive and undergo further coupling reactions,[105,202] intermediate **QP1** is further reacts with molecular oxygen present in the reaction mixture in a third reaction to the related C-C and/or C-O coupled products (**CP**).

The chemical reaction system was designed based on a literature-know procedure (Figure 4.9, left).[101] The reaction conditions were adapted using *para*-methoxyphenol instead of 2,4-di-*tert*-butylphenol as substrate with a DBED concentration of 4 mol% and a copper(I) salt concentration of 5 mol%. Due to the toxicity of chlorinated solvents, the solvent dichloromethane was replaced by tetrahydrofuran. The reaction temperature remained identical (Figure 4.7).

The reaction intermediate **QP1** (green, dotted) as well as reaction product **CP2** (blue, solid) display characteristic absorption signals in the UV/Vis-spectrum (Figure 4.8). Consequently, the consecutive competitive reaction is monitored via inline UV/Vis spectroscopy. To calculated the amount of substance formed from the absorbance values recorded, a known extinction coefficient of the substance or calibration measurements with a series of concentrations are necessary.

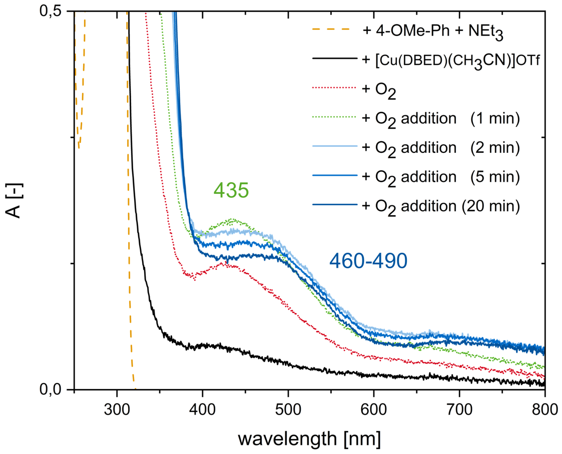

Figure 4.8: UV/Vis spectrum of the catalytic conversion of *para*-methoxyphenol with the peroxido complex [$^{\mathbf{S}}$**P4**]$(OTf)_2$ ($[Cu_2O_2(DBED)_2](CF_3SO_3)_2$) in competitive consecutive reaction.

In contrast to the *ortho*-quinone intermediate resulting from the conversion of 2,4-di-*tert*-butylphenol, the one resulting from *para*-methoxyphenol is unstable at ambient reaction conditions. Consequently, an isolation of the intermediate **QP1** for calibration measurements is impossible. Nevertheless, the final C-C or C-O coupled reaction product might be able to isolate. Using the reaction conditions given in the literature-known procedure, no C-C or C-O coupled reaction product could be isolated (Figure 4.9, right).

Therefore, the reaction conditions were modified in a broad study. The reaction time was varied between 10 min and 5 h. The molar ratio of DBED, copper(I) salt, *para*-methoxyphenol and triethylamine range from 4:5:50:50 as in literature[101] to 4:5:5:5 (Table 4.2).

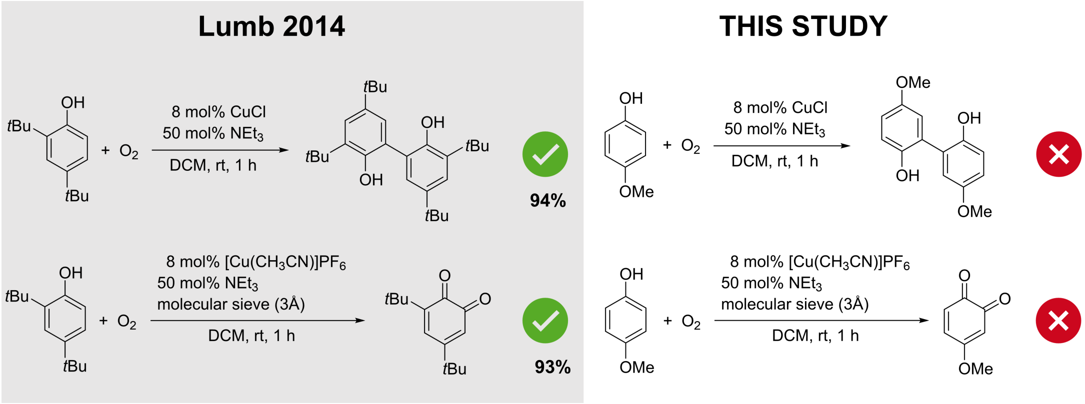

Figure 4.9: Comparison of the literature-known conversion of 2,4-di-*tert*-butylphenol to the related *ortho*-quinone or C-C coupled product with the conversion of *para*-methoxyphenol performed in this study.

With a reaction time of five hours and a molar ratio of 4:5:10:10 a C-C coupled product, the biphenol 5,5'-dimethoxy-[1,1'-biphenyl]-2,2'-diol (**CP2**; Figure 4.10), and a C-O coupled product, 2,6-bis(4-methoxyphenoxy)cyclohexa-2,5-diene-1,4-dione (**CP3**; Figure 4.11) were isolated successfully.

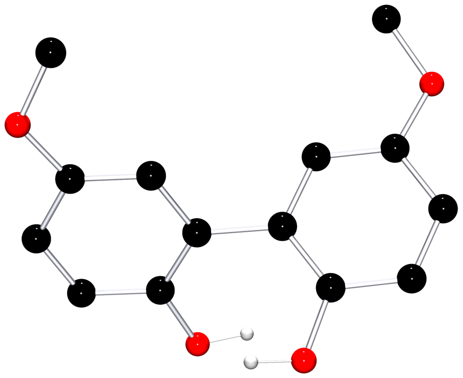

Figure 4.10: Molecular structure of the C-C coupled reaction product 5,5'-dimethoxy-[1,1'-biphenyl]-2,2'-diol (**CP2**) in the solid state. Hydrogen atoms, with the exception of the hydroxy groups, are omitted for clarity.

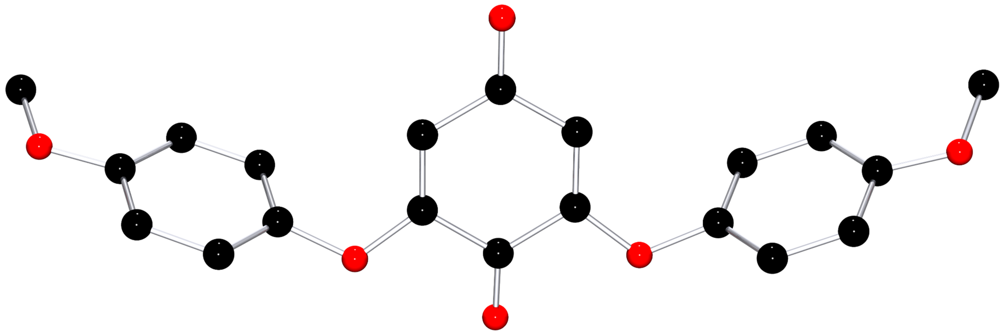

Figure 4.11: Molecular structure of the C-O coupled reaction product 2,6-bis(4-methoxyphenoxy)cyclohexa-2,5-diene-1,4-dione (**CP3**) in the solid state. Hydrogen atoms are omitted for clarity.

Table 4.2: Variation of reaction conditions used to synthesized C-C and C-O coupled reaction products **CP** resulting from the catalytic conversion of *para*-methoxyphenol with the peroxido complex $[^{\mathbf{S}}\mathbf{P4}](\mathrm{OTf})_2$ ($[\mathrm{Cu_2O_2(DBED)_2}](\mathrm{CF_3SO_3})_2$).

entry	t	Molar ratio [DBED] : [copper(I) salt] : [Ph]: [NEt$_3$]	Y[a] (unconverted S)	Y[a] (product)
1	10 min	4 : 5 : 50 : 50	33%	
2	20 min	4 : 5 : 50 : 50	62%	
3	2 h	4 : 5 : 50 : 50	67%	
4	13 h	4 : 5 : 50 : 50	87%	
5	13 h	4 : 5 : 10 : 10	25%	
6	13 h	4 : 5 : 5 : 5	57%	
7	24 h	4 : 5 : 10 : 10	81%	
8	5 h	4 : 5 : 10 : 10	18%	CP2 (92 mg)
9	5 h	4 : 5 : 10 : 10	38%	CP3 (128 mg)

[a] Isolated yield after purification via column chromatography

With the reaction products **CP2** and **CP3** isolated from the catalytic conversion of *para*-methoxyphenol mediated by $[^{\mathbf{S}}\mathbf{P4}](\mathrm{OTf})_2$, the reaction pathway presumed earlier (Figure 4.7) was updated as followed:

The first step remains unchanged, the peroxido complex **C** is formed by the reaction of two copper(I) species (**A**) with molecular oxygen. Subsequently, the substrate *para*-methoxyphenol (**Ph**) is oxidized to the intermediate **QP1** and the C-C coupled biphenol

CP2. Finally, the reaction product **CP3** is formed by the conversion of intermediate **CP1** with further substrate molecules (**Ph**) (Figure 4.12). As a result, the reaction competes for the substrate **Ph** instead for the molecular oxygen as presumed in the beginning.

As the intermediate species **QP1** can not be isolated, a distinction between oxygen consumed by the formation of **QP1** and **CP2** is impossible. However, the formation of **QP1** can be measured indirectly via the characteristic UV/Vis absorption signal of *ortho*-quinones at around 400 nm (430 nm; Figure 4.8). Just as intermediate **QP1**, the final product **CP3** displays characteristic absorption bands in the UV/Vis spectrum at around 460-490 nm (Figure 4.8). Thus, formation of intermediate **QP1** and final product **CP3** can be monitored in-situ via inline UV/Vis spectroscopy. As only the final product **CP3** can be isolated, calibration measurements to get more insights in the enhancement factor of the reaction can just be performed for the final reaction step, the formation of **CP3** (Figure 4.12).

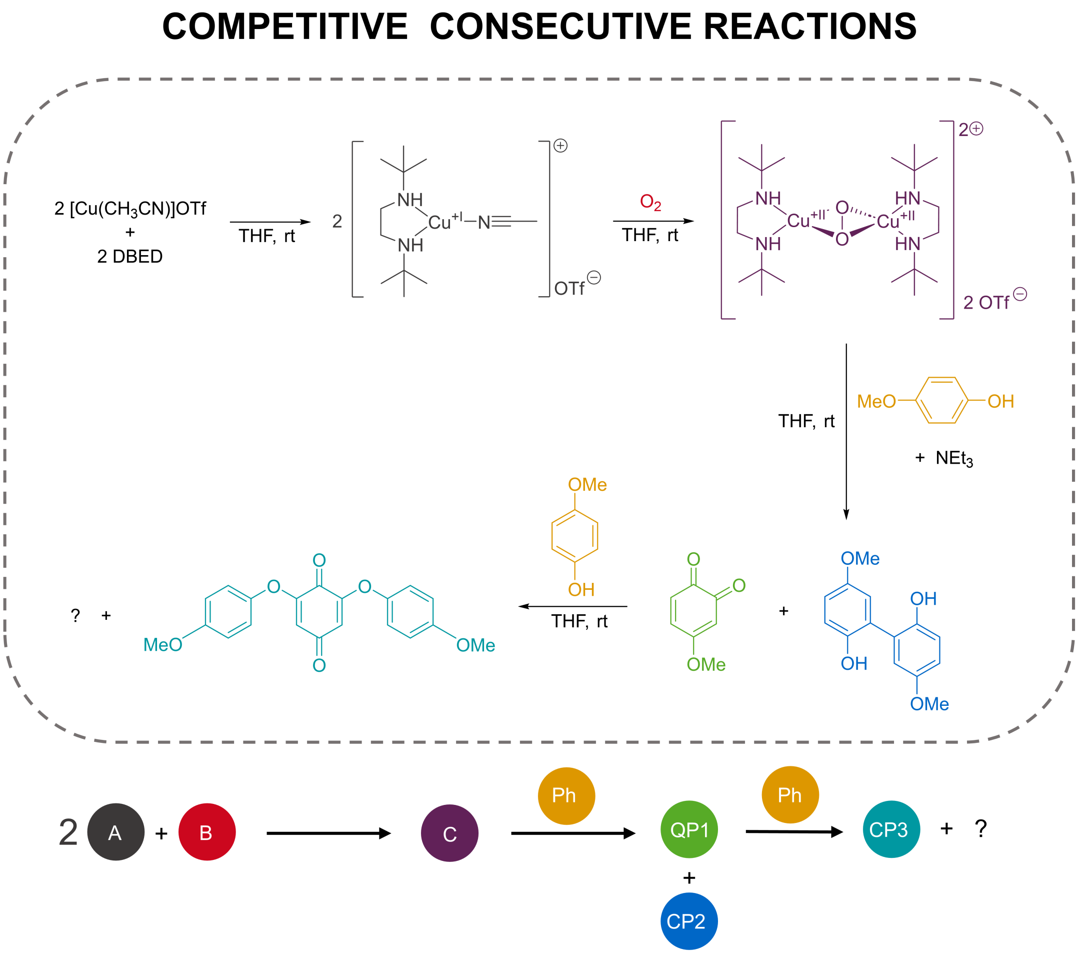

Figure 4.12: Revised reaction pathway of the catalytic conversion of *para*-methoxyphenol mediated by $[^S\mathbf{P4}](OTf)_2$ ($[Cu_2O_2(DBED)_2](CF_3SO_3)_2$).

The chemical reaction system used in this study is operating in tetrahydrofuran as a solvent. Tetrahydrofuran forms highly reactive hydroperoxides in a radical reaction with molecular oxygen catalyzed by light. At higher concentrations peroxides are explosive.[203,204] Thus, reactions should only be performed in peroxide-free tetrahydrofuran. To avoid contact with dioxygen, experiments are conducted under nitrogen atmosphere. As the copper(I) salt is sensitive to water, dried tetrahydrofuran with a residual water content in the ppm range should be used. The large volume of 2.2 l within the bubble column increases the solvent consumption. To minimize solvent consumption and work cost-efficient, tetrahydrofuran can be recycled from the reaction mixture. Therefore, the reaction mixture is distilled under inert gas conditions, preventing an oxidation to the peroxide. Traces of water are removed by adding molecular sieve to the crude mixture before distillation. To further increase the safety level working with large amounts of solvent, the reducing agent iron(II) chloride (1 g per 5 L of solvent) can be added to the reaction mixture. The iron salt does not affect the distillation process and remains in the crude mixture.

As working under water- and oxygen-free conditions is uncommon in chemical engineering, a method for oxygen-free handling under inert gas conditions was established using a minimum amount of simple laboratory equipment (Figure 4.13). The following tools are needed at least: A pressure- and vacuum-resistant glass round bottom flask with a glass stopcock (Schlenk flask), matching chemical-resistant silicone rubber plugs and glass plugs, polytetrafluoroethylene (PTFE) tube, stainless steel canula and a diaphragm or rotary vane pump ($p < 1$ mbar).

Fast and clean working are of high importance because copper(I) triflate is oxidized to copper(II) triflate within several seconds in the presence of oxygen. Handling errors can be identified visually as the salt turns from colorless Cu(I) to blue Cu(II) during the oxidation process within a minute.

In the first step, the solid chemicals, copper(I) salt $[Cu(CH_3CN)_4](CF_3SO_3)$ and *para*-methoxyphenol are weighed out and added to the flask, which is evacuated for 5 minutes and flushed with inert gas afterwards (A). Subsequently, the glass stopper is replaced by a silicone rubber stopper under an inert gas counterflow (B). With a PTFE tube fixed to the silicone rubber stopper, tetrahydrofuran can be pumped into the flask under inert gas atmosphere. To avoid overpressure and to control the flow of solvent, a stainless steel canula is used (C). When the required amount of solvent is transferred, removing of the canula stops the solvent flow and enables the flushing of the PTFE tube with inert gas. Subsequently, auxiliary base triethylamine and ligand species DBED are added with a syringe. Afterwards, the flask is being shaken until all chemicals are dissolved and a clear, purple solution occurs. Finally, the reaction mixture is transferred into the experimental setup by connecting the PTFE tube inserted into the reaction mixture with the bottom entrance of the bubble column. The flow velocity is controlled by a stainless-steel canula in the rubber stopper (D) (Figure 4.13). The addition of the reaction solution at the bottom of the column prevents the contact to a gas phase at the top of the column which could still contain small amounts of molecular oxygen.

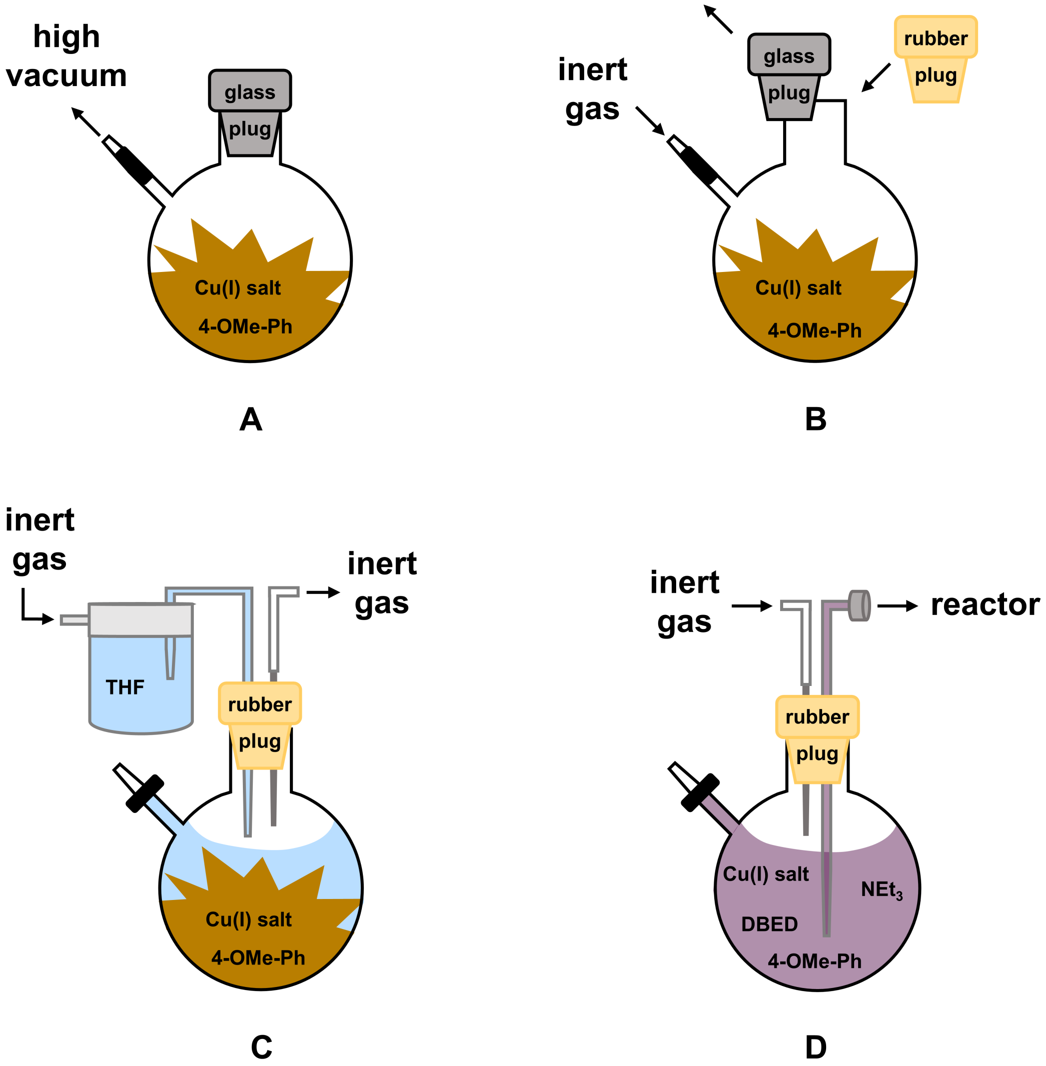

Figure 4.13: Handling of oxygen- and water-sensitive chemical reactions systems with minimum amount of simple laboratory equipment.

Reactive mass transfer experiments were performed by the working groups of Prof. Dr. M. Schlüter (Taylor-flow; inline UV/Vis spectroscopy) and the working group of of Prof. Dr. U. Nieken (industrial large scale bubble column; inline IR spectroscopy). Experiments were performed taking the reaction pathway presumed at the beginning of this chapter as a basis: The competitive consecutive reaction between the formation of quinone intermediate **QP1** and final C-O coupled product **CP3** (Figure 4.7).

As intermediate species **QP1** can not be isolated, the extinction coefficient of **QP1** can not be measured and calibration measurements can not be performed. Consequently, only qualitative statements about the concentration fields of **QP1** in the wake of the bubble can be made. In contrast, the final reaction product **CP3** was isolated successfully and calibration measurements were performed. The results of experiments performed in the Taylor-flow show an impact of the changing fluid dynamic conditions on the formation of the intermediate **QP1** and the resulting reaction product **CP3**. With an increasing degree of mixing in the wake of the bubble, the product formation is shifted from the reaction product **CP3** towards the intermediate species **QP1**.

The experiments performed in the large bubble column displayed a increase in product formation (**CP3**) with increasing bubble size. This is unexpected, since larger bubbles provide less surface area for oxygen transfer and less gas holdup due to higher bubble velocities than smaller bubbles. An explanation could be that the bubble wake of the bigger bubbles provides locations behind the bubbles with higher oxygen concentrations as shown in previous studies. Thereof, more intermediate **QP1** is formed which further reacts to reaction product **CP3**. The ratios of intermediate **QP1** and **CP3** calculated from the peak areas under the absoprtion signals, display that the bubble regime with larger bubbles leads to an increased relative production of **QP1**. This shows that the selectivity of a competitive consecutive reaction can be influenced by the utilization of a certain bubble wake structure. Additionally it means that with reaction systems which have reaction rates of the magnitude of the chemical system used in this study, we cannot only investigate the influence of the bubble size on overall conversions in gas-liquid-systems but also the influence of the wake structure on the selectivity of consecutive reactions under nearly industrial conditions in bubbly flows. Consequently, in a next step the design of a gas sparger can be tailored according to the kinetic demands of the chemical reaction.

4.2.2 Summary

Reactive mass transfer studies performed in a large bubble column near to industrial conditions using the catalytic conversion of *para*-methoxyphenol mediate by peroxido complex [$^{\mathbf{S}}$**P4**]$(\mathrm{OTf})_2$ successfully proved the controllability of yield and selectivity of the competing reaction products by the hydrodynamics within the bubble's wake structure. Nevertheless, the chemical reaction system used was not ideal, as not all reaction products and intermediates formed could be isolated necessary for calibration purposes. Consequently in future studies, the focus should be on chemical reaction system with known characteristic features (UV/Vis, IR and/or fluorescence maxima), reaction kinetics for each reaction step necessary for later proposing of scaling laws and known intermediate as well as product species which can be isolated for calibration measurements.

5 Conclusion and Perspective

Within this work the catalytic activity of several Cu_2O_2 species towards a broad spectrum of phenolic substrates was investigated. Resulting highly reactive-*ortho*-quinone products were further converted into phenazines stable under ambient conditions. Bis(µ-oxido) dicopper(III) species (**O**) as well as µ-η^2:η^2-peroxido dicopper(II) species ($^{\mathbf{S}}\mathbf{P}$) based on established hybrid and bisguanidine ligands were used. Additionally, a new hybrid guanidine ligand was introduced incorporating a pyridinyl N-donor unit. The initial step of substrate addition within the catalytic cycle of L-tyrosine conversion to L-DOPA catalyzed by the enzyme tyrosinase in nature is still under debate. Thus, a Cu_2O_2 species stabilized by a hybrid guanidine ligand was used to get new insights via EPR spectroscopic measurements performed during the conversion of phenolic substrates. Finally, Cu_2O_2 species stabilized by guanidine and diamino ligands are implemented in reactive gas-liquid mass transfer studies. Influencing factors on the gas-liquid mass transfer like bubble size, bubble rising velocity and reaction setup parameters are investigated in various (confined) geometries ranging from small, confined Taylor-flow and Hele-Shaw cell setups to a large, unconfined bubble column near to industrial conditions.

The new hybrid guanidine ligand 1,1,3,3-tetramethyl-2-(2-(pyridin-2-yl)phenyl)guanidine (TMGphpy) based on a 2-phenylpyridine spacer with a pyridine donor group incorporated and a TMG guanidine donor at the phenyl ring was introduced. Therefore, the literature-known synthesis of the primary amine 2-(2-aminophenyl)pyridine) was optimized. Subsequent conversion with the TMG-Vilsmeier salt resulted in the desired free guanidine base TMGphpy (56%). To evaluate the ability of TMGphpy to form Cu_2O_2 species, UV/Vis spectroscopic measurements converting the related Cu(I) precursor complexes with molecular oxygen were performed. The formation of a signal at 328 nm indicated the presence of a $^{\mathbf{S}}\mathbf{P}$ complex. Nevertheless, the formation of a $^{\mathbf{S}}\mathbf{P}$ species could not be verified as one of the literature-known signals (350 and 550 nm[53,54,72,80,84]) is missing. To prove the presence of a Cu_2O_2 species, cold-spray ionization mass spectrometry measurements at low temperature should be performed.

The Cu_2O_2 species $[Cu_2O_2(TMGdmap)_2](CF_3SO_3)_2$, $[Cu_2O_2(TMGphpy)_2](PF_6)_2$ and $[Cu_2O_2(TMG_2tol)_2](PF_6)_2$ ([**O1**]$(PF_6)_2$) were used to study the catalytic conversion of phenolic substrates like naphthols, quinolinols and indolols. Therefore, a literature-known procedure established in our working group with an oxido species stabilized by the hybrid guanidine ligand TMGbenza was used. The highly-reactive *ortho*-quinone products formed are further converted with 1,2-phenylenediamine to stable phenazine products.

Therein, the **O** species based on TMGbenza displayed an extraordinary substrate flexibility converting several, naphthols, quinolinols and indolols with a TON of 5-8 within one hour.[87]

All Cu_2O_2 species investigated in this study displayed a lower activity towards phenolic substrates than the literature system stabilized by TMGbenza. Cu_2O_2 systems based on the hybrid guanidines TMGdmap and new ligand TMGphpy only reached small amounts of desired phenazine product benzo[*a*]phenazine converting 2-naphthol (TON 2-3). For the Cu_2O_2 species based on the bisguanidine ligand TMG_2tol, 2-naphthol as well as 6-quinolinol were successfully converted to the related phenazines (TON 4/8). All further substrates tested remained unconverted or reached amounts within the range of blank experiments performed without the presence of a ligand species using pure copper salt (TON 1).

Despite the lower performance of tested Cu_2O_2 species, [**O1**]$(PF_6)_2$ stabilized by TMG_2tol displays one of the rare catalytically active **O** species converting naphthols and quinolinols to *ortho*-quinones intermediates subsequently condensated to desired phenazine products with a simple, time- and cost-efficient ligand synthesis pathway suitable for production in large-scale. Additionally, resulting phenazine products are a promising substrate class for pharmaceutical uses like the synthesis of antibiotics. Antibacterial test experiments performed in a cooperation project with biologists displayed a high antimicrobial effect against gram-negative as well as gram-positive bacteria. However, a more detailed assessment comparing phenazine activities with known, structurally-related antimicrobials or clinically established antibiotics is needed.

EPR spectroscopic investigations regarding the intermediate species present during the monophenolase cycle of tyrosinase revealed the presence of an asymmetric μ-η^2:η^1-catecholate-μ-hydroxidodicopper(II) complex ([**CAT2**]) in agreement with earlier findings of several working groups[176–179] and the monophenolase cycle recently published by Solomon and coworkers.[43] Furthermore, the absence of the possible side product, a copper(II) catecholate complex Cu(II)-3,5-di-*tert*-butylcatecholate-TMGdmap resulting from protonation reactions during the catalytic cycle, was verified.

Taking a look at gas-liquid mass transfer investigations performed in cooperation with chemical engineers, Cu_2O_2 species were proven as a successful tool with tunable structural characteristics, reaction kinetics and spectroscopic features. Experiments conducted in the confined small dimensional Hele-Shaw cell setup proved the independence of hydrodynamic regimes from the chemical system used. Thereby, formation and decay of the oxido complex [**O1**]$(OTf)_2$ based on the bisguanidine TMG_2tol were investigated and compared to data from the oxido species $[Cu_2O_2(TMG_2p)_2]I_2$ stabilized by the bisguanidine ligand TMG_2p investigated in earlier studies. As only influencing factors, the physico-chemical properties of the liquid, bubble characteristics like size and rising velocity as well as parameters of the reaction set-up like gap width and gas inlet size were found.

To propose scaling laws only depending on dimensionless numbers mandatory for the transfer into large reaction setups near to industrial conditions, further reactive mass transfer experiments conducted in different solvents with varied physico-chemical properties are necessary. As the hydrodynamic regimes were proven to be independent from the chemical system used, either the oxido complexes [**O1**]$(OTf)_2$ and $[Cu_2O_2(TMG_2p)_2]I_2$ already investigated in acetonitrile or another chemical reaction system displaying an intense color contrast ratio during the reaction could be used. Thereby, the focus should be on reaction systems with known kinetic parameters (reaction rate constant, reaction order) to circumvent limitations due to unknown constants necessary for the calculation of key factors. Thus, scaling laws can be designed predicting the influence of gas-liquid mass transfer by changing controllable influencing factors like the bubble size and rising velocity or the gap width of the reaction set-up.

Lastly, reactive mass transfer studies in large bubble column near to industrial conditions were conducted using an adapted, literature-known reaction system. The substrate *para*-methoxyphenol was catalytically converted by the $^{\mathbf{S}}\mathbf{P}$ complex $[Cu_2O_2(DBED)_2](CF_3SO_3)_2$ stabilized by the diamino ligand DBED. Within the competitive consecutive reaction the substrate *para*-methoxyphenol is oxidized to the related *ortho*-quinone. As *ortho*-quinones are unstable under ambient conditions, subsequent coupling reactions with a substrate molecule of *para*-methoxyphenol takes place resulting into different C-C and C-O coupled reaction products. Isolation of resulting reaction products for calibration purposes happen to be more complex than expected. Two C-C / C-O coupled reaction products were successfully isolated and analyzed via x-ray diffraction. However, only the C-O coupled product could be used for calibration purposes as the C-C coupled reaction product was only isolated in a small amount. After successful calibration, the controllability of yield an selectivity of the competing reaction products by the hydrodynamics within the bubble's wake structure could be proven. Nevertheless, isolation of a defined product species as well as determination of key parameters like reaction rate constants for each reaction step was not possible due to the formation of multiple C-C and C-O coupled reaction products and unstable reaction intermediates. Thus, in future studies the focus should be on chemical reaction system with known characteristic features (UV/Vis, IR and/or fluorescence maxima), reaction kinetics for each reaction step necessary for later proposing of scaling laws as well as isolable intermediate and product species.

This thesis represents a milestone towards applications of bioinorganic chemical systems in chemical engineering studies investigated within the framework of several cooperation projects. Cu_2O_2 species used for reactive gas-liquid mass transfer studies were proven as an excellent reaction system with tunable reaction conditions, reaction kinetics and spectroscopic features. Chemical systems have been designed meeting the needs of various reaction setups: from a small confined Hele-Shaw cell ($V = 80$ ml) up to an unconfined bubble column ($V = 2.2$ l). Thus, an avenue to tailored chemical systems was paved fulfilling a gap towards applications near to industrial conditions.

6 Experimental Part

6.1 General Remarks

All copper (I) precursor complexes ([**Pr1**]OTf, [**Pr1**]PF_6, [**Pr2**]Br, [**Pr2**]PF_6, [**Pr3**]OTf, [**Pr4**]OTf) were prepared in a glove box of the company M.BRAUN under a nitrogen atmosphere. All other experiments were carried out using Schlenk technique with nitrogen (99.996%, dried over phosphorus pentoxide) as inert gas if not stated otherwise. Solvents (HPLC grade) and triethylamine were purchased in analytical grade quality and distilled under nitrogen atmosphere over either sodium with benzophenone as indicator (tetrahydrofuran, pentane, diethyl ether), calcium hydride (acetonitrile, triethylamine, dichlormethane) or magnesium (methanol) before usage. Molecular sieve (3 Å) was dried with a heat gun (600°C) under vacuum for two hours and stored in a drying oven (150°C) afterwards. 2-Aminobenzylamine and N,N'-di-*tert*-butylethylenediamine were distilled under reduced pressure ($p = 0.05$ mbar) right before usage. Copper(I) bromide and copper(I) chloride were washed with ethanol (3x) and diethyl ether (6x), dried under reduced pressure ($p = 0.05$ mbar) and stored under nitrogen atmosphere before usage. Chloro-N,N,N',N'-tetramethylformamidinium chloride (TMG Vilsmeier salt),[114,115,119,121] 2-(3-(dimethylamino)propyl)-1,1,3,3-tetramethylguanidine (TMGdmap)[88] and sodium-X-phenolates (X = H, 4-Me, 2,4-di-*tert*-butyl),[205] synthesized after literature-known procedures, were provided by the working group. Tetrakisacetonitrile copper(I) trifluoromethanesulfonate ($[Cu(CH_3CN)_4](CF_3SO_3)$) and tetrakisacetonitrile copper(I) hexafluorophosphate ($[Cu(CH_3CN)_4]PF_6$) were synthesized in acetonitrile and recrystallized at least twice from acetonitrile/diethyl ether at $-30\,°C$ according to literature.[201] All other chemicals were used as purchased (Table 6.1). Product purification was performed under ambient conditions using purchased solvents (Table 6.1), Geduran Si 60 (40-63 µm; Merck), a glass column (diameter: 2.5 cm, length 40 cm) with glass filter frit (3 Å) and thin layer chromatography sheets (silicon dioxide, 0.2 mm, MACHEREY-NAGEL) for column chromatography.

Table 6.1: List of chemicals and solvents used with related supplier, purity and CAS number.

substance	purity	supplier	CAS
1-naphthol	$\geq$ 98%	Fluka	90-15-3
1,2-phenylendiamine	$>$ 98%	Fluka	95-54-5
2-aminobenzylamine	98%	TCI	4403-69-4
2-carbazolol	97 %	Alfa Aesar	86-79-3
2-iodaniline	98%	abcr	615-43-0
2-naphthol	98%	Sigma Aldrich	135-19-3
3-quinolinol	95%	abcr	580-18-7
3,5-di-*tert*-butyl-*ortho*-benzoquinone	98%	Alpha Aesar	3383-21-9
4-carbazolol	97%	abcr	52602-39-8
4-indolol	$>$ 99%	TCI	2380-94-1
4-methoxyphenol	99%	Sigma Aldrich	150-76-5
4-quinolinol	$>$ 98%	abcr	611-36-9
5-indolol	95%	abcr	1953-54-4
5-quinolinol	98%	abcr	578-67-6
6-indolol	95%	abcr	2380-86-1
6-quinolinol	96%	abcr	580-16-5
7-indolol	95%	abcr	2380-84-9
acetonitrile (MeCN)	99.9%	Chemsolute	75-05-8
ammonium chloride	99.5%	Gruessing	12125-02-9
benzophenone	99%	Alfa Aesar	119-61-9
bromo-2-pyridinylzinc (2-Py-ZnBr)	0.5 M in THF	Sigma Aldrich	218777-23-2
calcium hydride	93%	Acros Organics	7789-78-8
celite 535®	-	Carl Roth	68855-54-9
chloroform-d ($CDCl_3$)	99%	Euroisotop	865-49-6
copper(0) powder $<$ 425 µm	99.5%	Sigma Aldrich	7400-50-8
copper(I) bromide	98%	Alfa Aesar	7787-70-4
copper(I) chloride	99%	Alfa Aesar	7758-89-6
copper(I) oxide	87.5%	Riedel-de-Haen	1317-39-1
diethyl ether	99.5%	Fisher Scientific	60-29-7
dimethyl sulfoxide-d6 (DMSO-d_6)	$>$ 99.9%	Sigma Aldrich	2206-27-1
dichloromethane (DCM)	$>$ 99.8%	Fisher Scientific	75-09-2
ethyl acetate (EtOAc)	$>$ 99.5%	Fisher Scientific	141-78-6
ethylenediaminetetraacetic acid (EDTA)	99.5%	Fluka	60-00-4
hexafluorophosphoric acid	55% in water	Sigma Aldrich	16940-81-1
hydrochloric acid (HCl)	37%	Fisher Scientific	7647-01-0
n-hexane	$>$ 95%	Fisher Scientific	110-54-3
n-pentane	99.7%	VWR Chemicals	109-66-0
N,*N*'-di-*tert*-butylethylenediamine (DBED)	98%	Sigma Aldrich	4062-60-6
magnesium sulfate (water-free)	99%	Gruessing	7487-88-9
methanol (MeOH)	$>$ 99.9%	Fisher Scientific	67-56-1
molecular sieve 3 Å	-	Carl Roth	308080-99-1
oxygen 2.5	99.5%	Westfalen AG	-
potassium hydroxide	99%	Gruessing	1310-58-3
sodium (cubes in mineral oil)	99.9%	Sigma Aldrich	7440-23-5
sodium chloride	99.5%	Gruessing	7647-14-5
sodium hydroxide	99%	Fisher Scientific	1310-73-3
sodium thiosulfate (water-free)	98%	Gruessing	7772-98-7
sulfuric acid 1 N	95%	Fisher Scientific	7664-93-9
tetrahydrofuran (THF)	$>$ 99.8%	Fisher Scientific	109-99-9
tetrakis(triphenylphosphin)palladium(0) ($Pd[P(Ph_3)]_4$)	99.9%	abcr	14221-01-3
triethylamine	99%	abcr	121-44-8
trifluoromethanesulfonic acid	97%	carbolution	1493-13-6

6.2 Analytical Methods

6.2.1 Infrared (IR) Spectroscopy

FT-IR spectra were recorded on a Shimadzu IR Tracer 100 using a CsI beam splitter in combination with an ATR unit (Quest model from Specac utilising a robust monolithic crystalline diamond) in a resolution of 2 cm^{-1}. For data acquisition the software LabSolution IR (Version2.15) from Shimadzu was used.

6.2.2 Nuclear Magnetic Resonance (NMR) Spectroscopy

^{1}H-NMR and ^{13}C-NMR spectra were recorded on a Bruker Avance II 400 and Bruker Avance III HD 400 spectrometer at 25 °C in NMR tubes. Resonances were referenced to the residual solvent signal (^{1}H-NMR: δH(CD_3CN) = 1.94 ppm (q), δH(DMSO-d6) = 3.33 ppm (s), δH($CDCl_3$) = 7.26 ppm (s); ^{13}C-NMR: δH(MeCN-d3) = 118.7 ppm), relative to tetramethylsilane (0 ppm). Resonances in ppm are listed descending with their related multiplicity, coupling constants J in Hz and integration. Multiplicities are abbreviated with: s = singlet, d = doublet, t = triplet, m = multiplet. For the Bruker Avance III HD 400 and the Bruker Avance II 400 the software TOPSPIN (Version 3.63; Bruker, Ettlingen, Germany) was used for data acquisition. For visualization and examination of the NMR spectra the software MestReNova (Version 12.0.1-20560) from Mestrelab Research was used.

DOSY (diffusion-ordered-spectroscopy)-NMR spectroscopic data were acquired on the Bruker Avance II 400 spectrometer at 23 °C using the Bruker 1H 2D DOSY pulse sequence “dstebpgp3s”.[206] The DOSY time interval and gradient pulses were set at 80 ms (Δ) and 1.8 ms (0.5 δ), respectively. A total of 16 gradient increments, linearly varied from 5 to 95%, were collected with 32 scans for each increment using four dummy scans, an acquisition time of 2 s and a repetition delay of 3 s. For the NMR spectroscopic data post-processing distinct signals assigned to the copper complex between 6 and 7.6 ppm were selected from each 2D DOSY-NMR spectrum using a MATLAB© code. Calculation of the average diffusion coefficient was done in two steps: The direct, spectral data dimension was processed using the TOPSPIN-3.63 software (Bruker, Ettlingen, Germany). The indirect diffusion dimension was analyzed with the software Dynamics-Center-2.5.3 (Bruker). The MATLAB code is stored in the repository RADAR4Chem by FIZ Karlsruhe - Leibniz-Institut für Informationsinfrastruktur and is published under an Open Access model (CC BY-NC-SA 4.0 Attribution-NonCommercial-ShareAlike). The data can be found via: https://doi.org/10.22000/872.

6.2.3 Mass Spectrometry (MS)

For cold-spray ionization mass spectrometry (CSI-MS) and electrospray ionization mass spectrometry (ESI-MS) measurements an ESI-quadrupole time-of-flight (qToF) mass spectrometer (UHR-TOF Bruker Daltonik maXis II) in combination with a Bruker Daltonik

Cryospray unit was used. The spectrometer has a resolution of at least 80.000 FWHM. Spectra were detected in positive ion mode with a source voltage of 3.5 kV. The flow rate was 3.0 µl min^{-1}. The drying gas (N_2), to achieve solvent removal, and the spray gas were both held at –80°C for low-temperature measurements. The mass spectrometer was calibrated prior to every experiment via direct infusion of Agilent ESI-TOF low concentration tuning mixture, which provided a m/z range of singly charged peaks up to 3000 Da in both ion modes.

6.2.4 Single Crystal X-Ray Diffraction (SC-XRD)

The single crystal x-ray diffraction data were collected with a Stadivari diffractometer of STOE with an Eulerian cradle using an Dectris Pilatus3 R 200K hybrid-pixel detector with GeniX 3D high flux radiation of copper or molybdenum (Mo: λ = 0.71073 Å, Cu: λ = 1.54056 Å) at 100 K. The temperature was controlled by an Oxford Cryostream 800. Data were collected with X-Area Pilatus and integrated with X-Area Integrate and X-Area Recipe. The absorption correction was performed by Gaussian integration with Stoe X-Red32, afterwards scaling of reflections with X-Area LANA.[207–210] The structure were solved by direct method and all non-hydrogen atoms were refined anisotropically with full-matrix least-squares based on F^2 (XPREP,[211] ShelXT,[212] ShelXL[213] and SHELXLe[214]). All hydrogen atoms were localized at idealized positions and refined with isotropic displacement parameters $U_{iso}(H) = 1.2U_{eq}(C)$ and $1.5U_{eq}(C_{methyl})$. All methyl groups were allowed to rotate but not to tip.

6.2.5 Electron-Paramagnetic-Resonance (EPR) Spectroscopy

X-Band EPR spectra were recorded on a Magnettech MiniScope MS400 spectrometer with a microwave frequency of 9.4 Hz. Liquid samples were measured as a frozen solution in Wilmad© Suprasil-Young-tubes (EPR-silent, gas-tight) at 77 K. Solid samples were measured in glass capillaries at 77 K. The B0 field was adjusted to 320 mT with a range of 200 mT (220 – 420 mT), a sweep time of 90 s and a modulation amplitude of 0.200 mT. The microwave attenuation was configured to 5.0 db. Other parameters were adjusted as follows: smooth = 0.1000 s, NOPs = 4096, gain mantissa = 50 and gain exponent = 1.

EPR spectra were simulated using the MATLAB toolbox EasySpin (Matlab R2022a) unsing the pepper function. The program calculated a spectrum as convergent as possible with the experimental data by varying hyperfine coupling constants and the Landè g-factors. Spectra were simulated using g = [2.03 2.05 2.2] and A (MHz) = [70 50 550]. The hyperfine splitting was allowed to vary by [30 30 50] MHz.[181,215,216]

6.2.6 Ulraviolet/visible (UV/Vis) Spectroscopy

UV/Vis spectroscopic measurements were carried out on an Agilent Technologies Cary 60 UV/Vis spectrophotometer. The spectra were obtained with a fiber-optic quartz glass

UV/Vis spectroscopic immersion probe (Helma, 1.00 mm) connected via a Cary50 fiber-optic coupler. Measurements were performed in a commercial Schlenk measurement cell. Spectra were recorded using the program CaryWinUV Scanning kinetics 5.0.0.999.

6.2.7 Tensiometer

The surface tension was measured on a Drop Shape Analyzer DSA 100S from Kruess at 21.4 °C. Thereby the pendant-drop method was used with a zoom of 4.8, a focus of 4.4 and a tilt of 0°. The density was set as identical to the solvent acetonitrile which equals to $\rho_L = 782.5\,\mathrm{kg\,m^{-3}}$ (20 °C).[117]

6.3 Synthesis of Guanidine Ligands

6.3.1 Resynthesis of Bisguanidine 2-(2((bis(dimethylamino)methylene)amino)benzyl)-1,1,3,3-tetramethylguanidine (TMG$_2$tol, L1)

Ligand 2-(2((bis(dimethylamino)methylene)amino)benzyl)-1,1,3,3-tetramethylguanidine (TMG$_2$tol, L1) was resynthesized based on a modified literature procedure.[85]

2-Aminobenzylamine (13.90 g, 113.8 mmol, 1 eq.) and triethylamine (31.70 ml, 23.01 g, 227.4 mmol, 2 eq.) were added to acetonitrile (100 ml) and stirred in an ice bath (0°C). TMG Vilsmeier salt (38.92 g, 227.5 mmol, 2 eq.) dissolved in acetonitrile (250 ml) was added dropwise. Subsequently, the colorless suspension was refluxed over the course of five hours. After cooling to room temperature (20°C), an aqueous solution of sodium hydroxide (9.10 g, 227.5 mmol, 2 eq. in 80 ml water) was added and acetonitrile, water and triethylamine were removed under reduced pressure (p = 0.05 mbar). The following extraction and filtration were performed at ambient conditions (air atmosphere, no Schlenk technique used). The oily, yellow residue was dissolved in an aqueous solution of potassium hydroxide (50 wt%, 40.00 g in 40.00 ml water) and extracted with acetonitrile (4x 100 ml). The combined organic phases were dried over magnesium sulfate and filtered over celite before the solvent was removed under reduced pressure (p = 0.05 mbar). Fractional distillation under nitrogen atmosphere (p = 0.05 mbar, $T_{\mathrm{oilbath}} = 240$°C, $T_{\mathrm{head}} = 140$°C) resulted in a light yellow oil (27.30 g, 85.7 mmol, 75 %). Ligand TMG$_2$tol was confirmed via ^{1}H NMR spectroscopy (Figure 8.1 in the appendix).[142]

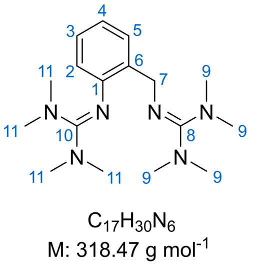

Figure 6.1: Molecular structure of 2-(2((bis(dimethylamino)methyl-ene)amino)benzyl)-1,1,3,3-tetramethylguanidine (TMG$_2$tol, **L1**), numbers refer to the labels given in the ^{1}H NMR spectrum.

^{1}H NMR (400 MHz, chloroform-d [7.26 ppm]): δ [ppm] = 7.50 (dd, J_{HH} = 7.8 Hz, 1.7 Hz, 1H, H-5), 7.00 (td, J_{HH} = 7.4 Hz, 1.7 Hz, 1H, H-4), 6.83 (td, J_{HH} = 7.4 Hz, 1.4 Hz, 1H, H-3), 6.51 (dd, J_{HH} = 7.8 Hz, 1.4 Hz, 1H, H-2), 4.20 (s, 2H, H-7), 2.71 (d, J_{HH} = 14.6 Hz, 12H, H-9), 2.63 (s, 12H, H-11).

6.3.2 Synthesis of Hybrid Guanidine 1,1,3,3-tetramethyl-2-(2-(pyridin-2-yl)phenyl)guanidine (TMGphpy, L2)

6.3.2.1 Resynthesis of Primary Amine 2(2-Aminophenyl)pyridine

2(2-Aminophenyl)pyridine was resynthesized based on a literature-known procedure.[165,166] Modifications of the procedure are listed in Table 6.2. A general description of the performed synthesis is given in the following. The scaling factor given in Table 6.2 refers to the amounts given in the general procedure (scaling factor = 1).

Tetrakis(triphenylphosphin)palladium(0) (Pd[P(Ph)$_3$]$_4$; 0.1004 g, 0.0870 mmol, 0.0100 eq.) and 2-iodaniline (2-I-Anil; 1.751 g, 7.99 mmol, 1.00 eq.) were placed in round bottom flask and evaporated under reduced pressure (p = 0.05 mbar). The flask was flushed with nitrogen afterwards and bromo-2-pyridinylzinc solution (2-Py-ZnBr, 0.5 M in THF; 2.234 g, 10.0 mmol, 1.25 eq.) was added with a syringe. The clear, red-colored solution was refluxed and/or stirred as given in Table 6.2.

The following extraction and filtration were performed at ambient conditions (air atmosphere, no Schlenk technique used). Saturated aqueous ammonium chloride solution (20 ml) was added to the brown-colored, cooled down reaction mixture. Subsequently, the brown suspension with yellow solids was extracted with ethyl acetate (3x 20 ml). The combined organic phases were washed (i) with saturated aqueous sodium thiosulfate solution (20 ml) and (ii) with saturated aqueous sodium chloride solution (20 ml). Afterwards, the solution was dried over magnesium sulfate and filtered before the solvent was removed under reduce pressure (p = 0.05 mbar).

The brown-colored residue was purified via column chromatography on Geduran Si 60. 2(2-Aminophenyl)pyridine (Amin$_{\mathrm{phpy}}$) was obtained as yellow oil (Table 6.2). Solvent ratios of ethyl acetate (EtOAc) and *n*-hexane (Hex) used as well as related retarding-front value (R_f) of the desired reaction are given in Table 6.2. 2(2-Aminophenyl)pyridine was confirmed via ^{1}H NMR spectroscopy (Figure 8.2 in the appendix).[165]

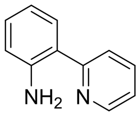

$C_{11}H_{10}N_2$
M: 170.22 g mol^{-1}

Figure 6.2: Molecular structure of 2(2-aminophenyl)pyridine.

^{1}H NMR (400 MHz, chloroform-d [s, 7.26 ppm]): δ [ppm] = 8.62 (ddd, J_{HH} = 4.9 Hz, 1.9 Hz, 1.0 Hz, 1H), 7.72 (dd, J_{HH} = 7.4 Hz, 1.9 Hz, 1H), 7.65 (dt, J_{HH} = 8.2 Hz, 1.0 Hz, 1H), 7.55 (dd, J_{HH} = 7.8 Hz, 1.6 Hz, 1H), 7.18 (m, 2H), 6.81 (m, 2H), 5.78 (s, 2H).

Table 6.2: Variations of scale factor, reaction conditions and amounts of reactants used for the synthesis of 2(2-aminophenyl)pyridine.

entry	*T* [°C]	*t* [h]	scale factor	EtOAc : Hex	R_f (Amin$_{\mathrm{phpy}}$)	Pd[P(Ph)$_3$]$_4$	2-I-Anil	2-Py-ZnBr	*Y* (Amin$_{\mathrm{phpy}}$)
1	20	24	0.5	20 : 80	0.32	0.0500 g 0.0430 mmol 0.0100 eq.	0.875 g 3.99 mmol 1.00 eq.	1.12 g 5.00 mmol 1.25 eq.	0.1366 g 0.800 mmol 20%
2	reflux	24	0.5	20 : 80	0.40	0.0500 g 0.0430 mmol 0.0100 eq.	0.875 g 3.99 mmol 1.00 eq.	1.12 g 5.0 mmol 1.25 eq.	0.1695 g 0.996 mmol 25%
3	20	48	1	30 : 70	0.54	0.1004 g 0.0870 mmol 0.0100 eq.	1.751 g 7.99 mmol 1.00 eq.	2.234 g 10.0 mmol 1.25 eq.	0.3422 g 2.01 mmol 25%
4	reflux	48	1	30 : 70	0.57	0.1004 g 0.0870 mmol 0.0100 eq.	1.751 g 7.99 mmol 1.00 eq.	2.234 g 10.0 mmol 1.25 eq.	0.4697 g 2.76 mmol 35%
5	reflux	69	1.5	30 : 70	0.50	0.1387 g 0.120 mmol 0.0100 eq.	2.627 g 12.0 mmol 1.00 eq.	3.351 g 15.0 mmol 1.25 eq.	0.6387 g 3.75 mmol 31%

6.3.2.2 Guanidine Synthesis with 2(2-Aminophenyl)pyridine

Ligand 1,1,3,3-tetramethyl-2-(2-(pyridin-2-yl)phenyl)guanidine (TMGphpy, **L2**) was synthesized based on a general literature procedure for bisguanidine ligands.[111]

2-(2-aminophenyl)pyridine (0.507 g, 2.98 mmol, 1.0 eq.) and triethylamine (0.42 ml, 0.305 g, 3.01 mmol, 1 eq.) were added to acetonitrile (10 ml) and stirred in an ice bath (0°C). TMG Vilsmeier salt (0.616 g, 3.60 mmol, 1.2 eq.) dissolved in acetonitrile (20 ml) was added dropwise. Subsequently, the colorless suspension was refluxed over the course of x hours (Table 6.3). After cooling to room temperature (20°C), an aqueous solution of sodium hydroxide (0.200 g, 5.00 mmol, 1.6 eq. in 1 ml water) was added and the reaction mixture was stirred for y hours (Table 6.3). Subsequently, acetonitrile, water and triethylamine were removed under reduced pressure (p = 0.05 mbar). The following extraction and filtration were performed at ambient conditions (air atmosphere, no Schlenk technique used). The oily, olivegreen residue was dissolved in an aqueous solution of potassium hydroxide (50 wt%, 10.00 g in 10.00 ml water) and extracted with acetonitrile (3x 20 ml). The combined organic phases were dried over magnesium sulfate and filtered over celite before the solvent was removed under reduced pressure (p = 0.05 mbar). Fractional distillation under nitrogen atmosphere (p = 0.05 mbar, $T_{oilbath}$ = 240°C, T_{head} = 150°C) resulted in a gold yellow oil of TMGphpy (**L2**) (Table 6.3). ^{1}H and ^{13}C NMR spectrum as well the IR spectrum of **L2** can be found in Figure 8.4 - 8.6 in the appendix.

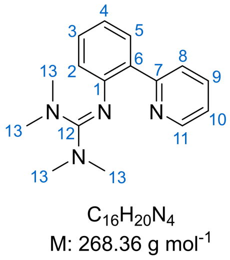

Figure 6.3: Molecular structure of 1,1,3,3-tetramethyl-2-(2-(pyridin-2-yl)phenyl)guanidine (TMGphpy, **L2**), numbers refer to the labels given in the ^{1}H and ^{13}C NMR spectrum.

^{1}H NMR (400 MHz, acetonitrile-d$_3$ [q, 1.94 ppm]): δ [ppm] = 8.56 (ddd, J_{HH} = 4.9, 1.9, 1.0 Hz, 1H, H-4), 7.73 (dt, J_{HH} = 8.0, 1.1 Hz, 1H, H-11), 7.63 (ddd, J_{HH} = 8.0, 7.4, 1.9 Hz, 1H, H-5), 7.53 (ddd, J_{HH} = 7.7, 1.7, 0.4 Hz, 1H, H-2), 7.19 (ddd, J_{HH} = 8.0, 7.2, 1.7 Hz, 1H, H-3), 7.14 (ddd, J_{HH} = 7.4, 4.8, 1.2 Hz, 1H, H-10), 6.89 (ddd, J_{HH} = 7.7, 7.2, 1.3 Hz, 1H, H-9), 6.67 (ddd, J_{HH} = 8.0, 1.3, 0.4 Hz, 1H, H-8), 2.43 (s, 12H, H-13).

^{13}C NMR (100 MHz, acetonitrile-d$_3$ [118.2 ppm]): δ [ppm] = 159.7 (C-6), 159.3 (C-12), 151.1 (C-1), 150.0 (C-4), 136.1 (C-5), 132.3 (C-7), 131.2 (C-2), 129.8 (C-3), 124.9 (C-11), 124.3 (C-8), 122.1 (C-10), 120.8 (C-9), 39.4 (C-13).

IR: ν [cm^{-1}] = 3057 (vw, ν(C-Harom.)), 3001 (w, ν(C-Harom.)), 2927 (w, ν(C-Harom.)), 2876 (w, ν(C-Haliph.)), 2799 (vw, ν(C-Haliph.)), 1586 (s, ν(C=Ngua.)), 1573 (vs, ν(C=Ngua.)), 1562 (vs, ν(C=Ngua.)), 1552 (vs, ν(C=Ngua.)), 1501 (m), 1479 (s), 1447 (s), 1421 (s), 1374 (vs), 1231 (m), 1202 (m), 1136 (s), 1058 (m), 1016 (s), 923 (w), 853 (m), 795 (m), 779 (m), 740 (vs), 696 (m), 613 (m), 565 (w), 464 (m).

HR-MS: m/z (%) = [C16H20N4Na+, M + Na$^+$] calculated: 291.15802, found: 291.16010 (100), [C16H21N4+, M + H$^+$] calculated: 269.17607, found: 269.17573 (13), [C12H18N3+, M - N(CH3)2] calculated: 224.11877, found: 224.11788 (71).

Table 6.3: Reaction conditions used for the synthesis of 1,1,3,3-tetramethyl-2-(2-(pyridin-2-yl)phenyl)guanidine (TMGphpy, **L2**).

entry	*T* [°C]	*t* [h]	Deprotonation with NaOH	*Y* (TMG$_{\text{phpy}}$)
1	reflux	8	2 days	0.244 g 0.910 mmol 30%
2	reflux	16	overnight	0.451 g 1.68 mmol 56%

6.4 Synthesis of Copper(I) Precursor Complexes

General discription of the preparation of copper(I) precursor complex solutions. Detailed information about the amounts used are given in the related discription of the experiment.

The copper(I) salt (CuBr, [Cu(CH$_3$CN)$_4$]PF$_6$ or [Cu(CH$_3$CN)$_4$](CF$_3$SO$_3$); 1 eq.) was diluted in acetonitrile (CH$_3$CN). A solution of guanidine ligand (1 eq.) dissolved in acetonitrile was added dropwise. The resulting copper(I) precursor solution was drawn in a gas-tight Hamilton syringe and stored in a Schlenk tube until further usage (max. 8 hours).

6.5 Formation of Cu$_2$O$_2$ Species

Cu$_2$O$_2$ species are formed in situ by injecting a copper(I) precursor species into stirring, oxygen-saturated solvent at a certain temperature. Reaction conditions and amounts used are varying depending on the objective in the experiment. Detailed discriptions can be found in the following sections.

6.5.1 UV/Vis Spectroscopic Studies of Cu$_2$O$_2$ Species Stabilized by TMGphpy

The copper(I) precursor complex solution was synthesized as a stock solution with the amounts of reactants given in Table 6.4 as described in section 6.4. A schlenk flask with an UV/Vis spectroscopic immersion probe was filled with tetrahydrofuran (9.5 ml). The reaction mixture was place in an ethanol / dry ice + liquid nitrogen cooling bath (−80 °C) or an ethanol /liquid nitrogen cooling bath (−100 °C) (T given in Table 6.4). The solvent was saturated with molecular oxygen by bubbling the gas through the stirring reaction mixture for 5 min. A background spectrum of the oxygen-saturated reaction mixture was recorded. Subsequently, a new UV/Vis spectroscopic measurement was started and one tenth of the copper(I) precursor solution was injected. The UV/Vis spectroscopic measurement was ended when no change in the absorbance was visible for more than 15 min. All tested reaction conditions are given in Table 6.4.

Table 6.4: Amounts of copper(I) salt, ligand TMGphpy and solvent used for the preparation of copper(I) precursor species [Cu(TMGphpy)(CH_3CN)]PF_6 ([**Pr2**]PF_6) and [Cu(TMGphpy)]Br ([**Pr2**]Br) as well as conditions for the subsequent formation of a Cu_2O_2 species with molecular oxygen.

entry	**copper(I) salt CuBr (V(CH_3CN) [ml])**	**copper(I) salt [Cu(CH_3CN)$_4$]PF_6 (V(CH_3CN) [ml])**	**guanidine ligand TMGphpy (V(CH_3CN) [ml])**	**copper(I) precursor complex solution (V(CH_3CN) [ml])**	**Cu_2O_2 species [Cu_2O_2(TMGphpy)$_2$] X_2 (X = Br or PF_6) (V(CH_3CN) [ml]) (V(THF) [ml])**	**T[°C] solvents**
1	-	37.3 mg 0.10 mmol 2.0 eq. (4 ml)	26.8 mg 0.10 mmol 2.0 eq. (1 ml)	0.01 mmol 2.0 eq. (0.5 ml)	0.005 mmol 1.0 eq. 0.5 mM (0.5 ml) (9.5 ml)	- 80 °C CH_3CN / THF (1:19)
2	14.3 mg 0.10 mmol 2.0 eq. (4 ml)	-	26.8 mg 0.10 mmol 2.0 eq. (1 ml)	0.01 mmol 2.0 eq. (0.5 ml)	0.005 mmol 1.0 eq. 0.5 mM (0.5 ml) (9.5 ml)	- 80 °C CH_3CN / THF (1:19)
2	14.3 mg 0.10 mmol 2.0 eq. (4 ml)	-	26.8 mg 0.10 mmol 2.0 eq. (1 ml)	0.01 mmol 2.0 eq. (0.5 ml)	0.005 mmol 1.0 eq. 0.5 mM (0.5 ml) (9.5 ml)	- 100 °C CH_3CN / THF (1:19)

6.5.2 UV/Vis Spectroscopic Studies of Oxido Complex [Cu_2O_2(TMGdmap)$_2$](CF_3SO_3)$_2$ ([O3](OTf)$_2$)

The copper(I) precursor complex solution was synthesized as a stock solution with the amounts of reactants given in Table 6.5 as described in section 6.4. A schlenk flask with an UV/Vis spectroscopic immersion probe was filled with tetrahydrofuran (9.5 ml). The reaction mixture was place in an ethanol / dry ice + liquid nitrogen cooling bath (−80 °C). The solvent was saturated with molecular oxygen by bubbling the gas through the stirring reaction mixture for 5 min. A background spectrum of the oxygen-saturated reaction mixture was recorded. Subsequently, a new UV/Vis spectroscopic measurement was started and one tenth of the copper(I) precursor solution was injected. The UV/Vis spectroscopic measurement was ended after 14 h.

Table 6.5: Amounts of copper(I) salt, ligand TMGdmap and solvent used for the preparation of copper(I) precursor species [Cu(TMGdmap)(CH_3CN)]OTf ([**Pr3**]OTf) as well as conditions for the subsequent stability study of [Cu_2O_2(TMGdmap)$_2$](CF_3SO_3)$_2$ ([**O3**](OTf)$_2$).

copper(I) salt [Cu(CH_3CN)$_4$](CF_3SO_3) (V(CH_3CN) [ml])	**guanidine ligand TMGdmap (V(CH_3CN) [ml])**	**copper(I) precursor complex solution (V(CH_3CN) [ml])**	**[O3](OTf)$_2$ [Cu_2O_2(TMGdmap)$_2$]OTf_2 (V(CH_3CN) [ml]) (V(THF) [ml])**	**T[°C] solvents**
36.2 mg 0.10 mmol 2.0 eq. (4 ml)	20.0 mg 0.10 mmol 2.0 eq. (1 ml)	0.01 mmol 2.0 eq. (0.5 ml)	0.005 mmol 1.0 eq. 0.5 mM (0.5 ml) (9.5 ml)	- 80 °C CH_3CN / THF (1:19)

6.6 Catalytic Activity Studies with Oxido Complex [Cu_2O_2(TMG_2tol)$_2$](PF_6)$_2$ ([O1](PF_6)$_2$)

The catalyst species, oxido complex [Cu_2O_2(TMG_2tol)$_2$](PF_6)$_2$ ([**O1**](PF_6)$_2$), was synthesized in-situ during the catalytic oxygenation reaction. Tetrahydrofuran (20 ml) and molecular sieve (3 Å, 400 mg) were placed in a round bottom flask and stirred in an ethanol / dry ice + liquid nitrogen cooling bath (−80 °C, 300 rpm). Molecular oxygen was bubbled through the solution for 5 minutes. The previously synthesized copper(I) precursor complex solution (section 6.4, Table 6.6) was added to form the catalyst species [**O1**](PF_6)$_2$ (0.1 mmol, 1 eq.) in-situ. The reaction mixture stirred for 15 minutes to insure a complete formation of the catalyst species.

Catalytic oxygenation of phenolic substrates with [**O1**](PF_6)$_2$ as catalyst was performed based on literature.[87] Varying the reaction time between 1 and 8 h (Table 8.1 in the appendix), the ideal reaction time was found to be 8 h. The reaction temperature was increased to −80 °C. The purification process was slightly adapted using different solvent mixtures for column chromatography.

Table 6.6: Amounts of copper(I) salt, ligand TMG_2tol and solvent used for the preparation of copper(I) precursor species [Cu(TMG_2tol)(CH_3CN)]PF_6 [**Pr1**]PF_6 as well as conditions of the catalytic oxygenation reaction mediated by oxido complex [**O1**](PF_6)$_2$.

copper(I) salt [Cu(CH_3CN)$_4$]PF_6 (V(CH_3CN) [ml])	**guanidine ligand TMG_2tol (V(CH_3CN) [ml])**	**catalyst [^{S}P2] (PF_6)$_2$ (V(CH_3CN) [ml]) (V(THF) [ml])**	**molar ratio (n [mmol]) [[O1] (PF_6)$_2$]:[S]:[NEt_3]:[PDA]**	**T[°C] t [h] solvents**
74.6 mg 0.20 mmol 2.0 eq. (4 ml)	63.6 mg 0.20 mmol 2.0 eq. (1 ml)	0.10 mmol 1.0 eq. 4.0 mM (5 ml) (20 ml)	1:25:50:50	- 80 °C 8 h CH_3CN / THF (1:4)

After the formation of the catalyst species [**O1**](PF_6)$_2$, the oxygenation reaction was started by adding the substrate solution (substrate (S) 2.5 mmol, 25 eq.; triethylamine 0.7 ml, 5.0 mmol, 50 eq.; solvent amount given in Table 6.7) to the stirring reaction mixture at −80 °C. After 8 hours 1,2-phenylenediamine (PDA; 540.7 mg, 5.0 mmol, 50 eq.) dissolved in tetrahydrofuran (5 ml) was added and the cooling bath was removed. The reaction mixture was allowed to warm up to room temperature and stirred overnight. After adding an aqueous solution of hydrochloride acid (0.5 M, 30 ml) and 3 tablespoons of ethylenediaminetetraacetic acid (EDTA) the solvents were removed under reduced pressure (p = 50 mbar). The residue was extracted with dichloromethane (3×40 ml). The combined organic phases were dried over magnesium sulfate. After filtration of the suspension, the solvents were removed under reduce pressure (p = 50 mbar). The crude product was further purified by column chromatography. All catalyses were performed two or three times at least to provide reproducibility (Table 8.3 in the appendix).

Table 6.7: Composition of substrate solutions used for the catalytic hydroxylation and subsequent oxidation of phenolic substrates **S**.

substrate	solvent	V (solvent) [ml]	V (NEt$_3$) [ml]
1-naphthol (S1)	THF	1	0.7
2-anphthol (S2)	THF	1	0.7
3-quinolinol (S3)	THF	5	0.7
4-quinolinol (S4)	MeOH	3	0.7
5-quinolinol (S5)	MeOH	5	0.7
6-quinolinol (S6)	THF	5	0.7
4-indolol (S7)	THF	5	0.7
5-indolol (S8)	THF	2	0.7
6-indolol (S9)	THF	12	0.7
7-indolol (S10)	THF	10	0.7

6.6.1 Isolation and Purification of Phenazine Products (P)

Individual purification by column chromatography for each isolated phenazine product **P** obtained from the catalytic conversion of phenolic substances **S** with [**O1**](PF_6)$_2$ is given in the following Section 6.6.1.1 - 6.6.1.5.

6.6.1.1 Benzo[*a*]phenazine (P1)

Conversion of 1-naphthol (**S1**) as well as 2-naphthol (**S2**) with [**O1**](PF_6)$_2$ and subsequent purification via column chromatography (*n*-hexane:ethylacetate:methanol, 80:15:5) led to crystalline, yellow needles (Starting from S1: 7.5 mg, 0.033 mmol, 1%, TON <1; Starting from S2: 178.5 mg, 0.78 mmol, 31%, TON 8) of benzo[a]phenazine (P1; $R_f = 0.5$). Product **P1** was confirmed by ^{1}H NMR spectroscopy (Figure 8.7 in the appendix).[87]

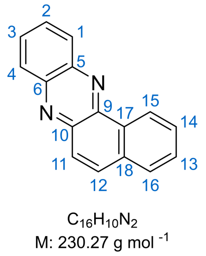

Figure 6.4: Molecular structure of benzo[*a*]phenazine (**P1**), numbers refer to the labels given in the ^{1}H NMR spectrum.

^{1}H NMR (400 MHz, dimethylsulfoxide-d$_6$ [s, 3.33 ppm]): δ [ppm] = 9.31 - 9.27 (m, 1H, H-15), 8.40 - 8.36 (m, 1H, H-1), 8.32 - 8.29 (m, 1H, H-4), 8.23 (dt, J_{HH} = 9.3 Hz, 0.6 Hz, 1H, H-11), 8.13 - 8.11 (m, 1H, H-16), 8.03 - 7.97 (m, 3H, H-2, H-3, H-12), 7.91 - 7.85 (m, 2H, H-13, H-14).

6.6.1.2 Quinolino[3,4-*b*]quinoxaline (P2)

Catalytic reaction of 3-quinolinol (**S3**) with [**O1**](PF_6)$_2$ followed by column chromatography (*n*-hexane:ethylacetate, 80:20) gave quinolino[3,4-*b*]quinoxaline (**P2**; $R_f = 0.52$) as a yellow solid (30.1 mg, 0.13 mmol, 5%, TON 1). Product **P2** was confirmed by ^{1}H NMR spectroscopy (Figure 8.8 in the appendix).[87]

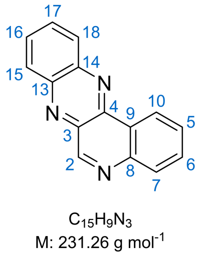

Figure 6.5: Molecular structure of quinolino[3,4-*b*]quinoxaline (**P2**), numbers refer to the labels given in the ^{1}H NMR spectrum.

^{1}H NMR (400 MHz, dimethylsulfoxide-d$_6$ [s, 3.33 ppm]): δ [ppm] = 9.61 (s, 1H, H-2), 9.17 (ddd, J_{HH} = 7.9, 1.5, 0.5 Hz, 1H, H-10), 8.45 – 8.41 (m, 2H, H-15, H-18), 8.23 (ddt, J_{HH} = 8.0, 1.4, 0.4 Hz, 1H, H-7), 8.18 – 8.07 (m, 2H, H-16, H-17), 8.01 (ddd, J_{HH} = 8.0, 7.2, 1.6 Hz, 1H, H-6), 7.94 – 7.90 (m, 1H, H-5).

6.6.1.3 Pyrido[3,2-*a*]phenazine (P3)

6-quinolinol (**S6**) was catalytically converted with [**O1**](PF_6)$_2$ resulting in brown needles (92.5 mg, 0.40 mmol, 16%, TON 4) of pyrido[3,2-*a*]phenazine (**P3**; $R_f = 0.34$) after purification via column chromatography (*n*-hexane:ethylacetate, 50:50). Product **P3** was confirmed by ^{1}H NNMR spectroscopy (Figure 8.9 in the appendix).[87]

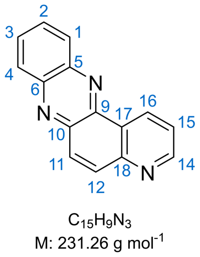

Figure 6.6: Molecular structure of pyrido[3,2-*a*]phenazine (**P3**), numbers refer to the labels given in the ^{1}H NMR spectrum.

^{1}H NMR (400 MHz, dimethylsulfoxide-d$_6$ [s, 3.33 ppm]): δ [ppm] = 9.57 (dd, J_{HH} = 8.2, 1.8 Hz, 1H, H-14), 9.15 (dd, J_{HH} = 4.5, 1.8 Hz, 1H, H-16), 8.43 – 8.34 (m, 2H, H-1, H-4), 8.28 (s, 2H, H-11, H-12), 8.09 – 8.03 (m, 2H, H-2, H-3), 7.90 (dd, J_{HH} = 8.2, 4.5 Hz, 1H, H-15).

6.6.1.4 3H-pyrrolo[3,2-*a*]phenazine (P4)

Starting from 5-indolol (**S8**) 3H-pyrrolo[3,2-a]phenazine (**P4**) was synthesized. Column chromatography (*n*-hexane:ethylacetate, 20:80) led to **P4** (**P3**; $R_f = 0.63$) as an orange solid (21.9 mg, 0.10 mmol, 4%, TON 1). Product **P4** was confirmed by ^{1}H NMR spectroscopy (Figure 8.10 in the appendix).[87]

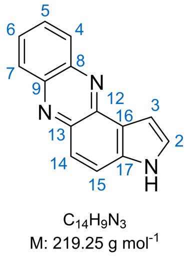

Figure 6.7: Molecular structure of pyrrolo[3,2-*a*]phenazine (**P4**), numbers refer to the labels given in the ^{1}H NMR spectrum.

^{1}H NMR (400 MHz, dimethylsulfoxide-d$_6$ [s, 3.33 ppm]): δ [ppm] = 12.09 (s, 1H, NH), 8.26 (dddd, J_{HH} = 13.5, 8.2, 1.8, 0.7 Hz, 2H, H-4, H-7), 8.07 (dd, J_{HH} = 9.2, 0.8 Hz, 1H, H-14), 7.97 – 7.84 (m, 2H, H-5, H-6), 7.79 (dd, J_{HH} = 9.2, 0.4 Hz, 1H, H-15), 7.57 (td, J_{HH} = 2.6, 0.4 Hz, 1H, H-2), 7.35 (ddd, J_{HH} = 2.9, 2.0, 0.8 Hz, 1H, H-3).

6.6.1.5 1H-pyrrolo[2,3-*a*]phenazine (P5)

Starting from 6-indolol (**S9**) the catalytic conversion with [**O1**](PF_6)$_2$ resulted in 1H-pyrrolo[2,3-*a*]phenazine (**P5**) as yellow solid (21.9 mg, 0.10 mmol, 4%, TON 1) after purification via column chromatography (*n*-hexane:ethylacetate:methanol, 48:48:4; R_f = 0.71). ^{1}H NMR signals of **P5** were in accordance with literature (Figure 8.11 in the appendix).[87]

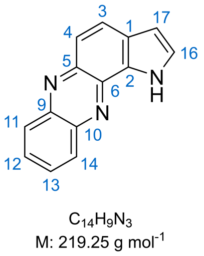

Figure 6.8: Molecular structure of pyrrolo[2,3-*a*]phenazine (**P5**), numbers refer to the labels given in the ^{1}H NMR spectrum.

^{1}H NMR (400 MHz, dimethylsulfoxide-d$_6$ [s, 3.33 ppm]): δ [ppm] = 12.85 (s, 1H, NH), 8.24 - 8.20 (m, 2H, H-11, H-14), 8.08 (dd, J_{HH} = 9.0 Hz, 0.6 Hz, 1H, H-4), 7.86 (dddd, J_{HH} = 20.7, 8.3, 6.7, 1.4 Hz, 2H, H-12, H-13), 7.65 (d, J_{HH} = 9.0 Hz, 1H, H-3), 7.53 (t, J_{HH} = 2.8 Hz, 1H, H-16), 6.74 (dd, J_{HH} = 2.8, 1.9 Hz, 1H, H-17).

6.6.2 Blank Experiments with copper(I) salt $[Cu(CH_3CN)_4]PF_6$ as Catalyst

Blank experiments were performed using the given amount of copper(I) salt $[Cu(CH_3CN)_4]PF_6$ to prepared the copper(I) precursor complex solution without any ligand species. Afterwards, the oxygenation reaction was performed as decribed in section 6.6. A list of all blank experiments performed is given in the appendix (Table 8.2).

Table 6.8: Amounts of copper(I) salt and solvent used for the preparation of copper(I) precursor species as well as conditions of the catalytic hydroxylation and subsequent oxidation reactions of phenolic substrates **S** performed with copper(I) salt $[Cu(CH_3CN)_4]PF_6$ as catalyst.

copper(I) salt $[Cu(CH_3CN)_4]PF_6$ ($V(CH_3CN)$ [ml])	**guanidine ligand TMG_2tol ($V(CH_3CN)$ [ml])**	**catalyst $[Cu(CH_3CN)_4]PF_6$ ($V(CH_3CN)$ [ml]) (V(THF) [ml])**	**molar ratio (n [mmol]) $[[Cu(CH_3CN)_4]PF_6]$:[S]:$[NEt_3]$:[PDA]**	**T[°C] t [h] solvents**
74.6 mg 0.20 mmol 2.0 eq. (5 ml)	-	0.20 mmol 2.0 eq. 8.0 mM (5 ml) (20 ml)	2:25:50:50	- 80 °C 8 h CH_3CN / THF (1:4)

6.6.3 Mass Spectrometry of Catalytic Conversions mediated by [O1]$(PF_6)_2$

The catalytic oxygenation reactions of 1-naphthol, 4-quinolinol and 4-indolol mediated by [**O1**]$(PF_6)_2$ were investigated using mass spectrometry. Experiments were performed as noted in section 6.6.

Cold-spray ionization mass spectrometry (CSI-MS) spectra were recorded at −80 °C directly after addition of the substrate solution. A few milliliter of the reaction mixture were removed with a gas-tight, pre-cooled Hamilton syringe and injected in the spectrometer. Electrospray ionization mass spectrometry (ESI-MS) spectra were recorded at room temperature after 8 hours reaction time, addition of PDA and extraction of the crude reaction mixture. A few milliliter of the reaction mixture were removed with a gas-tight Hamilton syringe and injected in the spectrometer. CSI-MS and ESI-MS spectra recorded can be found in **??** in the appendix (Figure 8.12 - 8.16).

6.7 Catalytic Activity Studies with Cu_2O_2 Species $[Cu_2O_2(TMGphpy)_2](PF_6)_2$ ([^{S}P2]$(PF_6)_2$)

Catalytic oxygenation of phenolic substrates with $[Cu_2O_2(TMGphpy)_2](PF_6)_2$ ([$^{\mathbf{S}}$**P2**]$(PF_6)_2$) as catalyst were performed as described in section 6.6 with a reaction time of 3 h at a temperature of −80 °C. The reaction was down scaled by a factor of 0.5 regarding the amount of reactants and solvents used (Table 6.9).

Table 6.9: Amounts of copper(I) salt, ligand TMGphpy and solvent used for the preparation of copper(I) precursor species [Cu(TMGphpy)(CH_3CN)]PF_6 [**Pr2**]PF_6 as well as conditions of the catalytic hydroxylation and subsequent oxidation reaction of phenolic substrates **S** mediated by presumed peroxido complex [$^{\mathbf{S}}$**P2**]$(PF_6)_2$.

copper(I) salt [Cu(CH_3CN)$_4$]PF_6 (V(CH_3CN) [ml])	guanidine ligand TMGphpy (V(CH_3CN) [ml])	catalyst [^{S}P2] $(PF_6)_2$ (V(CH_3CN) [ml]) (V(THF) [ml])	molar ratio (n [mmol]) [[O1] $(PF_6)_2$]:[S]:[NEt_3]:[PDA]	T[°C] t [h] solvents
37.3 mg 0.10 mmol 2.0 eq. (2 ml)	26.8 mg 0.10 mmol 2.0 eq. (0.5 ml)	0.05 mmol 1.0 eq. 4.0 mM (2.5 ml) (10 ml)	1:25:50:50	- 80 °C 3 h CH_3CN / THF (1:4)

6.8 Catalytic Activity Studies with Oxido Complex [Cu_2O_2(TMGdmap)$_2$](OTf)$_2$ ([O3](OTf)$_2$)

Catalytic oxygenation of phenolic substrates with [Cu_2O_2(TMGdmap)$_2$](OTf)$_2$ ([**O3**](OTf)$_2$) as catalyst were performed as described in section 6.6 with a reaction time of 3 h at a temperature of −80 °C. Amounts of copper(I) salt, ligand TMGdmap and solvent used for the preparation of copper(I) precursor species [Cu(TMGdmap)(CH_3CN)]CF_3SO_3 [**Pr3**]OTf as well as conditions of the catalytic oxygenation reaction mediated by oxido complex [**O3**](OTf)$_2$ are given in Table 6.10.

Table 6.10: Amounts of copper(I) salt, ligand TMGdmap and solvent used for the preparation of copper(I) precursor species [Cu(TMGdmap)(CH_3CN)]CF_3SO_3 [**Pr3**]OTf as well as conditions of the catalytic hydroxylation and subsequent oxidation reaction of phenolic substrates **S** mediated by oxido complex [**O3**](OTf)$_2$.

copper(I) salt [Cu(CH_3CN)$_4$]CF_3SO_3 (V(CH_3CN) [ml])	guanidine ligand TMGdmap (V(CH_3CN) [ml])	catalyst [O3] $(OTf)_2$ (V(CH_3CN) [ml]) (V(THF) [ml])	molar ratio (n [mmol]) [[O1] $(PF_6)_2$]:[S]:[NEt_3]:[PDA]	T[°C] t [h] solvents
72.2 mg 0.20 mmol 2.0 eq. (4 ml)	40.0 mg 0.20 mmol 2.0 eq. (1 ml)	0.1 mmol 1.0 eq. 4.0 mM (5 ml) (20 ml)	1:25:50:50	- 80 °C 3 h CH_3CN / THF (1:4)

6.9 Mechanistic Studies with TMGdmap

6.9.1 Resynthesis of Cu(II)-3,5-di-*tert*-butylcatecholate-TMGdmap ([3,5-DTB-CAT3])

Cu(II)-3,5-di-*tert*-butylcatecholate-TMGdmap ([**3,5-DTB-CAT3**]) was resynthesized after a literature-known protocol.[182]

The copper(II) catecholate complex [**3,5-DTB-CAT3**] was synthesized in a glovebox under nitrogen atmosphere. Copper powder was activated by washing with sulfuric acid (1 N), rinsing with methanol (three times) followed by diethyl ether (two times) and drying under high vacuum afterwards. The activated copper (50.0 mg, 0.80 mmol, 1.8 eq.) was dispersed in tetrahydrofuran (3.0 ml) and 3,5-di-*tert*-butyl-*o*-benzoquinone (100.0 mg, 0.45 mmol, 1 eq.) was added. The resulting suspension stirred overnight. TMGdmap (100.0 mg, 0.50 mmol, 1.1 eq.) was added and the reaction mixture stirred overnight for a second time. Subsequently, the dark suspension was filtered through a glass capillary filled with glass filter floss. The clear solution was overlaid with *n*-pentane (9 ml) resulting in small black crystals after two days suitable for X-ray diffraction. The molecular structure of [**3,5-DTB-CAT3**] was confirmed via SC-XRD. The molecular structure and crystal structure parameters can be found in the appendix (Table 8.4 and Figure 8.17).

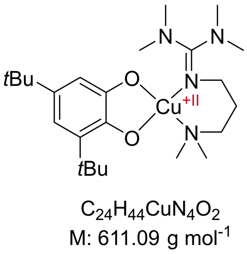

Figure 6.9: Molecular structure of Cu(II)-3,5-di-*tert*-butylcatecholate-TMGdmap ([**3,5-DTB-CAT3**]).

6.9.1.1 EPR Spectroscopic Measurements of [3,5-DTB-CAT3]

For EPR spectroscopic measurements of [**3,5-DTB-CAT3**] solutions, the complex was diluted in tetrahydrofuran at room temperature in a glovebox under nitrogen atmosphere, filled in a glass capillary and frozen in liquid nitrogen (−196 °C) until the measurement.

For EPR spectroscopic measurements of [**3,5-DTB-CAT3**] solid samples, the crystals were filled in a glass capillary in a glovebox under nitrogen atmosphere and frozen in liquid nitrogen afterwards (−196 °C)

6.9.2 Stoichiometric Conversion of Sodium Phenolates mediated by Oxido Complex $[Cu_2O_2(TMGdmap)_2](CF_3SO_3)_2$ ([O3](OTf)$_2$)

Substrate solutions were prepared in a twentyfold stock solution under inert conditions by dissolving the respective sodium phenolate (0.20 mmol) in tetrahydrofuran (4.0 ml). One-twentieth of the substrate stock solution (0.2 ml, 0.01 mmol, 2 eq.) was drawn up in a Hamilton syringe.

The precursor copper(I) complex [Cu(TMGdmap)(CH_3CN)](CF_3SO_3) ([**Pr3**]OTf) was prepared in a tenfold stock solution under inert conditions by dissolving equimolar amounts of guanidine ligand TMGdmap (20.0 mg, 0.100 mmol) and copper(I) salt [Cu(CH_3CN)$_4$]OTf (37.8 mg, 0.100 mmol) in acetonitrile (5 ml). One-tenth of the stock solution of the precursor copper(I) complex [**Pr3**]OTf (0.5 ml, 0.01 mmol, 2 eq.) was drawn up in a Hamilton syringe and added rapidly to stirring, oxygen-saturated tetrahydrofuran (9.5 ml) at −100 °C to generate the oxido complex [Cu_2O_2(TMGdmap)$_2$](CF_3SO_3)$_2$ ([**O3**](OTf)$_2$) (0.005 mmol, 1 eq.). The reaction mixture was stirred for 15 min to ensure full formation of the oxido complex.

To perform a reaction with substrate conversion, the phenolate conversion was started by injecting the substrate solution into the reaction mixture.

6.9.2.1 EPR Spectroscopic Measurements of the Stoichiometric Conversion of Sodium Phenolates mediated by [O3](OTf)$_2$

For EPR spectroscopic measurements of the stoichiometric conversion of sodium phenolates by [**O3**](OTf)$_2$ a gas-tight, EPR-silent Wilmad© Suprasil-Young-tube was cooled down to (−100 °C) in an ethanol/nitrogen cooling bath. A sample was taken from the reaction mixture with a Hamilton syringe and filled in the Young-tube rapidly under nitrogen counter-flow. The tube was closed immediately and stored in liquid nitrogen (−196 °C) until the measurement.

6.10 Hele-Shaw Cell Studies with Oxido Complex [Cu_2O_2(TMG_2tol)$_2$](OTf)$_2$ ([O1](OTf)$_2$)

6.10.1 Determination of the Diffusion Coefficient of the Diluted Reactant - Copper(I) Precursor Complex [Pr1]OTf

Acetonitrile-d$_3$ was distilled under nitrogen atmosphere over calcium hydride and subsequently degased before usage.

The copper(I) salt [Cu(CH_3CN)$_4$](CF_3SO_3)) (18.9 mg, 0.05 mmol,1 eq.) was diluted in acetonitrile-d$_3$ (2.0 ml). A solution of TMG_2tol (**L1**; 15.9 mg, 0.05 mmol, 1 eq.) dissolved in acetonitrile-d$_3$ (0.5 ml) was added dropwise. The resulting copper(I) precursor complex solution of [Cu(TMG_2tol)(CH_3CN)]CF_3SO_3 ([**Pr1**]OTf; c = 20 mM) was drawn in a gas-tight Young-NMR tube.

The diffusion coefficient of [**Pr1**]OTf in acetonitrile was determined by NMR spectroscopic measurements using diffusion-ordered spectroscopy (DOSY) and found equal to $D_{O_2} = 1.28 \pm 0.04 \cdot 10^{-9}\ m^2\,s^{-1}$.

6.10.2 Determination of the Surface Tension of the Final Product - Hydroxido Complex [Cu$_2$(OH)$_2$(TMG$_2$tol)$_2$](OTf)$_2$

The copper(I) salt [Cu(CH$_3$CN)$_4$](CF$_3$SO$_3$)) (37.8 mg, 0.1 mmol,1 eq.) was diluted in acetonitrile (4.0 ml). A solution of TMG$_2$tol (**L1**; 31.8 mg, 0.1 mmol, 1 eq.) dissolved in acetonitrile (1.0 ml) was added dropwise. The resulting copper(I) precursor complex solution of [Cu(TMG$_2$tol)(CH$_3$CN)]CF$_3$SO$_3$ ([**Pr1**]OTf; c = 20 mM) was drawn in a gas-tight Schlenk tube with stirring bar. Subsequently, molecular oxygen was bubbled through the stirring solution of [**Pr1**]OTf for 5 minutes at 20 °C to form the copper(II) hydroxido complex [Cu$_2$(OH)$_2$(TMG$_2$tol)$_2$](CF$_3$SO$_3$)$_2$.

The surface tension of [Cu$_2$(OH)$_2$(TMG$_2$tol)$_2$](OTf)$_2$ was measured on a tensiometer using the pendant-drop method and found to be equal to $\sigma = 28.9$ mN m^{-1} (T = 20 °C; $c = 20$ mmol l^{-1}).

6.10.3 High-Speed Gray-level Imaging

Gray-level images were recorded with a 16-bit sCMOS PCO Edge 2560×2160 px camera equipped with a 50 mm 1:12 Nikon lens within a region-of-interest (ROI) window. The ROI window (height: 57 mm, width: 161 mm) was horizontally centered on the cell front. The camera was located at a distance of 750 mm from the ROI window. Time-series of grey-level images at 100 Hz (exposure time 0.8 - 4 ms) were captured with a scale ratio of 15.9 px mm^{-1}.

For calibration measurements and experiments performed by A. Bèteille a red band-pass filter (MV660/20 from CHROMA©, center wavelength: 660 nm, optical density (OD) ≥ 6.0 below 640 nm, OD ≥ 6.0 at 680-760 nm) was attached to the camera lens.

6.10.4 Hele-Shaw Cell (HSC) Set-Up

The dimensions of the planar vertically-located thin-gap cell are 400 mm in height and 200 mm in width with a gap width of 1.062 mm ± 0.005 mm (measured by Confocal Laser Microscope). The liquid phase inside the cell is at rest. Single bubbles of molecular oxygen are generated by using a small quartz glass capillary ($d = 0.5$ mm) at the bottom of the cell connected to a gas cylinder of molecular oxygen over a gas line with a valve for manual opening and closing. The Hele-Shaw cell (HSC) is operated under oxygen-free conditions with a slight nitrogen overpressure. The cell is filled and emptied via stainless-steel tubes, valves using nitrogen overpressure. The cell was illuminated from behind (opposite to the camera direction) with a collimated white light-emitting-diode (LED) backlight panel (PHLOX, 400 × 200 mm^2, 24 V, A = 0.47 mA).

6.10.5 HSC Measurements of Single Rising Molecular Oxygen Bubbles

For experiments with freely-rising molecular oxygen bubbles, the copper(I) precursor complex solution of [Cu(TMG$_2$tol)(CH$_3$CN)]OTf ([**Pr1**]OTf) was prepared directly before the experiment in a glovebox (M. BRAUN) under argon atmosphere. Equimolar amounts of copper(I) salt (603 mg, 1.6 mmol) and guanidine ligand (510 mg, 1.6 mmol) were added in a beaker and diluted in acetonitrile (100 ml; Fisher Scientific, 100%, OPTIMA$^©$ LC/MS GRADE packed under nitrogen). The colorless copper(I) precursor complex solution (c ([**Pr1**]OTf) = 16.0 mM) was filled into a gas-tight stainless-steel vessel. The vessel was fixed to the stainless-steal tubes within the experimental set-up using a nitrogen counterflow to avoid air contact. The HSC was filled with the copper(I) precursor complex solution using nitrogen overpressure. A background image was recorded. The gray-level image recording was started. Single bubbles of molecular oxygen were injected in the HSC by opening and subsequently closing the valve at the glass capillary at the bottom of the cell quickly by hand. Oxido complex [Cu$_2$O$_2$(TMG$_2$tol)$_2$](OTf)$_2$ ([**O1**](OTf)$_2$) and hydroxido complex [Cu$_2$(OH)$_2$(TMG$_2$tol)$_2$](PF$_6$)$_2$ are formed in the bubble wake as well as the bubble's vicinity in situ. When the gas bubble had reached the top of the cell, the HSC was flushed with nitrogen for 10 s. When the liquid was at rest again, a new background image was recorded before another freely-rising molecular oxygen bubble was released. After the recording of ten bubbles the whole set-up was emptied out and cleaned by flushing it with acetonitrile (3x; VWR, 99.95%, for HPLC, SUPER GRADIENT, water $<$ 30 ppm) and nitrogen (2x) afterwards.

Five examples of the analyzed raw picture series of different bubble sizes are deposited in the repository RADAR4Chem by FIZ Karlsruhe - Leibniz-Institut für Informationsinfrastruktur and are published under an Open Access model (CC BY-NC-SA 4.0 Attribution-NonCommercial-ShareAlike). The data can be downloaded under: https://doi.org/10.22000/872

Colored video of a bubble freely rising in thin-gap cell, recorded to show the reaction and color changes taking place within the rising gas bubble and its bubble wake are deposited in the AV portal of the technical information library (TIB) Hannover. Data can be found and downloaded under: https://doi.org/10.5446/60173 (in real speed) and https://doi.org/10.5446/60174 (in slow motion).

6.10.6 Calibration Measurements

For calibration measurements, different copper(I) precursor complex solutions of [**Pr1**]OTf with various concentrations (Table 6.11) were synthesized as described before in Section 6.10.5. The HSC was filled with the solution. Subsequently, the reaction mixture was saturated with molecular oxygen by bubbling the gas through the solution for 30 s. When the solution was at rest again, a gray-level image was recorded. Finally, the whole set-up was emptied out and cleaned by flushing it with acetonitrile (3x; VWR, 99.95% for HPLC, SUPER GRADIENT, water < 30 ppm) and nitrogen (2x) afterwards.

Table 6.11: Amounts of copper(I) salt [Cu(CH$_3$CN)$_4$](CF$_3$SO$_3$) and ligand TMG$_2$tol used for the preparation of copper(I) precursor species [Cu(TMG$_2$tol)(CH$_3$CN)]CF$_3$SO$_3$ [**Pr1**]OTf as well as concentrations of the formed [**Pr1**]OTf solution and the resulting oxido complex [**O1**](OTf)$_2$ ([Cu$_2$O$_2$(TMG$_2$tol)$_2$](CF$_3$SO$_3$)$_2$) after conversion with molecular oxygen for calibration measurements performed in the Hele-Shaw cell.

guanidine ligand TMG$_2$tol [mg]	**copper(I) salt [Cu(CH$_3$CN)$_4$]OTf [mg]**	***c*([Pr1] OTf) [mM]**	***c*([O1] (OTf)$_2$) [mM]**
15.9	18.8	0.500	0.250
23.9	28.3	0.750	0.375
31.8	37.7	1.00	0.500
47.8	56.5	1.50	0.750
63.7	75.4	2.00	1.00
95.5	113.0	3.00	1.50
127.4	150.7	4.00	2.00
159.2	188.4	5.00	2.50
222.9	263.8	7.00	3.50
286.6	339.1	9.00	4.50
414.0	489.9	13.0	6.50
509.6	602.9	16.0	8.00

6.11 Large Scale Bubble Column Studies with Peroxido Complex [$^{\mathrm{S}}$P4](OTf)$_2$ and *para*-methoxyphenol

6.11.1 Targeted Synthesis of the *Ortho*-quinone Product

A literature-known synthesis protocol[101] was used switching the substrate 2,4-di-*tert*-butylphenol for *para*-methoxyphenol.

In a glove box (M.BRAUN) under nitrogen atmosphere, the copper(I) salt tetrakis(acetonitrile)copper(I) hexafluorophosphate ([Cu(CH$_3$CN)$_4$]PF$_6$; 149.1 mg, 0.4 mmol, 0.08 eq.) was diluted in dichloromethane (3 ml). The solution was drawn in a gas-tight Hamilton syringe and stored in a Schlenk tube until further usage.

A round bottom flask was filled with *para*-methoxyphenol (620.7 mg, 5.0 mmol, 1 eq.) and molecular sieve (3 Å, 300 mg). The flask was evacuated and flushed with nitrogen afterwards. Dichloromethane (27 ml) and triethylamine (0.35 ml, 2.5 mmol, 0.5 eq.) were added and the reaction mixture was stirred at room temperature. After addition of the copper(I) salt solution, the solution was stirred over the course of an hour. The reaction was terminated by the addition of sodium hydrogen sulfate solution (6 g in 60 ml water).

The mixture was extracted with dichloromethane (3x 30 ml). Subsequently, the combined organic phases were dried over magnesium sulfate and filtered. The solvent was removed under reduced pressure (50 mbar).

6.11.2 Targeted Synthesis of the Biphenol Product

A literature-known synthesis protocol[101] was used switching the substrate 2,4-di-*tert*-butylphenol for *para*-methoxyphenol.

In a glovebox (M.BRAUN) under nitrogen atmosphere, the copper(I) salt CuCl (22.9 mg, 0.17 mmol, 0.08 eq.) was diluted in dichloromethane (3 ml). The solution was drawn in a gas-tight Hamilton syringe and stored in a Schlenk tube until further usage.

A round bottom flask was filled with *para*-methoxyphenol (268.1 mg, 2.2 mmol, 1 eq.) and molecular sieve (3 Å, 300 mg). The flask was evacuated and flushed with nitrogen afterwards. Dichloromethane (7 ml) and triethylamine (0.15 ml, 1.1 mmol, 0.5 eq.) were added and the reaction mixture was stirred at room temperature. After addition of the copper(I) salt solution, the solution was stirred over the course of an hour. The reaction was terminated by the addition of pottasium hydrogen sulfate solution (2 g in 20 ml water). The mixture was extracted with dichloromethane (3x 20 ml). Subsequently, the combined organic phases were dried over magnesium sulfate and filtered. The solvent was removed under reduced pressure (50 mbar).

6.11.3 Targeted Synthesis of Formed Reaction Products

The synthesis was based on a literature-known synthesis protocol[101] whereby the substrate, 2,4-di-*tert*-butylphenol, was switched for *para*-methoxyphenol. All reaction were performed in tetrahydrofuran at room temperature. Reaction time as well as amounts of auxiliary base triethylamine and substrate *para*-methoxyphenol were varied (Table 6.12).

In a glove box (M.BRAUN) under nitrogen atmosphere, the copper(I) salt tetrakis(acetonitrile)copper(I) trifluoromethanesulfonate ($[Cu(CH_3CN)_4](CF_3SO_3)$; 47.1 mg, 0.125 mmol, 4 eq.) was diluted in tetrahydrofuran (4 ml). DBED (26.9 mg, 0.156 mmol, 5 eq.) was dissolved in tetrahydrofuran (1 ml) and added dropwise to the copper(I) salt solution. The resulting copper(I) precursor complex solution of [**Pr4**]OTf ($[Cu(DBED)(CH_3CN)]CF_3SO_3$) was drawn in a gas-tight Hamilton syringe and stored in a Schlenk tube until further usage.

A round bottom flask was filled with *para*-methoxyphenol. The flask was evacuated and flushed with nitrogen afterwards. tetrahydrofuran (15 ml) and triethylamine were added and the reaction mixture was stirred at room temperature. After addition of the copper(I) precursor complex solution ([**Pr4**]OTf), the reaction mixture was stirred over the course of the reaction time given in Table 6.12. The reaction was terminated by the addition of hydrochloride acid solution (0.5 M, 20 ml) and 3 tablespoons of ethylenediaminetetraacetic acid (EDTA). The solvents were removed under reduced pressure (p = 50 mbar). The residue was extracted with dichloromethane (3 × 20 ml). The combined organic phases were dried over magnesium sulfate. After filtration of the suspension, the solvents were removed under reduce pressure (p=50 mbar). The crude product was further purified by column chromatography (ethylacetat : *n*-hexane, 60:40). All varied reaction conditions were repeated two to four times. A summary of all experiments performed can be found in the appendix (Table 8.5).

Crystals suitable for X-ray diffraction were recrystallized from the solvent mixture after column chromatography (entry 9 and 13 in Table 8.5 in the appendix.)

Table 6.12: Reaction time and amounts of triethylamine and *para*-methoxyphenol used for the catalytic conversion with peroxido complex [^{S}**P4**](OTf)$_2$ ([Cu_2O_2(DBED)$_2$](CH_3SO_3)$_2$) as catalyst species.

triethylamine (NEt_3)	***para*-methoxy-phenol (4-OMe-Ph)**	**t**	**molar ratio [^{S}P] : [4-OMe-Ph]: [NEt_3]**
0.45 ml 3.24 mmol 50 eq.	388.0 mg 3.12 mmol 50 eq.	10 min	1 : 50 : 50
0.45 ml 3.24 mmol 50 eq.	388.0 mg 3.12 mmol 50 eq.	20 min	1 : 50 : 50
0.45 ml 3.24 mmol 50 eq.	388.0 mg 3.12 mmol 50 eq.	2 h	1 : 50 : 50
0.45 ml 3.24 mmol 50 eq.	388.0 mg 3.12 mmol 50 eq.	13 h	1 : 50 : 50
0.09 ml 0.648 mmol 10 eq.	77.6 mg 0.624 mmol 10 eq.	13 h	1 : 10 : 10
0.02 ml 0.145 mmol 5 eq.	18.0 mg 0.145 mmol 5 eq.	13 h	1 : 5 : 5
0.09 ml 0.648 mmol 10 eq.	77.6 mg 0.624 mmol 10 eq.	24 h	1 : 10 : 10
0.09 ml 0.648 mmol 10 eq.	77.6 mg 0.624 mmol 10 eq.	5 h	1 : 10 : 10
0.09 ml 0.648 mmol 10 eq.	77.6 mg 0.624 mmol 10 eq.	5 h	1: 10 : 10

7 References

[1] R. Goyal, O. Singh, A. Agrawal, C. Samanta, B. Sarkar*, Catal. Rev.: Sci. Eng.* **2022***, 64*, 229–285. DOI 10.1080/01614940.2020.1796190

[2] F. Cavani, J. H. Teles*, ChemSusChem* **2009***, 2*, 508–534. DOI 10.1002/cssc.200900020

[3] B. Schreiner*, Chem. Unserer Zeit* **2008***, 42*, 378–392. DOI 10.1002/ciuz.200800461

[4] O. Menke, F. Ruslim, U. Kuessel, G. Steidel, G. Schwabe, W. Ferstl, N. Kokarakis (BASF SE), EP3081923A1, **2016**.

[5] M. Baerns, A. Behr, A. Brehm, J. Gmehling, K.-O. Hinrichsen, H. Hofmann, R. Palkovits, U. Onken, A. Renken, *Technische Chemie*, 2nd Ed., Wiley-VCH, Weinheim, **2013**.

[6] W. E. Smith, *Minamata, Words and photos. By W. Eugene Smith and Aileen M. Smith*, 1st Ed., Chatto & Windus, London, **1975**.

[7] M. Harada, S. Tsushima, T. S. George, *Minamata disease*, English ed., Kumamoto Nichinichi Shinbun Culture & Information Center, [Kumamoto, Japan], **2004**, 215 pp.

[8] M. Kaji*, Ethics. Sci. Environ. Polit.* **2012***, 12*, 99–111. DOI 10.3354/esep00126

[9] Bundesinstitut für gesundheitlichen Verbraucherschutz und Veterinärmedizin, Robert Koch-Institut, Umweltbundesamt, Dokumentation zum Aktionsprogramm Umwelt und Gesundheit, Sachstand - Problemaufriß - Optionen, (Ed.: Bundesministerium für Gesundheit), **1999**, https://www.umweltbundesamt.de/sites/default/files/medien/4031/dokumente/apug_dokumentation_vollversion.pdf.

[10] P. T. Anastas, J. C. Warner, *Green chemistry, Theory and Practice*, Oxford University Press, New York, **1998**, 135 pp.

[11] I. T. Horváth, *Encyclopedia of catalysis*, 1st Ed., Horváth, István T. (Hrsg.), Wiley, Hoboken, NJ, **2003**.

[12] P. Anastas, N. Eghbali*, Chem. Soc. Rev.* **2010***, 39*, 301–312. DOI 10.1039/B918763B

[13] P. T. Anastas, M. M. Kirchhoff*, Acc. Chem. Res.* **2002***, 35*, 686–694. DOI 10.1021/ar010065m

[14] Classification and Labelling Inventory of the European Chemical Agency, cobalt di(acetate), (Ed.: Classification and Labelling Inventory of the European Chemical Agency), https://echa.europa.eu/information-on-chemicals/cl-inventory-database/-/discli/details/126330 (visited on 03/20/2024).

[15] Classification and Labelling Inventory of the European Chemical Agency, vanadium pentoxide, (Ed.: Classification and Labelling Inventory of the European Chemical Agency), https://echa.europa.eu/information-on-chemicals/cl-inventory-database/-/discli/details/103892 (visited on 03/20/2024).

[16] K. Ray, F. F. Pfaff, B. Wang, W. Nam*, J. Am. Chem. Soc.* **2014***, 136*, 13942–13958. DOI 10.1021/ja507807v

[17] L. M. Mirica, X. Ottenwaelder, T. D. P. Stack*, Chem. Rev.* **2004***, 104*, 1013–1045. DOI 10.1021/cr020632z

[18] J. J. Stephanos, A. W. Addison, *Chemistry of Metalloproteins: Problems and Solutions in Bioinorganic Chemis*, 1st Ed., John Wiley & Sons, Hoboken, NJ, USA, **2014**.

[19] L. Que, W. B. Tolman*, Nature* **2008***, 455*, 333–340. DOI 10.1038/nature07371

[20] X. Engelmann, I. Monte-Pérez, K. Ray*, Angew. Chem., Int. Ed.* **2016***, 55*, 7632–7649. DOI 10.1002/anie.201600507

[21] S. D. McCann, S. S. Stahl*, Acc. Chem. Res.* **2015***, 48*, 1756–1766. DOI 10.1021/acs.accounts.5b00060

[22] J. Reedijk, *Bioinorganic Catalysis*, 2nd Ed., in collab. with E. Bouwman, Reedijk, Jan (VerfasserIn) Bouwman, Elisabeth (MitwirkendeR), CRC Press - Taylor & Francis Group, Boca Raton, FL, USA, **1999**.

[23] W. Kaim, J. Rall*, Angew. Chem., Int. Ed. Engl.* **1996***, 35*, 43–60. DOI 10.1002/anie.199600431

[24] H. B. Gray, B. G. Malmström, R. J. Williams*, JBIC, J. Biol. Inorg. Chem.* **2000***, 5*, 551–559. DOI 10.1007/s007750000146

[25] M. Pascaly, I. Jolk, B. Krebs*, Chem. Unserer Zeit* **1999***, 33*, 334–341. DOI 10.1002/ciuz.19990330604

[26] R. L. Lieberman, A. C. Rosenzweig*, Nature* **2005***, 434*, 177–182. DOI 10.1038/nature03311

[27] H. Basch, K. Mogi, D. G. Musaev, K. Morokuma*, J. Am. Chem. Soc.* **1999***, 121*, 7249–7256. DOI 10.1021/ja9906296

[28] J. Bae, S. Jin, S. Kang, B.-K. Cho, M.-K. Oh **2022***, 78*, 102836. DOI 10.1016/j.copbio.2022.102836

[29] E. I. Solomon, U. M. Sundaram, T. E. Machonkin*, Chem. Rev.* **1996***, 96*, 2563–2606. DOI 10.1021/cr950046o

[30] P. M. Plonka, M. Grabacka*, Acta Biochim. Pol.* **2006***, 53*, 429–443.

[31] R. A. Sheldon, *Green Chemistry and Catalysis*, Wiley-VCH, Weinheim, **2007**.

[32] S. Wu, R. Snajdrova, J. C. Moore, K. Baldenius, U. T. Bornscheuer*, Angew. Chem., Int. Ed.* **2021***, 60*, 88–119. DOI 10.1002/anie.202006648

[33] H. Decker, F. Tuczek*, Trends Biochem. Sci.* **2000***, 25*, 392–397. DOI 10.1016/s0968-0004(00)01602-9

[34] A. Messerschmidt in *Chemistry and Biology*, (Eds.: L. Mander, H.-W. Liu), Comprehensive Natural Products II, Elsevier, Amsterdam, **2010**, pp. 489–545.

[35] W. Kaim, B. Schwederski, *Bioanorganische Chemie, Zur Funktion chemischer Elemente in Lebensprozessen*, 4th Ed., Vieweg+Teubner, Wiesbaden, **2010**.

[36] J. M. Guss, H. D. Bartunik, H. C. Freeman*, Acta Crystallogr., Sect. B* **1992***, 48 (Pt 6)*, 790–811. DOI 10.1107/S0108768192004270

[37] K. D. Karlin, S. Itoh in *Wiley Series on Reactive Intermediates in Chemistry and Biology*, (Ed.: S. E. Rokita), Wiley, Weinheim, **2011**.

[38] Y. Matoba, T. Kumagai, A. Yamamoto, H. Yoshitsu, M. Sugiyama*, J. Biol. Chem.* **2006***, 281*, 8981–8990. DOI 10.1074/jbc.M509785200

[39] N. Ito, S. E. Phillips, C. Stevens, Z. B. Ogel, M. J. McPherson, J. N. Keen, K. D. Yadav, P. F. Knowles*, Nature* **1991***, 350*, 87–90. DOI 10.1038/350087a0

[40] N. Ito, S. E. Phillips, K. D. Yadav, P. F. Knowles*, J. Mol. Biol.* **1994***, 238*, 794–814. DOI 10.1006/jmbi.1994.1335

[41] H. Decker, T. Rimke*, J. Biol. Chem.* **1998***, 273*, 25889–25892. DOI 10.1074/jbc.273.40.25889

[42] B. Hazes, K. A. Magnus, C. Bonaventura, J. Bonaventura, Z. Dauter, K. H. Kalk, W. G. Hol*, Protein Sci.* **1993***, 2*, 597–619. DOI 10.1002/pro.5560020411

[43] I. Kipouros, A. Stańczak, M. Culka, E. Andris, T. R. Machonkin, L. Rulíšek, E. I. Solomon*, Chem. Commun.* **2022***, 58*, 3913–3916. DOI 10.1039/d2cc00750a

[44] C. Gerdemann, C. Eicken, B. Krebs, *Acc. Chem. Res.* **2002**, *35*, 183–191. DOI 10.1021/ar990019a

[45] I. Kipouros, A. Stańczak, J. W. Ginsbach, P. C. Andrikopoulos, L. Rulíšek, E. I. Solomon, *Proc. Natl. Acad. Sci. U. S. A.* **2022**, *119*, e2205619119. DOI 10.1073/pnas.2205619119

[46] I. Galván, F. Solano, *Int. J. Mol. Sci.* **2016**, *17*, 520. DOI 10.3390/ijms17040520

[47] A. J. Nappi, E. Ottaviani, *BioEssays* **2000**, *22*, 469–480. DOI 10.1002/(SICI)1521-1878(200005)22:5%3C469::AID-BIES9%3E3.0.CO;2-4

[48] C. R. Scriver, *J. Inherited Metab. Dis.* **2008**, *31*, 580–598. DOI 10.1007/s10545-008-0984-9

[49] D. E. Wilcox, A. G. Porras, Y. T. Hwang, K. Lerch, M. E. Winkler, E. I. Solomon, *J. Am. Chem. Soc.* **1985**, *107*, 4015–4027. DOI 10.1021/ja00299a043

[50] T. Inoue, Y. Shiota, K. Yoshizawa, *J. Am. Chem. Soc.* **2008**, *130*, 16890–16897. DOI 10.1021/ja802618s

[51] T. Osako, K. Ohkubo, M. Taki, Y. Tachi, S. Fukuzumi, S. Itoh, *J. Am. Chem. Soc.* **2003**, *125*, 11027–11033. DOI 10.1021/ja029380+

[52] N. Kitajima, T. Koda, Y. Iwata, Y. Morooka, *J. Am. Chem. Soc.* **1990**, *112*, 8833–8839. DOI 10.1021/ja00180a026

[53] N. Kitajima, K. Fujisawa, C. Fujimoto, Y. Morooka, S. Hashimoto, T. Kitagawa, K. Toriumi, K. Tatsumi, A. Nakamura, *J. Am. Chem. Soc.* **1992**, *114*, 1277–1291. DOI 10.1021/ja00030a025

[54] L. Q. Hatcher, M. A. Vance, A. A. Narducci Sarjeant, E. I. Solomon, K. D. Karlin, *Inorg. Chem.* **2006**, *45*, 3004–3013. DOI 10.1021/ic052185m

[55] L. M. Mirica, M. Vance, D. J. Rudd, B. Hedman, K. O. Hodgson, E. I. Solomon, T. D. P. Stack, *Science* **2005**, *308*, 1890–1892. DOI 10.1126/science.1112081

[56] M. Rolff, J. Schottenheim, F. Tuczek, *J. Coord. Chem.* **2010**, *63*, 2382–2399. DOI 10.1080/00958972.2010.503273

[57] G. Battaini, M. de Carolis, E. Monzani, F. Tuczek, L. Casella, *Chem. Commun.* **2003**, 726–727. DOI 10.1039/B212683D

[58] L. Santagostini, M. Gullotti, E. Monzani, L. Casella, R. Dillinger, F. Tuczek, *Chem. Eur. J.* **2000**, *6*, 519–522. DOI 10.1002/(SICI)1521-3765(20000204)6:3%3C519::AID-CHEM519%3E3.0.CO;2-I

[59] M. Réglier, C. Jorand, B. Waegell, *J. Chem. Soc., Chem. Commun.* **1990**, 1752–1755. DOI 10.1039/C39900001752

[60] H. Decker, R. Dillinger, F. Tuczek, *Angew. Chem., Int. Ed.* **2000**, *39*, 1591–1595. DOI 10.1002/(SICI)1521-3773(20000502)39:9%3C1591::AID-ANIE1591%3E3.0.CO;2-H

[61] M. Rolff, J. Schottenheim, G. Peters, F. Tuczek, *Angew. Chem., Int. Ed.* **2010**, *49*, 6438–6442. DOI 10.1002/anie.201000973

[62] L. Q. Hatcher, K. D. Karlin, *JBIC, J. Biol. Inorg. Chem.* **2004**, *9*, 669–683. DOI 10.1007/s00775-004-0578-4

[63] K. Krumova, G. Cosa in *Singlet Oxygen: Applications in Biosciences and Nanosciences*, (Eds.: S. Nonell, C. Flors), 13 vols., Comprehensive Series in Photochemical and Photobiological Science 13, Royal Society of Chemistry, Cambridge, **2016**.

[64] *Singlet Oxygen: Applications in Biosciences and Nanosciences*, Vol. 1, (Eds.: S. Nonell, C. Flors), 13 vols., Royal Society of Chemistry, Cambridge, **2016**, 1 p.

[65] M. Metz, E. I. Solomon, *J. Am. Chem. Soc.* **2001**, *123*, 4938–4950. DOI 10.1021/ja004166b

[66] A. Volbeda, W. G. Hol, *J. Mol. Biol.* **1989**, *209*, 249–279. DOI 10.1016/0022-2836(89)90276-3

[67] A. Dei, D. Gatteschi, L. Pardi, A. L. Barra, L. C. Brunel, *Chem. Phys. Lett.* **1990**, *175*, 589–592. DOI 10.1016/0009-2614(90)85586-2

[68] L. Noodleman **1981**, *74*, 5737–5743. DOI 10.1063/1.440939

[69] J. Yoon, L. M. Mirica, T. D. P. Stack, E. I. Solomon, *J. Am. Chem. Soc.* **2004**, *126*, 12586–12595. DOI 10.1021/ja046380w

[70] R. R. Jacobson, Z. Tyeklar, A. Farooq, K. D. Karlin, S. Liu, J. Zubieta, *J. Am. Chem. Soc.* **1988**, *110*, 3690–3692. DOI 10.1021/ja00219a071

[71] Z. Tyeklar, R. R. Jacobson, N. Wei, N. N. Murthy, J. Zubieta, K. D. Karlin, *J. Am. Chem. Soc.* **1993**, *115*, 2677–2689. DOI 10.1021/ja00060a017

[72] N. Kitajima, K. Fujisawa, Y. Morooka, K. Toriumi, *J. Am. Chem. Soc.* **1989**, *111*, 8975–8976. DOI 10.1021/ja00206a062

[73] K. A. Magnus, B. Hazes, H. Ton-That, C. Bonaventura, J. Bonaventura, W. G. Hol, *Proteins: Struct., Funct., Genet.* **1994**, *19*, 302–309. DOI 10.1002/prot.340190405

[74] S. Mahapatra, J. A. Halfen, E. C. Wilkinson, G. Pan, X. Wang, V. G. Young, C. J. Cramer, L. Que, W. B. Tolman, *J. Am. Chem. Soc.* **1996**, *118*, 11555–11574. DOI 10.1021/ja962305c

[75] V. Mahadevan, Z. Hou, A. P. Cole, D. E. Root, T. K. Lal, E. I. Solomon, T. D. P. Stack, *J. Am. Chem. Soc.* **1997**, *119*, 11996–11997. DOI 10.1021/ja972946n

[76] M. Mizuno, H. Hayashi, S. Fujinami, H. Furutachi, S. Nagatomo, S. Otake, K. Uozumi, M. Suzuki, T. Kitagawa, *Inorg. Chem.* **2003**, *42*, 8534–8544. DOI 10.1021/ic0345166

[77] H. Hayashi, S. Fujinami, S. Nagatomo, S. Ogo, M. Suzuki, A. Uehara, Y. Watanabe, T. Kitagawa, *J. Am. Chem. Soc.* **2000**, *122*, 2124–2125. DOI 10.1021/ja992680f

[78] N. Kindermann, S. Dechert, S. Demeshko, F. Meyer, *J. Am. Chem. Soc.* **2015**, *137*, 8002–8005. DOI 10.1021/jacs.5b04361

[79] S. Kim, J. W. Ginsbach, A. I. Billah, M. A. Siegler, C. D. Moore, E. I. Solomon, K. D. Karlin, *J. Am. Chem. Soc.* **2014**, *136*, 8063–8071. DOI 10.1021/ja502974c

[80] M. Taki, S. Teramae, S. Nagatomo, Y. Tachi, T. Kitagawa, S. Itoh, S. Fukuzumi, *J. Am. Chem. Soc.* **2002**, *124*, 6367–6377. DOI 10.1021/ja026047x

[81] A. P. Cole, V. Mahadevan, L. M. Mirica, X. Ottenwaelder, T. D. P. Stack, *Inorg. Chem.* **2005**, *44*, 7345–7364. DOI 10.1021/ic050331i

[82] M. S. Askari, K. V. N. Esguerra, J.-P. Lumb, X. Ottenwaelder, *Inorg. Chem.* **2015**, *54*, 8665–8672. DOI 10.1021/acs.inorgchem.5b01297

[83] C. He, J. L. DuBois, B. Hedman, K. O. Hodgson, S. J. Lippard, *Angew. Chem., Int. Ed.* **2001**, *40*, 1484–1487. DOI 10.1002/1521-3773(20010417)40:8%3C1484::AID-ANIE1484%3E3.0.CO;2-Z

[84] J. A. Halfen, S. Mahapatra, E. C. Wilkinson, S. Kaderli, V. G. Young, L. Que, A. D. Zuberbühler, W. B. Tolman, *Science* **1996**, *271*, 1397–1400. DOI 10.1126/science.271.5254.1397

[85] F. Strassl, B. Grimm–Lebsanft, D. Rukser, F. Biebl, M. Biednov, C. Brett, R. Timmermann, F. Metz, A. Hoffmann, M. Rübhausen, S. Herres–Pawlis, *Eur. J. Inorg. Chem.* **2017**, *2017*, 3350–3359. DOI 10.1002/ejic.201700528

[86] F. Strassl, A. Hoffmann, B. Grimm-Lebsanft, D. Rukser, F. Biebl, M. Tran, F. Metz, M. Rübhausen, S. Herres-Pawlis, *Inorganics* **2018**, *6*, 114. DOI 10.3390/inorganics6040114

[87] M. Paul, M. Teubner, B. Grimm-Lebsanft, C. Golchert, Y. Meiners, L. Senft, K. Keisers, P. Liebhäuser, T. Rösener, F. Biebl, S. Buchenau, M. Naumova, V. Murzin, R. Krug, A. Hoffmann, J. Pietruszka, I. Ivanović-Burmazović, M. Rübhausen, S. Herres-Pawlis, *Chem. Eur. J.* **2020**, *26*, 7556–7562. DOI 10.1002/chem.202000664

[88] S. Herres-Pawlis, P. Verma, R. Haase, P. Kang, C. T. Lyons, E. C. Wasinger, U. Flörke, G. Henkel, T. D. P. Stack, *J. Am. Chem. Soc.* **2009**, *131*, 1154–1169. DOI 10.1021/ja807809x

[89] S. Herres-Pawlis, S. Binder, A. Eich, R. Haase, B. Schulz, G. Wellenreuther, G. Henkel, M. Rübhausen, W. Meyer-Klaucke, *Chem. Eur. J.* **2009**, *15*, 8678–8682. DOI 10.1002/chem.200901092

[90] M. Paul, M. Teubner, B. Grimm-Lebsanft, S. Buchenau, A. Hoffmann, M. Rübhausen, S. Herres-Pawlis, *J. Inorg. Biochem.* **2021**, *224*, 111541. DOI 10.1016/j.jinorgbio.2021.111541

[91] V. Mahadevan, M. J. Henson, E. I. Solomon, T. D. P. Stack, *J. Am. Chem. Soc.* **2000**, *122*, 10249–10250. DOI 10.1021/ja002527h

[92] L. Laurini, A. Béteille, G. Fink, S. Herres-Pawlis, K. Loubière, *Chem. Eng. Technol.* **2023**, *46*, 1664–1672. DOI 10.1002/ceat.202300031

[93] X. Ottenwaelder, D. J. Rudd, M. C. Corbett, K. O. Hodgson, B. Hedman, T. D. P. Stack, *J. Am. Chem. Soc.* **2006**, *128*, 9268–9269. DOI 10.1021/ja061132g

[94] Y. Funahashi, T. Nishikawa, Y. Wasada-Tsutsui, Y. Kajita, S. Yamaguchi, H. Arii, T. Ozawa, K. Jitsukawa, T. Tosha, S. Hirota, T. Kitagawa, H. Masuda, *J. Am. Chem. Soc.* **2008**, *130*, 16444–16445. DOI 10.1021/ja804201z

[95] A. Hoffmann, C. Citek, S. Binder, A. Goos, M. Rübhausen, O. Troeppner, I. Ivanović-Burmazović, E. C. Wasinger, T. D. P. Stack, S. Herres-Pawlis, *Angew. Chem., Int. Ed.* **2013**, *52*, 5398–5401. DOI 10.1002/anie.201301249

[96] B. Herzigkeit, B. M. Flöser, N. E. Meißner, T. A. Engesser, F. Tuczek, *ChemCatChem* **2018**, *10*, 5402–5405. DOI 10.1002/cctc.201801606

[97] R. Dalhoff, R. Schmidt, L. Steeb, K. Rabatinova, M. Witte, S. Teeuwen, S. Benjamaâ, H. Hüppe, A. Hoffmann, S. Herres-Pawlis, *Faraday Discuss.* **2023**. DOI 10.1039/D2FD00162D

[98] P. Liebhäuser, K. Keisers, A. Hoffmann, T. Schnappinger, I. Sommer, A. Thoma, C. Wilfer, R. Schoch, K. Stührenberg, M. Bauer, M. Dürr, I. Ivanović-Burmazović, S. Herres-Pawlis, *Chem. Eur. J.* **2017**, *23*, 12171–12183. DOI 10.1002/chem.201700887

[99] K. D. Karlin, R. W. Cruse, J. W. McKown, J. C. Hayes, P. L. Dahlstrom, J. Zubieta, *Transition Met. Chem.* **1984**, *9*, 404–405. DOI 10.1007/BF00637030

[100] J. E. Bulkowski, US4545937A, **1985**.

[101] K. V. N. Esguerra, Y. Fall, L. Petitjean, J.-P. Lumb, *J. Am. Chem. Soc.* **2014**, *136*, 7662–7668. DOI 10.1021/ja501789x

[102] M. Paul, A. Hoffmann, S. Herres-Pawlis, *JBIC, J. Biol. Inorg. Chem.* **2021**, *26*, 249–263. DOI 10.1007/s00775-021-01849-9

[103] J. S. Wallerstein, R. T. Alba, M. G. Hale, H. Levy, *Biochim. Biophys. Acta* **1947**, *1*, 327–334. DOI 10.1016/0006-3002(47)90145-5

[104] T. E. Smithgall, R. G. Harvey, T. M. Penning, *J. Biol. Chem.* **1988**, *263*, 1814–1820. DOI 10.1016/S0021-9258(19)77949-6

[105] E. J. Land, C. A. Ramsden, P. A. Riley, *Acc. Chem. Res.* **2003**, *36*, 300–308. DOI 10.1021/ar020062p

[106] J. N. Hamann, M. Rolff, F. Tuczek, *Dalton Trans.* **2015**, *44*, 3251–3258. DOI 10.1039/c4dt03010a

[107] J. H. Zhu, J. A. Olmstead, D. G. Gray, *J. Wood Chem. Technol.* **1995**, *15*, 43–64. DOI 10.1080/02773819508009499

[108] M. E. Hernandez, A. Kappler, D. K. Newman, *Appl. Environ. Microbiol.* **2004**, *70*, 921–928. DOI 10.1128/AEM.70.2.921-928.2004

[109] L. S. Thomashow, D. M. Weller, R. F. Bonsall, L. S. Pierson, *Appl. Environ. Microbiol.* **1990**, *56*, 908–912. DOI 10.1128/aem.56.4.908-912.1990

[110] E. K. Perry, D. K. Newman, *Appl. Environ. Microbiol.* **2022**, *88*, e0232021. DOI 10.1128/aem.02320-21

[111] S. Herres-Pawlis, A. Neuba, O. Seewald, T. Seshadri, H. Egold, U. Flörke, G. Henkel, *Eur. J. Org. Chem.* **2005**, *2005*, 4879–4890. DOI 10.1002/ejoc.200500340

[112] R. Schwesinger, *Nachr. Chem. Tech. Lab.* **1990**, *38*, 1214–1226. DOI 10.1002/nadc.19900381005

[113] H. Wittmann, V. Raab, A. Schorm, J. Plackmeyer, J. Sundermeyer, *Eur. J. Inorg. Chem.* **2001**, *2001*, 1937–1948. DOI 10.1002/1099-0682(200108)2001:8%3C1937::AID-EJIC1937%3E3.0.CO;2-I

[114] W. Kantlehner, E. Haug, W. W. Mergen, P. Speh, T. Maier, J. J. Kapassakalidis, H.-J. Bräuner, H. Hagen, *Eur. J. Org. Chem.* **1984**, *1984*, 108–126. DOI 10.1002/jlac.198419840112

[115] H. Wittmann, A. Schorm, J. Sundermeyer, *Z. anorg. allg. Chem.* **2000**, *626*, 1583–1590. DOI 10.1002/1521-3749(200007)626:7%3C1583::AID-ZAAC1583%3E3.0.CO;2-3

[116] S. Pohl, M. Harmjanz, J. Schneider, W. Saak, G. Henkel, *Inorg. Chim. Acta* **2000**, *311*, 106–112. DOI 10.1016/S0020-1693(00)00310-8

[117] W. M. Haynes, *CRC Handbook of Chemistry and Physics*, 95th Ed., CRC Press - Taylor & Francis Group, Boca Raton, FL, USA, **2014**.

[118] G. Wieland, G. Simchen, *Eur. J. Org. Chem.* **1985**, *1985*, 2178–2193. DOI 10.1002/jlac.198519851108

[119] H. Eilingsfeld, G. Neubauer, M. Seefelder, H. Weidincer, *Chem. Ber.* **1964**, *97*, 1232–1245. DOI 10.1002/cber.19640970504

[120] A. Hoffmann, J. Börner, U. Flörke, S. Herres-Pawlis, *Inorg. Chim. Acta* **2009**, *362*, 1185–1193. DOI 10.1016/j.ica.2008.06.002

[121] V. Raab, J. Kipke, R. M. Gschwind, J. Sundermeyer, *Chem. Eur. J.* **2002**, *8*, 1682–1693. DOI 10.1002/1521-3765(20020402)8:7%3C1682::AID-CHEM1682%3E3.0.CO;2-R

[122] V. Raab, J. Kipke, O. Burghaus, J. Sundermeyer, *Inorg. Chem.* **2001**, *40*, 6964–6971. DOI 10.1021/ic010563r

[123] A. Peters, E. Kaifer, H.-J. Himmel, *Eur. J. Org. Chem.* **2008**, *2008*, 5907–5914. DOI 10.1002/ejoc.200800900

[124] L. Lohmeyer, E. Kaifer, H. Wadepohl, H.-J. Himmel, *Chem. Eur. J.* **2020**, *26*, 5834–5845. DOI 10.1002/chem.201905471

[125] A. Neuba, M. Rohrmüller, R. Hölscher, W. G. Schmidt, G. Henkel, *Inorg. Chim. Acta* **2015**, *430*, 225–238. DOI 10.1016/j.ica.2015.03.015

[126] P. M. Schäfer, M. Fuchs, A. Ohligschläger, R. Rittinghaus, P. McKeown, E. Akin, M. Schmidt, A. Hoffmann, M. A. Liauw, M. D. Jones, S. Herres-Pawlis, *ChemSusChem* **2017**, *10*, 3547–3556. DOI 10.1002/cssc.201701237

[127] L. Lohmeyer, F. Schön, E. Kaifer, H.-J. Himmel, *Angew. Chem., Int. Ed.* **2021**, *60*, 10415–10422. DOI 10.1002/anie.202101423

[128] A. Hermann, S. Hill, A. Metz, J. Heck, A. Hoffmann, L. Hartmann, S. Herres-Pawlis, *Angew. Chem., Int. Ed.* **2020**, *59*, 21778–21784. DOI 10.1002/anie.202008473

[129] M. Paul, Dissertation, RWTH Aachen University, **2021**.

[130] S. Herres–Pawlis, U. Flörke, G. Henkel, *Eur. J. Inorg. Chem.* **2005**, *2005*, 3815–3824. DOI 10.1002/ejic.200400822

[131] F. Felis, F. Strassl, L. Laurini, N. Dietrich, A.-M. Billet, V. Roig, S. Herres-Pawlis, K. Loubière, *Chem. Eng. Sci.* **2019**, *207*, 1256–1269. DOI 10.1016/j.ces.2019.07.045

[132] *Reactive Bubbly Flows*, Vol. 128, (Eds.: M. Schlüter, D. Bothe, S. Herres-Pawlis, U. Nieken), Springer International Publishing, Cham, **2021**.

[133] P. Kemper, E. Küstermann, W. Dreher, J. Thöming in *Reactive Bubbly Flows*, (Eds.: M. Schlüter, D. Bothe, S. Herres-Pawlis, U. Nieken), Fluid Mechanics and Its Applications, Springer International Publishing, Cham, **2021**, pp. 137–162.

[134] M. Paul, F. Strassl, A. Hoffmann, M. Hoffmann, M. Schlüter, S. Herres–Pawlis, *Eur. J. Inorg. Chem.* **2018**, *2018*, 2101–2124. DOI 10.1002/ejic.201800146

[135] F. Kexel, S. Kastens, J. Timmermann, A. von Kameke, M. Schlüter in *Reactive Bubbly Flows*, (Eds.: M. Schlüter, D. Bothe, S. Herres-Pawlis, U. Nieken), Fluid Mechanics and Its Applications, Springer International Publishing, Cham, **2021**, pp. 267–307.

[136] S. Kastens, J. Timmermann, F. Strassl, R. F. Rampmaier, A. Hoffmann, S. Herres-Pawlis, M. Schlüter*, Chem. Eng. Technol.* **2017***, 40*, 1494–1501. DOI 10.1002/ceat.201700047

[137] D. Schurr, F. Strassl, P. Liebhäuser, G. Rinke, R. Dittmeyer, S. Herres-Pawlis*, React. Chem. Eng.* **2016***, 1*, 485–493. DOI 10.1039/C6RE00119J

[138] O. Mierka, S. Turek, G. Rinke, S. Simon, S. Schindler, A. Hoffmann, M. Hoffmann, M. Schlüter, S. Herres-Pawlis in *Reactive Bubbly Flows*, (Eds.: M. Schlüter, D. Bothe, S. Herres-Pawlis, U. Nieken), Fluid Mechanics and Its Applications, Springer International Publishing, Cham, **2021**, pp. 479–506.

[139] M. Schlüter, F. Kexel, A. von Kameke, M. Hoffmann, S. Herres-Pawlis, P. Klüfers, M. Oßberger, S. Turek, O. Mierka, N. Kockmann, W. Krieger in *Reactive Bubbly Flows*, (Eds.: M. Schlüter, D. Bothe, S. Herres-Pawlis, U. Nieken), Fluid Mechanics and Its Applications, Springer International Publishing, Cham, **2021**, pp. 507–543.

[140] S. Gast, U. Tuttlies, L. Laurini, F. Kexel, D. Merker, L. Böhm, M. A. Taborda, M. Sommerfeld, M. Kraume, M. Schlüter, S. Herres-Pawlis, U. Nieken in *Reactive Bubbly Flows*, (Eds.: M. Schlüter, D. Bothe, S. Herres-Pawlis, U. Nieken), Fluid Mechanics and Its Applications, Springer International Publishing, Cham, **2021**, pp. 621–642.

[141] D. Merker, L. Böhm, M. Kraume in *Reactive Bubbly Flows*, (Eds.: M. Schlüter, D. Bothe, S. Herres-Pawlis, U. Nieken), Fluid Mechanics and Its Applications, Springer International Publishing, Cham, **2021**, pp. 231–265.

[142] L. Laurini, Master thesis, RWTH Aachen University, Aachen, **2019**.

[143] L. Laurini, S. M. Conte, K. Hüser, P. R. F. Cordero, H. M. Núñez Ponce, S. Zimmer, L. Lauterbach, S. Herres–Pawlis*, Eur. J. Inorg. Chem.* **2024**. DOI 10.1002/ejic.202300700

[144] H.-.-J. Teuber, S. Benz*, Chem. Ber.* **1967***, 100*, 2077–2092. DOI 10.1002/cber.19671000635

[145] J. Schottenheim, N. Fateeva, W. Thimm, J. Krahmer, F. Tuczek*, Z. anorg. allg. Chem.* **2013***, 639*, 1491–1497. DOI 10.1002/zaac.201300065

[146] A. Gerega, L. Lapinski, M. J. Nowak, A. Furmanchuk, J. Leszczynski*, J. Phys. Chem. A* **2007***, 111*, 4934–4943. DOI 10.1021/jp070408j

[147] Y. Pan, K.-C. Lau, M. M. Al-Mogren, A. Mahjoub, M. Hochlaf*, Chem. Phys. Lett.* **2014***, 613*, 29–33. DOI 10.1016/j.cplett.2014.08.033

[148] V. Gold, *Compendium of Chemical Terminology*, 2nd Ed., International Union of Pure and Applied Chemistry (IUPAC), Oxford, **1997**.

[149] F. Jensen, *Introduction to Computational Chemistry*, 3rd Ed., Jensen, Frank (VerfasserIn), Wiley, Chichester, West Sussex, Hoboken, NJ, and Oxford, **2017**.

[150] P. K. Chattaraj, *Chemical Reactivity Theory, A Density Functional View*, 1st Ed., Chattaraj, Pratim Kumar (Hrsg.), CRC Press, Boca Raton, FL, USA, **2009**.

[151] R. Schneider, T. A. Engesser, C. Näther, I. Krossing, F. Tuczek*, Angew. Chem., Int. Ed.* **2022***, 61*, e202202562. DOI 10.1002/anie.202202562

[152] Q. Ye, S. Ren, H. Huang, G. Duan, K. Liu, J.-B. Liu*, ACS Omega* **2020***, 5*, 20698–20706. DOI 10.1021/acsomega.0c03111

[153] J. Wang, H. Li, Y. Cai, D. Wang, L. Bian, F. Dong, H. Yu, Y. He*, Anal. Chem.* **2019***, 91*, 6155–6161. DOI 10.1021/acs.analchem.9b00759

[154] A. V. Biradar, T. V. Kotbagi, M. K. Dongare, S. B. Umbarkar*, Tetrahedron Lett.* **2008***, 49*, 3616–3619. DOI 10.1016/j.tetlet.2008.04.005

[155] A. Hartmann, M. Rothballer, M. Schmid*, Plant Soil* **2008***, 312*, 7–14. DOI 10.1007/s11104-007-9514-z

[156] C. Diederich, M. Leypold, R. Breinbauer, W. Blankenfeldt*, Nachr. Chem.* **2014***, 62*, 975–980. DOI 10.1002/nadc.201490357

[157] M. G. P. Page*, Handb. Exp. Pharmacol.* **2012**, 67–86. DOI 10.1007/978-3-642-28951-4_5

[158] A. Papkou, J. Hedge, N. Kapel, B. Young, R. C. MacLean*, Nat. Commun.* **2020***, 11*, 3970. DOI 10.1038/s41467-020-17735-y

[159] K. T. Schiessl, F. Hu, J. Jo, S. Z. Nazia, B. Wang, A. Price-Whelan, W. Min, L. E. P. Dietrich*, Nat. Commun.* **2019***, 10*, 762. DOI 10.1038/s41467-019-08733-w

[160] K. Kise, H. Kosaka, M. Nakabayashi, K. Kishida, T. Shiga, Y. Tano*, Ophthalmic Res.* **1994***, 26*, 41–50. DOI 10.1159/000267373

[161] T. D. M. Pham, Z. M. Ziora, M. A. T. Blaskovich*, MedChemComm* **2019***, 10*, 1719–1739. DOI 10.1039/C9MD00120D

[162] K. Katagiri, T. Yoshida, K. Sato in *Mechanism of Action of Antimicrobial and Antitumor Agents*, (Eds.: J. W. Corcoran, F. E. Hahn, J. F. Snell, K. L. Arora), Springer, Berlin, **1975**, pp. 234–251.

[163] L. Heide*, Nat. Prod. Rep.* **2009***, 26*, 1241–1250. DOI 10.1039/b808333a

[164] A. Sugino, C. L. Peebles, K. N. Kreuzer, N. R. Cozzarelli*, Proc. Natl. Acad. Sci. U. S. A.* **1977***, 74*, 4767–4771. DOI 10.1073/pnas.74.11.4767

[165] S.-H. Kim, R. D. Rieke*, Tetrahedron* **2010***, 66*, 3135–3146. DOI 10.1016/j.tet.2010.02.061

[166] S.-H. Kim, R. D. Rieke*, Tetrahedron Lett.* **2009***, 50*, 6985–6988. DOI 10.1016/j.tetlet.2009.09.160

[167] E. Negishi, D. E. van Horn*, J. Am. Chem. Soc.* **1977***, 99*, 3168–3170. DOI 10.1021/ja00451a055

[168] A. F. Holleman, E. Wiberg, *Lehrbuch der anorganischen Chemie*, 102th Ed., Wiberg, Nils (Bearb.), de Gruyter, Berlin, **2008**.

[169] R. D. Rieke*, Science* **1989***, 246*, 1260–1264. DOI 10.1126/science.246.4935.1260

[170] R. U. S. Schmidt, Dissertation, RWTH Aachen University, Aachen, **2024**.

[171] S. Itoh, S. Fukuzumi*, Acc. Chem. Res.* **2007***, 40*, 592–600. DOI 10.1021/ar6000395

[172] C. Benelli, A. Dei, D. Gatteschi, L. Pardi*, Inorg. Chem.* **1990***, 29*, 3409–3415. DOI 10.1021/ic00343a027

[173] C. Jørgensen **1966***, 1*, 164–178. DOI 10.1016/S0010-8545(00)80170-8

[174] K. Ray, T. Petrenko, K. Wieghardt, F. Neese*, Dalton Trans.* **2007**, 1552–1566. DOI 10.1039/B700096K

[175] C. G. Pierpont **2001***, 216-217*, 99–125. DOI 10.1016/S0010-8545(01)00309-5

[176] H. Decker, T. Schweikardt, F. Tuczek*, Angew. Chem., Int. Ed.* **2006***, 45*, 4546–4550. DOI 10.1002/anie.200601255

[177] B. T. Op't Holt, M. A. Vance, L. M. Mirica, D. E. Heppner, T. D. P. Stack, E. I. Solomon*, J. Am. Chem. Soc.* **2009***, 131*, 6421–6438. DOI 10.1021/ja807898h

[178] M. Güell, J. M. Luis, M. Solà, P. E. M. Siegbahn **2009***, 14*, 229–242. DOI 10.1007/s00775-008-0443-y

[179] A. W. J. W. Tepper, L. Bubacco, G. W. Canters*, J. Am. Chem. Soc.* **2005***, 127*, 567–575. DOI 10.1021/ja0454687

[180] S. Herres-Pawlis, P. Klüfers, *Bioanorganische Chemie, Metalloproteine, Methoden und Modelle*, 1th Ed., Wiley-VCH, Weinheim, **2017**.

[181] S. Stoll, A. Schweiger **2006***, 178*, 42–55. DOI 10.1016/j.jmr.2005.08.013

[182] R. Haase, Dissertation, Universität Paderborn, Paderborn, **2010**.

[183] L. Yang, D. R. Powell, R. P. Houser*, Dalton Trans.* **2007**, 955–964. DOI 10.1039/B617136B

[184] R. M. Buchanan, C. Wilson-Blumenberg, C. Trapp, S. K. Larsen, D. L. Greene, C. G. Pierpont*, Inorg. Chem.* **1986**, 3070–3076. DOI 10.1021/ic00237a029

[185] J. Rall, M. Wanner, M. Albrecht, F. M. Hornung, W. Kaim, *Chem. Eur. J.* **1999**, *5*, 2802–2809. DOI 10.1002/(SICI)1521-3765(19991001)5:10%3C2802::AID-CHEM2802%3E3.0.CO;2-5

[186] L. M. Berreau, S. Mahapatra, J. A. Halfen, R. P. Houser, V. G. Young, W. B. Tolman, *Angew. Chem.* **1999**, *111*, 180–183. DOI 10.1002/(SICI)1521-3757(19990115)111:1/2%3C180::AID-ANGE180%3E3.0.CO;2-Z

[187] G. Speier, S. Tisza, Z. Tyeklar, C. W. Lange, C. G. Pierpont, *Inorg. Chem.* **1994**, *33*, 2041–2045. DOI 10.1021/ic00087a047

[188] G. A. Abakumov, V. K. Cherkasov, V. I. Nevodchikov, V. A. Kuropatov, G. T. Yee, C. G. Pierpont, *Inorg. Chem.* **2001**, *40*, 2434–2436. DOI 10.1021/ic001449w

[189] J. Guhathakurta, D. Schurr, G. Rinke, D. Grottke, M. Kraut, R. Dittmeyer, S. Simon in *Reactive Bubbly Flows*, (Eds.: M. Schlüter, D. Bothe, S. Herres-Pawlis, U. Nieken), Fluid Mechanics and Its Applications, Springer International Publishing, Cham, **2021**, pp. 163–196.

[190] R. Kipping, H. Kryk, U. Hampel in *Reactive Bubbly Flows*, (Eds.: M. Schlüter, D. Bothe, S. Herres-Pawlis, U. Nieken), Fluid Mechanics and Its Applications, Springer International Publishing, Cham, **2021**, pp. 115–136.

[191] S. Gast, U. Tuttlies, U. Nieken in *Reactive Bubbly Flows*, (Eds.: M. Schlüter, D. Bothe, S. Herres-Pawlis, U. Nieken), Fluid Mechanics and Its Applications, Springer International Publishing, Cham, **2021**, pp. 197–230.

[192] F. Strassl, Dissertation, RWTH Aachen University, Aachen, **2019**.

[193] M. Roudet, A.-.-M. Billet, S. Cazin, F. Risso, V. Roig, *AlChE J.* **2017**, *63*, 2394–2408. DOI 10.1002/aic.15562

[194] A. Filella, P. Ern, V. Roig, *J. Fluid Mech.* **2015**, *778*, 60–88. DOI 10.1017/jfm.2015.355

[195] J. M. Achord, C. L. Hussey, *Anal. Chem.* **1980**, *52*, 601–602. DOI 10.1021/ac50053a061

[196] M. Becker, M. Tuinier, P. Rollbusch, G. Skillas, M. Orabi **2012**, *84*, 1223. DOI 10.1002/cite.201250497

[197] P. Rollbusch, M. Bothe, M. Becker, M. Ludwig, M. Grünewald, M. Schlüter, R. Franke, *Chem. Eng. Sci.* **2015**, *126*, 660–678. DOI 10.1016/j.ces.2014.11.061

[198] R. Schäfer, C. Merten, G. Eigenberger **2002**, *26*, 595–604. DOI 10.1016/S0894-1777(02)00189-9

[199] K. N. Clark, *Chem. Eng. Sci.* **1990**, *45*, 2301–2307. DOI 10.1016/0009-2509(90)80109-R

[200] R. Pohorecki, W. Moniuk, A. Zdrójkowski, P. Bielski, *Chem. Eng. Sci.* **2001**, *56*, 1167–1174. DOI 10.1016/S0009-2509(00)00336-5

[201] G. J. Kubas, B. Monzyk, A. L. Crumbliss in *Inorganic Synthesis*, *Vol. 19*, (Ed.: D. F. Shriver), Wiley, Hoboken, NJ, USA, **1979**, pp. 90–92.

[202] Z. Huang, J.-P. Lumb, *Angew. Chem., Int. Ed.* **2016**, *55*, 11543–11547. DOI 10.1002/anie.201606359

[203] K. P. C. Vollhardt, N. E. Schore, *Organische Chemie*, 4th Ed., Wiley-VCH, Weinheim, **2009**.

[204] R. Brückner, *Reaktionsmechanismen, Organische Reaktionen, Stereochemie, Moderne Synthesemethoden*, 3rd Ed., Springer Spektrum, Berlin, **2015**.

[205] A. Company, S. Palavicini, I. Garcia-Bosch, R. Mas-Ballesté, L. Que, E. V. Rybak-Akimova, L. Casella, X. Ribas, M. Costas, *Chem. Eur. J.* **2008**, *14*, 3535–3538. DOI 10.1002/chem.200800229

[206] A. Jerschow, N. Müller **1997**, *125*, 372–375. DOI 10.1006/jmre.1997.1123

[207] Stoe, X-Area Recipe 1.33.0.0, Darmstadt, Germany: Stoe & Cie GmbH, **2015**.

[208] Stoe, X-Area Integrate 1.71.0.0, Darmstadt, Germany: Stoe & Cie GmbH, **2016**.

[209] Stoe, X-Area Pilatus3_SV 1.31.131.0, Darmstadt, Germany: Stoe & Cie GmbH, **2017**.

[210] Stoe, X-Area LANA 1.71.4.0, Darmstadt, Germany: Stoe & Cie GmbH, **2017**.

[211] Bruker, XPREP 5.1, Madison (WI), USA: Bruker AXS Inc., **1997**.

[212] G. M. Sheldrick*, Acta Crystallogr., Sect. A: Found. Adv.* **2015***, 71*, 3–8. DOI 10.1107/S2053273314026370

[213] G. M. Sheldrick, *Acta Crystallogr., Sect. C: Struct. Chem.* **2015***, 71*, 3–8. DOI 10.1107/S2053229614024218

[214] C. B. Hübschle, G. M. Sheldrick, B. Dittrich*, J. Appl. Crystallogr.* **2011***, 44*, 1281–1284. DOI 10.1107/S0021889811043202

[215] *Multifrequency Electron Paramagnetic Resonance*, (Ed.: S. K. Misra), Wiley-VCH, Weinheim, **2014**.

[216] *Electron Paramagnetic Resonance Investigations of Biological Systems by Using Spin Labels, Spin Probes, and Intrinsic Metal Ions Part A*, 1st Ed., (Eds.: P. Z. Qin, K. Warncke), Academic Press, Amsterdam, **2015**.

8 Appendix

Analytical Data and Spectra of Bisguanidine Ligand TMG$_2$tol (L1)

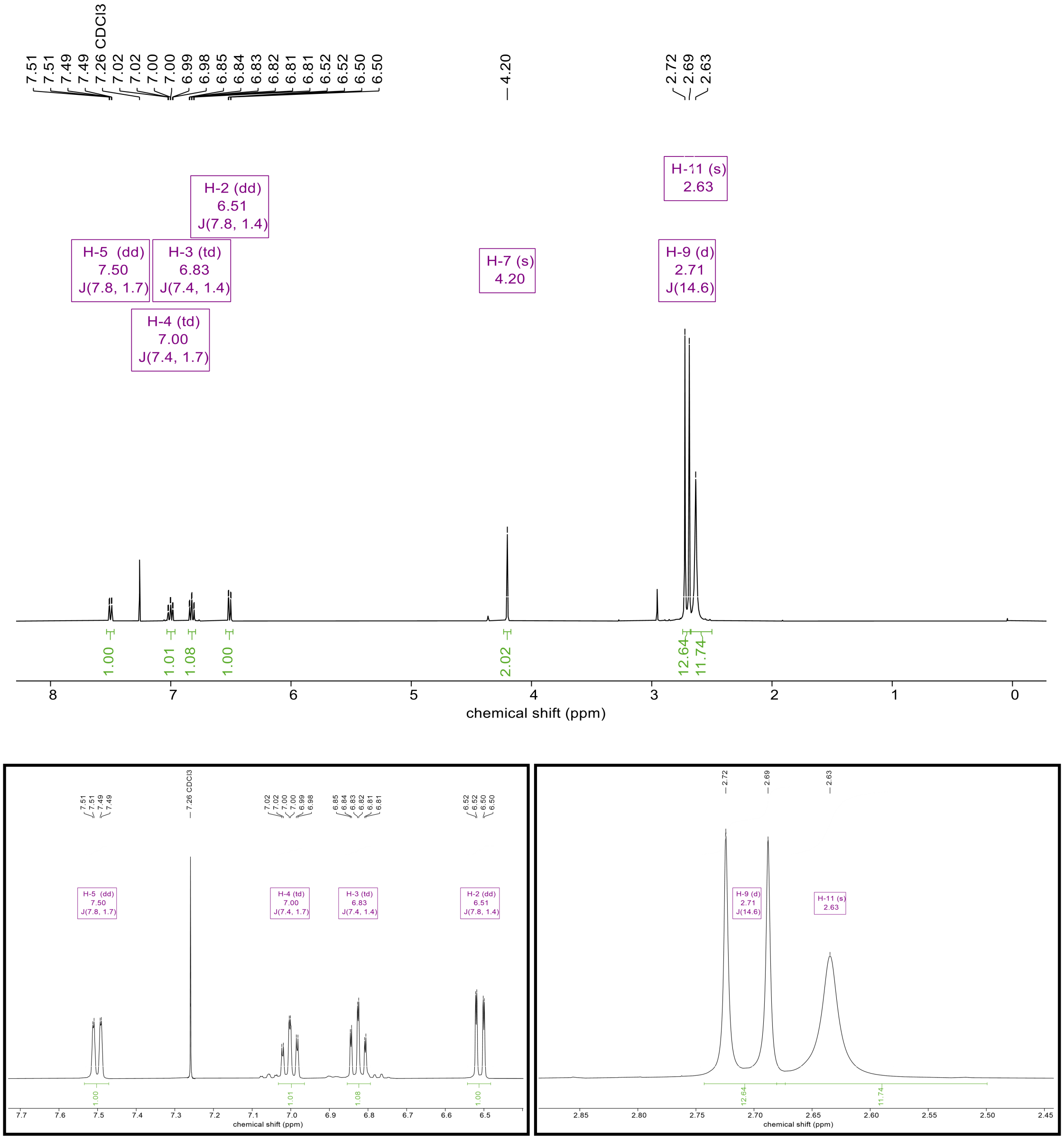

Figure 8.1: ^{1}H NMR spectrum (400 MHz, chloroform-d [7.26 ppm]) of bisguanidine ligand 2-(2((bis(dimethylamino)methylene)amino)benzyl)-1,1,3,3-tetramethylguanidine (TMG$_2$tol; **L1**).

Analytical Data and Spectra of Primary Amine 2(2-Aminophenyl)pyridine

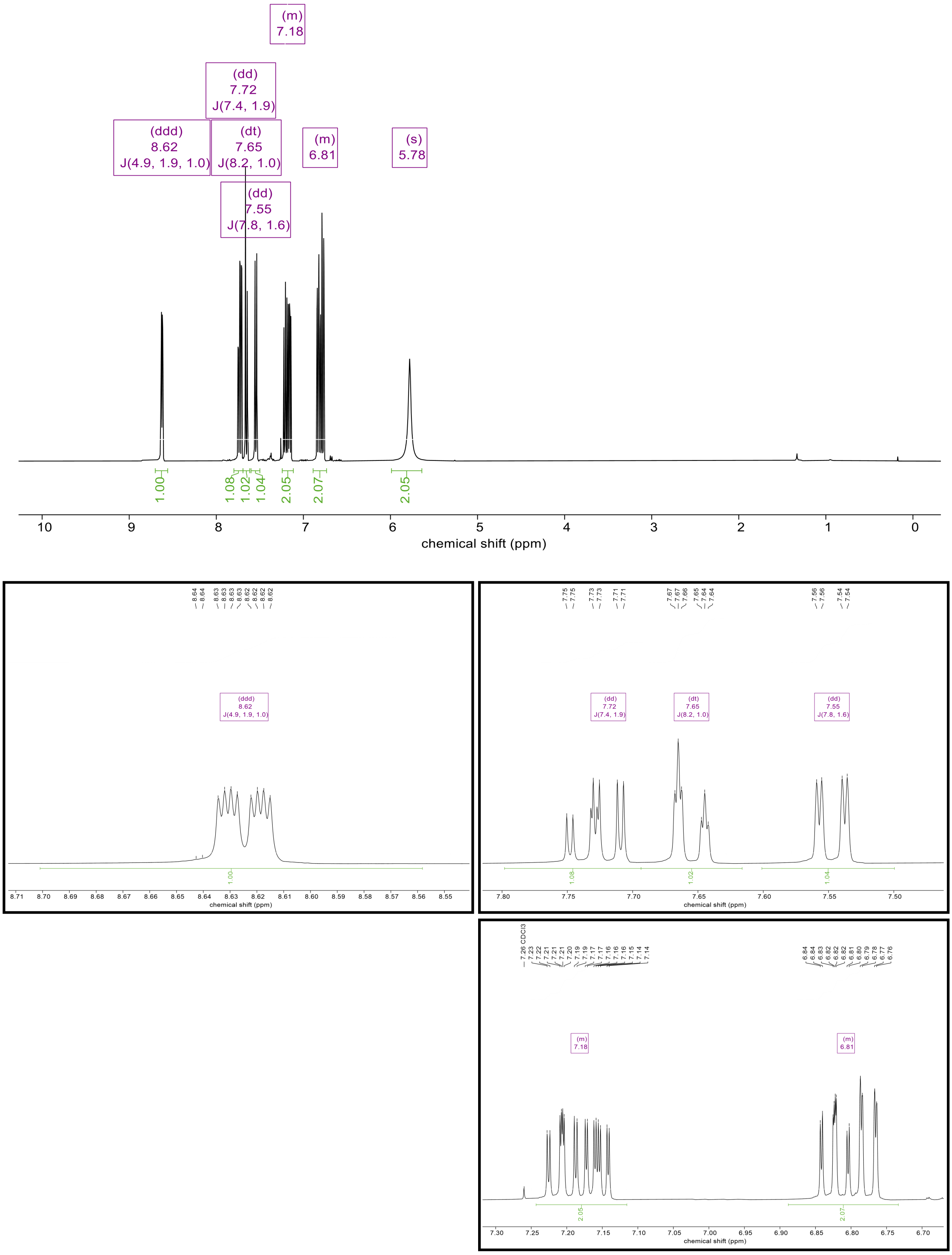

Figure 8.2: ^{1}H NMR spectrum (400 MHz, chloroform-d [7.26 ppm]) of primary amine 2(2-aminophenyl)pyridine.

Analytical Data and Spectra of Hybrid Guanidine Ligand TMGphpy

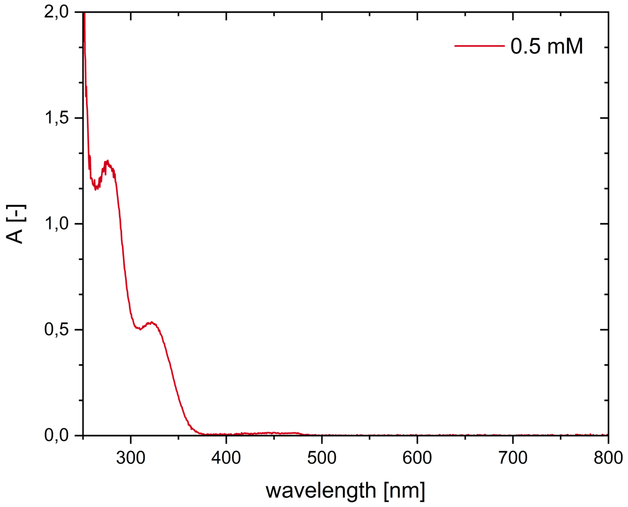

Figure 8.3: UV/Vis spectrum of hybrid guanidine ligand 1,1,3,3-tetramethyl-2-(2-(pyridin-2-yl)phenyl)guanidine (TMGphpy; **L2**) (c(**L2**) = 0.5 mM, THF, −80 °C).

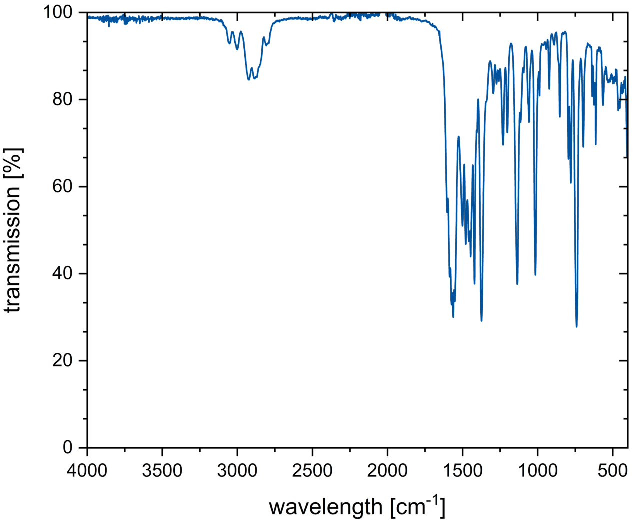

Figure 8.4: IR spectrum of hybrid guanidine ligand 1,1,3,3-tetramethyl-2-(2-(pyridin-2-yl)phenyl)guanidine (TMGphpy; **L2**).

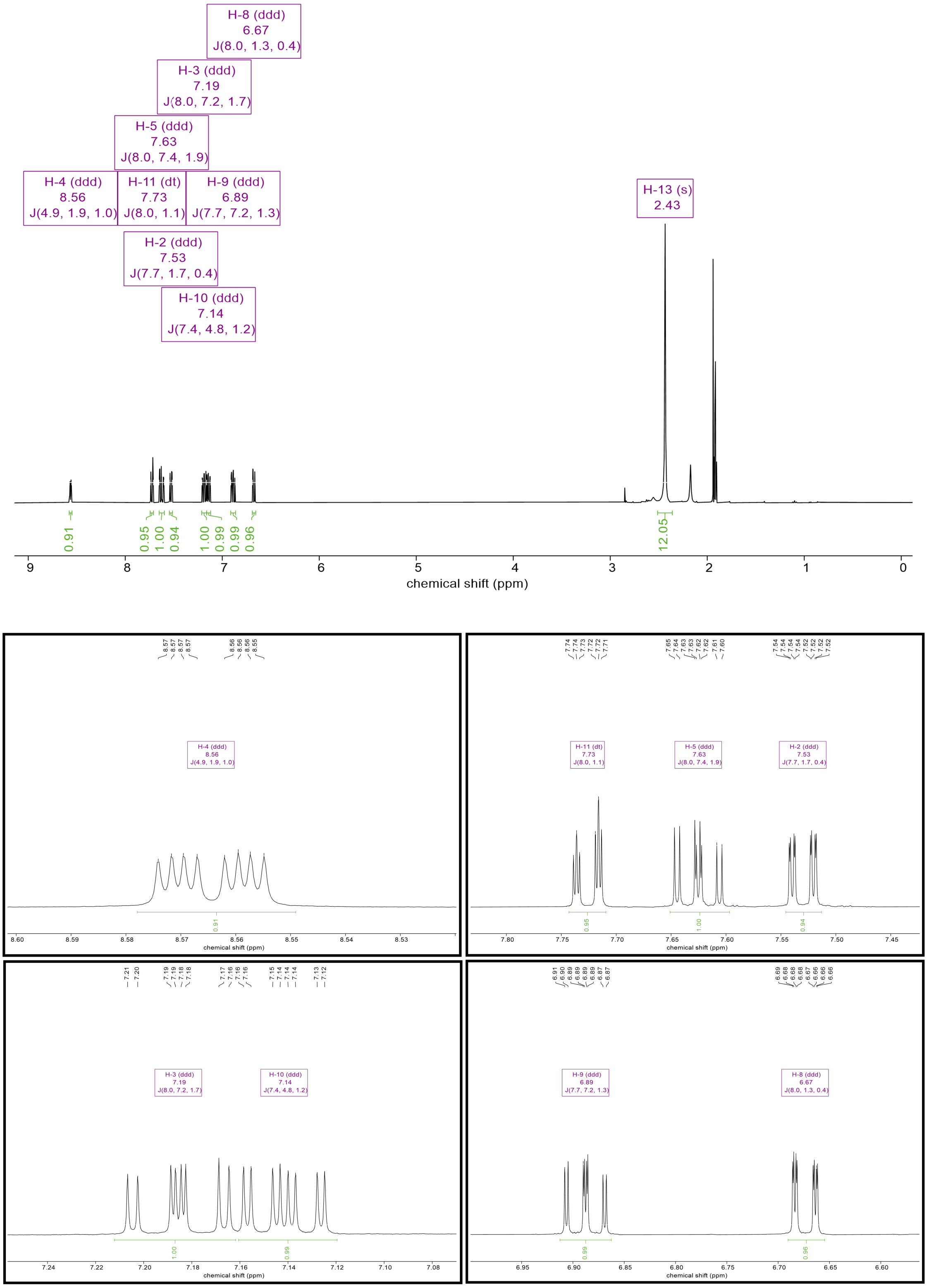

Figure 8.5: ^{1}H NMR spectrum (400 MHz, acetonitrile-d$_3$ [q, 1.94 ppm]) of hybrid guanidine ligand 1,1,3,3-tetramethyl-2-(2-(pyridin-2-yl)phenyl)guanidine (TMGphpy; **L2**).

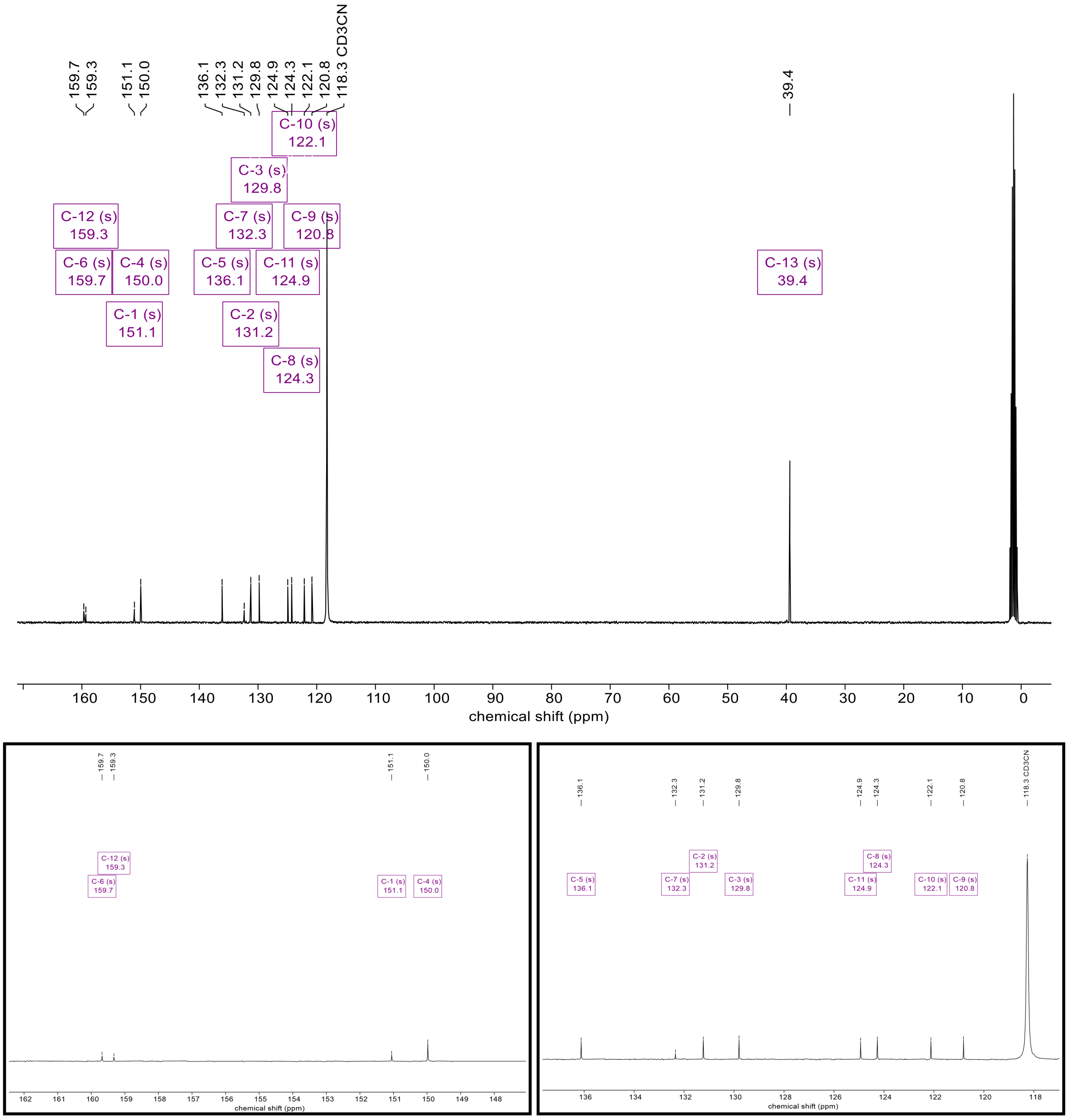

Figure 8.6: ^{13}C NMR spectrum (100 MHz, acetonitrile-d$_3$ [118.2 ppm]) of hybrid guanidine ligand 1,1,3,3-tetramethyl-2-(2-(pyridin-2-yl)phenyl)guanidine (TMGphpy; **L2**).

Catalytic Activity Studies with $[Cu_2O_2(TMG_2tol)_2](PF_6)_2$ ($[\mathbf{O1}](PF_6)_2$)

Table 8.1: Summary of catalytic conversions of phenolic substrates **S** with varied reaction time mediated by $[\mathbf{O1}](PF_6)_2$ (THF, −80 °C) and related isolated yields and TON of phenazine products **P** are given after oxidation and subsequent hydroxylation followed by condensation with 1,2-phenylenediamine overnight, organic work-up and subsequent purification by column chromatography.

entry	reaction time [h]	substrate	phenazine product	yield [%] [a] (unconverted substrate)	yield [%] [a] (phenazine)	TON [b] (phenazine)
1	1	S9	P5	50	4	1
2	3	S9	P5	26	3	1
3	5	S9	P5	1	3	1
4	8	S9	P5	1	4	1
5	5	S2	P1	86	14	4
6	8	S2	P1	37	31	8
7	5	S6	P3	0	11	3
8	8	S6	P3	0	16	4

Table 8.2: Performed catalytic conversions of phenolic substrates **S** with copper salt $[Cu(MeCN)_4]PF_6$ (THF, −80 °C, 8 h). Related isolated yields and TON of phenazine product **P** are given after oxidation and subsequent hydroxylation followed by condensation with 1,2-phenylenediamine overnight, organic work-up and subsequent purification by column chromatography.

entry	substrate	phenazine product	yield (phenazine) [%]	TON (phenazine)
1	S2	P2	5	<1
2	S2	P2	6	<1
3	S6	P3	5	<1
4	S6	P3	6	<1
5	S8	P4	4	<1
6	S8	P4	4	<1

Table 8.3: Summary of catalytic conversions performed with phenolic substrates **S** using [**O1**](PF_6)$_2$ as catalyst (THF, −80 °C, 8 h) and subsequent condensation with 1,2-phenylenediamine as well as isolated yields and TON of desired phenazine product **P** given after purification by column chromatography.

entry	substrate	phenazine product	yield [%] [a] (phenazine)	TON [b] (phenazine)
1	S1	P1	1	<1
2	S1	P1	1	<1
3	S1	P1	2	<1
4	S2	P1	31	8
5	S2	P1	30	8
6	S2	P1	32	8
7	S3	P2	4	1
8	S3	P2	6	1
9	S3	P2	5	1
10	S4	P2	0	0
11	S4	P2	0	0
12	S4	P2	0	0
13	S5	P3	0	0
14	S5	P3	0	0
15	S5	P3	0	0
16	S6	P3	16	4
17	S6	P3	11	3
18	S6	P3	20	5
19	S7	P4	0	0
20	S7	P4	0	0
21	S7	P4	0	0
22	S8	P4	4	1
23	S8	P4	4	1
24	S8	P4	3	1
25	S9	P5	4	1
26	S9	P5	5	1
27	S9	P5	4	1
28	S10	P5	0	0
29	S10	P5	0	0
30	S10	P5	0	0
31	S11	P6 / P7	<1	<1
32	S11	P6 / P7	0	0
33	S12	P8	0	0
34	S12	P8	0	0

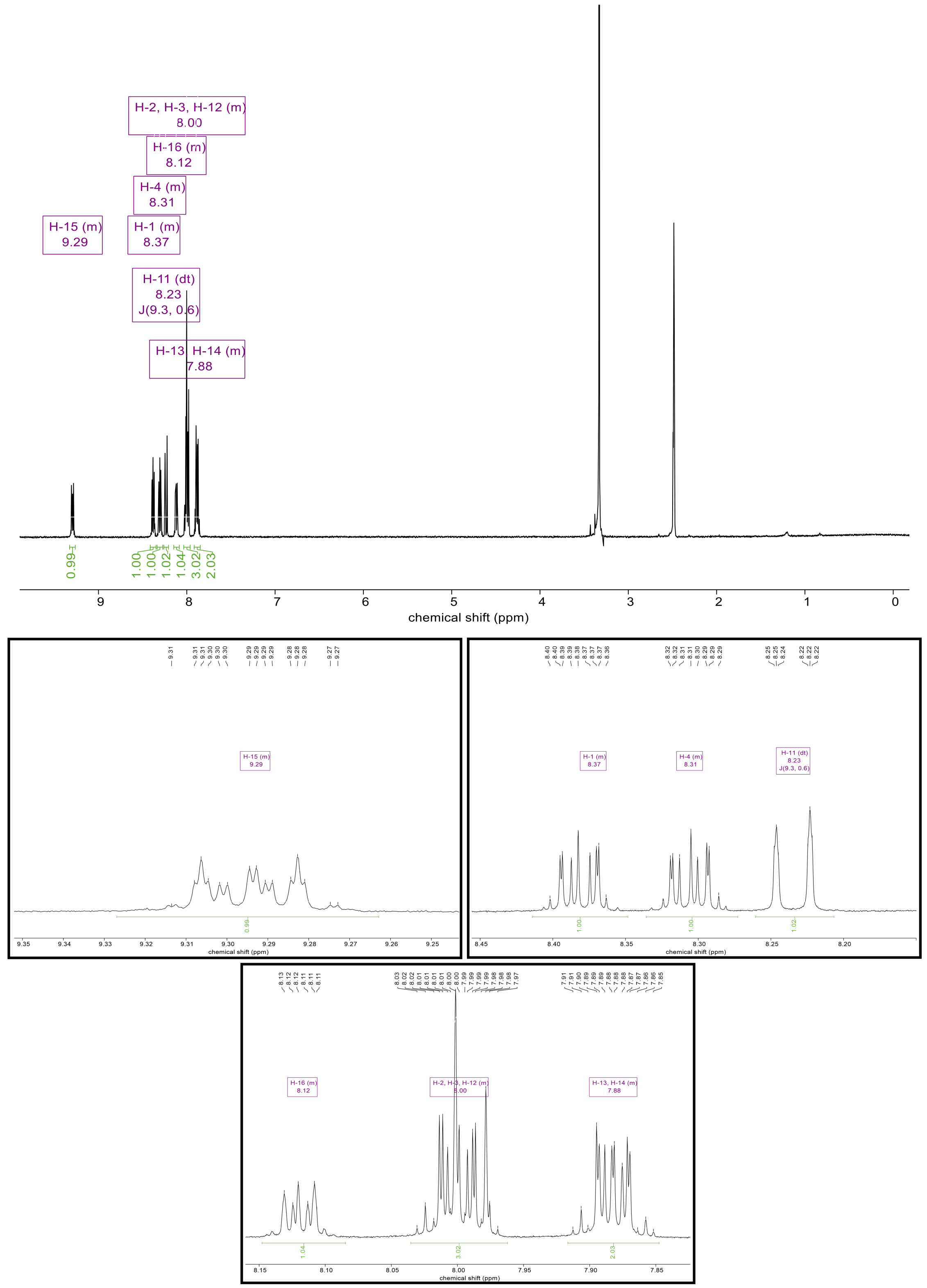

Figure 8.7: ^{1}H NMR spectrum (400 MHz, dimethylsulfoxide-d$_6$ [s, 3.33 ppm]) of phenazine product benzo[*a*]phenazine (**P1**).

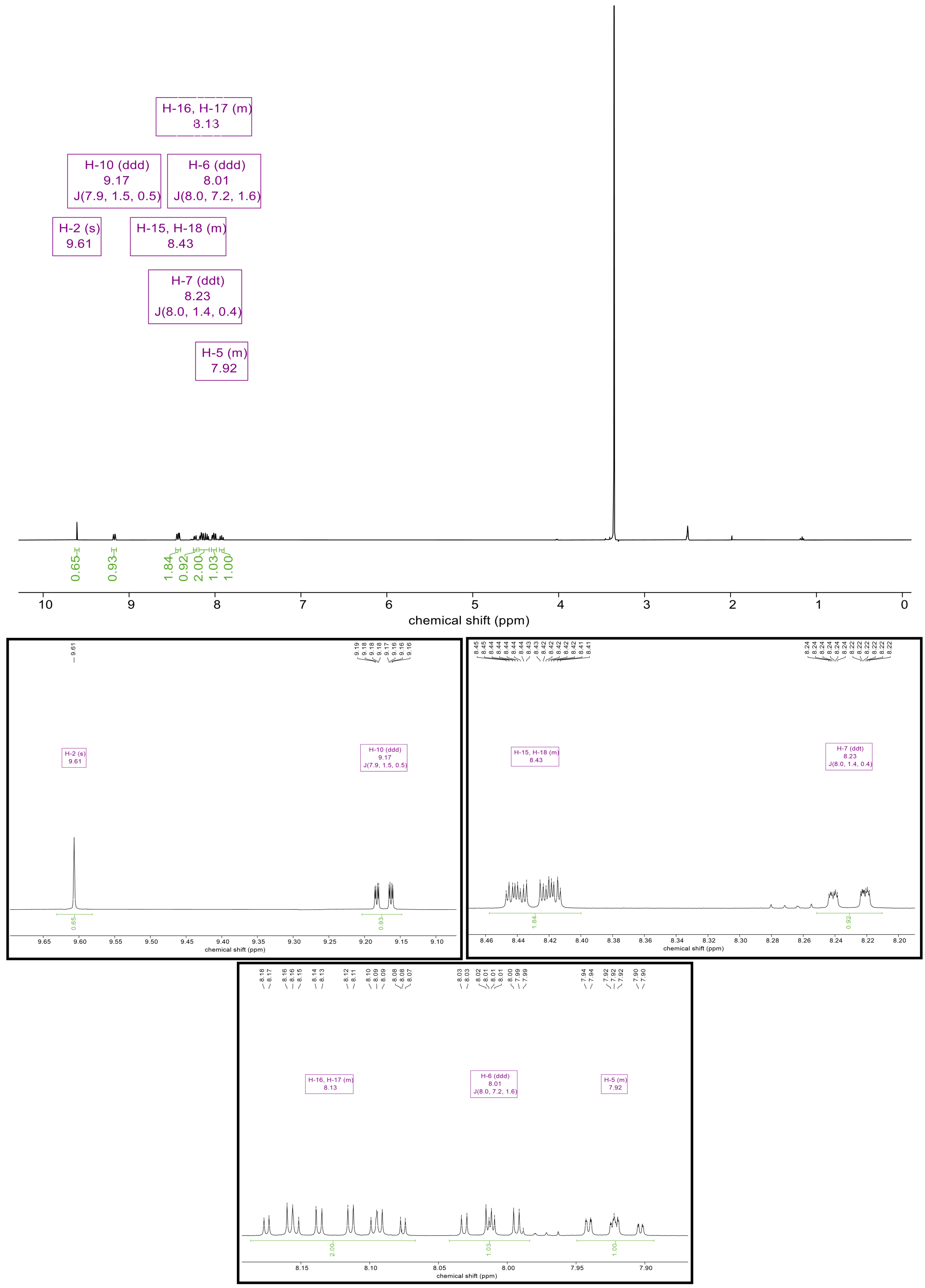

Figure 8.8: ^{1}H NMR spectrum (400 MHz, dimethylsulfoxide-d$_6$ [s, 3.33 ppm]) of phenazine product quinolino[3,4-*b*]quinoxaline (**P2**).

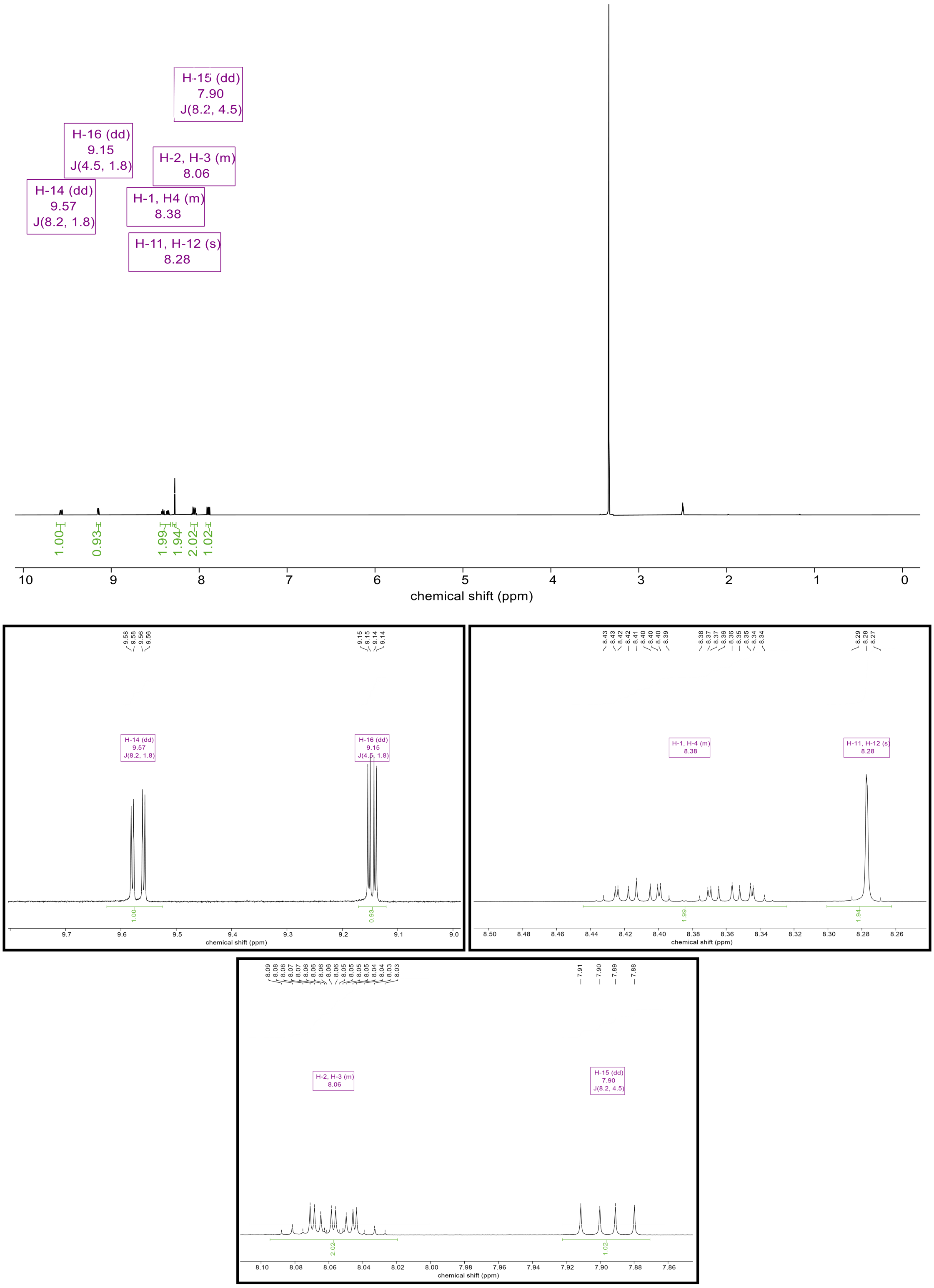

Figure 8.9: ^{1}H NMR spectrum (400 MHz, dimethylsulfoxide-d$_6$ [s, 3.33 ppm]) of phenazine product pyrido[3,2-*a*]phenazine (**P3**).

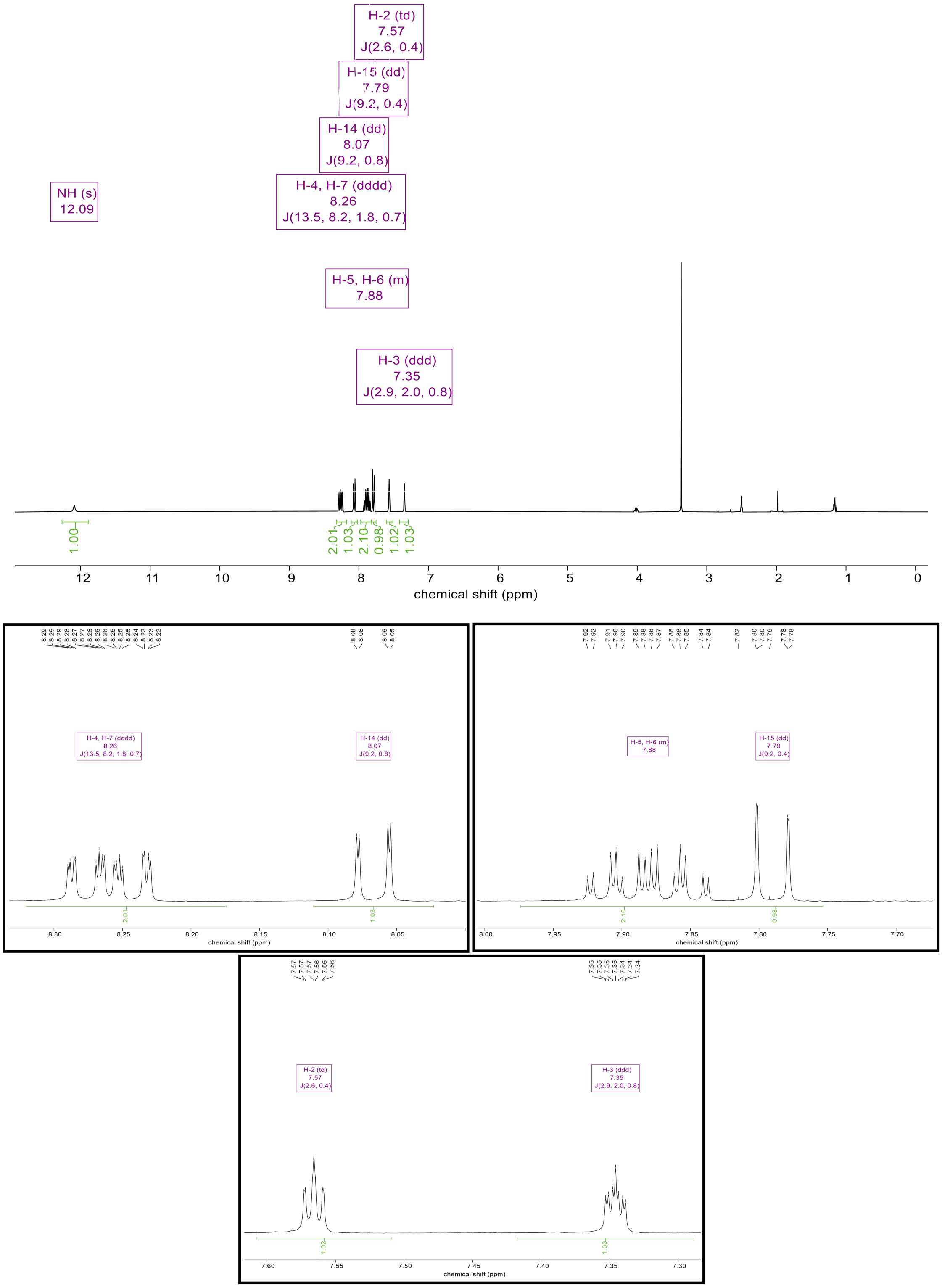

Figure 8.10: ^{1}H NMR spectrum (400 MHz, dimethylsulfoxide-d$_6$ [s, 3.33 ppm]) of phenazine product 3H-pyrrolo[3,2-*a*]phenazine (**P4**).

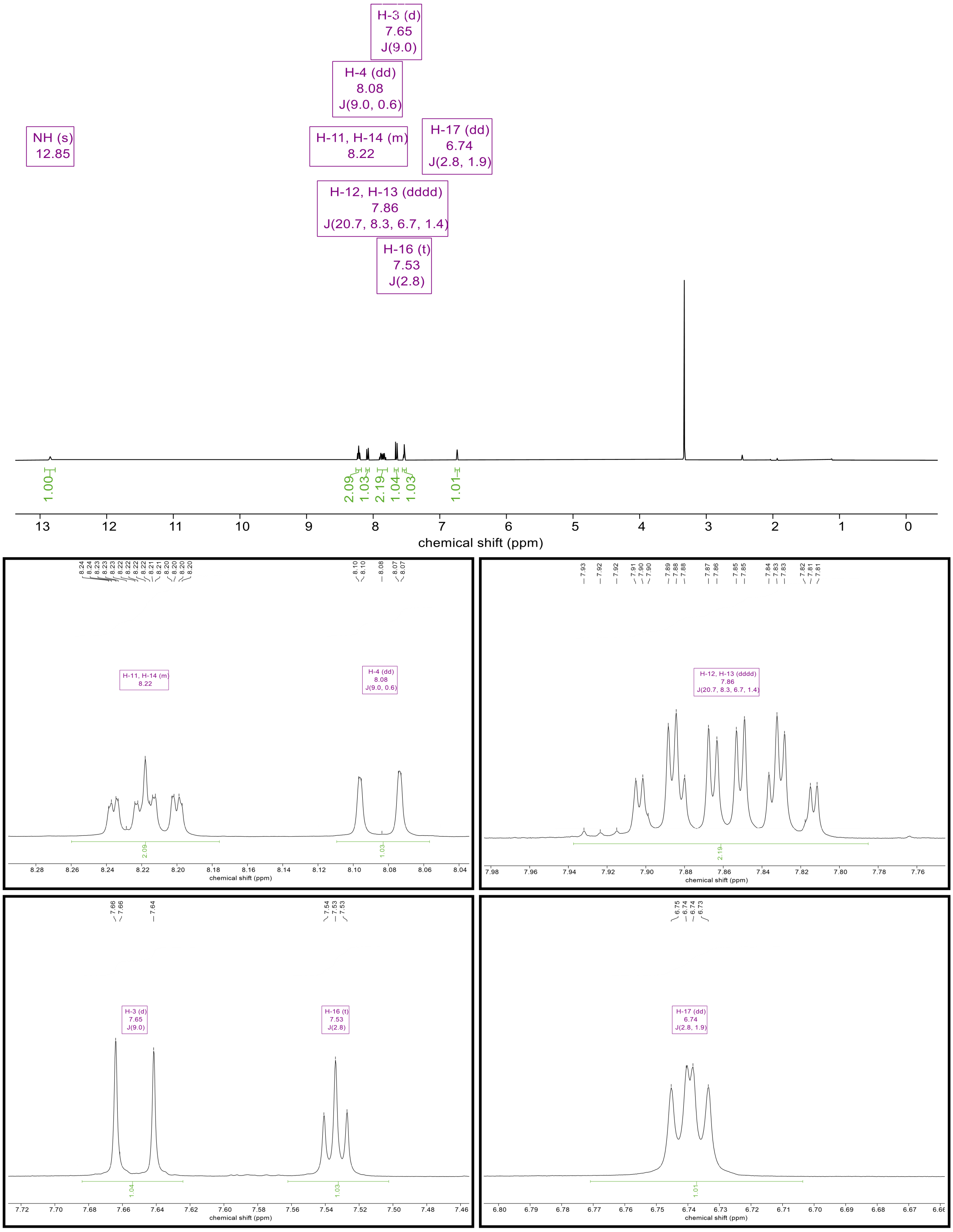

Figure 8.11: ^{1}H NMR spectrum (400 MHz, dimethylsulfoxide-d$_6$ [s, 3.33 ppm]) of phenazine product 1H-pyrrolo[2,3-*a*]phenazine (**P5**).

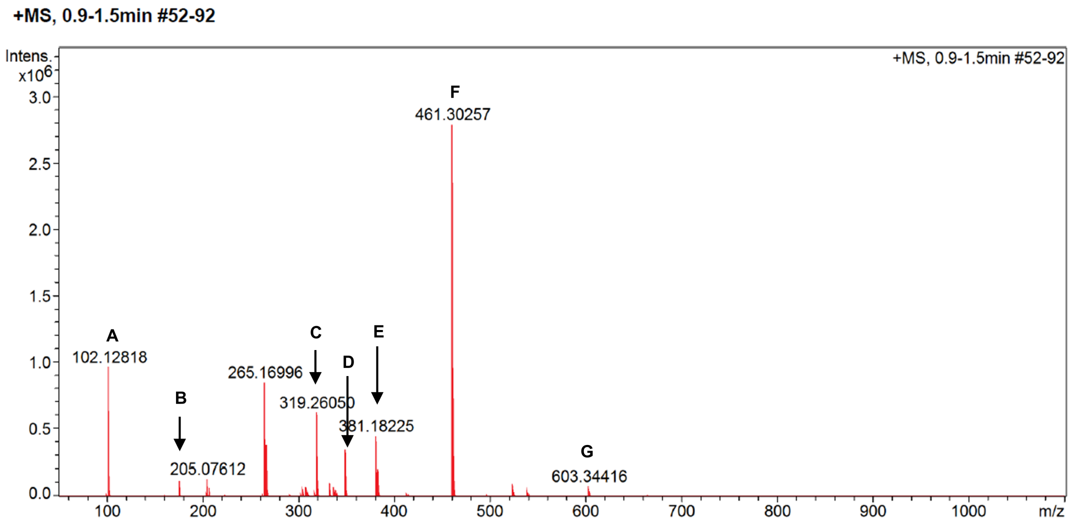

Figure 8.12: CSI-MS spectrum of the catalytic conversion of 1-naphthol (**S1**) using [**O1**]$(PF_6)_2$ as catalyst recorded after addition of the substrate solution (THF, −80 °C).

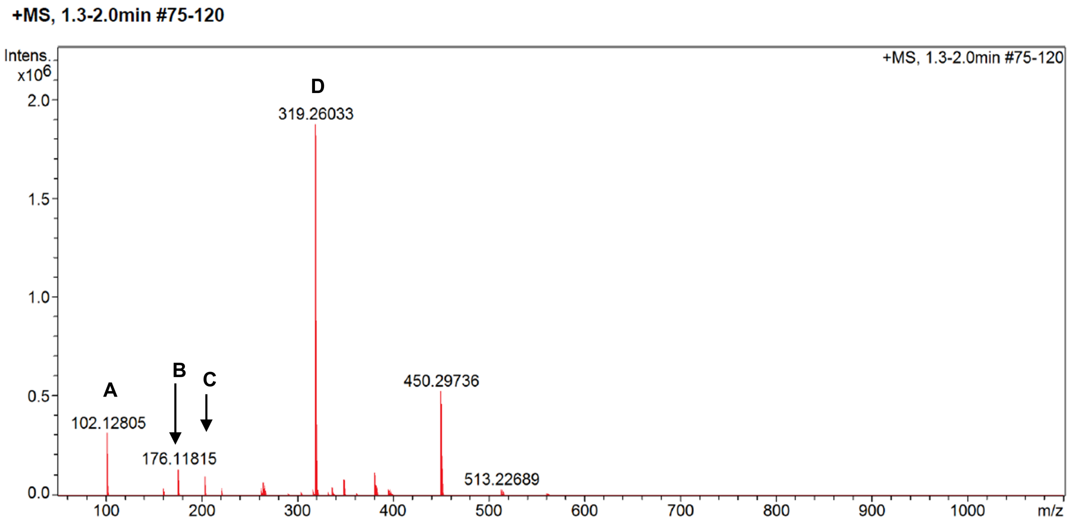

Figure 8.13: CSI-MS spectrum of the catalytic conversion of 4-quinolinol (**S4**) using [**O1**]$(PF_6)_2$ as catalyst recorded after addition of the substrate solution (THF, −80 °C).

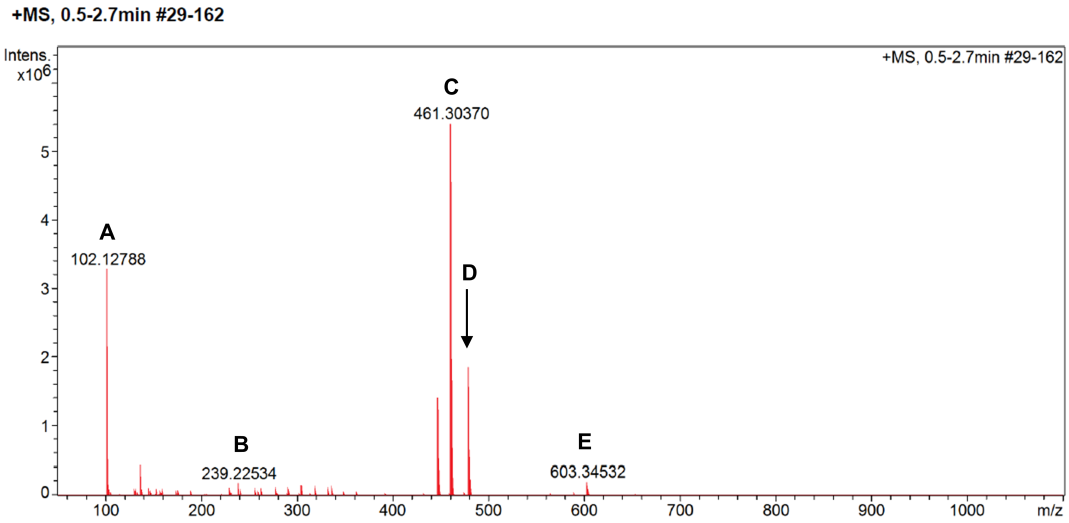

Figure 8.14: ESI-MS spectrum of the catalytic conversion of 1-naphthol (**S1**) using [**O1**](PF_6)$_2$ as catalyst (THF, −80 °C, 8 h) and subsequent condensation with 1,2-phenylenediamine (PDA) at room temperature overnight recorded after extraction of the crude reaction mixture with dichlormethane.

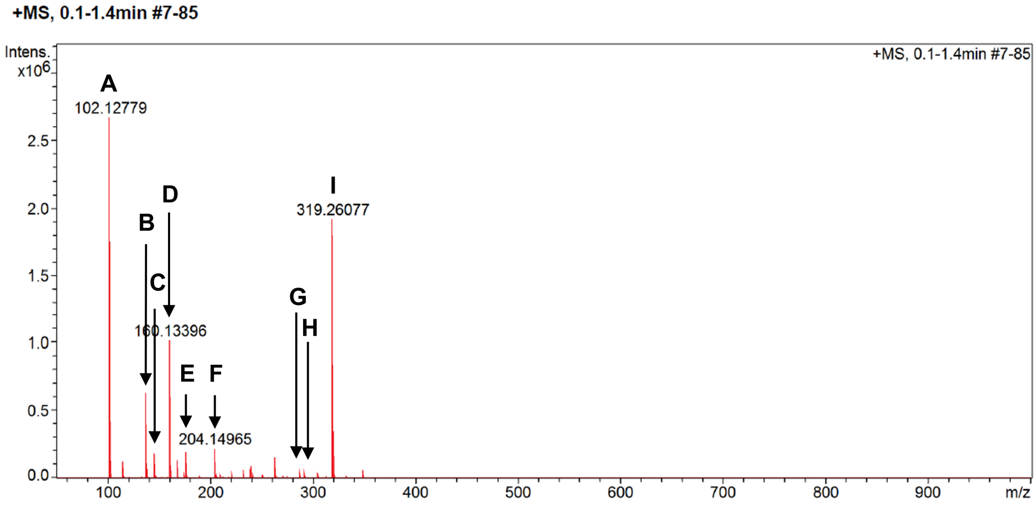

Figure 8.15: ESI-MS spectrum of the catalytic conversion of 4-quinolinol (**S4**) using [**O1**](PF_6)$_2$ as catalyst (THF, −80 °C, 8 h) and subsequent condensation with 1,2-phenylenediamine (PDA) at room temperature overnight recorded after extraction of the crude reaction mixture with dichlormethane.

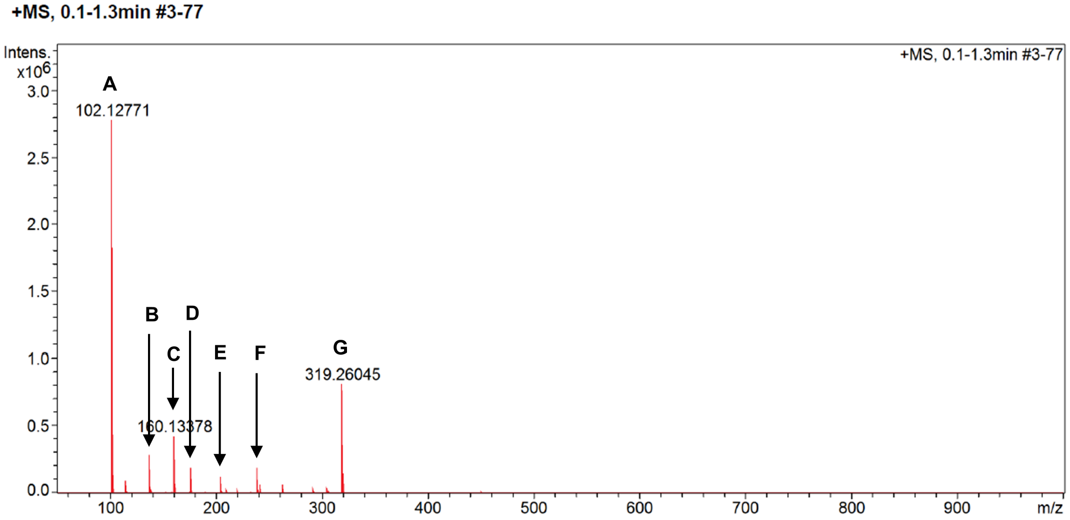

Figure 8.16: ESI-MS spectrum of the catalytic conversion of 4-indolol (**S7**) using [**O1**](PF_6)$_2$ as catalyst (THF, −80 °C, 8 h) and subsequent condensation with 1,2-phenylenediamine (PDA) at room temperature overnight recorded after extraction of the crude reaction mixture with dichlormethane.

Crystallographic Data of Cu(II)-3,5-di-*tert*-butylcatecholate-TMGdmap ([3,5-DTB-CAT3])

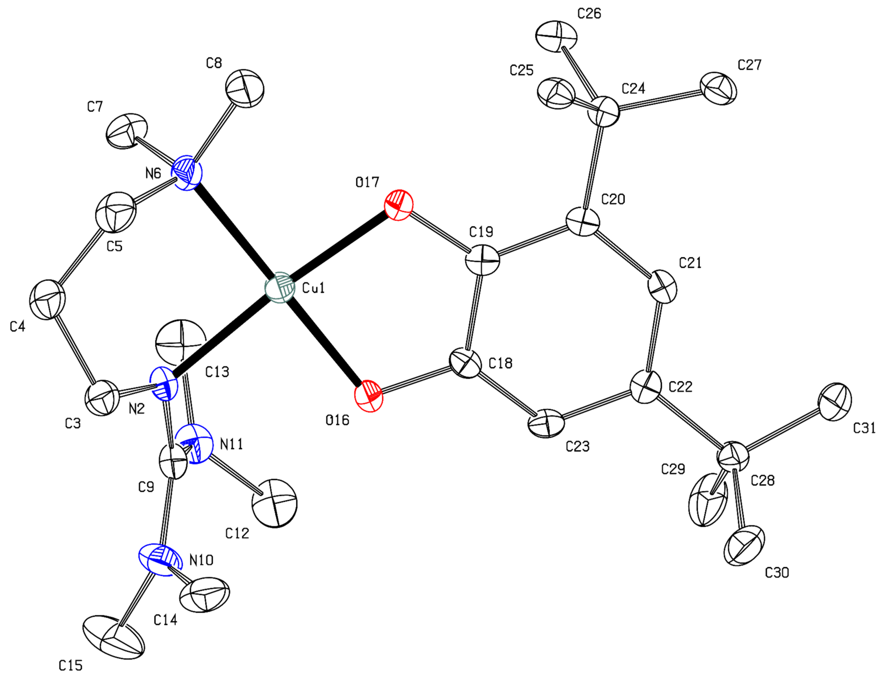

Figure 8.17: Molecular structure of Cu(II)-3,5-di-*tert*-butylcatecholate-TMGdmap ([**3,5-DTB-CAT3**]) in the solid state (ellipsoids drawn with 50% probability level). Hydrogen atoms were omitted for clarity.

Table 8.4: Crystal structure parameters of Cu(II)-3,5-di-*tert*-butylcatecholate-TMGdmap ([**3,5-DTB-CAT3**]).

	[3,5-DTB-CAT3]
empirical formula	$C_{24}H_{44}CuN_4O_2$
formula weight [g mol^{-1}]	484.17
temperature [K]	100
wavelength [Å]	0.71073
crystal system, space group	monoclinic, $P2_1/n$
a [Å]	11.772 (2)
b [Å]	12.012 (2)
a [Å]	19.510 (4)
α [°]	90
β [°]	106.58 (3)
γ [°]	90
volume [Å]	2644.3(10)
Z	4
calculated density [Mg m^{-3}]	1.216
absorption coefficient [mm^{-1}]	0.851
F(000)	1044
crystal size [mm]	0.150 x 0.110 x 0.060
hkl range	-14 ≤ h ≤14
	-14 ≤ k ≤ 13
	-20 ≤ l 23
reflections collected	57505
independent reflections	4927
R_{int}	0.0979
number of parameters	292
R_1 [$I \geq 2\sigma(I)$]	0.0384
wR_2 (all data)	0.0884
goodness-of-fit	0.937
largest diff. peak hole [eÅ^{-3}]	0.366, -0.334

Large Scale Bubble Column Studies with $[Cu_2O_2(DBED)_2](CF_3SO_3)_2$ ($[^{S}P4](OTf)_2$) and *Para*-methoxyphenol

Table 8.5: Summary of catalytic conversions performed with *para*-methoxyphenol using [^{S}**P4**]$(OTf)_2$ as catalyst (THF, rt).

entry	t	[^{S}P] : [S]: [NEt_3]	Y[a] (unconverted S)	Y[a] (product)
1	10 min	1 : 50 : 50	33%	-
2	20 min	1 : 50 : 50	62%	-
3	2 h	1 : 50 : 50	67%	-
4	2 h	1 : 50 : 50	68%	-
5	13 h	1 : 50 : 50	87%	-
6	13 h	1 : 10 : 10	25%	-
7	13 h	1 : 4 : 4	57%	-
8	24 h	1 : 10 : 10	81%	-
9	5 h	1 : 10 : 10	18%	P2 (92 mg)
10	5 h	1: 10 : 10	49%	-
11	5 h	1: 10 : 10	37%	-
12	5 h	1: 10 : 10	25%	-
13	5 h	1: 10 : 10	38%	P3 (128 mg)

[a] Isolated yield after purification via column chromatography